Scuola Dottorale di Ateneo
Graduate School Global Change Science and Policy

Dottorato di ricerca
in Scienza e Gestione dei Cambiamenti Climatici
Ciclo XXIV
Anno di discussione 2013

Sea Level changes over the Global Ocean in the XX and XXI centuries

Settore scientifico disciplinare di afferenza: FIS/06
Tesi di Dottorato di Ida Russo, matricola 955560

Coordinatore del Dottorato	Tutore del Dottorando
Prof. Carlo Barbante	Dott.ssa Simona Masina
	Co-tutore del Dottorando
	Prof. Nadia Pinardi

CONTENTS

Chapter 1
Introduction

Sea level is defined as the height of the ocean that at a particular location changes regularly with the tides and irregularly due to conditions such as wind and currents. Other factors that contribute to such variation include water temperature and salinity, atmospheric pressure, freshwater fluxes, and the amount of water that is stored as ice or snow. The global mean sea level of the oceans is one of the most important indicators of climate change and it incorporates the effects of several components of the climate system.

1.1- How can we measure sea level

Measuring the amount of sea level change during the past has been possible thanks to two types of observations: tide gauge measurements and satellite altimetry observations, the latter available only for the last two decades.

Until the early 1990s, sea level change was measured only by tide gauges along continental coastlines and mid-ocean islands. Even if tide gauge measurements are the principal dataset used to determine the historical rate of sea level change, these records suffer from some limitations due to their poor spatial distribution and large temporal gaps. Another limitation in the use of this dataset arises from the fact that in active tectonic regions, in areas subject to strong subsidence or glacial isostatic adjustment (GIA), tide gauges data are directly affected by the corresponding ground vertical motions thus creating an apparent sea level variability that is unrelated to climate variations. Thus corrections are needed to interpret tide gauge measurements in terms of absolute sea level change. Several studies have concentrated on estimating past century sea level rise from historical tide gauges. Some authors (Douglas et al., 2001; Holgate and Woodworth, 2004; Holgate 2007) considered only tide gauges located in stable continental regions away from tectonically active areas. Other authors considered larger sets of sparse tide gauges records and developed reconstruction methods (Church et al., 2004; Church and White, 2006; Llovel et al., 2009). In all these studies a global mean sea level rise of 1.7 to 1.8 mm/yr for the second half of the 20th century has been reported.

Since the early 1990s, satellite altimetry has become the main tool for precisely measuring sea level with quasi-global coverage (Nerem and Mitchum, 2001) and a continuous sampling in time with a precision of about 2 cm (Le Traon and Ogor, 1997). The satellite era began in October 1992 with the launch of TOPEX/Poseidon and ERS-1 and continues with the launch of their successors ERS-2 in 1995, Jason-1 in 2001 and Jason-2 in 2008, that have a number of improvements over previous radar altimeters and allow to improve spatial resolution by combining all these missions together (e.g., Chelton et al., 2001). Over the period 1993-2008 satellite observations have shown a strong increasing global sea level trend of 3.1 mm/yr (Ablain et al., 2009); this estimate has shown to keep constant for the period 2008-present (AVISO web site).

To visualise what discussed so far, Figure 1 from IPCC AR4 (WG1 Chapter 5, 2007) shows annual averages of global mean sea level for the 20th century based on reconstructed sea level fields from tide gauge records from 1870 to 1950, direct tide gauge measurements since 1950 and satellite altimetry data since 1992. As previously discussed and as evident from the plot, the global mean sea level has continuously increased during the last century and it was subject to a further acceleration during the last decade of the 20th century, passing from 1.7-1.8 mm/yr to 3.1 mm/yr.

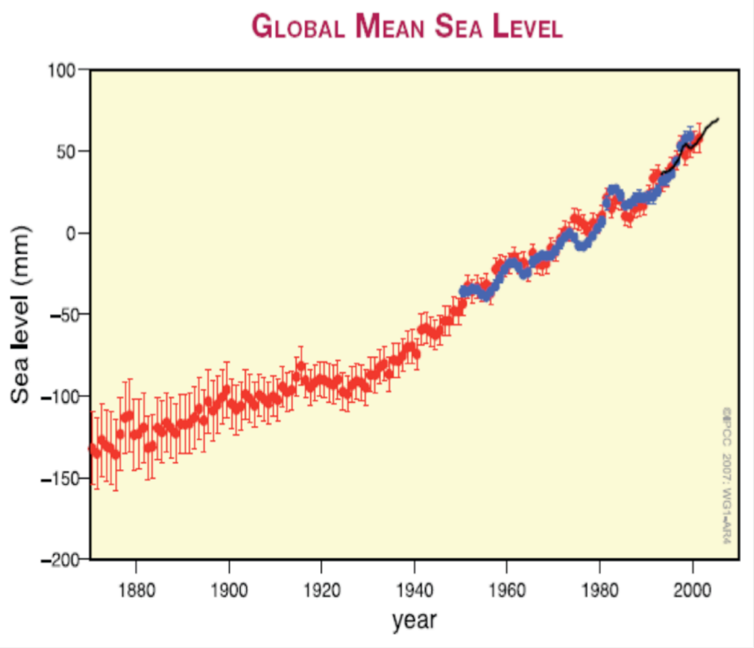

Figure 1- *Annual averages of the global mean sea level. Reconstructed sea level fields since 1870 (red curve); coastal tide gauge measurements since 1950 (blue curve) and satellite altimetry (black curve). The red and blue curves are deviations from their averages for 1961 to 1990, and the black curve is the deviation from the average of the red curve for the period 1993 to 2001 (from IPCC AR4, 2007).*

1.2- Causes of sea level change

Which are the physical processes responsible for sea level change?

The causes of global mean sea level change, on decadal and longer time scales, rely on two major processes that alter the volume of sea water. Firstly the thermal expansion of the water column, associated with an increase in the global ocean temperature, which changes the ocean water density. Secondly a change in the land-ice-ocean global water exchange, with a tiny contribution from land water reservoirs (ground water, soil water, snowpack and wetlands) and an increased freshwater income into the ocean from glaciers and ice caps (G&IC) and Greenland and Antarctica ice sheets, which produces changes in the water mass.

To have an idea of the various contribution to the budget of global sea level change, we can look at Figure 2, taken from IPCC AR4 (WG1 Chapter 5, 2007). The contribution from G&IC, from ice sheets melting and especially from the thermal expansion has increased during 1993-2003 with respect to 1961-2003. According to Cazenave and Llovel (2010), during the period 2003-2007 the highest contribution to sea level rise comes from G&IC (1.4 mm/yr) and the contribution from Greenland and Antarctica ice sheets has become even higher than that from the thermal expansion of the water column, the former causing a global mean sea level rise of 0.5 to 1.0 mm/yr while the latter a 0.25 mm/yr rising.

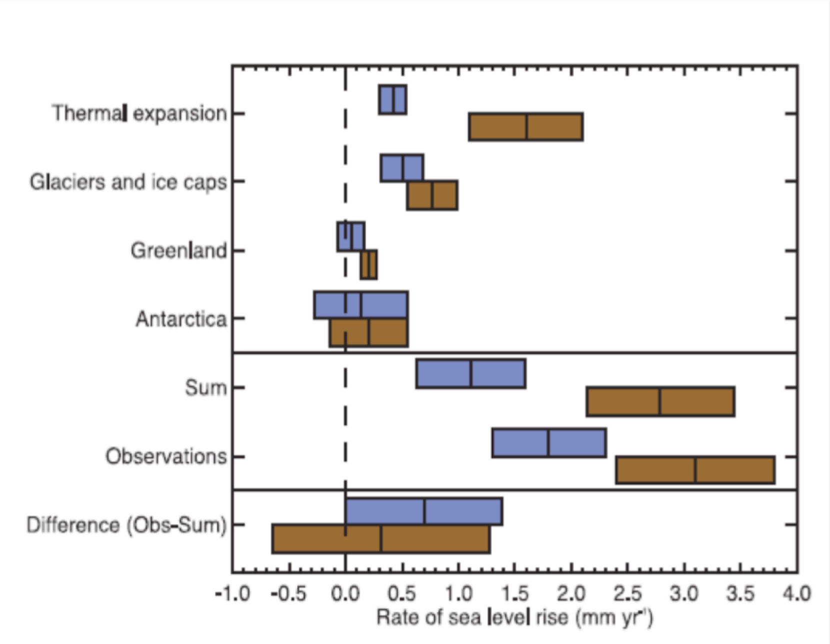

Figure 2– *Estimates of the various contributions to the budget of the global mean sea level change (upper four entries), the sum of these contributions and the observed rate of rise (middle two), and the observed rate minus the sum of contributions (lower), all for 1961 to 2003 (blue) and 1993 to 2003 (brown) (from IPCC Fourth Assessment Report, 2007).*

Satellite altimetry shows that sea level is not rising uniformly; in fact there are regions, such as the western Pacific, where rates of sea level rise are up to 3 times of the global mean rate, while other regions are characterized by sea level falling (e.g., eastern Pacific). At regional scale, the spatial patterns of sea level trends mainly result from ocean temperature and salinity changes (Bindoff et al., 2007), but also surface and deep ocean circulation changes due to variations in wind stress (Stammer, 2008), heat and freshwater fluxes play and important role in sea level regional variability. Local sea level variations are also due to other processes such as changes in atmospheric pressure (that alters sea level through the ‘inverted barometer effect’) and vertical land movements such as tectonic displacements, natural and anthropogenic subsidence and GIA effect, which is the response of the solid Earth to the last deglaciation and to the ongoing melting of land ice that give rise to secular change of the geoid (Plag, 2006; Mitrovica et al., 2009). A representation of the main processes responsible for sea level change is shown in Figure 3.

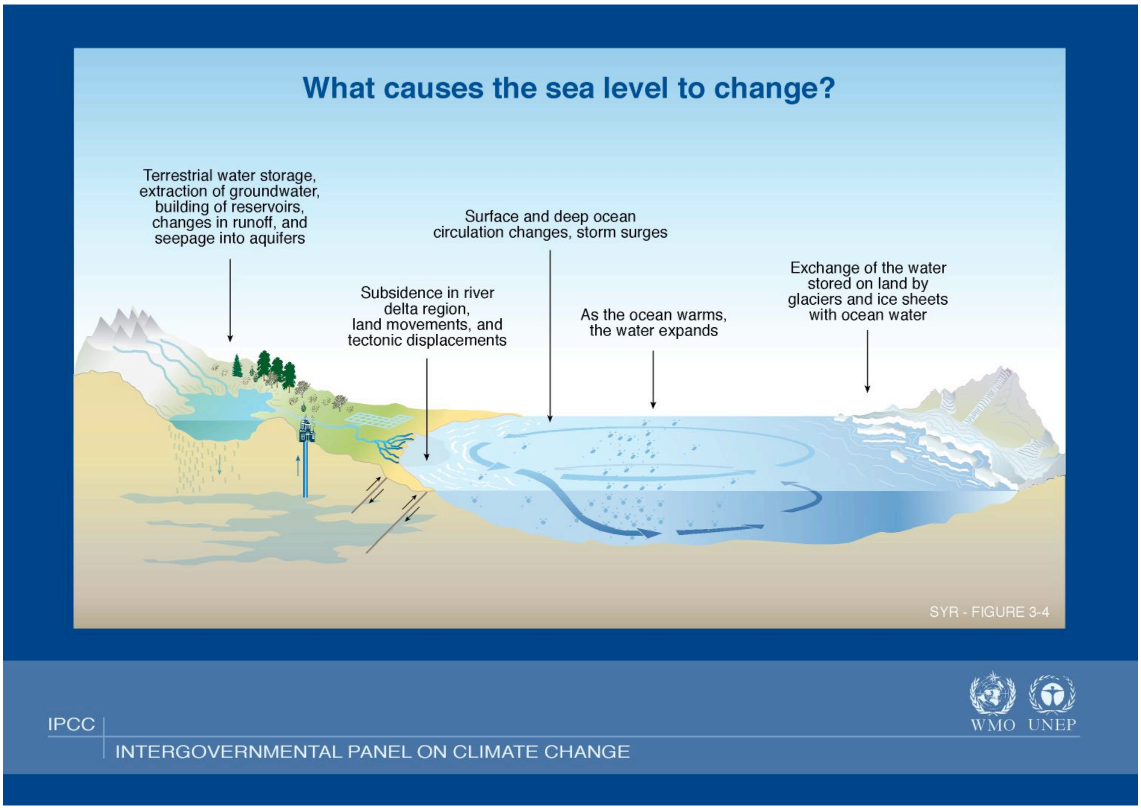

Figure 3– *Depiction of the main processes responsible for change in sea level (from IPCC Third Assessment Report, 2001).*

1.3- Why do we care about sea level change

Sea level change is a global problem involving both natural and anthropogenic changes in the climate system and in particular sea level rise is a major long-term consequence of the global warming.

The study of sea level is of great interest for several reasons. Since long-term global mean sea level changes are intimately related to variations in the mean climate state, understanding the causes of sea level change can therefore provide knowledge on how the Earth is responding to climate change. Furthermore, sea level change has important impacts on low-lying regions and, in general, on coastal areas, particularly on the vulnerable regions where a positive regional sea level trend has been observed. Thus it is crucial to determine whether this rate is accelerating and to identify the causes of the changes. Risks associated with coastal sea level rise include both socio-economic and environmental impacts. The primary environmental impacts consist in inundation and coastal flooding due to storm surge, loss of coastal wetlands, increased coastal erosion, inland saltwater intrusion into freshwater resources, changes in water quality and biological activity. Among the socio-economic impacts of sea level rise the most noticeable are: flood risk of coastal population, damages to economic and agricultural activities and loss of infrastructure.

Regions that are acknowledged to be the most vulnerable to climate-induced sea level rise together with increased frequency and intensity of extreme weather events (McCarthy et al., 2001) are the Small Islands of Pacific (Nicholls and Cazenave, 2010), due to their high population density along with the fact that the most of the territory of these islands lies few meters above the mean sea level. Furthermore their thin water lenses easily contaminated by salt water, their small size, isolation and low level of income, render these islands particularly vulnerable to sea level rise and associated impacts of climate change (Mcleod et al., 2010). The increasing rate of sea level rise and the increasing frequency and intensity of extreme weather events are likely to cause problems for the inhabitants of some of these islands during the 21st century (Nurse and Sem, 2001; Church et al., 2004; Church et al., 2006).

1.4- Sea Level change in the future

The increasing attention to the sea level rise issue is also strengthened by the fact that sea level projections from several Atmosphere-Ocean General Circulation

Models (AOGCMs) agree on an acceleration in the rate of sea level rise for the 21st century (Church et al., 2001; IPCC, 2007). Projections results, in fact, show that sea level will continue to increase at an even larger rate during the 21st century as a result of green house gases induced global warming. The mean estimate is expected to be equal to 3.8 mm/yr, which means a rise twice higher than the one experienced in the previous 100 years. It is worth to note that a significant spread is present among different AOGCMs projections, i.e. the range of variation is large, approaching a factor of 2 between the biggest and the smallest estimate. This wide range of results reflects systematic uncertainty in AOGCMs projections. One of the reasons could be that the resolutions of AOGCMs used so far are too coarse (1° to 2°) to provide realistic estimates of sea level rise and its geographical variability.

1.5- Methods and objectives of the thesis

Ocean General Circulation Models (OGCMs) are a powerful tool for the study of sea level change and have been used for a wide range of applications to sea level studies (e.g. Wunsch et al., 2007; Yin et al., 2009; Gregory et al., 2004; Lombard et al., 2009; Song et al., 2011). OGCMs give the possibility to have a global, tridimensional and physically consistent view of the ocean state. This is particularly important for estimating past sea level before the satellite altimetry era. Furthermore, also at present-day, they can provide ocean state estimation even in regions, such as the deep ocean below 1000 m of depth, where there is a lack of temperature and salinity observations, which are necessary in the estimation of density-induced sea level changes. Finally, only thanks to OGCMs simulations we have the possibility to project future sea level changes and to detect possible acceleration of sea level trend in the future. However, attention should be payed when analyzing OGCMs results, as they can bear systematic errors due, for instance, to the coarse resolution, inaccuracy of physical and numerical schemes, and to the fact that many physical phenomena are not represented. In this thesis we have analyzed past and future sea level changes over the global ocean by using an eddy-permitting OGCM, NEMO (*Nucleus for*

European Modelling of the Ocean), at a spatial resolution of 1/4° in order to have a realistic representation of sea level variability. Indeed, as demonstrated by Penduff et al. (2010), eddy-permitting spatial resolution is necessary for the correct simulation of sea level within eddy-active mid- and high- latitude regions (e.g. Gulf Stream, North Atlantic Current, Kuroshio, ACC). For example, they showed that doubling the resolution from 1/2° to 1/4° enhances the resolved sea level anomaly (SLA) variability at interannual timescales, especially in eddy-active regions.

A limit of sea level simulations performed with current OGCMs is the fact that, due to the lack of time-varying runoff measurements, land and ice sheets runoff inputs are usually climatological dataset (e.g. Dai and Trenberth, 2002; Bourdallé-Badie and Treguier, 2006). Hence, the ocean simulations do not take into account an important source of sea level change such as the ice sheets contribution. Satellite-derived ice surface elevation combined with ice flux velocity data, show in fact a rapid acceleration of ice discharge from Greenland and Antarctica ice sheets during the past two decades (Howat et al. 2007, Witze 2008). In terms of sea level rise, Greenland and Antarctica contributions are estimated to be $0.7 \pm 0.5\, mm/yr$ during the period 1993-2003 and $1.0 \pm 0.4\, mm/yr$ during 2003-2008, which means that a 40% increase in mass loss compared to 1993-2003 period occurred (Cazenave et al., 2009; Van den Broeke et al., 2011). Our work aims at addressing this important issue by creating an interannual ice sheet runoff dataset, deduced from satellite gravimetry and atmospheric model data, for further use as input in our model in order to study the response of the ocean to a realistic freshwater income from ice sheets coasts. The present study differs from the previous works for two main aspects that aim to improve the results of our simulations. First of all the eddy-permitting resolution of the OGCM used, which is necessary to simulate the coastal currents involved in the transport of the freshwater input from the coasts (Marsh et al. 2010). Then, differently from previous works designed to study the sensitivity of OGCMs to an idealized freshwater perturbation (e.g. Gerdes et al., 2005; Stammer, 2008; Yin et al., 2010; Hu et al., 2011), we have compiled a realistic monthly runoff dataset based on 2003-2010 observations of ice sheets mass loss.

A further objective of this thesis is to provide future projections of sea level for the next 20 years. This has been performed by forcing NEMO with atmospheric fluxes from the CMCC coupled model, under IPCC (Intergovernmental Panel on Climate Change) RCP4.5 emission scenario. While most of future projections are based on coupled model simulations (e.g. Landerer et al. 2007), we will rather exploit the eddy-permitting resolution of our model, which allows to resolve the mesoscale variability of sea level.

The chapters of the thesis address the following scientific questions.

Chapter 2:

- Can we improve the NEMO OGCM simulation of the ocean state, and hence of the sea level, by applying proper corrections to the heat, momentum and precipitation fluxes used to force our model? Are we able to partially recover from the model biases with this improved configuration?

Chapter 3:

- Are we able to realistically reproduce past mean sea surface height and regional sea level variability with NEMO OGCM? And hence, is our OGCM suitable for sea level studies?
- How is sea level changed in the different ocean basins during the period 1989-2010 and which regions have experienced an acceleration/deceleration in the trend during the last years?
- Which is the relative importance of the density- and mass- induced sea level changes, in terms of trends and seasonal variability, in the different ocean basins during the period 1989-2010?
- Which depth range of the water column plays the major role on sea level variability?
- Which are the causes and the physical mechanisms that bring sea level to rise

around the critical region of the Small Islands of Pacific?

Chapter 4:

- Which is a proper strategy to estimate a realistic ice sheets runoff by combining gravimetry data of water mass variation with atmospheric model water fluxes?
- Which is the sensitivity of our ocean model to the newly estimated runoff?
- Which is its impact on the simulation of sea level and its components?
- Does the use of the newly estimated runoff cause any improvement in reducing the model biases?

Chapter 5:

- How will sea level change in the next 20 years and which will be its causes, according to our eddy-permitting OGCM projections under the mitigation RCP4.5 emission scenario?
- Which is the range of uncertainties of the projections?
- At which extent the regional sea level patterns will differ from the present?

References

Ablain M., Cazenave A., Guinehut S., Valladeau G., 2009. A new assessment of global mean sea level from altimeters highlights a reduction of global slope from 2005 to 2008 in agreement with in-situ measurements. *Ocean Sciences,* 5, 193-201.

Bindoff N., Willebrand J., Artale V., Cazenave A., Gregory J., Gulev S., Hanawa K., Le Quéré C., Levitus S., Nojiri Y., Shum C.K., Talley L., Unnikrishnan A., 2007. Observations: oceanic climate and sea level. In: *Climate change 2007: The physical Science Basis. Contribution of Working Group I to the Fourth Assessment report of the Intergouvernmental Panel on Climate Change* [Solomon S., D. Qin, M. Manning, Z. Chen, M. Marquis, K.B. Averyt, M. Tignor and H.L. Miller (eds.)]. Cambridge University Press, Cambridge, UK, and New York, USA.

Bourdallé-Badie R. and Treguier A.M., 2006. A climatology of runoff for the global ocean-ice model ORCA025. Mercator-Ocean reference : MOO-RP-425-365-MER.

Cazenave A., Dominh K., Guinehut S., Berthier E., Llovel W., et al., 2009. Sea Level budget over 2003-2008: A reevaluation from GRACE space gravimetry, satellite altimetry and Argo. *Glob. Planet. Change* 65:83-88, doi:10.1016/j/gloplacha.2008.10.004.

Cazenave A. and Llovel W., 2010. Contemporary sea level rise. *Annu. Rev. Mar. Sci.*, 2(1), 145–173, doi:10.1146/annurev-marine-120308-081105.

Church J.A., Gregory J.M., Huybrechts P., Kuhn M., Lambeck K., Nhuan M.T., Qin D. and Woodworth P.L., 2001. Changes in Sea Level, In *Climate Change 2001: The Scientific Basis. Contribution of Working Group 1 to the Third Assessment Report of the Intergovernmental Panel on Climate Change* (eds. J.T. Houghton, Y. Ding, D.J. Griggs, M. Noguer, P. van der Linden, X. Dai, K. Maskell and C.I. Johnson).

Cambridge University Press, Cambridge DI.

Church J.A., White N.J., Coleman R., Lambeck K., Mitrovica J.X., 2004. Estimates of the regional distribution of sea-level rise over the 1950 to 2000 period. *J. Clim.* 17(13):2609–25.

Church J.A. and White N.J., 2006. A 20th century acceleration in global sea-level rise. *Geophys. Res. Lett. 33,* doi:10.1029/2005GL024826.

Church J.A.,White N.J., Hunter J.R., 2006. Sea-level Rise in the tropical Pacific and Indian Ocean islands. *Global and Planetary Change, Volume 53, Issue 3*, September 2006, 155-68. doi:10.1016/j.gloplacha.2006.04.001.

Dai A. and Trenberth K.E., 2002. Estimates of freshwater discharge from continents: Latitudinal and seasonal variations. *J. Hydrometeorol.*, 3, 660-687.

Douglas, B. C., 2001. Sea level change in the era of the recording tide gauge. In *Sea Level Rise, History and Consequences*, edited by B. C. Douglas, M. S. Kearney, and S. P. Leatherman, pp. 37–64, Academic, San Diego, Calif.

Gregory J.M., Banks H.T., Stott P.A., Lowe J.A., Palmer M.D., 2004. Simulated and observed decadal variability in ocean heat content. *Geophys. Res. Lett.*, 31, L15312, doi:10.1029/2004GL020258.

Gerdes R., Hurlin W., and Griffies S. M., 2006. Sensitivity of a global ocean model to increased run-off from Greenland. *Ocean Modell.,* 12, 416–435.

Holgate S., 2007. On the decadal rates of sea level change during the twentieth century. Geophys. Res. Lett. 34:L01602, doi:10.1029/2006GL028492.

Holgate S. J. and Woodworth P. L., 2004. Evidence for enhanced coastal sea level rise during the 1990s. *Geophys. Res. Lett., 31*(L07305), doi:10.1029/2004GL019626.

Howat I.M., Joughin I.R., Scambos T.A., 2007. Rapid changes in ice discharge from Greenland outlet glaciers. *Science* 315:1559-61, doi:10.1126/science.1138478.

Hu A., Meehl G. A., Han W., and Yin J., 2011. Effect of the potential melting of the Greenland Ice Sheet on the Meridional Overturning Circulation and global climate in the future, *Deep Sea Res. Part II,* 58,1914-1926.

IPCC, 2007: Climate Change 2007: The Physical Science Basis. Contribution of Working Group I to the Fourth Assessment Report of the Intergovernmental Panel on Climate Change [Solomon, S., D. Qin, M. Manning, Z. Chen, M. Marquis, K.B. Averyt, M.Tignor and H.L. Miller (eds.)]. Cambridge University Press, Cambridge, United Kingdom and New York, NY, USA.

Landerer F. W., Jungclaus J. H., Marotzke J., 2007. Regional dynamic and steric sea level change in response to the IPCC-A1B scenario. *J. Phys. Oceanogr.* 37, 296312.

Le Traon P.Y. and Ogor F., 1997. ERS-1 orbit improvement using TOPEX/POSEIDON: the 2 cm challenge. *J. Geophys. Res.*

Llovel W., Cazenave A., Rogel P., Berge-Nguyen M., 2009. 2-D reconstruction of past sea level (1950–2003) using tide gauge records and spatial patterns from a general ocean circulation model. *Clim. Past.* 5:1–11.

Lombard A., Garric G., Penduff T., 2009. Regional patterns of observed sea level change: insights from a 1/4 global ocean/sea-ice hindcast. Ocean Dynam., 59, 3, 433–

449, doi:10.1007/s10236-008-0161-6.

Marsh R., Desbruyères D., Bamber J. L., De Cuevas B. A., Coward A. C., Aksenov Y., 2010. Short-term impacts of enhanced Greenland freshwater fluxes in an eddy-permitting ocean model, *Ocean Sci., 6, 749-760.*

McCarthy J., Canziani O., Leary N., Dokken D., White K., 2001. Climate Change 2001: Impacts, Adaptation & Vulnerability. *Cambridge University Press*, Cambridge.

Mcleod E., Poulter B., Hinkel J., Reyes E., Salm R., 2010. Sea-level rise impact models and environmental conservation: A review of models and their applications- *Ocean Coast. Manage.*, 53, 507–517, doi:10.1016/j.ocecoaman.2010.06.009.

Mitrovica J.X., Gomez N., Clark P.U., 2009. The sea-level fingerprint of West Antarctic collapse. *Science*, Vol. 323, p. 753.

Nerem S., Leuliette E., Cazenave A., 2006. Present-day sea level change. *C.R. Geosci.* 338:1077–83.

Nicholls R.J. and Cazenave A., 2010. Sea-level rise and its impact on coastal zones. *Science* 328, 1517.

Nurse L. and Sem G., 2001. "Small Islands States" in McCarthy J., Canziani O., Leary N., Dokken D., White K., 2001. Climate Change 2001: Impacts, Adaptation & Vulnerability. *Cambridge University Press*, pp. 842-875.

Penduff T., Juza M., Brodeau L., Smith G. C., Barnier B., Molines J.-M., Treguier A.-M., Madec G., 2010. Impact of global ocean model resolution on sea-level variability with emphasis on interannual time scales. *Ocean Sci.*, 6, 269–284, doi:10.5194/os-6-269-2010.

Plag H.P., 2006. Recent relative sea level trends; An attempt to quantify forcing factors. *Phil. Trans. Roy, Soc. Lond*, A, 364, 1841-1869.

Song Y. T. and Colberg R., 2011. Deep ocean warming assessed from altimeters, gravity recovery and climate experiment, in situ measurements, and a non-Boussinesq ocean general circulation model. *J. Geophys. Res.* 116, C02020.

Stammer D., 2008. Response of the global ocean to Greenland and Antarctica melting. *J. Geophys. Res.,* 113, C06022, doi:10.1029/2006JC001079.

Van den Broeke M.R., Bamber J., Lenaerts J., Rignot E., 2011. Ice sheets and sea level: thinking outside the box. *Sur. Geophys.* 32 495–505, doi 10.1007/s10712-011-9137-z.

Witze A., 2008. Loosing Greenland. Science 452:798-802.

Wunsch C., Ponte R.M., Heimbach P., 2007. Decadal trends in sea level patterns: 1993–2004. *J. Clim.*, 20, 5889–5911, doi:10.1175/2007JCLI1840.1.

Yin J., Schlesinger M.E., Stouffer R.J., 2009. Model projections of rapid sea-level rise on the northeast coast of the United States. *Nat. Geosci.*, 2, 262–266, doi:10.1038/NGEO468.

Yin J., Stouffer R. J., Spelman M. J., Griffies S. M., 2010. Evaluating the uncertainty induced by the virtual salt flux assumption in climate simulations and future projections. *J. Clim.* 23, 80-96. doi:10.1175/2009JCLI3084.1.

Chapter 2

Validation of NEMO-ORCA025 and correction of forcing fields

Abstract

In this Chapter the impact of heat, momentum and precipitation forcing field corrections on NEMO Ocean General Circulation Model (OGCM) simulations, at 1/4 degree resolution, is discussed. A bulk formulation was adopted as forcing method; the experiments were forced by 3-hourly ERA-Interim turbulent fluxes and daily radiative and freshwater fluxes. The general approach is to compare ERA-Interim fields with observational datasets for certain periods to deduce spatially-varying climatological corrective factors.

Large-scale downward short-wave (SW) and long-wave (LW) radiation fluxes have been corrected by means of a large-scale climatological correction coefficient derived by the GEWEX Surface Radiation Budget (SRB) dataset for the period 1999-2007. The correction is verified also against the experiment that directly uses GEWEX data as forcing radiation dataset. The radiation correction was proved to have a positive impact on the reduction of the surface and near-surface warm temperature bias in the Antarctic Circumpolar Current (ACC) region and in the Tropics, especially in correspondence of the eastern upwelling areas.

With regards to scatterometer climatologies, wind stress fields calculated from ERA-Interim wind velocities were found systematically underestimated within the 40°S-40°N latitudinal belt and overestimated elsewhere. For this reason, two alternative approaches are evaluated: i) the correction of 10 meter wind speed prior to the wind stress calculation – to recover from ERA-Interim wind biases; ii) the correction of the wind stress after the bulk formula application – to recover from the bulk formula weaknesses. Both corrective coefficients are derived from the SCOW QuickScat monthly climatology averaged over the period 1999-2009. Only the wind stress correction yields a slightly positive impact on the near-surface circulation, by increasing the underestimated near-surface current speed in the Tropical Ocean.

Finally, since ERA-Interim exhibits a systematic overestimation of precipitation in the ITCZs and underestimation in mid- and high- latitude areas, ERA-Interim precipitation fluxes have been corrected by means of a climatological monthly coefficient, computed within the period 1989-2008 by comparison between ERA-Interim and the Remote Sensing Systems (REMSS) Passive Microwave Water Cycle (PMWC) precipitation product. The correction reduces the near-surface salinity fresh bias in the Tropics and improves the representation of the sea-level variability, especially in the Southern Ocean.

2.1- Model description and configuration

The ocean general circulation model (OGCM) used in this study is NEMO (Nucleus for European Modelling of the Ocean) v3.2.1 (Madec, 2008) in ORCA025-L50 configuration, coupled to LIM2 (Louvain-la-Neuve) sea-ice model (Fichefet and Morales Maqueda, 1997).

2.1.1- Grid

The model has 1442x1021 grid points on a tripolar irregular grid with two artificial poles on the North American and Asian continents. The horizontal resolution has a constant value of 1/4° in the zonal direction: the corresponding resolution in km ranges from 5.6 km at poles to 27.8 km at equator. The meridional resolution is equal to 1/4° of latitude at equator and it increases poleward.

The vertical meshing consists of 50 levels ranging from 0.5 m to 5727.9 m of depth with partial steps at the bottom. There are 10 levels up to 15 m and 22 levels up to 100 m. The spacing between the vertical levels ranges from 1m at the surface up to 458 m at the bottom.

2.1.2- Boundary conditions

The lateral boundary condition on momentum allows for a free slip. For the upper boundary a filtered linear free-surface formulation has been used. At the ocean bottom, a non-linear friction (Treguier 1992) is assumed and no geothermal heat flux is considered. The bathymetry used combines the GEBCO bathymetry, for coastal and shelf areas, and the ETOPO2 used for the deep ocean below 300 m (Molines et al., 2007).

2.1.3- Physics

Concerning the physics of the model the Turbolent Eddy Kinetic (TKE) dependent vertical diffusion scheme has been used to compute the eddy vertical mixing coefficient. The vertical parameterizations include: i) the Enhanced Vertical Diffusion

(EVD) scheme, ii) double diffusion mixing parameterization for temperature and salinity, iii) a mixing length scale surface value as function of wind stress.

Furthermore the solar radiation penetration scheme depends on the chlorophyll concentration (Lengaigne et al., 2007). We used a monthly chlorophyll climatology (1999-2005) derived from the Sea-Viewing Wide-Field Sensor (SeaWiFS) on the OrbView-2 satellite . The use of chlorophyll data was proved to improve the model representation of the sea surface temperature and its vertical profile.

For the lateral mixing of tracers we used the Total Variation Diminishing (TVD) scheme and a laplacian isopycnal lateral diffusion scheme with horizontal eddy diffusivity equal to $300 m^2/s$ (the coefficient is grid size dependent). The lateral viscosity of momentum is parametrized with a bilaplacian operator and a horizontal eddy viscosity coefficient equal to $-1 x 10^{11} m^2/s$, in accordance with the sensitivity experiments performed within the DRAKKAR Project (Molines et al., 2007). The coefficient is grid size power 3 dependent. More details about the model configuration can be found in Barnier et al. 2006.

2.1.4- Surface forcing fields and reference experiment setup

The reference experiment (hereafter called CTRL) consists of a 32-year (1979-2010) simulation initialized from rest and from the National Oceanographic Data Center (NODC) World Ocean Atlas 1998 Series (Levitus et al., 1998) monthly climatology of temperature and salinity fields, blended with the Polar science center Hydrographic Climatology (PHC2.1, Steele et al., 2001) climatology for the polar regions. The LIM2 sea-ice model has been initialized with sea-ice cover from the National Snow and Ice Data Centre and other sea-ice parameters (ice-thickness, ice-temperature, snow-thickness) from the Mercator-Ocean GLORYS1V1 ocean reanalyses (Ferry et al., 2010).

The CTRL simulation has been performed with the CORE bulk-formulas forcing method (Large and Yeager, 2008) by using 3-hourly turbulent fluxes and daily radiative and freshwater fluxes from ERA-Interim (Simmons et al., 2007).

The following atmospheric variables have been used:

- 3-hourly turbulent variables (wind vector at 10 m above mean sea-level; temperature and specific humidity at 2 m above mean sea-level);
- daily radiative fluxes variables (downward shortwave and downward longwave radiation); the diurnal cycle of shortwave radiation is modulated according to an analytical formulation proposed Bernie et al. (2007);
- daily fresh water flux variables (total precipitation and snow).

All the forcing fields are provided by the European Centre for Medium-Range Weather Forecast (ECMWF) ERA-Interim atmospheric reanalysis project (Simmons et al., 2007). For the river runoff, the monthly climatology of Bourdalle-Badie and Treguier (2006), derived from Dai and Trenberth (2002), that includes 99 major rivers and coastal runoff was used.

2.2- Forcing corrections

Several corrections have been applied to the forcing fields in order to improve the model representation of the ocean state. Large-scale downward short-wave and long-wave radiation fluxes have been corrected by means of a large-scale climatological correction coefficient (Garric and Verbrugge, 2010) derived by the Global Energy and Water Cycle Experiment (GEWEX) Surface Radiation Budget (SRB) project (Stackhouse et al., 2011).

Two options have been considered for potentially improving the momentum flux. A first experiment has been performed by adjusting the wind stress magnitude by means of a climatological correction coefficient derived from the SCOW (Scatterometer climatology of Ocean Winds) QuickScat monthly climatology (Risien and Chelton, 2008) averaged over the period 1999-2009; in a second experiment the wind speed was instead re-calibrated from the same dataset, which also provides 10 m wind speed estimates.

ERA-Interim precipitation fluxes have been corrected by means of a spatially-varying climatological monthly coefficient, computed within the period 1989-2008 by comparison between of ERA-Interim and the Remote Sensing Systems (REMSS) Passive Microwave Water Cycle (PMWC) precipitation product (Hilburn, 2009).

Furthermore, in order to avoid artificial drifts of the globally-averaged sea-surface height due to the unbalanced fresh water budget, the global average of evaporation minus precipitation minus runoff has been forced to be equal to zero at each model time-step.

In the following Section we will explore the impact of these corrections on the simulation of the ocean state. The characteristics of the experiments are summarized in Table 1.

2.2.1- Radiation

The net shortwave (SW) and longwave (LW) radiations are calculated in NEMO model by bulk formulas (1) and (2) respectively (Gill, 1982):

$$Q_S = Q_{DS}(1-\alpha) \tag{1}$$

$$Q_L = Q_{DL} - \sigma(SST)^4 \tag{2}$$

where Q_{DS} is the downward SW radiation, i.e. the solar insolation incident on the ocean surface; α is the ocean albedo; Q_{DL} is the downward LW radiation and $\sigma = 5.67 \cdot 10^{-8}\, W/(m^2 \cdot K^4)$ is the Stefan-Boltzmann constant.

By using ERA-Interim SW and LW radiations forcing (CTRL experiment), the model representation of sea surface temperature (SST) and near-surface temperature show several biases with respect to independent observational datasets, as described in details in paragraph 2.4. In general the model shows cold biases at mid-latitudes (20° - 50°) and warm biases at high latitudes and in the Tropics (20°S – 20°N), with peaks in correspondence of the eastern upwelling regions.

In the attempt to reduce model biases we have corrected the large-scale downward SW and LW ERA-Interim radiation fluxes by means of a large-scale climatological correction coefficient derived by the GEWEX SRB project, as proposed by Garric and Verbrugge (2010), which represent a high quality radiation dataset. The motivation is to keep the accurate representation of the small-scale processes that the high resolution ERA-Interim forcing allow for, differently from GEWEX data, and that the eddy-permitting resolution of NEMO in ORCA025 configuration is able to simulate. The SRB Program of GEWEX provides a dataset of 1°x1° gridded surface longwave and shortwave radiations for the period 1983-2007. The dataset is produced using satellite-derived cloud parameters and ozone fields from many different space missions. Full description of the algorithm for the surface radiance calculation are given in Pinker and Laszlo (1992) for the shortwave radiation algorithm and Fu et al. (1997) for the longwave radiation algorithm. Cloud data are in turn taken from the International Satellite Cloud Climatology Project (ISCCP) and the processing takes massive advantage of all geostationary and polar-orbiting available satellite observations. Prior to July 1998 there is no coverage of geostationary satellite products on the Indian Ocean, which affects the quality of the data in that region.

By comparison between ERA-Interim and GEWEX downward radiative fluxes (not shown) we found that ERA-Interim shows higher values of downward SW radiation between 40°N–60°N, in the Antarctic Circumpolar Current (ACC) and in the tropical upwelling areas (where the positive bias reaches peaks of more then $20\,W/m^2$), while it shows lower values with respect to GEWEX downward SW radiation within the tropical latitudes band; the ERA-Interim downward LW radiation is also smaller than GEWEX except at higher latitudes and in the Equatorial Pacific.

The correction procedure is the following: first we use a low-pass Shapiro filter to split the ERA-Interim (LW and SW) radiations into large-scale and small-scale components (the filter has been tuned to attenuate the signal amplitude, at the spatial scales of 900 km, by 20%); then the large-scale component is multiplied by a corrective coefficient and summed to the small-scale component in order to obtain the new corrected radiative fluxes:

$$Rad_{corr} = coeff \cdot Rad_{LS}^{Ei} + R_{SS}^{Ei} \tag{3}$$

where *Rad* indicates either the SW or the LW radiations.

The corrective coefficient is calculated as the ratio between the daily climatology of GEWEX and ERA-Interim radiations, computed over the period 1999-2007:

$$coeff = \frac{\overline{Rad_{LS}^{Gewex(1999-2007)}}}{\overline{Rad_{LS}^{Ei\,(1999-2007)}}} \tag{4}$$

Due to a systematic overestimation of GEWEX climatological zonal mean radiation between 40°S and 40°N (Large and Yeager, 2004), the LW and SW radiations have been reduced by 3% and 6%, respectively, within this latitudinal belt, as proposed by Large and Yeager (2004).

2.2.2- Wind stress and wind speed

The wind stress $\vec{\tau_{as}}$ is parametrized by bulk formula (5) in terms of the atmosphere density ρ, the drag coefficient C_D and the difference $\Delta\vec{U} = \vec{U}_{10} - \vec{U}_O$ between the wind velocity at 10 m above the sea surface ($\vec{U}_{10}$) and the ocean current at the sea surface ($\vec{U}_O$):

$$\vec{\tau_{as}} = \rho C_D |\Delta\vec{U}| \Delta\vec{U} \tag{5}$$

The drag coefficient depends on the atmospheric stability and it is formulated in accordance with Large and Yeager (2008).

Wind stress field calculated from ERA-Interim wind at 10 m were found to be systematically underestimated within the 40°S-40°N latitudinal belt and overestimated polewards. In the attempt to reduce model biases we have tested, separately, the correction of both the 10 m ERA-Interim wind speed and wind stress magnitude through comparison with the Scatterometer Climatology of Ocean Winds (SCOW) QuickScat data. The SCOW dataset (Risien and Chelton, 2008) consists of a monthly climatology of both wind stress at sea surface and 10 m wind speed computed from the QuickScat scatterometer data, by using regression coefficient deduced from the comparison between in-situ observations and scatterometer measurements.

We have firstly calculated two monthly climatological corrective coefficients over the period 1999-2009 (shown in Figure 1), by comparing SCOW QuickScat wind speed with ERA-Interim 10 m wind speed (equation (6)) and SCOW QuickScat wind stress with bulk estimated wind stress (equation (7)). In the former case the correction aims to adjust the input wind field without modifying the bulk formulation itself, while the latter approach is intended to recover from the bulk formula inaccuracies. The two coefficients can be formalized as:

$$coeff1=\sqrt{\frac{\overline{u(qscat)^2+v(qscat)^2}^{(1999-2009)}}{\overline{u(Ei)^2+v(Ei)^2}^{(1999-2009)}}} \tag{6}$$

$$coeff2=\sqrt{\frac{\overline{\tau_x(qscat)^2+\tau_y(qscat)^2}^{(1999-2009)}}{\overline{\tau_x(bulk)^2+\tau_y(bulk)^2}^{(1999-2009)}}} \tag{7}$$

We have then multiplied the climatological coefficients by the time-varying zonal and meridional wind velocities (wind stress) to obtain the corrected wind speed (wind stress) fields:

$$(u)_{corr}=u(Ei)*coeff1 \tag{8}$$

$$(v)_{corr}=v(Ei)*coeff1 \tag{9}$$

$$(\tau_x)_{corr}=\tau_x(bulk)*coeff2 \tag{10}$$

$$(\tau_y)_{corr}=\tau_y(bulk)*coeff2 \tag{11}$$

where u (τ_x) and v (τ_y) are the zonal and meridional components of the wind speed (stress). Both the corrections have been applied between 60°S–60°N. In general the wind speed coefficient has higher absolute values with respect to the wind stress coefficient (Figure 1), namely the differences between ERA-Interim and SCOW wind speed are greater than the differences between the wind stress calculated by the bulk formula and SCOW wind stress.

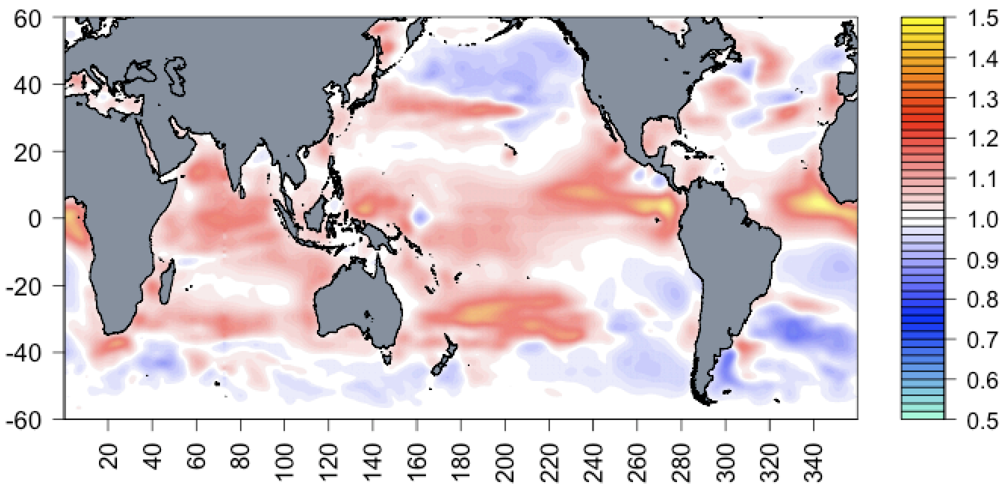
Wind Stress corrective factor, climatology 1999-2009

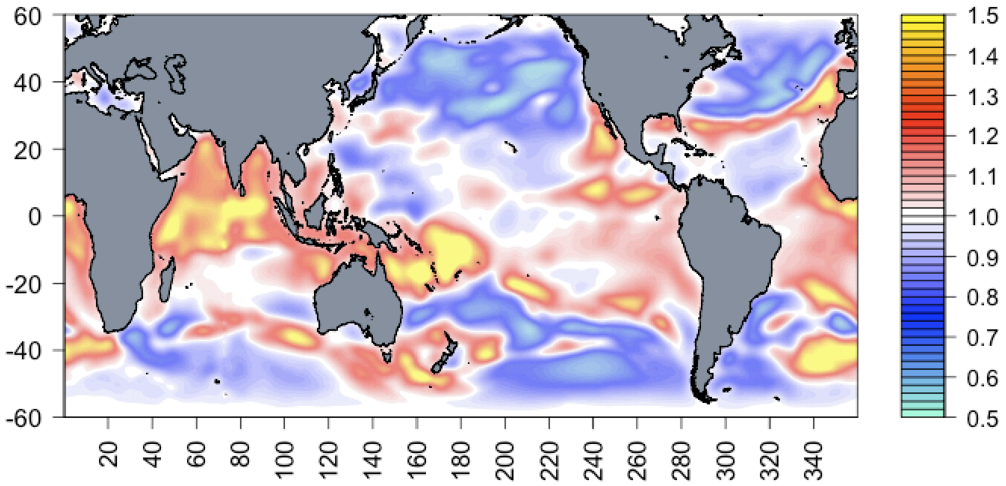
Wind Velocity corrective factor, climatology 1999-2009

Figure 1– *Climatology of the wind stress (top) and wind speed (bottom) corrective coefficients, as formulated in Section 2.2.2, over the period 1999-2009. Positive (negative) values indicate that ERA-Interim wind stress/speed is underestimated (overestimated) with respect to SCOW QuickScat data.*

This might be due to the effect of the bulk formula to attenuate the wind speed biases or to the inaccuracy of the QuickScat derived wind speed. Note that, in both cases, only the module and not the direction of the wind is corrected. This choice has been adopted because of the low accuracy of the wind direction data from scatterometers.

2.2.3- Precipitation

The daily ERA-Interim precipitation fluxes have been corrected by means of a monthly climatological coefficient, inferred from the comparison between the ERA-Interim precipitation and the satellite-based Passive Microwave Water Cycle (PMWC) precipitation product. PMWC is produced by Remote Sensing Systems (REMSS) in the frame of the NASA Energy and Water Cycle Study (Hilburn, 2009). PMWC data of precipitation are essentially rain rate retrievals from the instruments Special Sensor Microwave/Imager (SSM/I) on board the satellites of the United States Air Force Defense Meteorological Satellite Program (DMSP) according to Hilburn and Wentz (2008), with snow adjustments at high latitudes. The latter are based on the comparison between uncorrected PMWC and GPCP rain rates.

The monthly climatological coefficient c is calculated as:

$$c = \left\langle \left(10^3 \frac{\exp(P_M^{LS})}{\exp(P_E^{LS})} \right) - 10^3 \right\rangle_{1989-2008} \tag{12}$$

where P_M^{LS} and P_E^{LS} are the large-scale precipitation values from REMSS/PMWC and ECMWF/ERA-Interim, respectively, and $\langle \dots \rangle_{1989-2008}$ denotes the temporal mean over the period 1989-2008. c is spatially-varying and computed at the full model horizontal resolution; the value 10^3 is a normalization factor. The daily-corrected values P used within the ocean model are then computed as:

$$P = P_E^{SS} + \log\{(10^{-3}[10^3 + c])\exp(P_E^{LS})\} \tag{13}$$

where the upper-script SS stands for small scale. In both equation (12) and (13) the separation between small and large scales is obtained through the application of a two-dimensional low-pass Shapiro filter. The low-pass filter was applied in an attempt of neglecting precipitation location error and consistently with the wish of keeping ERA-Interim small scales as explained formerly. In equation (13), the monthly corrective coefficient of equation (12) is linearly interpolated in time to provide daily values.

In Figure 2 contours of the precipitation corrective coefficient are shown as a function of latitude and month. A value of zero means that the correction is not needed, while positive (negative) values indicate that ERA-Interim underestimates (overestimates) the precipitation with respect to the satellite-based precipitation. The zonal averages show that the precipitation is enforced more in the Arctic than in the Antarctic, and maxima of the positive correction are found for the Arctic area in the winter season.

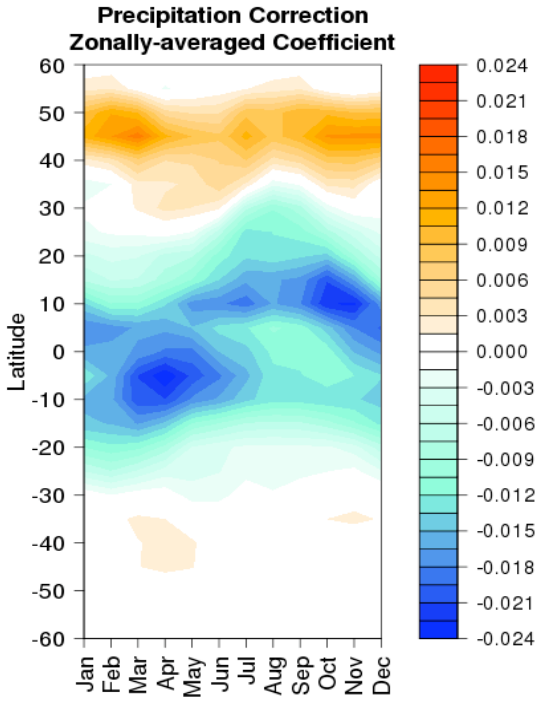

Figure 2- *Contours of the zonally-averaged climatological precipitation corrective coefficient as a function of latitude and months. The coefficient is calculated as explained in Section 2.2.3. Positive (negative) values indicate that ERA-Interim precipitation is underestimated (overestimated) with respect to REMSS/PMWC data.*

2.3- Experiments set up

In the attempt to have a more accurate representation of the sea surface and subsurface temperature, we adopted two approaches applied in different experiments. The first approach, adopted in the RAD_GWX experiment, consists in the direct use of GEWEX downward LW and SW radiations instead of ERA-Interim ones; the second, used in the RAD_CORR experiment, is the approach adopted by Garric and Verbrugge (2010), which consists in the correction of the large-scale downward SW and LW ERA-Interim radiation fluxes by means of the large-scale climatological correction coefficient introduced in Section 2.2.1. The correction is applied south of 65°N because at higher latitudes the geostationary satellite do not provide reliable data. Both the experiments started in 1989 from the ocean state of the CTRL run; RAD_GWX experiment ended in 2007 since GEWEX data are not available afterwards, while for the RAD_CORR experiment we have extended the simulation period up to 2010.

In order to have a better simulation of ocean circulation, two approaches have been tested in two different 22-year (1989-2010) experiments, whose methodology is detailed in Section 2.2.2. Both the experiments started in 1989 from the ocean state of the CTRL run. In the first experiment (called WSP_CORR) the 10 m ERA-Interim wind speed field has been corrected following equations (8) and (9), while in the second experiment (called WSTR_CORR) the wind stress magnitude was instead adjusted according to equations (10) and (11).

The ERA-Interim precipitation correction explained in the previous Section, has been tested in the PREC_CORR experiment. The experiment is a 21-year simulation (1989-2009) initialized from a 5-year spinup. The spinup started from rest and from Levitus98 monthly climatology of temperature and salinity. In this experiment 6-hourly ERA-Interim turbulent fluxes and daily ERA-Interim freshwater fluxes have been used.

2.4- Results and model validation

2.4.1- Impact of downward SW and LW radiation corrections

In Figure 3 the difference between SST climatology (1989-2007) of the CTRL, RAD_CORR and RAD_GWX experiments with respect to Reynolds SST dataset (Reynolds et al., 2007) are shown. As mentioned in Section 2.2.1, the CTRL experiment (Figure 3 top panel) shows warm SST biases at high latitudes and in the Topical belt (20°S-20°N), reaching peaks of more than 2°C in correspondence of the upwelling areas in the eastern Pacific and Atlantic Oceans, in the Labrador Sea and in some areas of the ACC region; cold biases are evident at mid-latitudes (20°-50°).

By using GEWEX downward SW and LW radiations instead of ERA-Interim ones (Figure 3 bottom panel) the tropical warm bias increases even more, spreading toward higher latitudes, while some benefits are visible in the ACC region and in proximity of the Bering Strait. The reason of the RAD_GWX experiment warming resides on the increased net SW radiation flux (Figure 4 bottom panel) that in correspondence of the Tropics is higher than the CTRL experiment radiation by up to $20\, W/m^2$; the net LW radiation also contributes, to a lesser extent, to the increase of the warm bias in the Tropics (Figure 5 bottom panel). On the other hand, the weaker SW and LW radiations at high latitudes in the RAD_GWX experiment produces a cooling of SST therein, which is found in better agreement with the observed SST.

Similar improvements at high latitudes are also visible in the RAD_CORR experiment (Figure 3 middle panel), with the addition that also the warm bias in the Tropical Pacific, in the Indian Ocean and in correspondence of the upwelling areas are strongly attenuated by approximately 1°C. In correspondence of these regions, in fact, the net SW (Figure 4 top panel) and LW radiations (Figure 5 top panel) present smaller values with respect to CTRL experiment ones, with peaks of less than $-20\, W/m^2$.

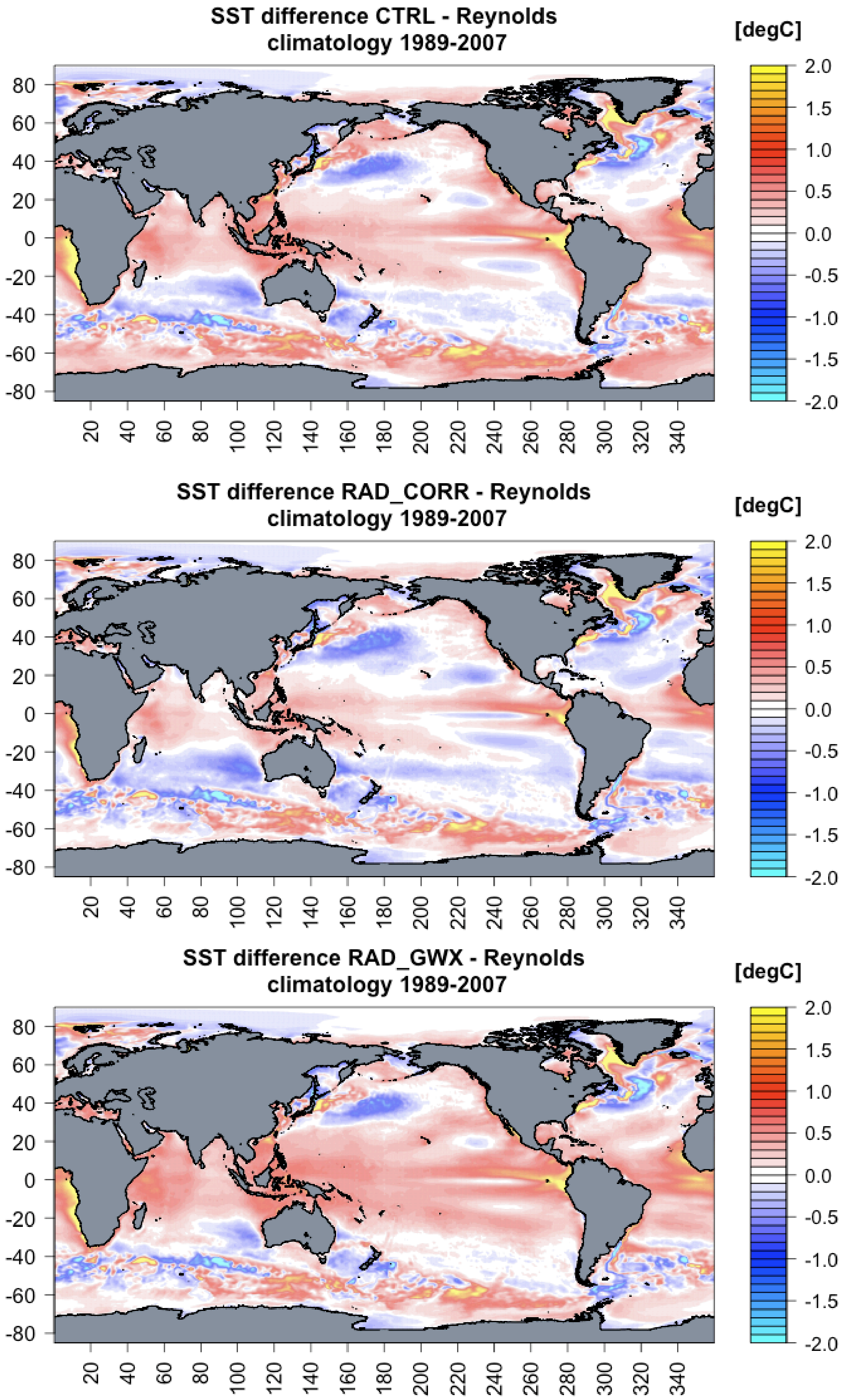

Figure 3– *SST bias (1989-2007) with respect to the Reynolds SST data for the CTRL (top), RAD_CORR (middle) and RAD_GWX (bottom) experiments.*

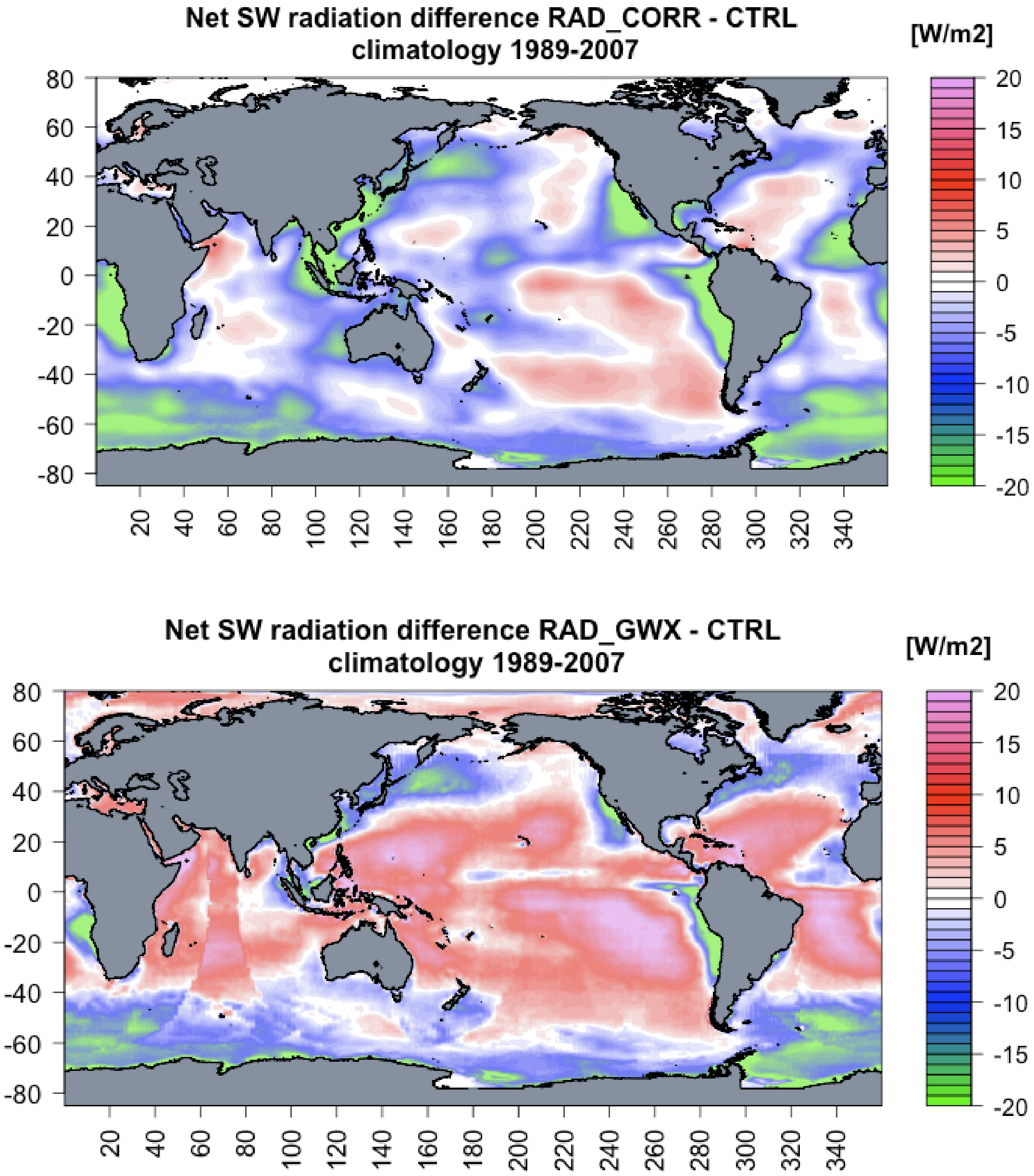

Net SW radiation difference RAD_CORR - CTRL climatology 1989-2007

Net SW radiation difference RAD_GWX - CTRL climatology 1989-2007

Figure 4– *Difference of net short-wave radiation climatology (1989-2007) between RAD_CORR and CTRL (top panel) and RAD_GWX and CTRL (bottom panel) experiments.*

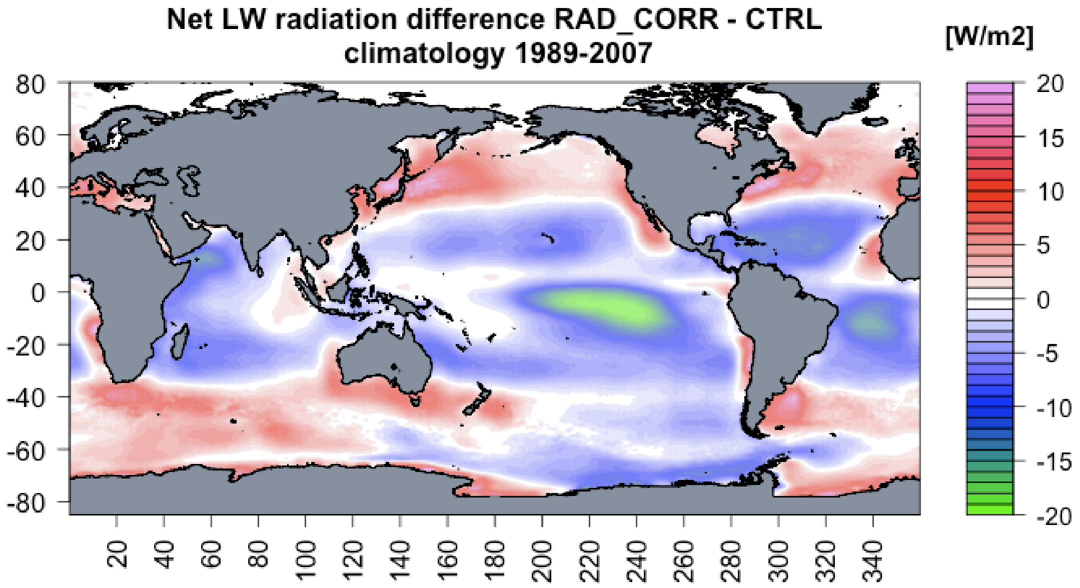

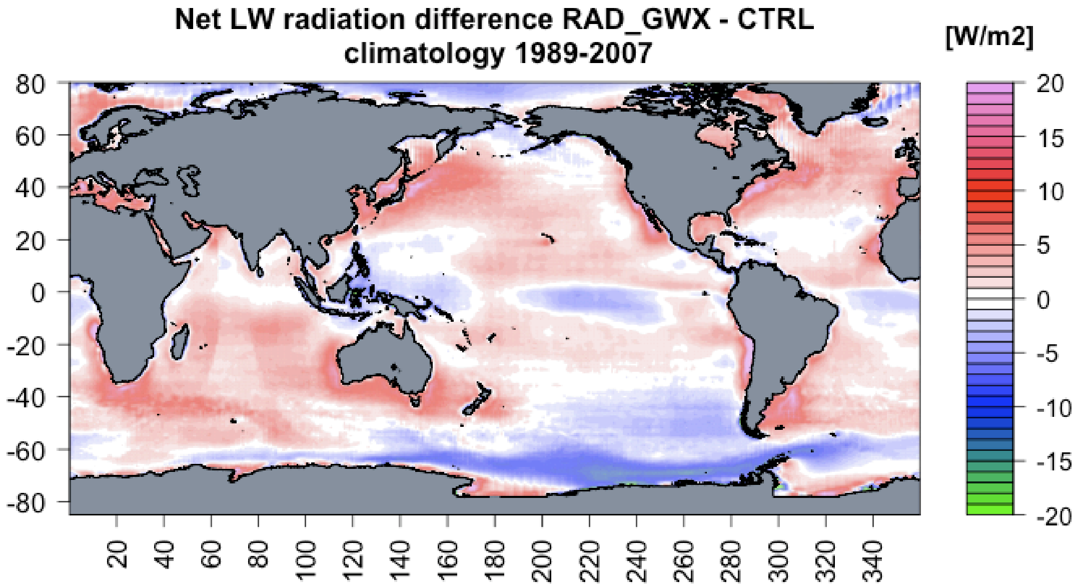

Figure 5– *Difference of net long-wave radiation climatology (1989-2007) between RAD_CORR and CTRL (top panel) and RAD_GWX and CTRL (bottom panel) experiments.*

The comparison with Reynolds SST proves that the adjustment of the large-scale component of downward LW and SW radiations by means of the corrective coefficient (4) has a positive impact on the model simulation of SST fields, both in the Tropics and at high latitudes. On the other hand, the mere use of GEWEX radiative fluxes is not able to correct the model biases in the Tropics, where instead the warm bias is amplified. The main reason for the differences in SST values between RAD_GWX and RAD_CORR experiments has to be attributed to the decrease by 3% and 6% of the downward LW and SW radiative fluxes from GEWEX, respectively, as previously mentioned. This proves that the re-calibration of GEWEX prior to its use is crucial to improve near-surface model performances.

By looking at the SST monthly mean time series it is clear that the interannual behavior is well represented in all the experiments (not shown); in terms of seasonal amplitudes the CTRL experiment overestimates both the summer maximum and the winter minimum while in the RAD_CORR experiment the amplitude of the signal is more accurately reproduced.

The 60S-60N bias against Reynolds dataset (Figure 6) demonstrates the effectiveness of the radiation correction of RAD_CORR, which presents a reduction in the bias all over the time series. The time mean bias is indeed reduced from 0.20°C in the CTRL to 0.03°C, while the RAD_GWX bias is even larger (0.30°C). In particular, the correction has a large impact in the Tropical region (20°S-20°N), where the RMSE (Figure 7) decreases by 21% (from 0.77°C in the CTRL to 0.61°C in RAD_CORR experiment). The RMSE is even larger before 2002 while it decreases in the last years of the time series.

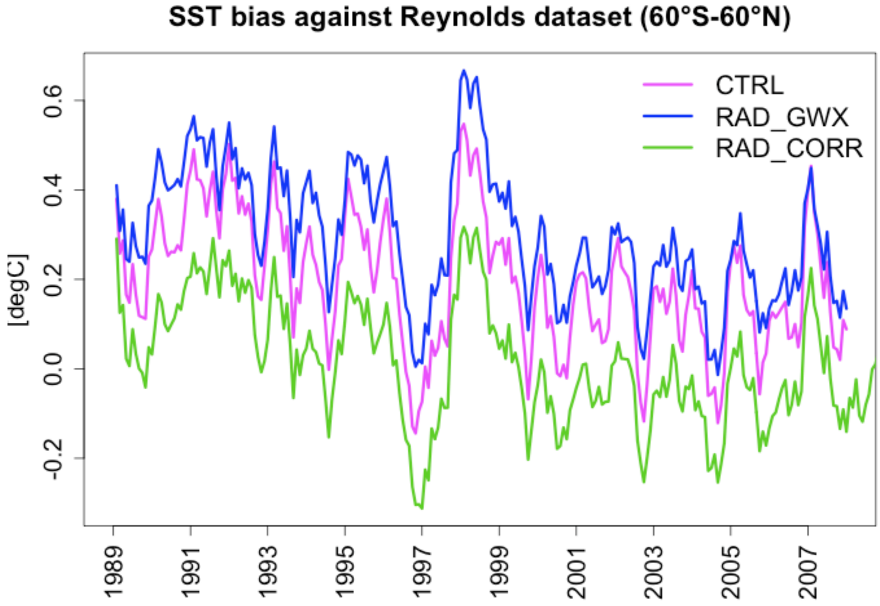

Figure 6– *Time series of monthly SST bias against Reynolds dataset, averaged between 60°S and 60°N. The bias has been calculated as model minus observations.*

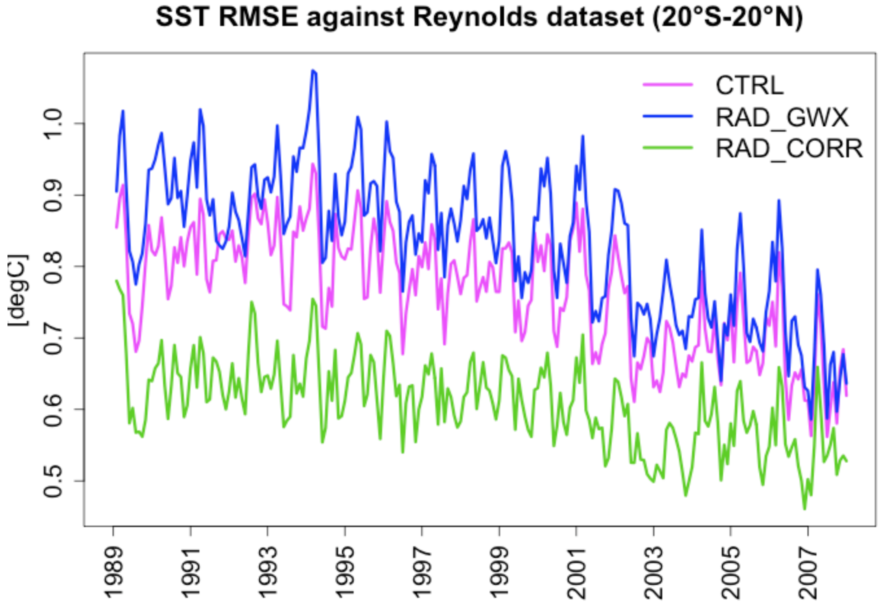

Figure 7– *Time series of monthly SST root mean square error against Reynolds dataset, averaged between 20°S and 20N°.*

At 56 m of depth (Figure 8) the correction is still effective in terms of temperature warm bias reduction, in particular in the central Tropical Pacific, against the World Ocean Atlas 2009 climatology (Locarnini et al., 2010). Some weak improvements are also visible up to 100 m of depth (not shown). In Figure 9 and Figure 10 a comparison with TAO (Tropical Pacific) and PIRATA (Tropical Atlantic) moorings, respectively, are shown. Biases have been averaged over different ranges of depth (0-50 m, 50-100 m, 100-200 m). As expected, the impact of SW and LW radiation correction decreases with depth. The warm bias reduction in the RAD_CORR experiment is evident in the 0-50 m vertical range of the Tropical Ocean (top panels of Figure 9 and Figure 10, not shown for the Indian Ocean), with a reduction from 0.29°C (CTRL) to 0.08°C (RAD_CORR); the bias attenuation is weakly visible in the 100-200 m (bottom panels of Figure 9 and Figure 10) where time-mean bias moves from 0.37°C (CTRL) to 0.28°C (RAD_CORR).

Although the impact of the radiation correction was proved effective at high latitudes, no significant variations in the sea ice concentration were found between the three experiments.

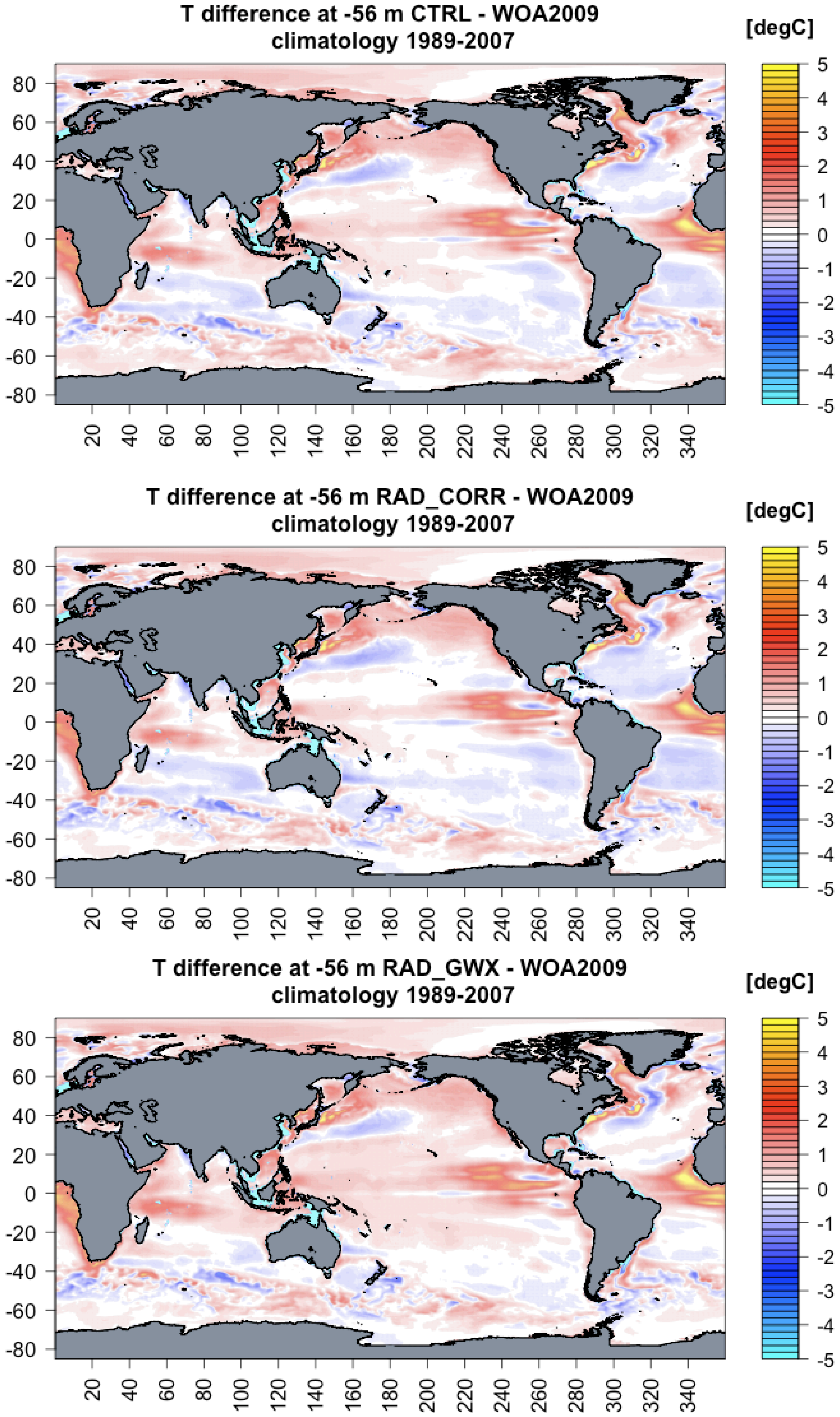

Figure 8– *Temperature bias (1989-2007) at 56 m of depth with respect to WOA2009 for the CTRL (top), RAD_CORR (middle) and RAD_GWX (bottom) experiments.*

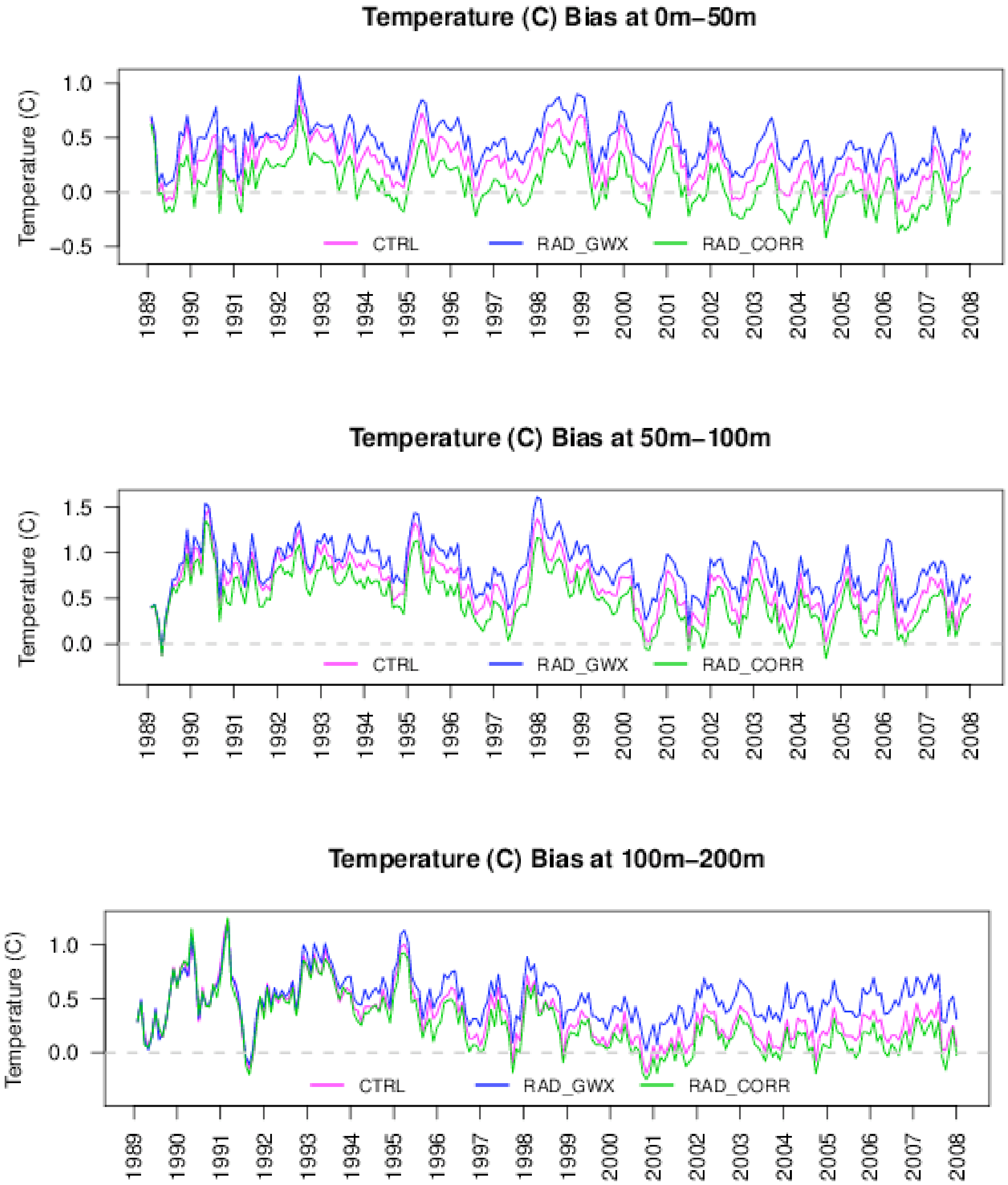

Figure 9– *Time series of monthly temperature bias against TAO moorings observations in the Tropical Pacific, averaged over different ranges of depth: 0-50m (top), 50-100m (middle), 100-200m (bottom). The bias has been calculated as model minus observations.*

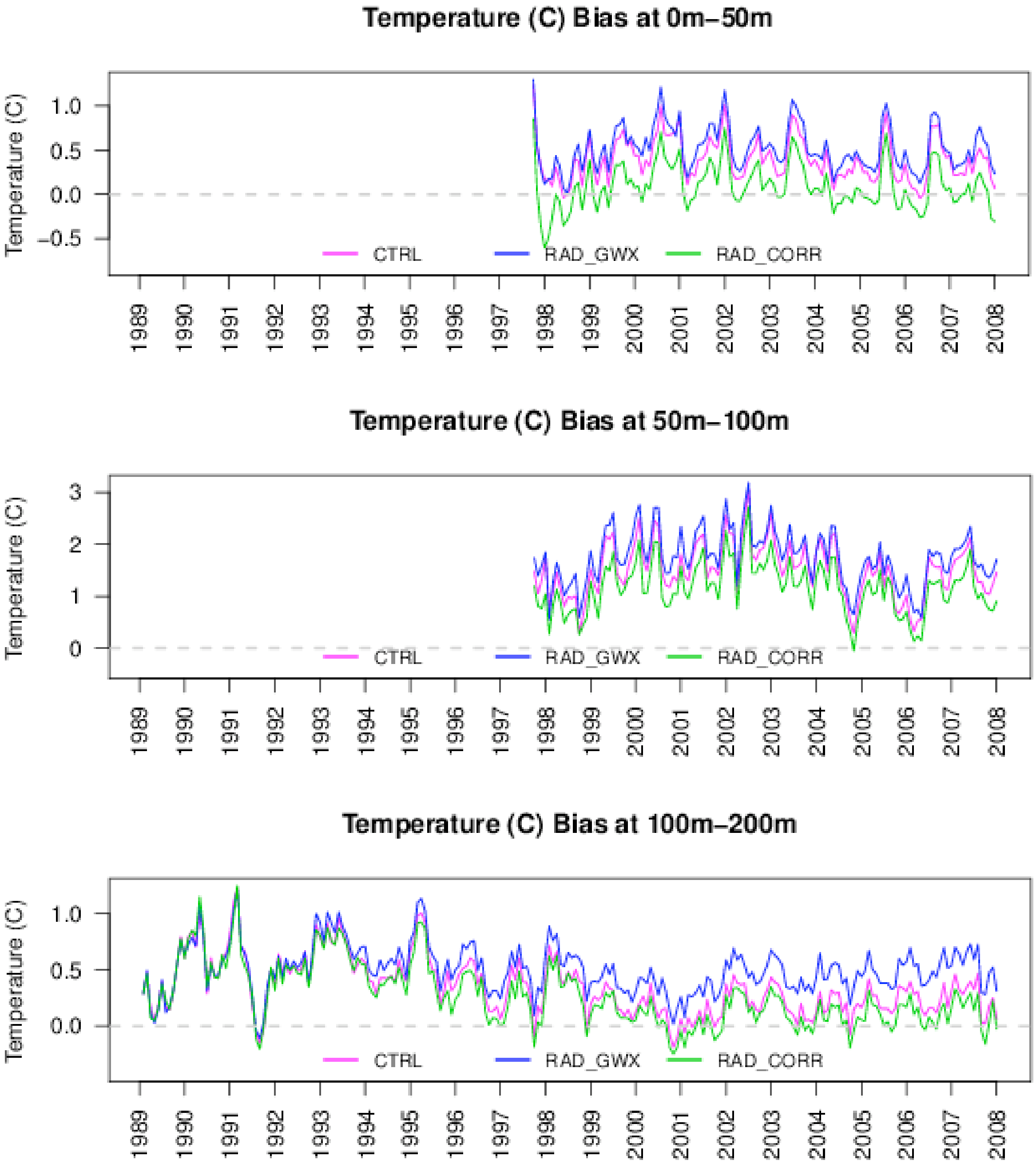

Figure 10– *Time series of monthly temperature bias against PIRATA moorings observations in the Tropical Atlantic, averaged over different ranges of depth: 0-50m (top), 50-100m (middle), 100-200m (bottom). The bias has been calculated as model minus observations.*

2.4.2- Impact of wind stress and wind speed corrections

In the comparison with NOAA drifters observations (Lumpkin and Garraffo, 2005) the near-surface current speed (averaged over 0-15 m of depth) simulated by the CTRL, WSTR_CORR and WSP_CORR experiments is underestimated almost everywhere except at the Equator, where the model shows a positive bias of about 20 cm/s (Figure 11), mostly due, especially in the Eastern Pacific, to a misplacement of the Equatorial current system. No significant impact on the climatological current speed is found in the WSTR_CORR experiment (Figure 11 middle panel). On the other hand, the correction of the 10 m wind speed (WSP_CORR experiment) not only strengthens the differences at the Equator but also introduces further biases, particularly visible in the western Tropical Pacific, in the Indian Ocean and in correspondence of northern boundary of the ACC (40°S).

An additional verification was performed against the NOAA Ocean Surface Current Analyses Real time (OSCAR, Bonjean and Lagerloef, 2002) which provides monthly estimates of near-surface currents (0-15 m) derived from scatterometers and altimeters. In the Tropical Ocean the underestimation of the near-surface velocities is attenuated in the WSTR_CORR experiment with respect to the CTRL (Figure 12). The time-mean negative bias is in fact mitigated increasing from -2.38 cm/s (CTRL) to -1.54 cm/s (WSTR_CORR). No significant improvements have been found in other ocean regions. In the WSP_CORR experiment the correction has a too strong effect on the tropical near-surface currents: the current velocities become too fast and the bias turns to positive, with a time-mean value of 1.24 cm/s (Figure 12 orange line). Furthermore, no impact of wind stress correction is visible on the RMSE time series, while WSP_CORR shows very large errors reaching peak of 20 cm/s in the boreal summer with a pronounced seasonal cycle. Similarly, negative impacts of the wind speed correction were found in the South- and North-Extratropics and in the ACC (not shown).

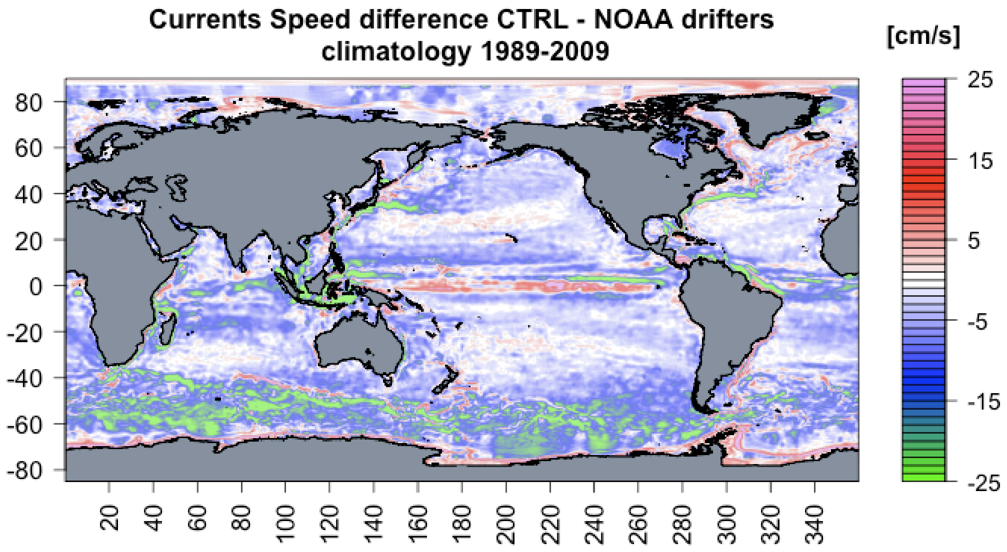

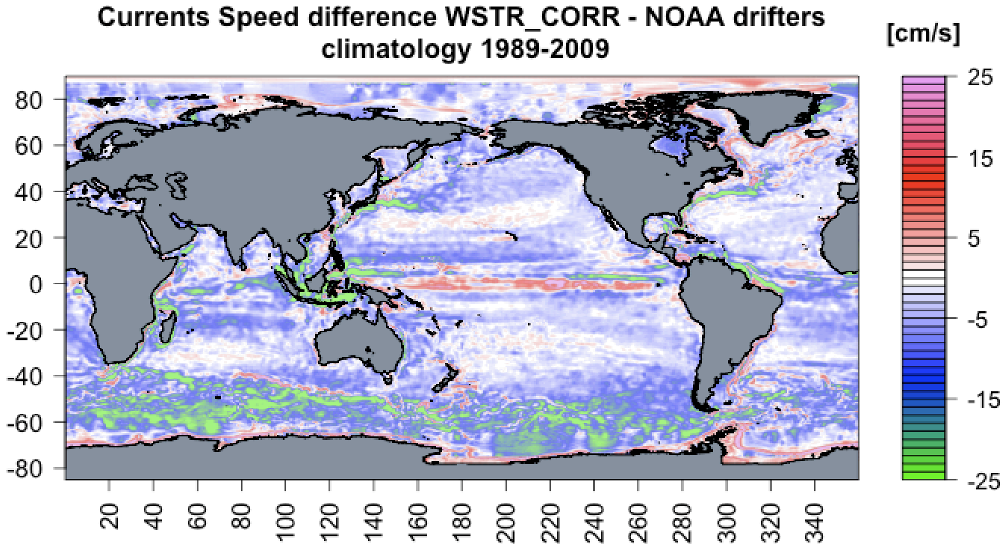

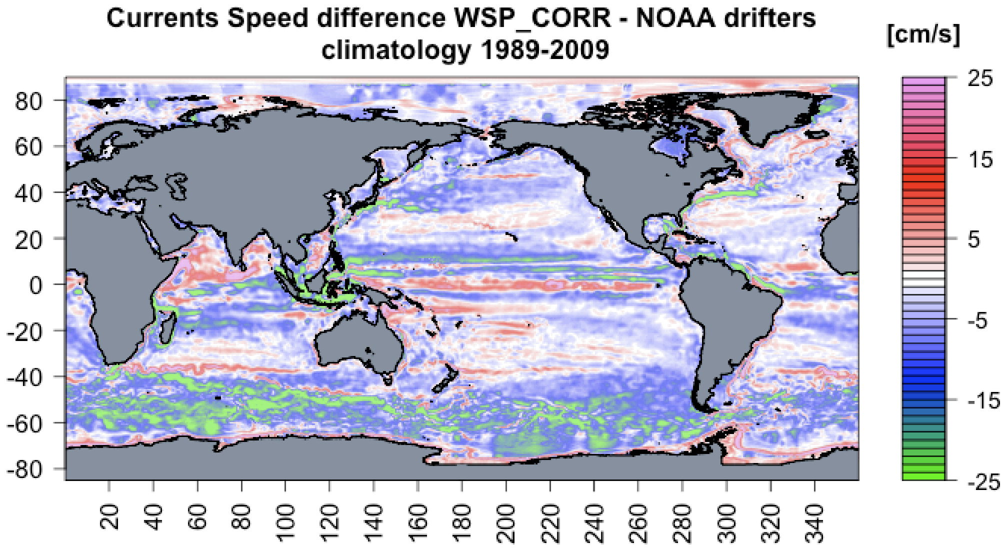

Figure 11– *Near-surface (0-15m) current speed bias (1989-2009) with respect to NOAA drifters currents data for the CTRL (top), WSTR_CORR (middle), WSP_CORR (bottom) experiments.*

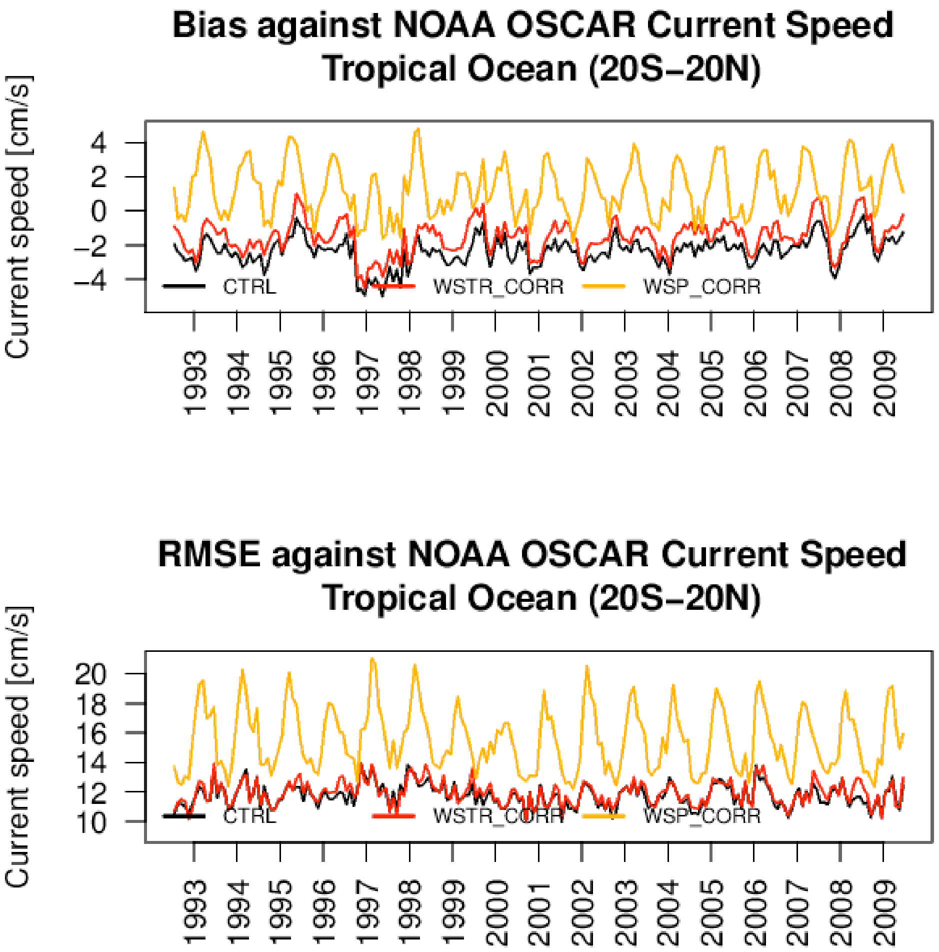

Figure 12– *Time series of monthly bias (top) and RMSE (bottom) of near surface current speed against OSCAR dataset, averaged over the Tropical Ocean (20°S-20°N). The bias has been calculated as model minus observations.*

A further verification was done with a few mooring stations (4 in the Equatorial Pacific and 1 in the Equatorial Atlantic), from the TAO/RAMA/PIRATA network, which provide current measurements at different depths (Figure 13). Although such few stations can not be representative of the tropical ocean, they offer a unique dataset to understand how deep the effect of the correction penetrates. The WSP_CORR zonal current bias differs from that of the other two experiments up to 200 m of depth (reaching a peak of 20 cm/s at 100 m of depth). In the same figure is visible that the surface RMSE increase from 21 cm/s in the CTRL and WSTR_CORR experiments to 26 cm/s in the WSP_CORR experiment; a slight positive impact (5%) in the reduction of RMSE at 100 m of depth is appreciable in the WSTR_CORR experiment.

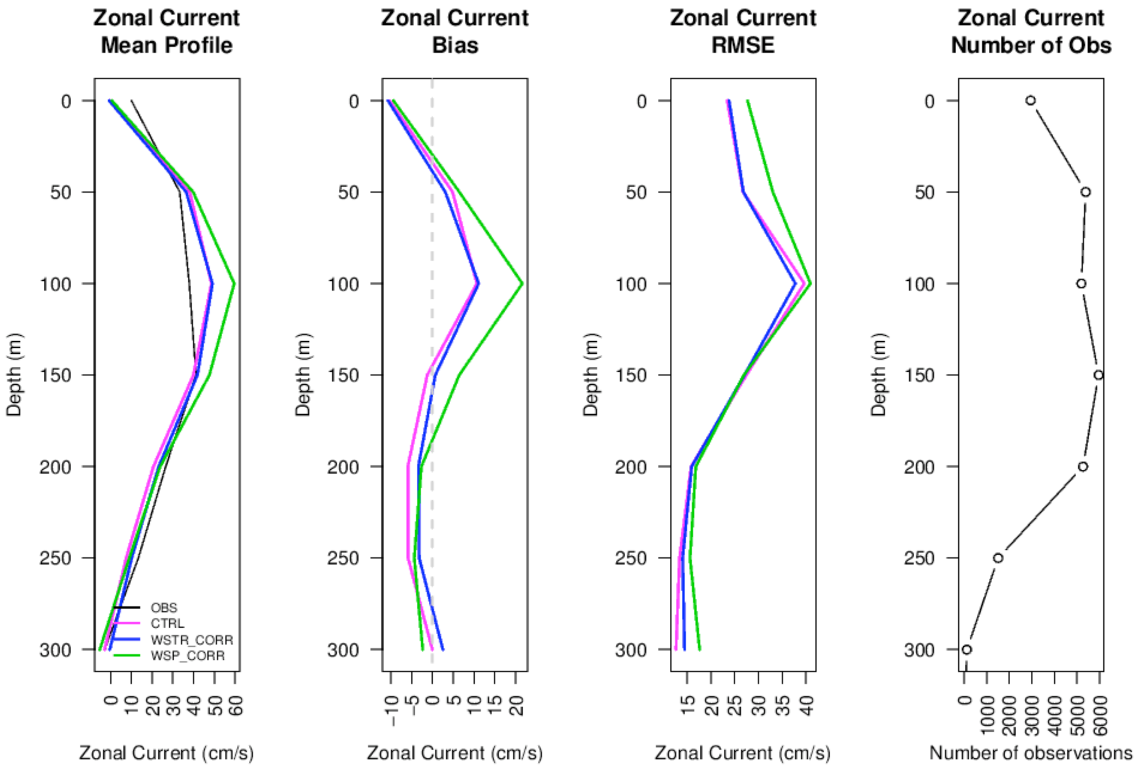

Figure 13– *Verification of zonal currents against TAO/RAMA/PIRATA moorings in the Tropical Ocean for the period 1990-2007. The figure shows mean profile, bias (model-observations), RMSE for the CTRL (magenta line), WSTR_CORR (blue line) and WSP_CORR (green line) experiments. The number of verifying observations is also shown.*

These results suggest that, when correcting 10 m wind velocities, the wind stress magnitude calculated by equation (5) is too strong compared to the uncorrected one, producing too fast surface velocities, especially in the Tropics. In fact, by looking at wind stress magnitude difference between the experiments (Figure 14), the wind stress magnitude in WSP_CORR is notably larger than the uncorrected experiment (CTRL) (Figure 14 bottom panel). The difference reaches its maximum value ($0.10\, N/m^2$) during June and July consistently with the tropical summer peaks of RMSE for the WSP_CORR experiment, thus indicating that the strong seasonality in the winds induced by the wind velocity correction negatively impacts the ocean currents. The regions where the differences are maximum (in the Tropics and in correspondence of 40°S) are in fact in agreement with the areas where the current speed are overestimated (see Figure 11).

On the other hand, the wind stress correction leads to a much weaker increase of wind stress magnitude (Figure 14 top panel) and presents smaller seasonal variability. This was shown to have a positive impact on the current speed in the Tropics.

As a general remark, these results prove that inducing the 10 m wind velocity to get closer to QuickScat scatterometer observations is not appropriate for the momentum flux bulk formulation adopted here (Large and Yeager, 2008). A possible cause might be the fact that the computation of the drag coefficient within the bulk formula has been appositely tuned for use with atmospheric model fields, which intrinsically bring a weaker spatial variability, due to the courser resolution of the atmospheric model fields compared to QuickScat.

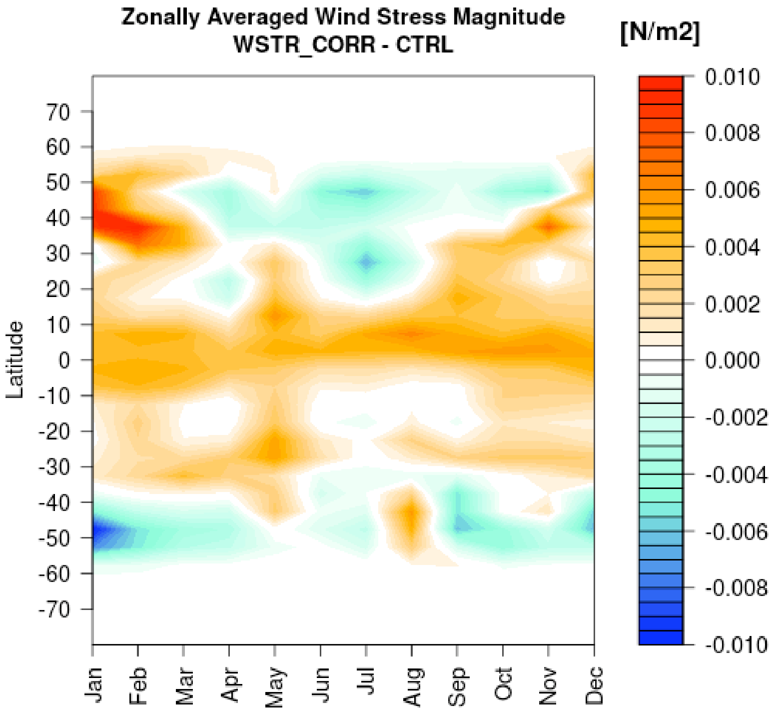

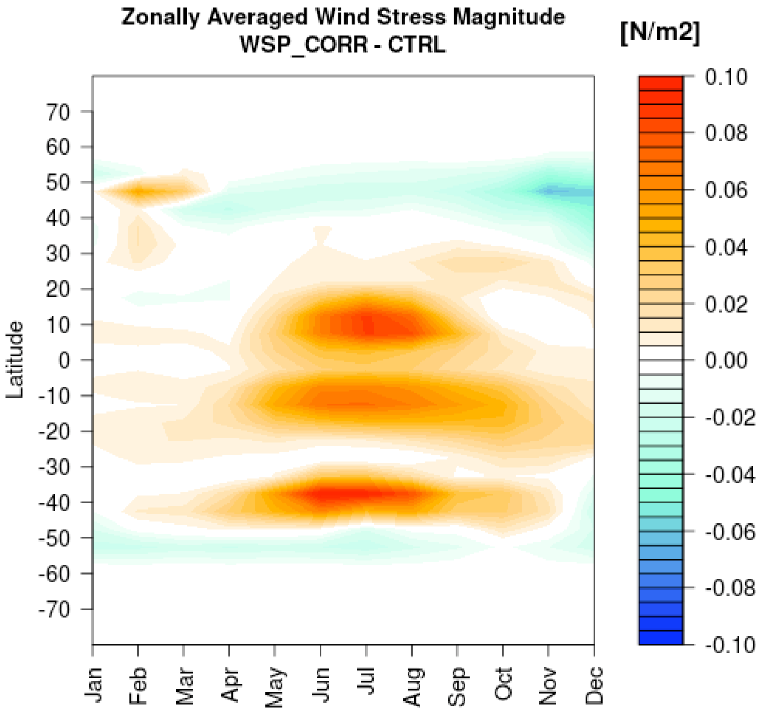

Figure 14– *Zonally averaged difference of wind stress magnitude between WSTR_CORR and CTRL (top) and WSP_CORR and CTRL (bottom) experiments, as a function of latitude and months. Note the different palette for the two contour plots.*

2.4.3- Impact of precipitation correction

Compared to the World Ocean Atlas 2009 salinity climatology (Antonov *et al.*, 2010), the uncorrected precipitation leads to a fresh bias in the Tropical sea surface salinity (SSS) as visible in Figure 15. The bias is of the order of 1 to 2.3 psu in the western Tropical Pacific and Atlantic and in the eastern Tropical Indian Oceans. These biases are clearly reduced when the precipitation correction is applied, to values generally below 0.5 psu. In the storm track regions of the North Atlantic and Pacific Oceans and in the Southern Hemisphere high latitudes, the SSS salty bias of about 0.5 to 1 psu is mitigated by the precipitation correction of a factor 2.

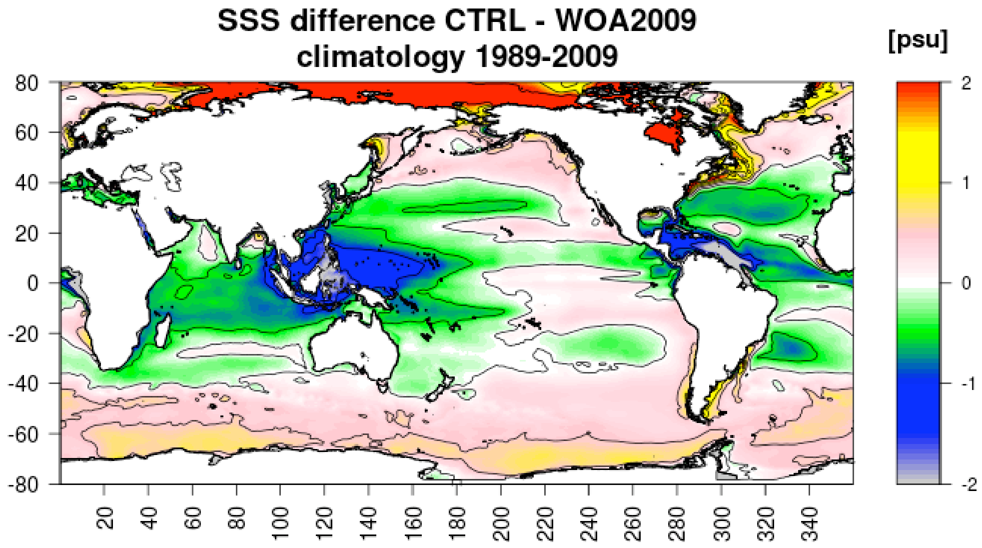
SSS difference CTRL - WOA2009
climatology 1989-2009

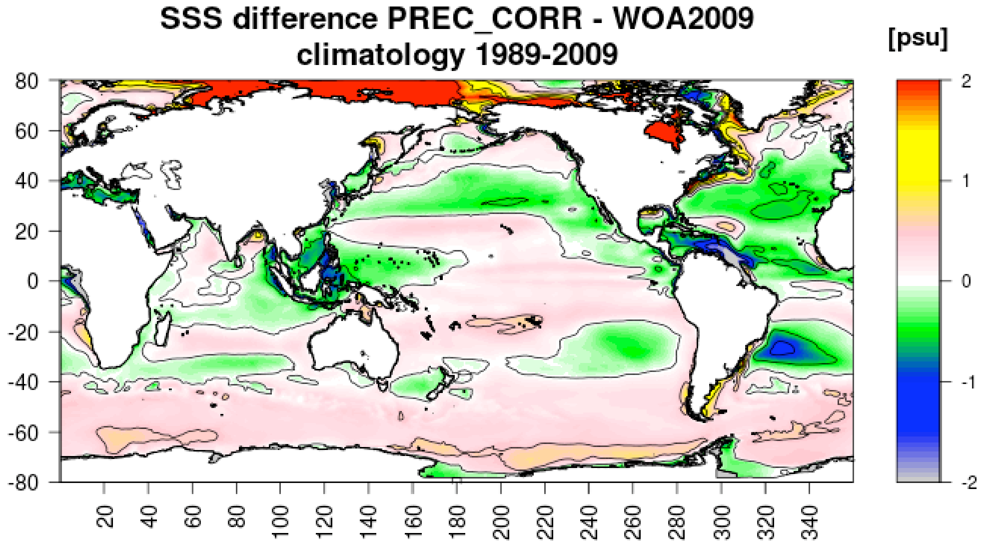
SSS difference PREC_CORR - WOA2009
climatology 1989-2009

Figure 15– *Difference between ocean model SSS and WOA2009 dataset climatologies (1989-2009) for the experiment without (top) and with (bottom) the precipitation flux correction.*

The verification against the mooring arrays in the Pacific (TAO/TRITON), Indian (RAMA) and Atlantic (PIRATA) Oceans shows consistent results (Figure 16): fresh near-surface biases are reduced and the root mean square error (RMSE) in the sea-surface salinity is reduced from about 0.8 to 0.4 psu.

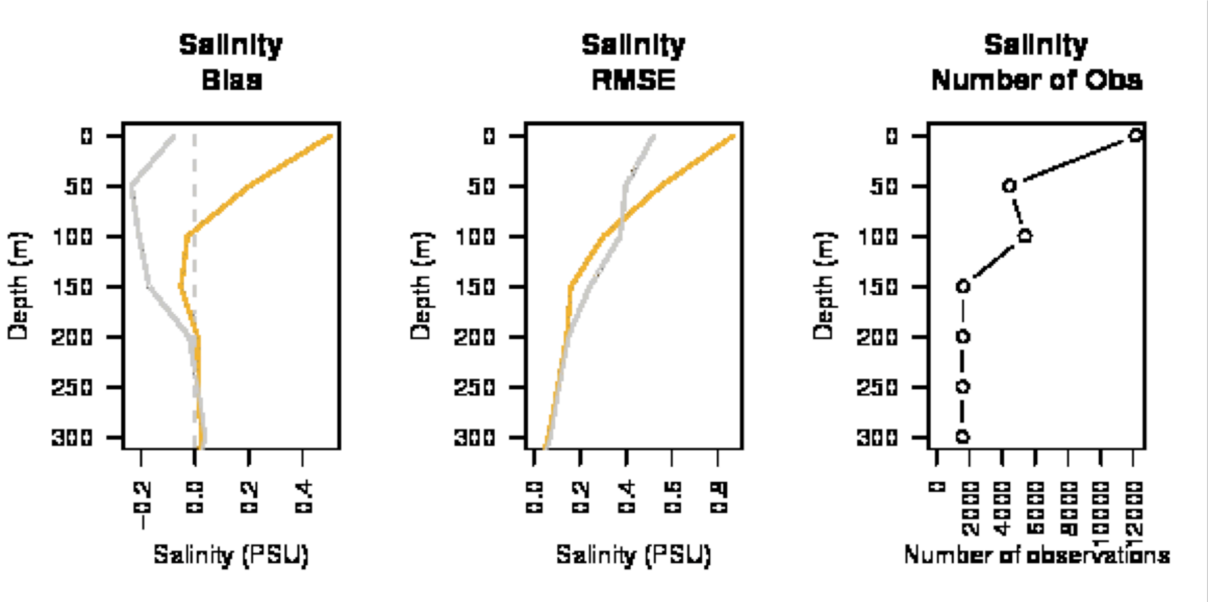

Figure 16– *Vertical profiles of bias, RMSE and number of verifying observations of salinity against the TAO/TRITON, RAMA and PIRATA mooring arrays for the experiments with (grey line) and without (orange line) the precipitation correction.*

Changes in the sea-level variability due to the precipitation correction are expected to be important as a consequence of i) the local variations of the EMP fluxes; ii) the global variations of the EMP fluxes; iii) induced variations in the thermo-haline circulation and in the baroclinic component of sea-level height. An important effect of the salinity decrease in the western boundaries of the Tropical Oceans is the corresponding sea-level lowering of 5-7, 5-6 and 1-3 cm in the Pacific, Indian and Atlantic Oceans, respectively (visible in Figure 17 upper panel), which might be due to the simultaneous effect of a precipitation decrease and salinity increase in those regions. The root mean square error decrease of sea-surface height fields verified against the AVISO sea-level anomaly monthly products has a global mean of 0.5 cm, with zonal means which reach 2 cm from 50S to 45S and local peaks of more than 20 cm in the South Pacific Ocean (Figure 17 bottom panel). The comparison is performed by removing the globally averaged value of SSH from the AVISO maps, in order to neglect the time varying global steric (expansion/contraction) and eustatic (freshwater imbalance) variations of the Global Ocean measured by satellite altimetry, which are not simulated by the NEMO OGCM. The precipitation correction is able to positively impact the sea-surface height variability, especially in correspondence of the ACC.

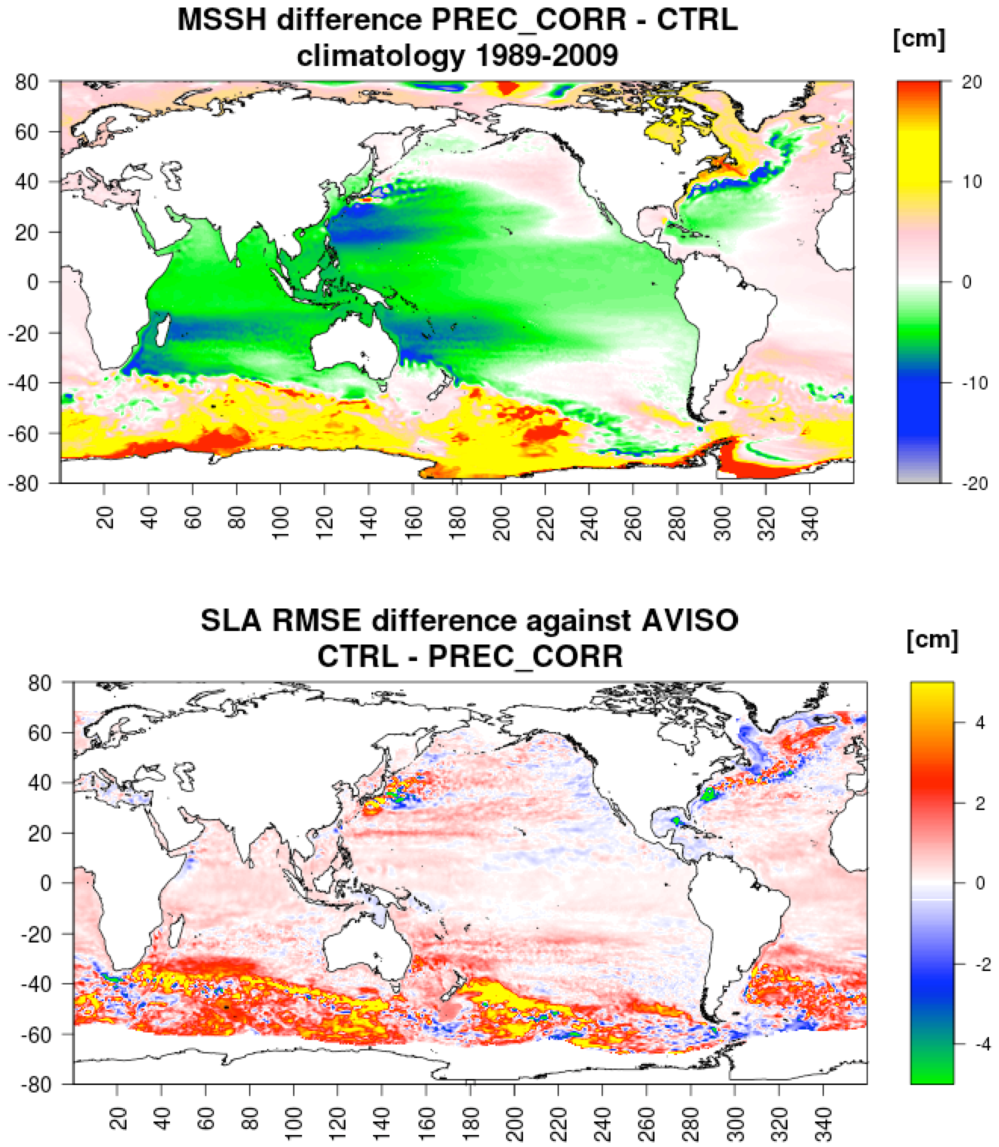

Figure 17– *Top: mean sea surface heigh difference (1989-2009) between the experiment with and without the precipitation correction. Bottom: sea surface height RMSE (against AVISO SLA) difference between the experiment with and without the precipitation correction; positive (negative) values indicate a decrease (increase) of RMSE due to the precipitation correction.*

2.5- Conclusions

In this Chapter we have described the implementation of a global eddy-permitting resolution ocean general circulation model, coupled with a sea-ice model. We have adopted the bulk CORE forcing method (Large and Yeager, 2008) and used 3-hourly turbulent fluxes and daily radiative and freshwater fluxes provided by the ECMWF ERA-Interim atmospheric reanalysis. The model has been extensively validated against observational datasets for the period 1989-2010. Although the model performance is generally satisfactory, several biases were detected. In the attempt to recover from these biases, a number of corrections to the air-sea fluxes used to force our model has been tested. In particular near surface temperature biases were found to be in part generated by inaccuracies in the ERA-interim radiative forcing, producing warm biases at tropical and high latitudes and cold biases at mid-latitudes. The use of a large-scale climatological corrective coefficient for both downward short-wave and long-wave ERA-Interim radiations, deduced from the comparison with the GEWEX SRB dataset, has proved efficient in reducing the above mentioned biases. Note that we have also tested the direct use of the GEWEX radiative fluxes instead of ERA-interim, which resulted detrimental with respect to the use of the corrective coefficient.

Similarly, the tropical overestimation of precipitation fluxes in ERA-Interim has been mitigated by using a climatological corrective coefficient computed through the comparison with a passive microwave precipitation product. The correction has reduced the tropical salinity fresh biases and improved the model representation of the sea level variability, especially in the Southern Ocean.

Finally, two different approaches for the improvement of the momentum flux have been considered, consisting respectively in the correction of the wind stress magnitude and wind speed, both derived from the comparison with QuickSCAT monthly climatologies. The wind stress was in fact found underestimated in the tropical belt while overestimated at high latitudes. The direct correction of wind stress was demonstrated to have a slightly positive impact in the near-surface currents simulation. On the other hand correcting the wind speed field led to the simulation of too fast and too seasonally variable current speeds. The latter result suggests that the successful correction of wind velocity field requires the use of a more accurate dataset, also more consistent with the physics of our ocean model.

In light of these achievements, we have adopted the radiative, precipitation and wind stress magnitude corrections as the reference configuration of our model for the simulation discussed in the next Chapter (the ALL_CORR experiment of Table 1).

EXP	PERIOD	INITIALIZATION STRATEGY	FORCING	CORRECTIONS
CTRL	1979-2010	Initialized from rest, from Levitus98 monthly climatology of T and S and from the NSIDC sea-ice concentration	3-hourly ERA-Interim turbulent variables; daily ERA-Interim radiative and freshwater fluxes	NO
RAD_GWX	1989-2007	Initialized from CTRL exp restart	3-hourly ERA-Interim turbulent variables; daily GEWEX radiative fluxes and daily ERA-Interim freshwater fluxes	NO
RAD_CORR	1989-2010	Initialized from CTRL exp restart	3-hourly ERA-Interim turbulent variables; daily ERA-Interim radiative and freshwater fluxes	Correction of large-scale downward SW and LW radiations by means of a daily climatological (1999-2007) coefficient derived from GEWEX SRB dataset
WSTR_CORR	1989-2010	Initialized from CTRL exp restart	3-hourly ERA-Interim turbulent variables; daily ERA-Interim radiative and freshwater fluxes	Correction of wind stress by means of a monthly climatological (1999-2009) coefficient derived from the SCOW QuickScat dataset
WSP_CORR	1989-2010	Initialized from CTRL exp restart	3-hourly ERA-Interim turbulent variables;	Correction of 10 m ERA-Interim wind

			daily ERA-Interim radiative and freshwater fluxes	speed by means of a monthly climatological (1999-2009) coefficient derived from the SCOW QuickScat dataset
PREC_CORR	1989-2009	Initialized from a 5-year spinup with climatological forcing fields. The spinup started from rest and from Levitus98 monthly climatology of T and S and from the NSIDC sea-ice concentration	6-hourly ERA-Interim turbulent and radiative variables; daily ERA-Interim freshwater fluxes	Correction of precipitation fluxes by means of a monthly climtological (1989-2008) coefficient derived from the REMSS/PMWC dataset
ALL_CORR	1979-2010	Initialized from rest, from Levitus98 monthly climatology of T and S and from the NSIDC sea-ice concentration	3-hourly ERA-Interim turbulent variables; daily ERA-Interim radiative and freshwater fluxes	Application of all the corrections as in RAD_CORR, WSTR_CORR and PREC_CORR experiments

Table 1- Summary of the experiments set up.

References

Antonov J.I., Seidov D., Boyer T.P., Locarnini R.A., Mishonov A.V., Garcia H.E., Baranova O.K., Zweng M.M., Johnson D.R., 2010. World Ocean Atlas 2009, Volume 2: Salinity. Ed. NOAA Atlas NESDIS 69. U.S. Government Printing Office, Washington D.C., 184 pp.

Barnier B., Madec G., Penduff T., Molines J.-M., Treguier A.-M., Le Sommer J., et al. 2006: Impact of partial steps and momentum advection schemes in a global ocean circulation model at eddy-permitting resolution. Ocean Dynamics, 56(5-6), 543–567.

Bernie D.J., Guilyardi E., Madec G., Slingo J.M., Woolnough S.J., 2007. Impact of resolving diurnal cycle in an ocean- atmosphere GCM. Part 1: a diurnally forced OGCM. Clim. Dyn. 29,575-590.

Bonjean F. and Lagerloef G.S.E., 2002. Diagnostic Model and Analysis of the Surface Currents in the Tropical Pacific Ocean, Journal of Physical Oceanography, Vol. 32, No. 10, pages 2938-2954.

Bourdalle-Badie R. and Treguier A.M., 2006. A climatology of runoff for the global ocean-ice model ORCA025. Mercator-Ocean report, MOO-RP-425-365-MER.

Dai A. and Trenberth K.E., 2002. Estimates of freshwater discharge from continents: Latitudinal and seasonal variations. J. Hydrometeorol., 3, 660-687.

Ferry N., Parent L., Garric G., Barnier B., Jourdain N.C. and the Mercator Ocean team, 2010. Mercator global eddy permitting ocean reanaly-sis GLORYS1V1:

Description and results. Mercator Quarterly Newsletter 36, January 2010.

Fichefet T. and Morales Maqueda M.A., 1997. Sensitivity of a global sea ice model to the treatment of ice thermodynamics and dynamics. Journal of Geophysical Research, 102, 12,609-12,646.

Fu Q., Yang P., Sun W.B., 1997. An Accurate Parameterization of the Infrared Radiative Properties of Cirrus Clouds for Climate Models. *J. Climate*, 11, 2223–2237.

Garric G. and Verbrugge N., 2010. Large scale ECMWF radiative surface fluxes assessment, correction and application to 3D global ocean simulations. Geophysical Research Abstracts, Vol.12 EUGU2010-12044, EGU General Assembly 2010.

Gill A., 1982. Atmosphere-Ocean Dynamics, 1st Edition, Academic Press, pp. 662.

Grieco G. and Masina S., 2009. Implementation and Validation of NEMO-OPA in configuration ORCA-R025 at ANS, CMCC. Technical Reports.

Hilburn K., Wentz F., 2008. Intercalibrated passive microwave rain products from the Unified Microwave Ocean Retrieval Algorithm (UMORA). *Journal of Applied Meteorology and Climatology* **47**, 778-794.

Hilburn K., 2009. The passive microwave water cycle product. Remote Sensing Systems (REMSS) Technical Report 072409, Santa Rosa (CA), 30 pp.

Large W.G. and Yeager S.G., 2004. Diurnal to decadal global forcing for ocean and sea-ice models: The data sets and flux climatologies. *Technical Report TN-460+STR*, NCAR, 105pp.

Large W.G. and Yeager S.G., 2008. The global climatology of an interannually varying air-sea flux dataset. Climate Dynamics, 33, 341-364, doi:10.1007/s00382-008-0441-3.

Lengaigne M., Menkes C., Aumont O., Gorgues T., Bopp L., J.-M. André, Madec G., 2007. Influence of the oceanic biology on the tropical Pacific climate in a coupled general circulation model. Clim. Dyn., 28, 503–516. DOI 10.1007/s00382-006-0200-2.

Levitus S., Boyer T.P., Conkright M.E., O' Brien T., Antonov J., Stephens C., Stathoplos L., Johnson D., Gelfeld R., 1998. NOAA Atlas NESDIS 18,World Ocean Database 1998. U.S. Gov. Printing Office, Wash., D.C.

Locarnini R.A., Mishonov A.V., Antonov J.I., Boyer T.P., Garcia H.E., Baranova O.K., Zweng M.M., Johnson D.R., 2010. World Ocean Atlas 2009, Volume 1: Temperature. S. Levitus, Ed. NOAA Atlas NESDIS 68, U.S. Government Printing Office, Washington, D.C., 184 pp.

Lumpkin R. and Garraffo Z., 2005. Evaluating the Decomposition of Tropical Atlantic Drifter Observations. J. Atmos. Oceanic Techn. 22, 1403-1415.

Madec G., 2008. "NEMO ocean engine". Note du Pole de modélisation, Institut Pierre-Simon Laplace (IPSL), France, No 27 ISSN No 1288-1619.

Molines J.M., Barnier B., Penduff T., Brodeau L., Treguier A., Theetten S., Madec G., 2007. Definition of the interannual experiment ORCA025-G70, 1958-2004. LEGI report, LEGI-DRA-2-11-2006.

Pinker R. and Laszlo I., 1992. Modeling Surface Solar Irradiance for Satellite Applications on a Global Scale, J. Appl. Met., 31, 194-211.

Reynolds R.W., Smith T., Liu C., Chelton D.B., Casey K.S., Schlax M.G., 2007. Daily high-resolution blended analyses for sea surface temperature. J. Climate, 20, 5473-5496.

Risien C.M. and Chelton D.B., 2008. A Global Climatology of Surface Wind and Wind Stress Fields from Eight Years of QuikSCAT Scatterometer Data. J. Phys. Oceanogr., 38, 2379-2413.

Simmons A., Uppala S., Dee D., Kobayashi S., 2007. ERA-Interim: New ECMWF reanalysis products from 1989 onwards. In Newsletter 110. ECMWF.

Stackhouse P.W., Gupta S., Cox S., Zhang T., Mikovitz J.C., Hinkelman L., 2011. 24.5-Year SRB dataset Released. GEWEX News Feb. 2011, Vol.1 N.1, 10-12.

Steele M., Morley R., Ermold W., 2001. PHC: A global ocean hydrography with a high quality Arctic Ocean, J. Climate, 14, 2079-2087.

Treguier A., 1992. Kinetic energy analysis of an eddy resolving, primitive equation north atlantic model. J. Geophys. Res, 97, 687–701.

Chapter 3

Sea Level variability during the last 20 years

Abstract

In order to examine spatial pattern and regional trends of sea level changes during the last two decades (1989-2010), we have performed a numerical simulation using an eddy-permitting ocean/sea-ice Ocean General Circulation Model NEMO_LIM2. For that purpose we have first tested the skill of the model (pure forced global ocean model simulations without any data assimilation) to reproduce the 1993-2010 Mean Sea Surface Height (MSSH), regional sea level trends, seasonal amplitude and seasonal phase, by comparing the simulated fields with satellite altimetry data, using. The regional MSSH patterns and sea level variability are correctly reproduced both in magnitude and in geographical distribution; the largest deviations are found in regions with strong mesoscale dynamics, such as the western boundary currents and the Antarctic Circumpolar Current (ACC), where the highest values of sea level anomalies Root Mean Square Error (RMSE) reach 30 cm. The comparison with satellite altimetry data shows a close agreement between the model results and the observed regional sea level trend patterns, with the exception of the North Atlantic basin and the ACC location, where the trend values are quantify positive and negative with respect to observations, respectively.

Assessed the capability of the model in realistically reproducing past sea level change, we have further extended our analysis over all the length of the simulation (1989-2010) to investigate sea level trend, and possible acceleration/deceleration of the patterns trend, in the main ocean basins. Results show that regions exhibiting a negative sea level trend, such as the East Pacific and South Atlantic, experience a deceleration in the sea surface height (SSH) decrease, while in the North Atlantic, where sea level exhibits a positive trend, the trend value slightly decreases between the two decades; the extreme case is the Indian Ocean, where the trend reverses from negative during the period 1991-2000 (-1.49 mm/yr) to positive in the last decade (1.45 mm/yr); the West Pacific Ocean still remains the region with highest values of sea level rise and hence the most sensitive to this event.

Furthermore we have examined the respective contributions of changes in the eustatic and steric components to the total regional sea level trend and seasonal variability; the two sea level components have been previously validated, the former with GRACE gravimetry observations and the latter with ARMOR objective analyses data of temperature and salinity. The model results show that in terms of regional trends and seasonal variability the sea level signal is almost totally explained by the steric contribution. The eustatic contribution to SSH change is in general negligible except in the Southern Ocean and north of 60°N, where the trend, and mainly the seasonal variability of sea level, are largely explained by the barotropic component. For the

steric component, we have also analyzed the distinct contributions of temperature and salinity changes, and the contributions from different depth ranges, in order to detect the portion of the water column that plays the major role on sea level trend and variability.

To conclude we have performed a regional sea level study on the Small Islands of Pacific, which is one of the most critical and highly sensitive region to sea level rise, as the climate system of the Pacific Ocean is subject to strong interannual variability. We have found an area-averaged sea level rise of 2.6 mm/yr, with the dominant contribution from the steric component (2.3 mm/yr). A detailed analysis of the different contributors allowed us to quantify that sea level rises by 0.86 mm/yr due to the positive balance of the net downward heat flux at the sea surface, by 0.54 mm/yr due to an increase of incoming heat from the South Pacific gyre and the Equatorial Current System, which is not compensated by a corresponding heat loss. Finally, the salinity contribution (0.87 mm/yr) is confined to the first 100m of depth and mostly produced by freshwater transport from the western Pacific into the Small Islands region.

3.1- Introduction

3.1.1- Sea level change

Sea level change is an important consequence of climate change and its current and future rise is closely associated with global warming. Since the mid-19th century, sea level has been rising, likely especially in response of human-induced climate change.

Estimates from tide gauges records collected over the last century highlight a global-average sea level change of 1.7 ± 0.3 mm/yr (Church and White, 2006). Altimetric observations from different satellite missions (as TOPEX/Poseidon and Jasons satellites), available since the beginning of satellite era in October 1992, have shown a further acceleration of sea level rise over the last two decades (1993-2008), when the rate of rise amounts to 3.1 mm/yr (Ablain et al., 2009); sea level trend has shown no acceleration for the period 2008-present (AVISO web site).

Global sea level is currently rising as a result of both ocean thermal expansion and land-ice melting, with each accounting for about half of the observed sea level rise, and each caused by recent increases in global mean temperature. According to the IPCC AR4 (2007), for the period 1961-2003, the observed sea level rise due to thermal expansion was 0.42 mm/yr and 0.69 mm/yr due to total land-ice melt, i.e. small glaciers and ice caps (G&IC) and ice sheets; between 1993 and 2003 the contribution to sea level rise increased for both sources to 1.60 mm/yr and 1.19 mm/yr, respectively. Hence, during the 1993-2003 period the thermal expansion has given the main contribution to sea level rise, followed by G&IC and Greenland and Antarctica ice sheets (IPCC 2007); during the last years (2003-2007) the highest contribution to sea level rise has come from G&IC (1.4 mm/yr) and the contribution from the two ice sheets has become even higher than that from the thermal expansion of the water column, the former causing a global mean sea level rise of 0.5 to 1.0 mm/yr while the latter a 0.25 mm/yr rising (Cazenave and Llovel, 2010).

Satellite altimetry measurements showed that sea level is not rising uniformly around the world (Figure 1); in some regions (e.g., western Pacific) rates of sea level rise are faster by a factor of 3 than the global mean rate, while in other regions the sea level has been falling (e.g., eastern Pacific) (Cazenave and Llovel, 2010). Spatial variability of the rates of sea level is mostly due to non-uniform changes in local temperature and salinity (e.g., Bindoff et al., 2007) but also changes in ocean circulation, which results from changes in surface wind stress, heat and freshwater fluxes, as well as atmospheric pressure variations and glacial isostatic adjustment (GIA) effects (e.g., Plag, 2006; Mitrovica et al., 2009; Milne et al., 2009) also cause local variability of sea level trend. Many studies (Cabanes et al., 2001; Willis wt al., 2004; Lombard et al., 2006) have shown that spatial patterns of global sea level change are mainly due to thermal expansion of the upper 700 m of the ocean, computed using global in situ temperature observations (Willis et al., 2004; Guinehut et al., 2004; Levitus et al., 2005; Ishii et al., 2006), even if the deep ocean warming contribution, below 700 m of depth, has been proved to have a significant role in the present-day sea level rise (e.g. Song and Colberg, 2011).

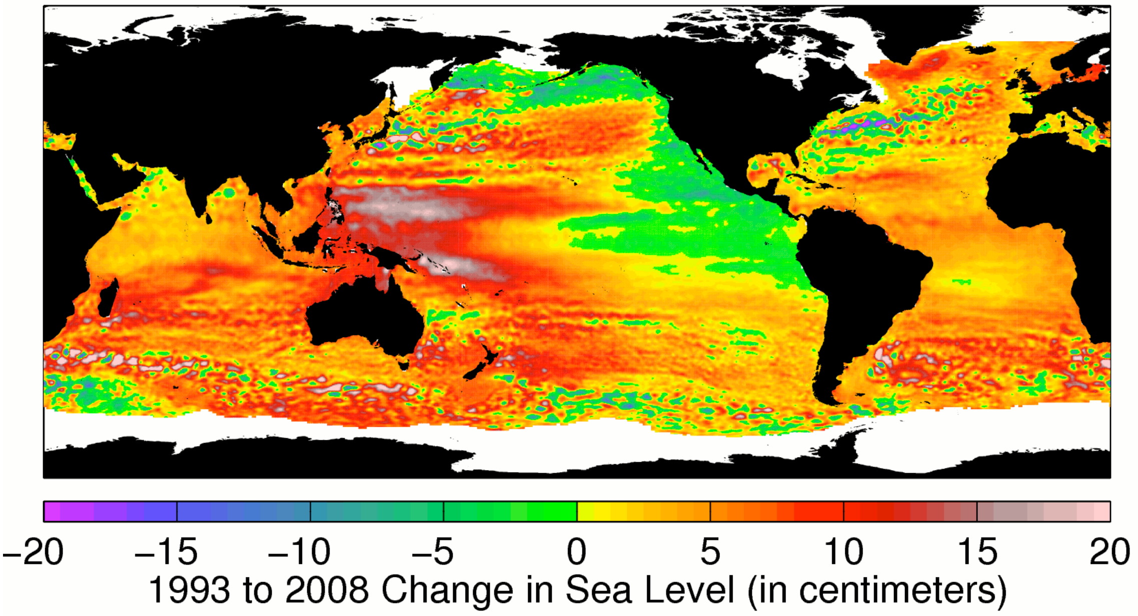

Figure 1– *Sea level trend over the period 1993-2008 from satellite altimetry (http://climate.nasa.gov/blogs/).*

The Small Islands in the West Pacific Ocean are one of the most vulnerable coastal areas to the phenomenon of sea level rise, as the Pacific Ocean region is the centre of the strongest interannual variability of the climate system. Recent studies (Chowdhury et al., 2007; Becker et al., 2012) have described the degree of sensitivity of sea level anomalies in the tropical Pacific Island communities to the phase of the El Niño-Southern Oscillation (ENSO) cycle; the studies have identified the ENSO climate cycle to have a significant impact on the sea level variability of the western tropical Pacific, with lower-than-average sea level observed during El Niño events and higher-than-average sea level observed during La Niña events, of the order of ± 20-30 cm. The Small Islands territories are characterised by many common features that accentuate their vulnerability to projected impacts of climate change and in particular of sea level rise: their small size, isolation, limited natural resources, high population density, thin water lenses, their low lying position above sea level (many of theses islands rarely exceed 3-4 m above present mean sea level). Erosion, storm surge and flood risks, coastal land loss, soil salinitation are examples of damages produced by the sea level rise. To make an example of the magnitude of the impacts, recent estimates indicates that with a 1m rise in sea level $10\,Km^2$ of land in Tongatapu Island (Tonga) would be lost (Mimure & Plesikoti 1997). This estimate would increase to $37\,Km^2$ (14%) with storm surge superimposed on a 1m sea level rise scenario.

For the above mentioned reasons the West Pacific is the oceanic region where sea level is experiencing its highest positive trend, as revealed by satellite altimetry data (Figure 1). Global sea level reconstruction from 1950 to 2009, performed by combining long good quality tide gauge records (over 1950-2009) with 50-year (1958-2007) gridded sea surface heights from OGCM, shows in fact that sea level in the Pacific Islands region is characterised by a strong positive trend pattern. For the sub-regions between 15°N-15°S, 5°N-18°S and 18°S-20°S the reconstructed sea level rise over 1950-2009 amounts to 1.1 ± 0.6 mm/yr, 2.6 ± 0.6 mm/yr and 1.5 ± 0.5 mm/yr, respectively (Becker et al., 2012).

3.1.2- Sea level formulation in NEMO

The free surface equation in the NEMO model can be derived by vertically integrating the continuity equation written under the incompressibility hypothesis and by using the kinematic boundary conditions, which define the ocean domain and describe its volume budget, at the surface and at the bottom of the ocean. In the linear (fixed volume) case, the sea surface height η is supposed to be small relative to the total depth *H* and hence the interval of integration is taken between z = 0 and z = -H.

The "incompressible" continuity equation (or mass conservation equation) is written as:

$$\nabla \cdot \vec{u} = 0 \tag{1}$$

i.e. the three dimensional divergence of the velocity field $\vec{u}=(u, v, w)$ is assumed to be zero.

The kinematic surface boundary condition expresses the rate of change of the difference of the free surface displacement η and a *z* reference depth, determined by the volume per unit time per unit area of freshwater entering the ocean through the surface (q_w) :

$$\frac{D(\eta - z)}{Dt} = q_w \tag{2}$$

where $q_w = P - E + R$ and P is the precipitation, E is the evaporation, R is the river plus ice melting runoff. From the definition of vertical velocity $w|_{z=\eta} = \frac{Dz}{Dt}$ equation (2) becomes:

$$w|_{z=\eta} = \frac{\partial \eta}{\partial t} + \vec{u}_h|_{z=\eta} \cdot \nabla_h \eta - P + E - R \tag{3}$$

where $\vec{u}_h = (u, v)$ is the horizontal velocity field.

As there is no flow across solid boundaries (i.e. the velocity normal to the ocean bottom and coastlines is equal to zero) at the bottom (*z*=-*H*), the kinematic boundary condition is expressed as:

$$w|_{z=-H} = -\vec{u}_h|_{z=-H} \cdot \nabla_h H \tag{4}$$

Integrating (1) vertically we obtain:

$$\int_{-H}^{0} \left(\frac{\partial u}{\partial x} + \frac{\partial v}{\partial y}\right) dz' = -w|_{z=\eta} + w|_{z=-H} \tag{5}$$

and by means of equations (3) and (4), the equation becomes:

$$\frac{\partial \eta}{\partial t} = -\frac{\partial}{\partial x}\int_{-H}^{0} u dz' - \frac{\partial}{\partial y}\int_{-H}^{0} v dz' + P - E + R \tag{6}$$

that is the linear sea level equation used in incompressible dynamical ocean circulation models. The terms on the right hand side, the horizontal divergence of the vertically integrated velocities and the freshwater flux, represent the eustatic (or barotropic) component of sea level. The eustatic component is related to global changes in the ocean volume caused by mass redistribution (due to a response to local atmospheric wind change or a redistribution of mass within the ocean through advection) and to local changes of the net water flux at the atmosphere-ocean interface (P and E terms) or ocean-land interface (runoff from rivers, glaciers and ice caps, ice sheets, land water reservoirs).

Another component of sea level, which does not explicitly appear in equation (6), is the baroclinic or, commonly called steric component defined as the variation in sea surface height (SSH) caused by the expansion/contraction of ocean volume due to density variation associated with temperature (thermosteric component) and salinity (halosteric component) changes in the water column. As shown by Greatbatch (1994), Ezer and Mellor (1994) and Mellor and Ezer (1995), regional steric sea level changes are adequately represented in models that conserve volume rather than mass, as we will show later on; what is not explicitly taken into account in such kind of models is the global mean expansion/contraction of the oceans. Hence, if we want to compare the model-calculated sea level with observations, simulated sea level has to be adjusted by a globally uniform time-varying factor, determined by the net expansion/contraction of the global ocean (Greatbatch, 1994). For this reason, in our experiments the steric component has been calculated from simulated temperature and salinity fields by vertically integrating the density anomalies using the classical equation of state for sea water proposed by the UNESCO (Gill 1982). The steric component η_{st} has been then added a posteriori every month to the model SSH as the global area average, leading to:

$$\frac{\partial \eta}{\partial t} = -\frac{\partial}{\partial x}\int_{-H}^{0} u dz' - \frac{\partial}{\partial y}\int_{-H}^{0} v dz' + P - E + R + \frac{1}{A}\int \frac{\partial \eta_{st}}{\partial t} dA \tag{7}$$

where A is the area of our global domain and η_{st} is computed as:

$$\eta_{st} = -\frac{1}{\rho_0}\int_{-H}^{0} (\rho(T,\bar{S}) - \rho(\bar{T},\bar{S}))dz - \frac{1}{\rho_0}\int_{-H}^{0} (\rho(\bar{T},S) - \rho(\bar{T},\bar{S}))dz \tag{8}$$

T and S are monthly means and the overbar indicates the temporal mean over the period of interest. The first integral on the right hand side of equation (8) is the thermosteric contribution to SSH (that is the expansion/contraction of the water column due to an increase/decrease of sea water temperature) and the other term is the halosteric contribution (expansion/contraction if sea water salinity decrease/increase). As a result, we estimate, at each grid point, the total steric sea level change that is due to both temperature and salinity variations in all model layers from surface to bottom.

Since steric and eustatic sea level components are not available as separate model outputs, in the next sections we will diagnose the former from equation (8) and the latter as the difference between the simulated SSH (equation (7)) and the steric component (as usually done, e.g. Lombard et al., 2009). Equation (8) also offers the possibility to further analyze the distinct contributions of thermosteric and halosteric sea level changes.

Being U and V the barotropic velocity component defined as the depth-integral horizontal components of the velocity, the sea level equation (6) becomes:

$$\frac{\partial \eta}{\partial t}=-\frac{\partial}{\partial x}(HU)-\frac{\partial}{\partial y}(HV)+P-E+R \tag{9}$$

The barotropic velocities can be explained by vertically integrating the primitive equations of motion and substituting the horizontal pressure gradient terms, in the equations for *u* and *v,* with the vertically integrated hydrostatic equation, obtaining:

$$\frac{\partial U}{\partial t}+\frac{1}{H}\int_{-H}^{0}\vec{u}\cdot\vec{\nabla}u-fV=-g\frac{\partial \eta}{\partial x}-\frac{g}{\rho_0 H}\frac{\partial}{\partial x}\int_{-H}^{0}(z+H)\rho\, dz''+\frac{1}{H}\int_{-H}^{0}F^{x}dz \tag{10}$$

$$\frac{\partial V}{\partial t}+\frac{1}{H}\int_{-H}^{0}\vec{u}\cdot\vec{\nabla}v+fU=-g\frac{\partial \eta}{\partial y}-\frac{g}{\rho_0 H}\frac{\partial}{\partial y}\int_{-H}^{0}(z+H)\rho\, dz''+\frac{1}{H}\int_{-H}^{0}F^{y}dz \tag{11}$$

Equations (10) and (11) show that even for a volume conserving model, local variations of density are taken into account and represented within the sea level structure through the barotropic velocity field, which includes, in fact, a baroclinic gradient term (second terms of the right hand side).

Under the geostrophic approximation Equations (10) and (11) show that η has two components: a barotropic component (or eustatic component) related to the depth-mean horizontal circulation; a baroclinic component (usually called steric component) related to the vertical integral of ocean density and its horizontal structure (Pinardi et al., 1995; Lowe and Gregory, 2006).

3.2- Simulated sea level change

For the study of sea level spatial and temporal variability, we have analyzed a 22-year (1989-2010) eddy-permitting (1/4° of horizontal resolution) ocean/sea-ice simulation from NEMO_LIM2 OGCM, forced by 3-hourly turbulent fluxes and daily radiative and freshwater fluxes from ERA-Interim reanalysis (ALL_CORR experiment described in Chapter 2). In order to reduce the model biases, the forcing field corrections, illustrated in Chapter 2, have been used. The corrections applied are summarized as follows: i) correction of large-scale downward LW and SW radiations by means of a climatological (1999-2007) coefficient derived from GEWEX-SRB dataset; ii) correction of precipitation fluxes by means of a monthly climatological (1989-2008) coefficient derived from the REMSS/PMWC dataset; iii) correction of wind stress by means of a monthly climatological (1999-2009) coefficient derived from the SCOW QuickScat product. The reader should note that in this work we analyze the results of a global OGCM without assimilation of observational data (e.g., altimetry or in situ data), unlike other studies that used ocean reanalyses for sea level investigation (Carton et al., 2005; Wunsch et al., 2007; Köhl et al., 2007; Köhl and Stammer, 2008). Indeed, one of the goals of our study is to check whether our OGCM simulation do correctly reproduce sea level and steric changes and can be thus fruitfully used to predict future pattern of sea level change.

We have firstly validated the simulated SSH through the comparison with independent data sets (Section 3.2.1). In Section 3.2.2, we have analyzed and validate the different components of sea level in terms of trend, annual amplitude and phase, and the extent of their contributions to sea level change; the analysis has been performed on the 2003-2010 period since this is the common period between the available datasets used in the comparison. In Section 3.2.3 we have further extended our analysis over all the length of the simulation (1989-2010) to investigate sea level trend, and possible acceleration/deceleration of the patterns trend, over the all oceanic basins. To conclude (Section 3.3) we have performed a case study focussing on the analysis of a critical region that is highly vulnerable to sea level rise, such as the Small Islands of Pacific.

3.2.1- Model validation

In order to have confidence in our ability to predict future sea level changes, we need to confirm that our numerical simulations can reproduce qualitatively and quantitatively the relevant sea level features and its components. The global mean sea surface height (MSSH) simulated by the model and its comparison with the mean dynamic topography (MDT) computed by Rio et al. (2011) (the MDT_CNES-CLS09 product) are shown in Figure 2. The MSSH patterns are in general well captured by the model both in magnitude and in regional geographical distribution, and the model biases (visible in the bottom panel of Figure 2) are in agreement with previous studies of Barnier et al. (2006) and Penduff et al. (2010), showing some improvements in the tropical belt. The differences between model and observations show that the model generally tends to overestimate the MSSH in the North Atlantic, with a maximum of ~15 cm in the Gulf of Mexico and western tropical region; while the MSSH is underestimated in the Gulf Stream and North Atlantic Current (NAC) locations. As in most eddy-permitting models (i.e. Penduff et al., 2010), the Gulf Stream and the NAC are displaced to the east creating a negative bias of about -15 cm. The largest anomalies, up to ± 20 cm, are found in regions of strong currents, such as the western boundary currents (WBCs) and the Antarctic Circumpolar Current (ACC). In particular, the signature in the ACC region implies that this current is represented too broadly by the model: the simulated ACC tend to spread southwards, compared to observations, and the northernmost branch of the ACC is shifted northward in the model simulation, producing a positive and a negative anomalies, respectively. The sea level anomaly (SLA) Root Mean Square Error (RMSE), estimated against AVISO altimetric data, exhibits similar pattern with the largest values in the regions characterized by strong mesoscale dynamics (Figure 3). There the RMSE reaches peaks of 30 cm, while in the rest of the ocean the error is quite low, around 5 cm. In terms of sea level temporal variability, the correlation between the model output and the altimetry data (Figure 4) is low (close to zero) in that regions (ACC, Kuroshio and the Gulf Stream), while the sea level variability is very well reproduce at the Equator and at the Tropics with correlation values of 1 almost everywhere, especially in the Pacific and Indian Ocean. The temporal correlation is in good agreement with that from previous works (e.g., Lombard et al., 2009).

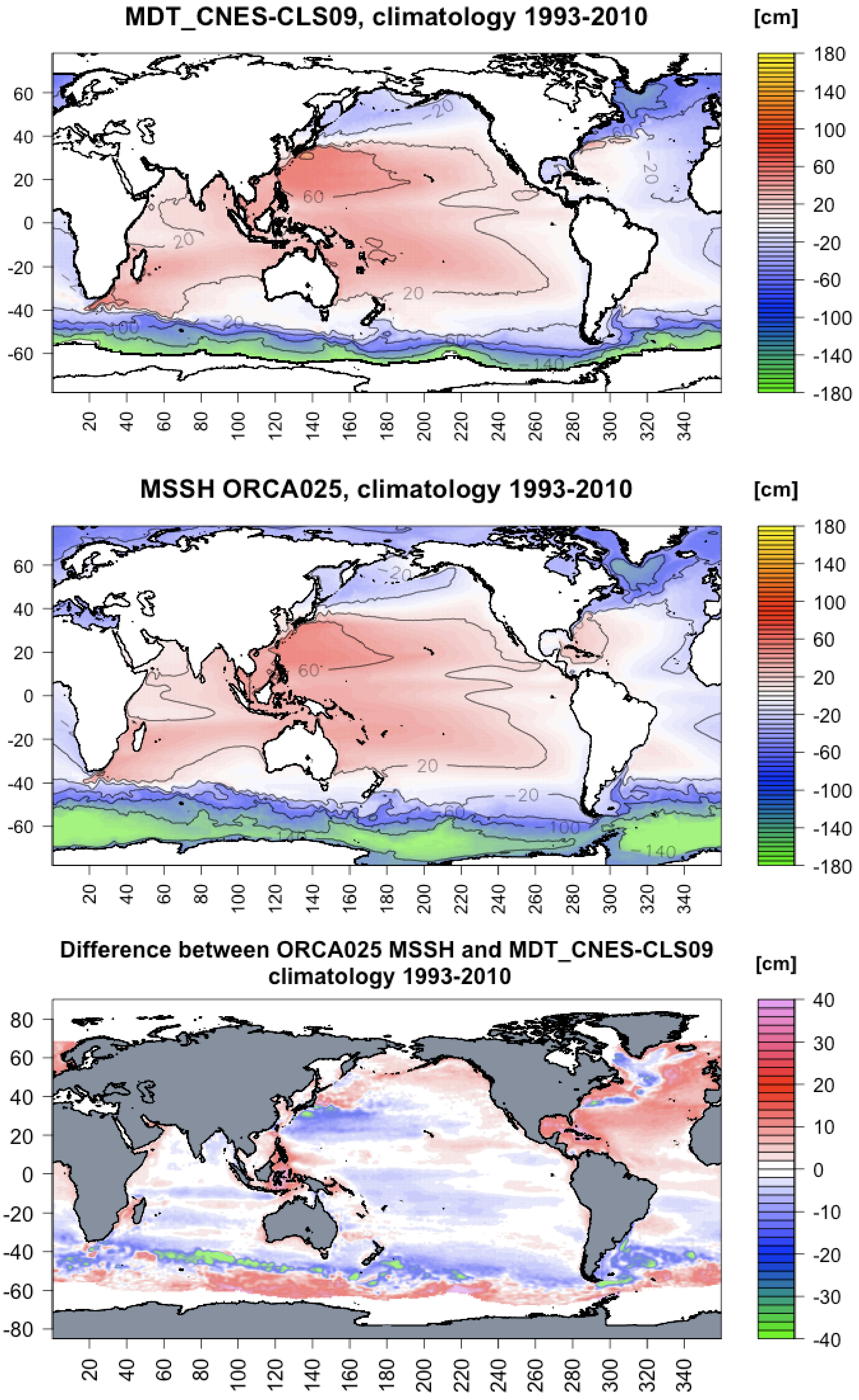

Figure 2- *Upper: MDT from Rio et al. (2011). Middle: Mean sea surface height from model simulation. Bottom: Difference between the simulated MSSH and the reference MDT. All maps show 1993-2010 climatologies.*

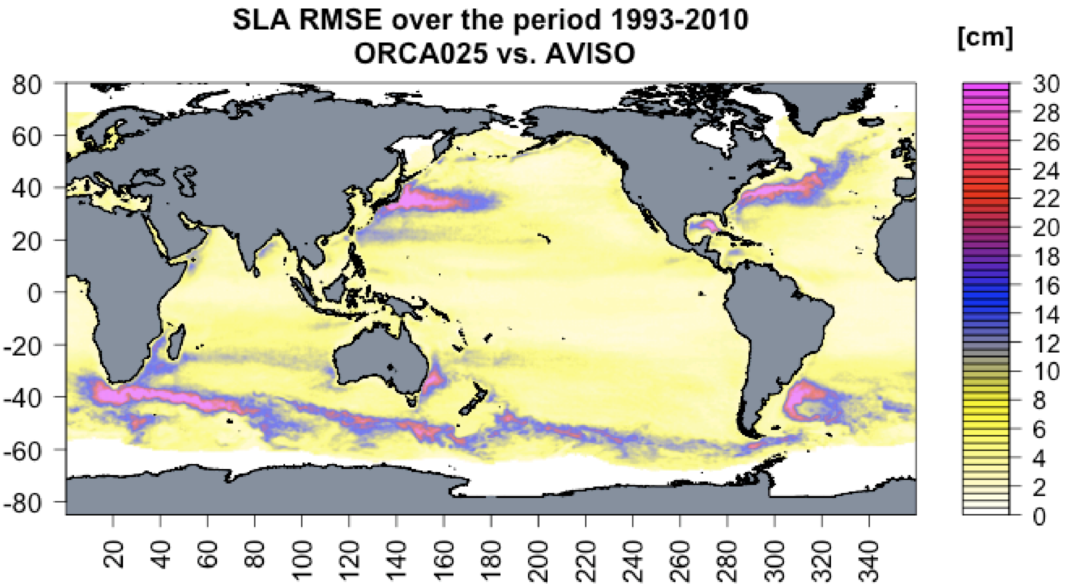

Figure 3- *Sea level anomaly RMSE over the period 1993-2010, Model vs. AVISO altimetry data.*

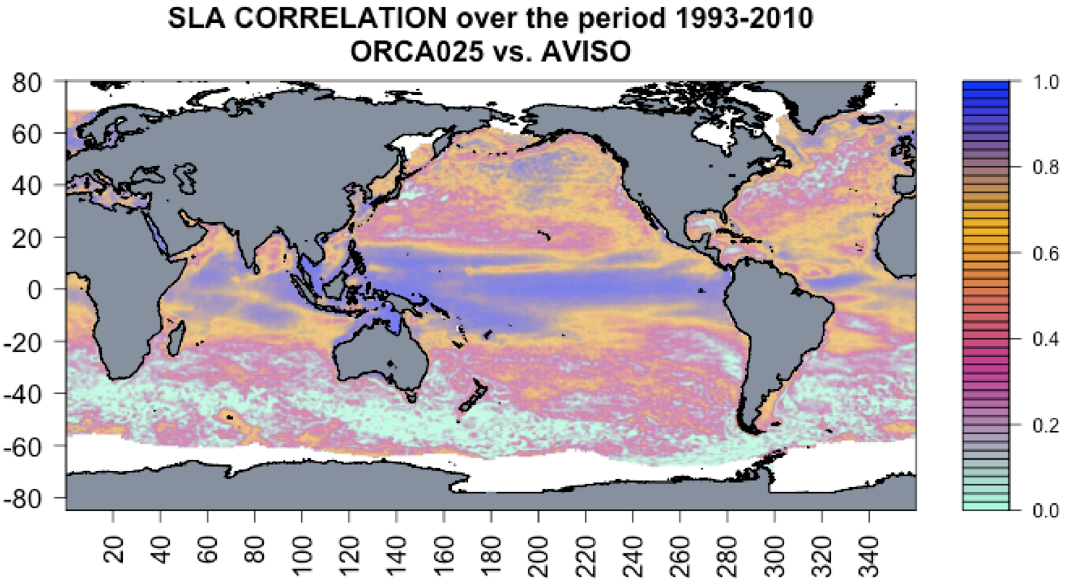

Figure 4- *Sea level anomaly correlation over the period 1993-2010, Model vs. AVISO altimetry data.*

3.2.2- Analysis of sea level components and their contribution to sea level change

In this Section, we have investigated the sea level over a 8-years period (2003-2010) in terms of its regional trend and seasonal variability (annual amplitude and phase). Trends are computed at each grid point by fitting line to time series using a linear least square regression. The monthly sea level time-series *y(t)* can be represented by the following curve:

$$y(t) = at + b + A\cos(\omega t + \phi)$$

where a is the slope of the curve that represents the linear trend estimated at every grid point and b is the intercept; $\omega = \frac{2\pi}{T}$ with T=1-year; the parameter A is the annual amplitude of sea surface height (2A is the difference between the summer and winter peak of the signal); ϕ is the phase of the signal that represents the month of the year where the maximum amplitude occurs. To further deepen sea level investigation, we have split the total SSH in its steric and eustatic components, analyzing how they separately contribute to SSH. To asses the reliability of the model, we also compare the simulated total SSH with AVISO SLA altimetry data, its steric component with ARMOR (Guinehut et al., 2004) temperature and salinity objective analysis from in-situ measurements and the eustatic component with GRACE data, where glacial isostatic adjustment (GIA) trend has been removed (Peltier, 2004). In particular, we use monthly means of multi-mission sea level anomaly from altimetric satellites processed and provided by CLS/AVISO after removal of tidal signals (Le Traon et al., 1998) to validate the sea surface height from NEMO. Altimetric satellites in facts estimate the sea surface height with respect to the mean dynamic topography (i.e. the mean sea surface height over a certain period relative to the Geoid), thus including both the baroclinic and barotropic processes involving the sea level evolution. Gravimetric data from GRACE mission (available for the 2003-2010 period) depict the gravitational field on the ocean, which in turn may be used to determine the ocean water mass variations induced by a change in the sea-land and air-sea water fluxes and, locally, by ocean mass redistribution (Chambers and Schröter, 2011), and can be used to validate the ocean mass variations (eustatic sea level component) represented in NEMO by the difference between the total sea surface height and the steric sea level.

Sea level trends and its components are shown and compared with observations in Figure 5. Sea level does not rise uniformly but displays large regional heterogeneity (upper panels). The spatial distribution of the SSH trend is generally well captured by the model, able to reproduce realistically the positive trend in the East Pacific Ocean (with a peak of more than 24 mm/yr in correspondence of the Indonesian Archipelago) and the negative trend in the western Pacific with a minimum in the ACC. Both the positive and the negative trends are slightly underestimated by the model. The trend patterns in the Indian Ocean is in close agreement with altimetry data. The efficiency of the model decreases south of Australia and in the North Atlantic, where the trend values are lower and higher, respectively, with respect to observations. It is worthy to note that thanks to to the eddy-permitting resolution of our configuration, the Gulf Stream and Kuroshio current trends are captured and well represented.

The spatial distribution of simulated steric trend and its magnitude (middle panel) resamble the total SSH trend, suggesting that the sea level signal is almost totally explained by the steric component. The simulated steric trend is in good agreement with ARMOR data, except in the southern Indian Ocean and a region in the North Atlantic around 30°N, where trends values are too low.

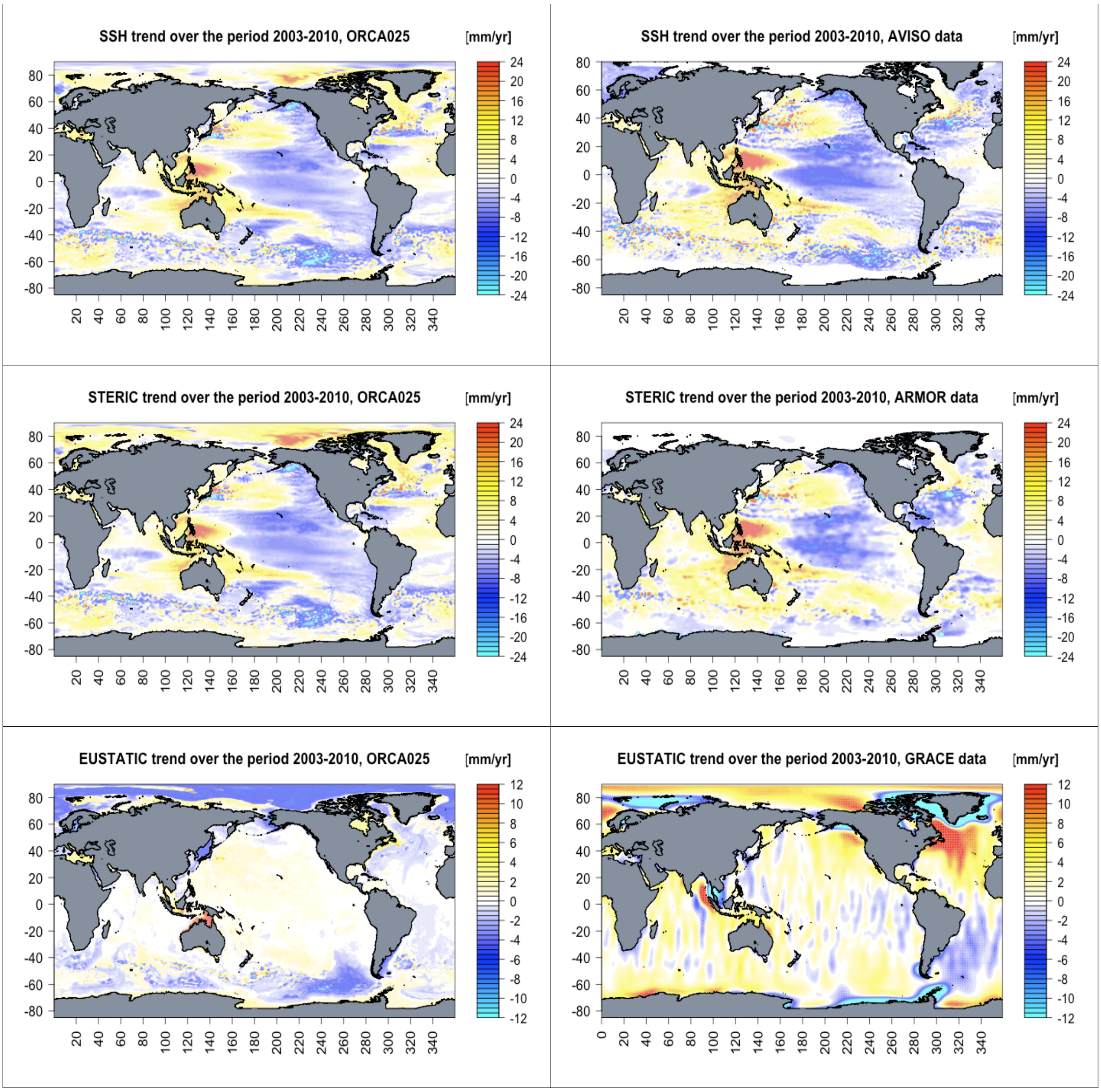

Figure 5- *Maps of spatial trend patterns over the period 2003-2010. Upper panels: sea level trend from the model (left) and from AVISO altimetry data (right); middle panels: steric component trend from the model (left) and from ARMOR data (right); bottom panels: eustatic component trend from the model (left) and from GRACE gravimetry data (right).*

The eustatic sea level trend are generally weaker and more spatially uniform than regional steric sea level trends (bottom panels, note the different palette). Generally, the eustatic component gives a negligible contribution to the total sea level trend, except in the Southern Ocean, especially in the South Pacific (50°S – 70°S). Our results are in accordance with the geographical distribution of the eustatic trend found by Wenzel and Schroter (2007), even though they used a global ocean data assimilation system for the study of sea level change contributions. In the Pacific sector of the ACC, the decreasing trend areas can be attributed to a strong eustatic sea level fall, mainly caused by a loss of mass through the divergence in the ocean mass transport that is not totally balanced by the net surface freshwater supply. A non-negligible barotropic contribution is also visible, in our simulation, in t he seas north of Australia, in the Sea of Japan, in the North Atlantic sub-polar gyre, in the Baffin Bay and in the Bering Strait, where local eustatic effects are locally important in our results. As noted by many authors (Ponte et al., 2007; Vinogradov et al., 2008), the eustatic trends do not clearly respond to forcing variability, in particular are not sensitive to net freshwater fluxes, probably due to fast barotropic adjustments that tends to hide the freshwater signature (Lombard et al., 2009).

Most of the seasonal variability of SSH is related to the major oceanic circulation features (Song and Colberg, 2011). The seasonal amplitude of SSH reaches its maximum, higher than 12 cm, in the East Equatorial Pacific (related to the Equatorial Currents System) and in the WBC regions, especially Gulf Stream and Kuroshio (Figure 6). The amplitude peak is reached between July and September in the northern hemisphere, and in correspondence with the boreal summer in the southern hemisphere (Figure 7). As for the spacial trend, also for the annual amplitude and phase, the baroclinic contribution generally dominates with the exception of the Southern Ocean and the region north of 60°N, where the sea level seasonal variability is largely explained by the barotropic component (Vinogradov et al., 2008). The model SSH and its steric component agrees well with altimetry and ARMOR observations, respectively, both in amplitude (Figure 6) and in phase (Figure 7).

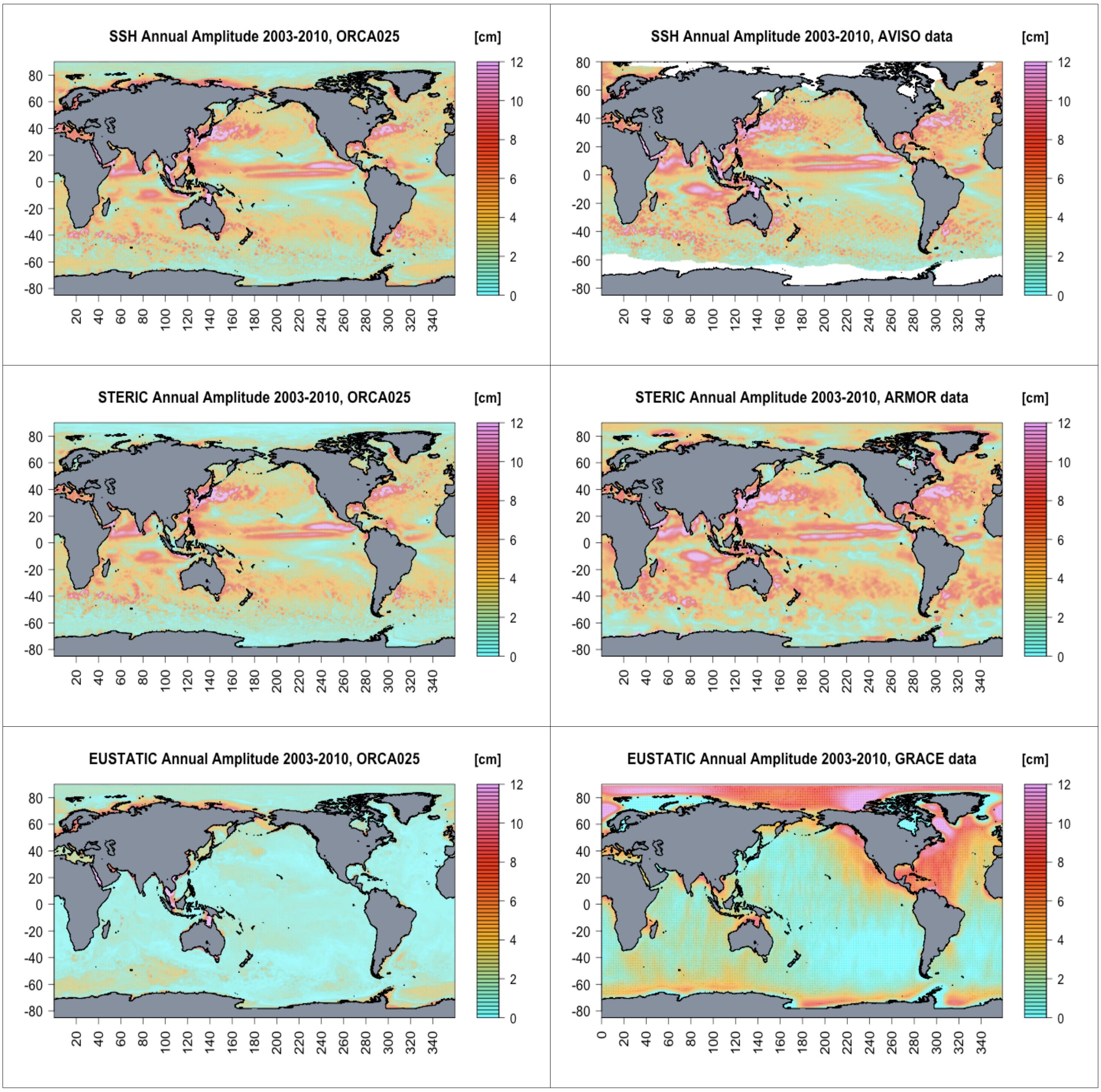

Figure 6- *Maps of annual amplitude over the period 2003-2010. Upper panels: sea level trend from the model (left) and from AVISO altimetry data (right); middle panels: steric component trend from the model (left) and from ARMOR data (right); bottom panels: eustatic component trend from the model (left) and from GRACE gravimetry data (right).*

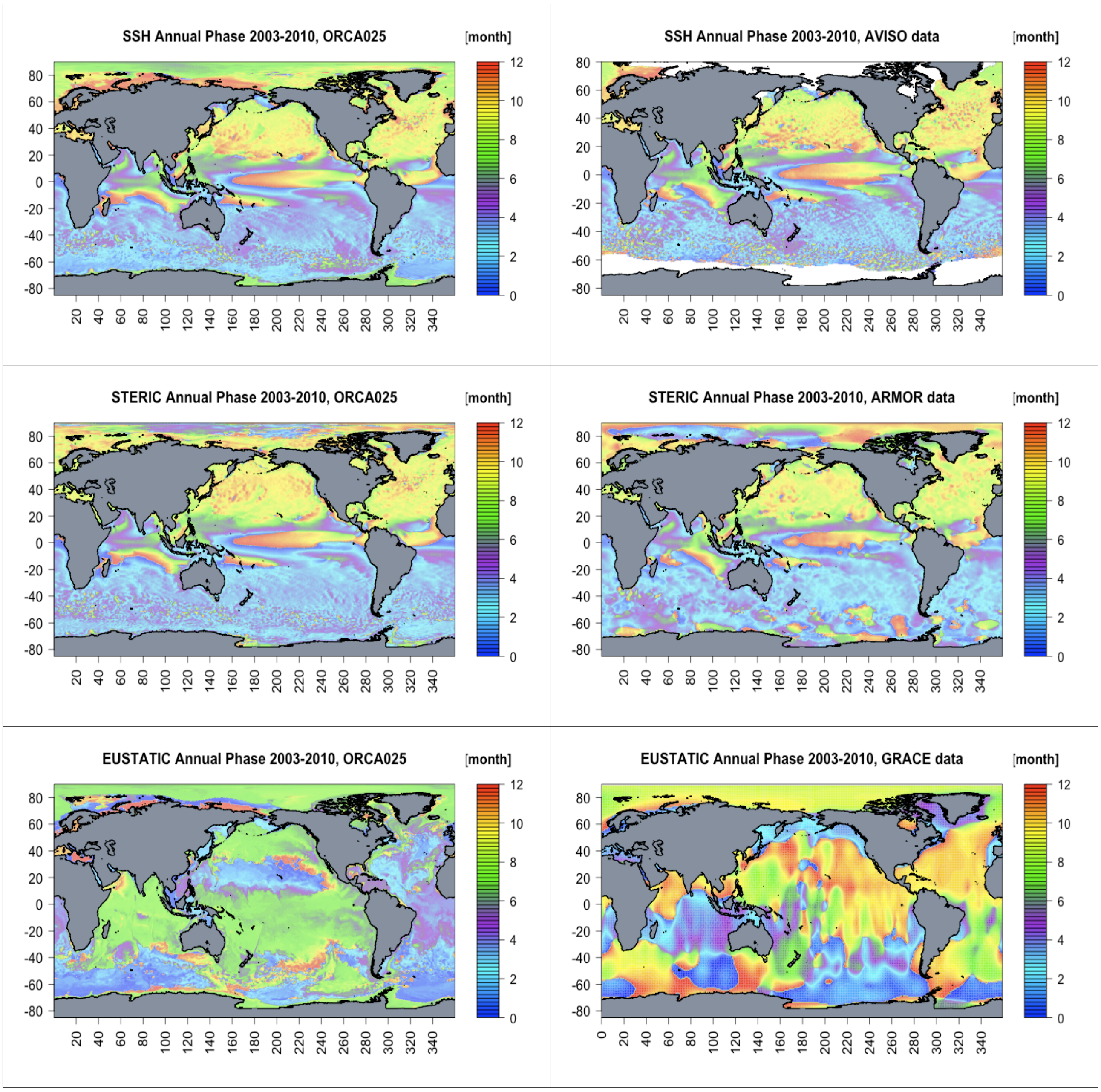

Figure 7- *Maps of annual phase over the period 2003-2010. Upper panels: sea level trend from the model (left) and from AVISO altimetry data (right); middle panels: steric component trend from the model (left) and from ARMOR data (right); bottom panels: eustatic component trend from the model (left) and from GRACE gravimetry data (right).*

The annual eustatic phase simulated by the model (Figure 7 bottom left panel) shows no phase reversal across the tropics and it is nearly in-phase over most of the Pacific and Indian Oceans, apart from band at 20°- 40°N (in agreement with results from Vinogradov et al., 2008). The simulated eustatic component differs from the GRACE data in amplitude, phase and trends (bottom panel Figures 5-7). For most regions, the agreement with gravimetry data is only qualitative (Ponte et al., 2007). The seasonal amplitude and regional trend are generally underestimated by the model, although the areas with largest variability present in the Southern Ocean are captured. Indeed this area is known to have a large barotropic variability also at seasonal scale (Stammer et al., 2000). A large difference is noticeable in the Arctic region where the model shows a negative trend in opposition to the positive GRACE trend. The reason for the differences seen in the trends may be a consequence of sea-floor motions that have been observed by GRACE, but not included in the model simulation. In addition our simulation is forced with climatological runoff, therefore the interannual variability of glaciers and ice sheets melting, as well as land water exchange, are not included in the model. GRACE data, on the other hand, contain both internal (ocean masses redistribution) and external (freshwater sources) mass variations and hence are not fully comparable to model values per se. It is worthy to note that inconsistencies between our model simulation and GRACE can be also attributed to uncertainties in the GRACE dataset (see Chapter 4 for the uncertainties quantification) and to the limits of the sea-ice model coupled to NEMO, which strongly impacts the high latitudes sea level variability.

3.2.3- Variability of sea level trends over different ocean basins

After the analysis of the capability of the model in realistically reproducing the spatial variability of sea level trend, and its seasonal amplitude and phase, through comparisons with independent observations, in this Section we continue our study investigating sea level trend over all the length of the simulation (1989-2010) and over different ocean sub-domains. In particular, we want to study how the positive and negative patterns of sea level trend have changed in time, to detect acceleration or deceleration of sea level change during the last years. Furthermore, for every ocean basin we want to understand to what extent the steric and eustatic component explain the total signal of sea level, during the last two decades, in terms of trend and seasonal variability.. In order to make this analysis we have divided the global ocean in six sub-basins following the differences in the spatial distribution of SSH trend. The rectangles drawn in Figure 8 represent the six areas analyzed: East and West Pacific, Indian Ocean, North and South Atlantic and the Southern Ocean.

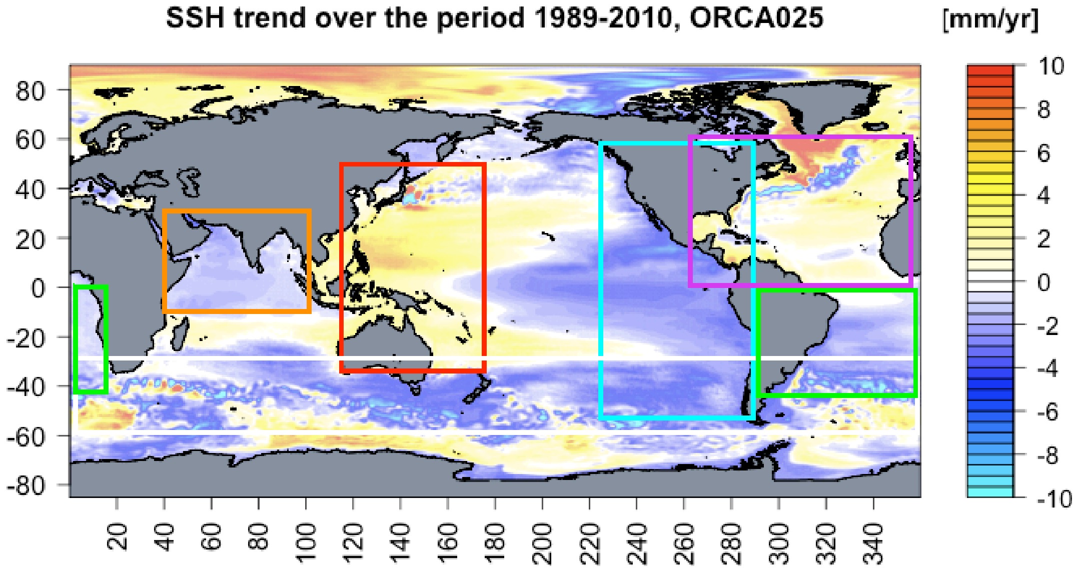

Figure 8- *Sea level linear trend over the period 1989-2010 from NEMO OGCM simulation. The rectangles correspond to the regions analyzed in Figure 11 and 12: East Pacific (cyan), West Pacific (red), Indian Ocean (orange), North Atlantic (violet), South Atlantic (green) and Southern Ocean (white); note that ocean basins masks have been used.*

For each sub-basin, we have compared the time series of the total SSH model against its components and AVISO altimetry data, computing the sea level anomalies with respect to the common period 1993-2010 and making a seasonal running mean (3 months) to filter the high frequency signal (Figure 9 and 10). The straight lines in Figure 9 and 10 represent the linear trends of the simulated SLA calculated separately for the two last decades: 1991-2000 and 2001-2010 (values are printed in the figures).

In Figures 9 and 10 the simulated SLA time series is in good agreement with altimetric data both in terms of slope and in terms seasonal amplitudes. In the Atlantic Ocean, especially in the North, the amplitude of the seasonal peaks are generally underestimated in the model simulation. There are also differences in the Southern Ocean where the simulated negative trend is not present in AVISO at the beginning of the time series, but it seems to recover since 1999. It is interesting to note the capability of the model in correctly reproduce the large variability of SLA in the Pacific with positive (negative) trend in the Eastern (Western) part. The peaks related to the strong El Niño event of 1998, acting in decreasing (increasing) the SSH in the West (East) Pacific with respect to the normal conditions, are also captured by the model. In all sub-basins almost the totality of sea level interannual and seasonal variability is explained by the steric component, except in the Southern Ocean and South Atlantic where the eustatic component gives a non-negligible contribution to the negative SSH trend, and in the Indian Ocean where the sea level variability is well explained by both the eustatic and the steric signal. It is worthy to note that the eustatic component generally shows a higher frequency variability (sub-seasonal), but a weaker amplitude.

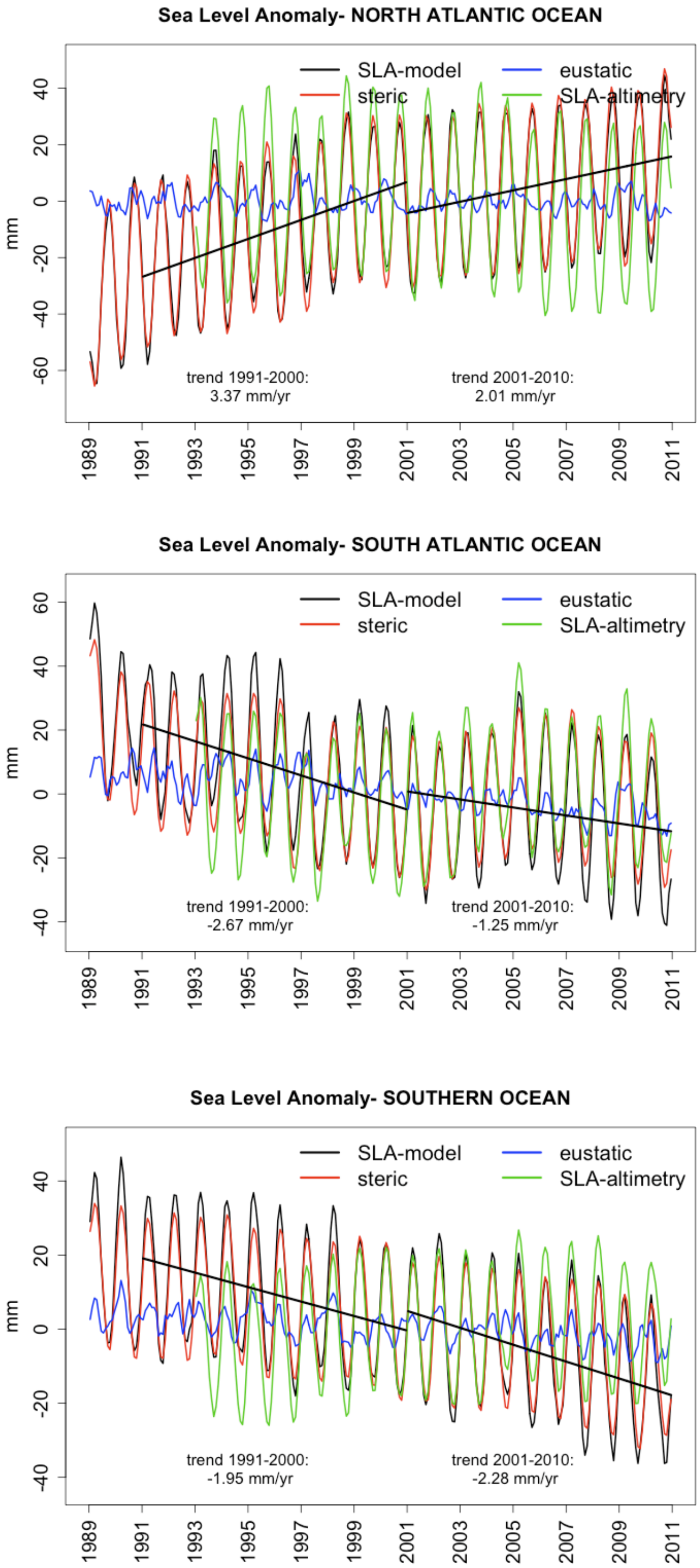

Figure 9- *SLA time series from model simulation (black line) and its steric (red line) and eustatic (blue line) components, averaged over the North Atlantic (upper), South Atlantic (middle) and Southern Ocean (bottom). SLA from AVISO altimetry data is plotted for comparison (green line).*

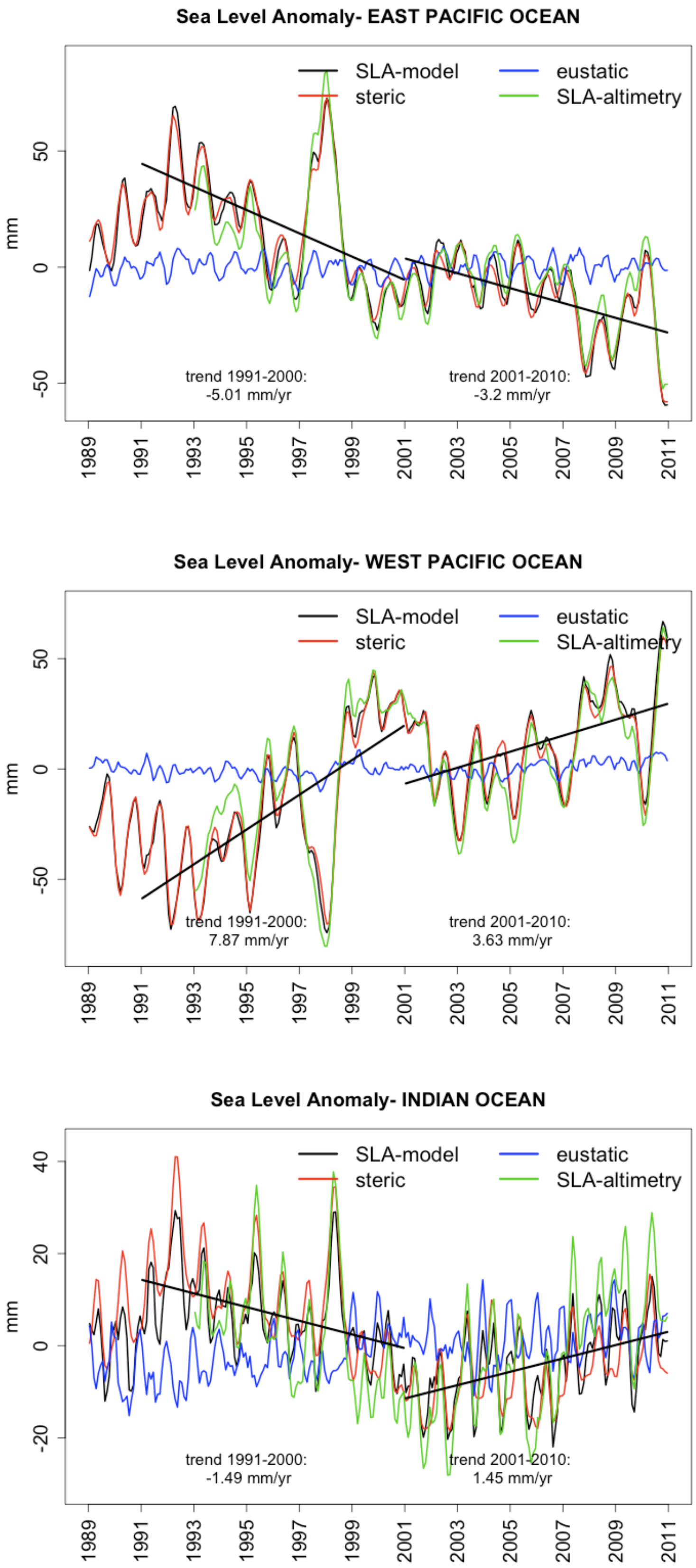

Figure 10- *SLA time series from model simulation (black line) and its steric (red line) and eustatic (blue line) components, averaged over the East Pacific (upper), West Pacific (middle) and Indian Ocean (bottom). SLA from AVISO altimetry data is plotted for comparison (green line).*

Comparing the two decades trends (printed in the Figures), we can see that all the regions that exhibits a negative sea level trend, except the Southern Ocean, have experienced an increase in sea surface height trend during the last decade, passing from -5.01 to -3.2 mm/yr in the East Pacific, from -2.67 to -1.25 mm/yr in the South Atlantic. The extreme case is the Indian Ocean where the trend has reversed from negative during the period 1991-2000 (-1.49 mm/yr) to positive in the last decade (1.45 mm/yr). In the Southern Ocean, the simulation shows a decreasing negative trend during the entire period in contrast with satellite data that shows a slight positive trend. The explanation lies in the fact that in the Southern Ocean the model results are not reliable since, as seen in the validation, the numerical calculations present high and extended values of SLA RMSE in this region and shows a very low correlation with satellite altimetry data. In the North Atlantic, where sea level exhibits a positive trend, the value slight decreases between the two decades from 3.37 to 2.01 mm/yr. The West Pacific Ocean is the region where sea level trend reaches the maximum value even if statistically the positive trend has decelerated during the last decade because of a drop of the 2001-2002 SSH. The large sea level rise makes this region one of the most vulnerable to future climate changes. We will study this region, and in particular the Small Islands area, in the next Section.

Anomalies in temperature and salinity in the ocean water column change density, which further gives rise to steric variations through the two distinct components: thermosteric or halosteric associated with only temperature or salinity variations, respectively. We extend our analysis quantifying the separete contribution of those terms in different range of depth (e.g., Lombard et al., 2009). In Lombard et al. (2009), the contributions to regional steric sea level change is presented as a comparison between the upper 0–735m and the deep 735m-bottom layers with the prevailing of the first range. We have extended their analyses by dividing the water column in three ranges of depth (surface-300m, 300-700m, 700m-bottom) in order to detect the portion of water column that plays the major role on sea level trend and its variability. In Figures 11 and 12 the thermosteric and halosteric contributions from different ranges of depth have been respectively averaged over the six sub-basins of Figure 8; the total steric component is overplotted (the dashed line). The steric contribution to sea level change is mainly caused by the thermosteric effect in the Pacific and Indian Oceans, where the main contributions comes from the upper 300 m, suggesting that most of the variations of heat content occur in the upper thermocline; in the Indian Ocean an important contribution coming from the deeper ocean (700m-bottom) is also visible. In the Atlantic Ocean the halosteric contribution plays an important role. In the North Atlantic, the thermo- and halo- steric components have an opposite behavior and almost compensate each other (see also Figure 13 where the spatial patterns of total, thermo- and halo- steric trends in the 1989-2010 period are shown), the first showing a decreasing the second an increasing trend resulting in a low, slightly positive, steric trend. The main contribution to the total steric is due to the thermosteric effect from the upper 300m layer and to the halosteric effect from the entire water column (quite homogeneous probably due to the weak ocean stratification at high latitudes, which does not allow to separate upper layers from deep ocean). In the South Atlantic, the situation reverses with the net prevailing of the halosteric contribution from the first 300m of depth, which generates a negative steric trend. Such mechanisms have already been observed with in situ hydrographic data in the subpolar North Atlantic (Antonov et al., 2002; Levitus et al., 2005), at high latitudes, and in the whole Atlantic Ocean (Ishii et al., 2006). In the Southern Ocean, the dominance of the negative halosteric trend, especially between 30°S-40°S (see Figure 13), produces a decreasing steric sea level. Our results agree with previous work (e.g. Lombard et al., 2009); in contrast to Lombard et al. (2009), in our study all the annual cycle and the majority of the steric signal is contained in the first 300 m of depth, both for the thermo- and for the halo-steric components.

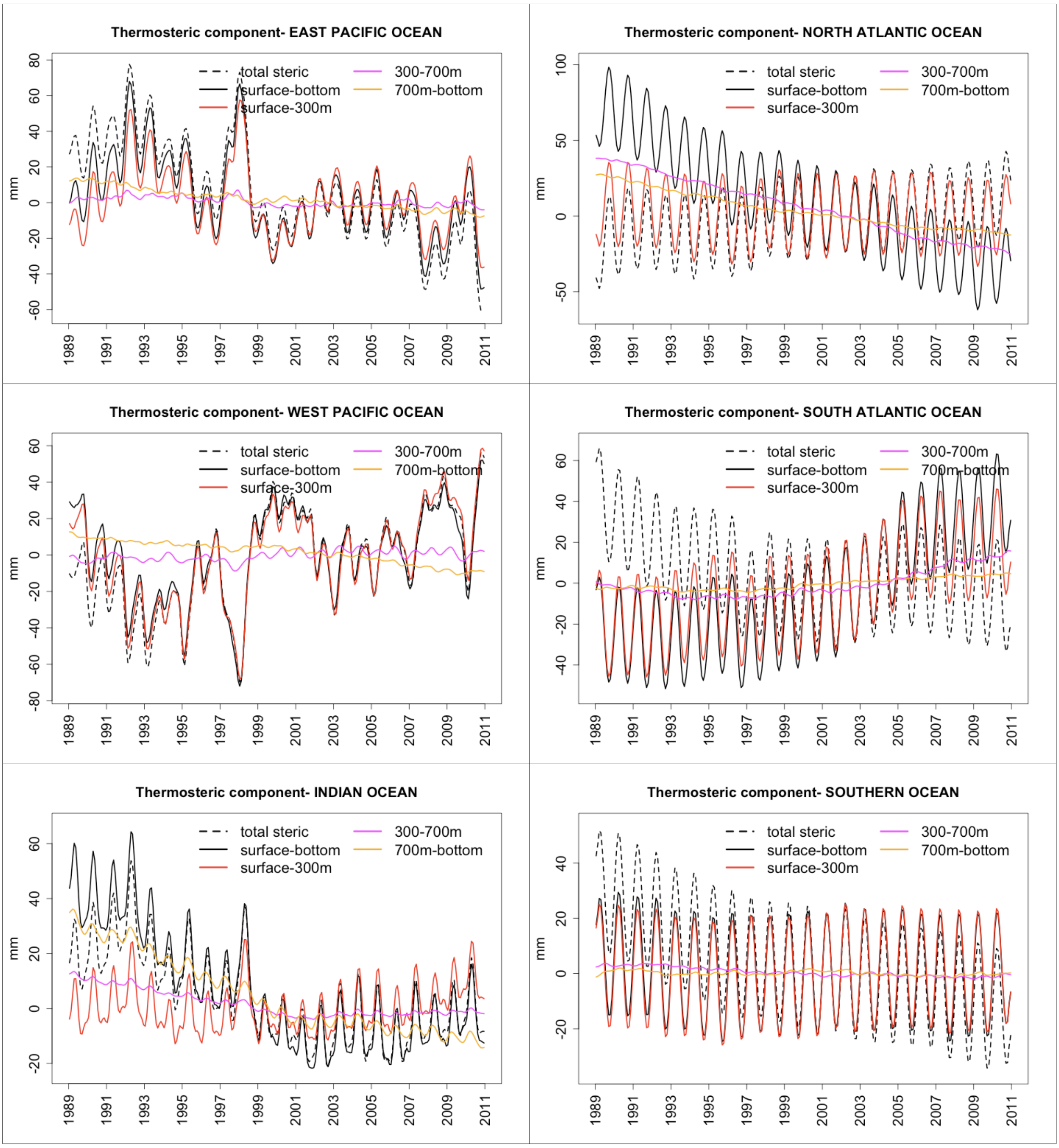

Figure 11- Thermosteric contribution from different depth ranges and total steric component (dashed line), averaged over different basins. Left: East Pacific (upper), West Pacific (middle) and Indian Ocean (bottom). Right: North Atlantic (upper), South Atlantic (middle) and Southern Ocean (bottom). Depth ranges: surface bottom (black line), surface-300m (red line), 300-700m (pink line), 700m-bottom (orange line).

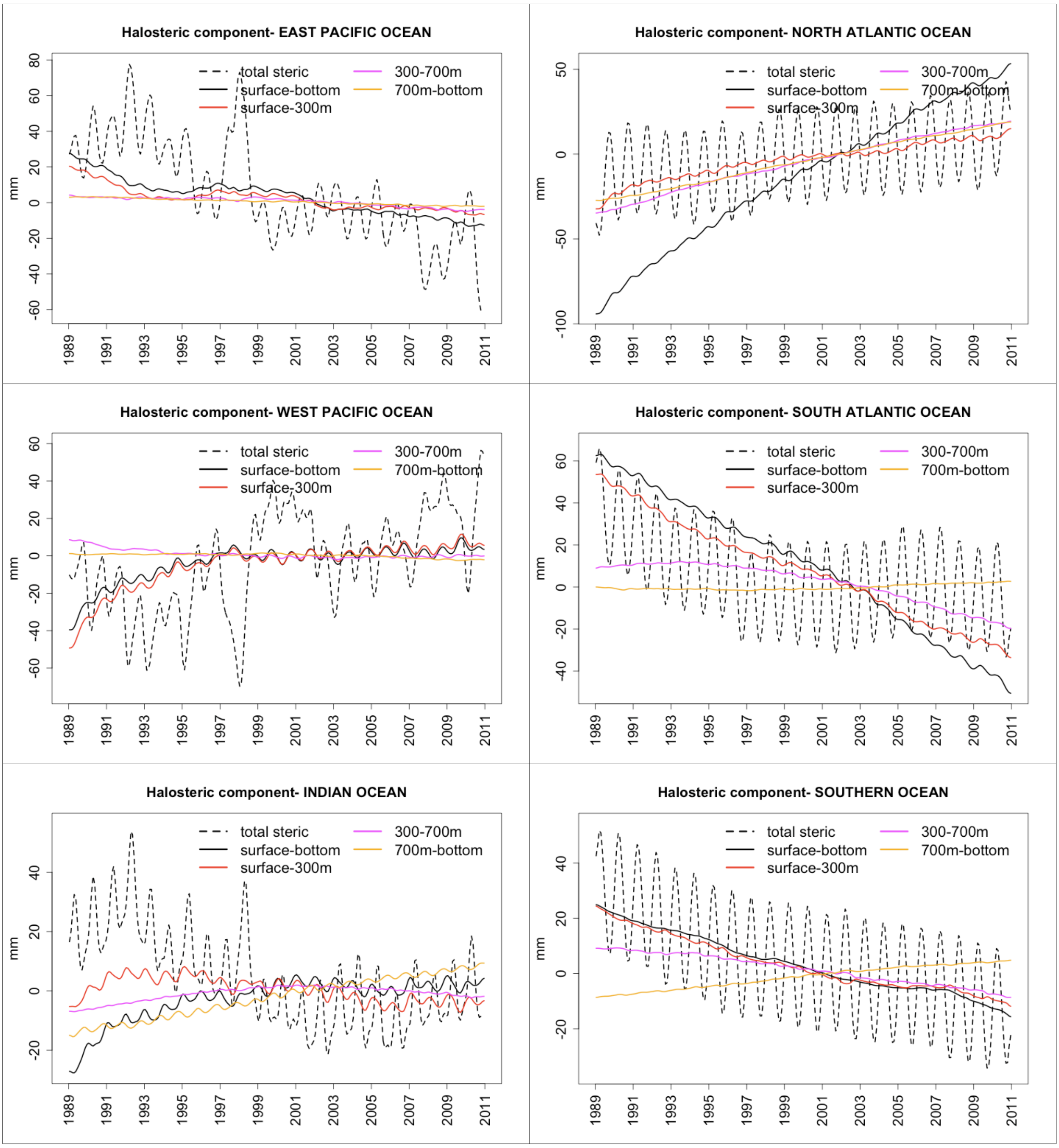

Figure 12- *Halosteric contribution from different depth ranges and total steric component (dashed line), averaged over different basins. Left: East Pacific (upper), West Pacific (middle) and Indian Ocean (bottom). Right: North Atlantic (upper), South Atlantic (middle) and Southern Ocean (bottom). Depth ranges: surface bottom (black line), surface-300m (red line), 300-700m (pink line), 700m-bottom (orange line).*

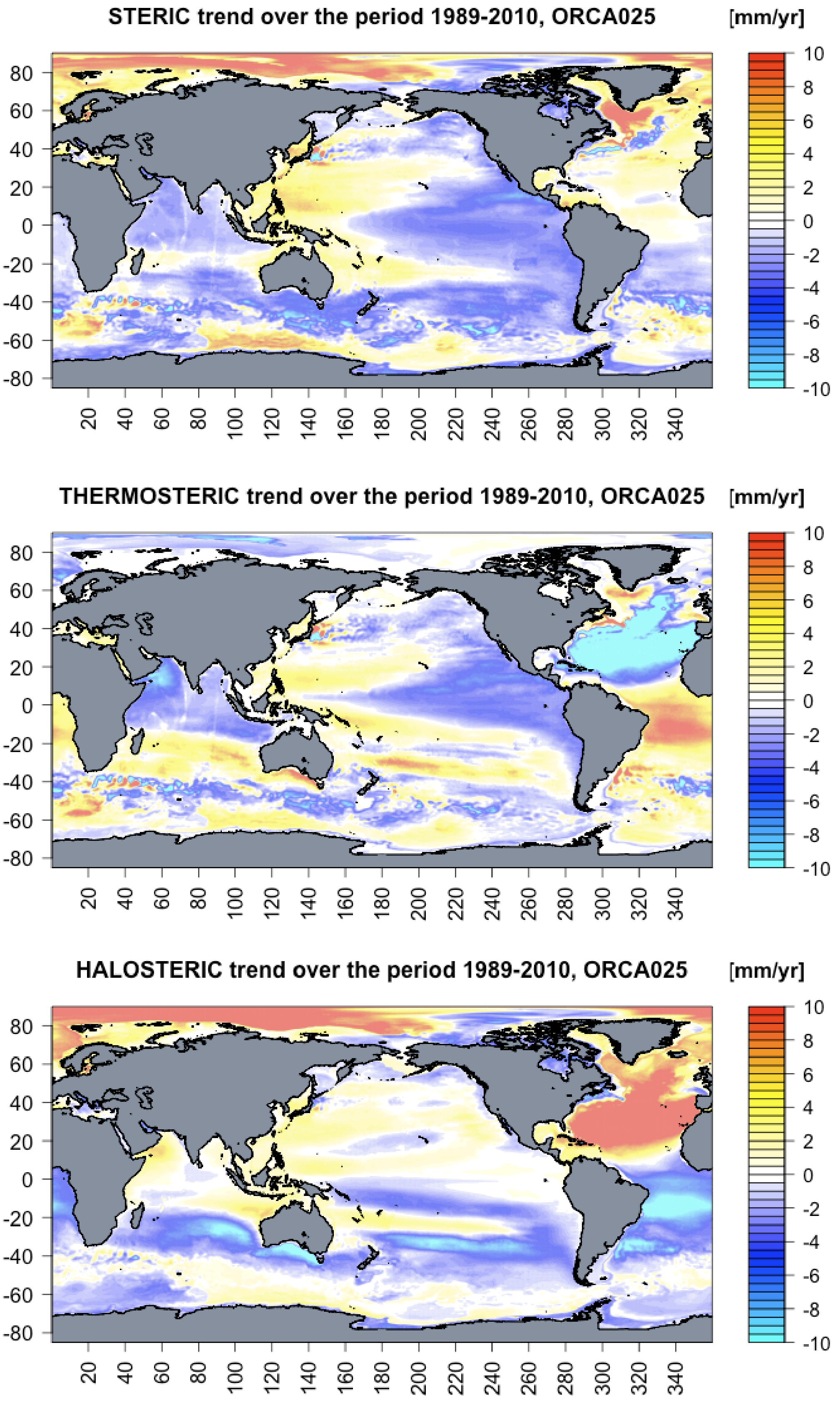

Figure 13- *Maps of steric (upper), thermosteric (middle) and halosteric (bottom) linear trend over the period 1989-2010 from NEMO OGCM simulation.*

3.3- Case study: causes of sea level rise in the Pacific Small Islands region

The Small Islands in the West Pacific Ocean are one of the most vulnerable coastal areas to the phenomenon of sea level rise. The West Pacific is the oceanic region where sea level is experiencing its highest positive trend (Figures 5 and 8); estimates from satellite altimetry data in the period 1993-2010 show that the area-averaged Small Islands sea level trend (5.63 mm/yr) exceeds the mean global trend (2.96 mm/yr) almost by a factor of 2, reaching local peaks of 12 mm/yr and 35 mm/yr during 2003-2010 period (Figure 5 top right panel, the colour bar is saturated to the maximum). Hence, we have chosen this critical and interesting coastal region of the ocean, to make a detailed and deep analysis in order to understand and quantify the causes of sea level rise. The boundaries of our area of interest are represented by the black rectangle in Figure 14.

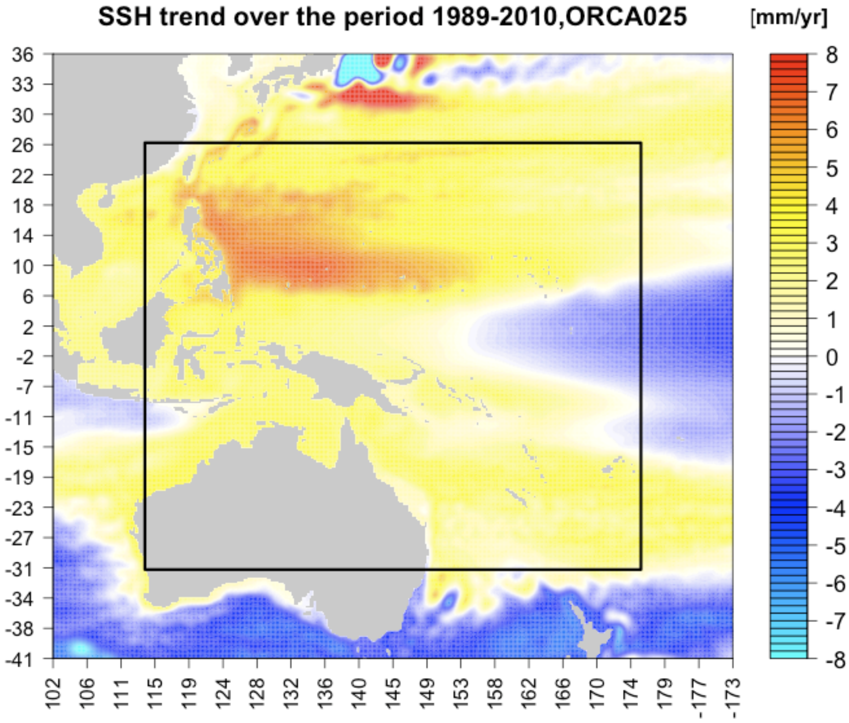

Figure 14- *Sea level linear trend over the period 1989-2010 from NEMO OGCM simulation. The rectangle represents the boundaries of our study area.*

In Figure 15 we have compared the area-averaged (over the region of interest) SLA time-series from model simulation (black line) with its steric (red line) and eustatic (blue line) components and with SLA from satellite observations (green line). The information we want to detect is whether the high values of SSH trend that characterise this region are caused by changes in sea water mass (the barotropic or eustatic sea level component) or in sea water density (the baroclinic or steric sea level component). In Figure 15, it is evident how the simulated time series of SLA is in good agreement with satellite altimetry data and it is definitely explained by its baroclinic component in terms of both trend and annual cycle, while the barotropic component shows a high frequency sub-seasonal variability and almost no trend. In particular, the SSH trend, averaged in space and time (1989-2010), is equal to 2.6 mm/yr and the mean steric trend is ~2.3 mm/yr, hence only 0.3 mm/yr can be ascribed to the eustatic contribution.

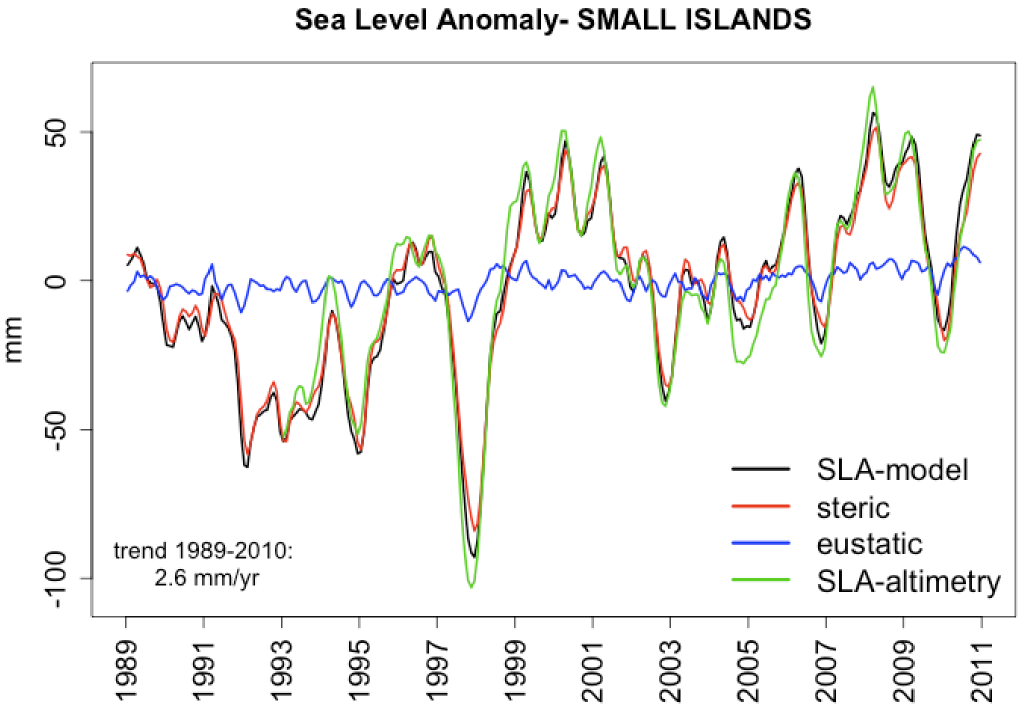

Figure 15- SLA time series from model simulation (black line) and its steric (red line) and eustatic (blue line) components, averaged over the Small Islands of Pacific region represented by the black rectangle in Figure 16. SLA from AVISO altimetry data is plotted for comparison (green line).

Which are the causes and the physical mechanisms responsible for the steric and the (small) eustatic trends that bring sea level to rise around the Small Islands of Pacific?

To answer to this question we have estimated, in our study area, the volume, heat and freshwater balances responsible for the eustatic, thermosteric and halosteric sea level change, respectively, and analysed the individual components of the balances.

The total volume transport in the domain is equal to the mass fluxes at the ocean surface plus the mass fluxes across the lateral boundaries. At sea surface, water volume is exchanged with atmosphere through precipitation (P) and evaporation (E) and with land through freshwater runoff (R); hence, the volume transport at surface V_{surf} has been calculated as the surface integral of the net water flux over the Small Islands region:

$$V_{surf}=\int_{\Omega_S}\frac{(P-E+R)}{\rho_{fw}}dA \qquad (16)$$

where $\rho_{fw}=1000\frac{Kg}{m^3}$ is the freshwater density, *dA* is the area of each grid cell of the spatial domain Ω_S . The oceanic circulation is responsible for the lateral volume transport V_{lat} across the vertical boundaries of the domain, which has been calculated as the integral of the horizontal velocity field normal $(\vec{u}\cdot\vec{n})$ to the lateral section Ω_L taken from ocean surface to the bottom:

$$V_{lat}=\int_{\Omega_L}(\vec{u}\cdot\vec{n})\,d\,\Omega_L \qquad (17)$$

where $\vec{u}=(u,v)$.

The time series of the eustatic sea level (blue line) and of the individual components of the volume balance are plotted in Figure 16, where the transports of equations (16) (orange line) and (17) (magenta line), in $\frac{m^3}{s}$, have been converted into the corresponding mm of sea level, by integrating the volume transport over the period 1989-2010 and dividing for the total area of the Small Islands region. The eustatic sea level trend (the same of Figure 15), which corresponds to the change in time of the volume transport balance $V_{surf}+V_{lat}$ in the domain, is due to an increase of the lateral volume transport that starts in 1994. It means that the small increasing eustatic trend, that causes 0.3 mm/yr of sea level rise in the Small Islands region, has to be attributed to an increase in the lateral mass fluxes into the domain.

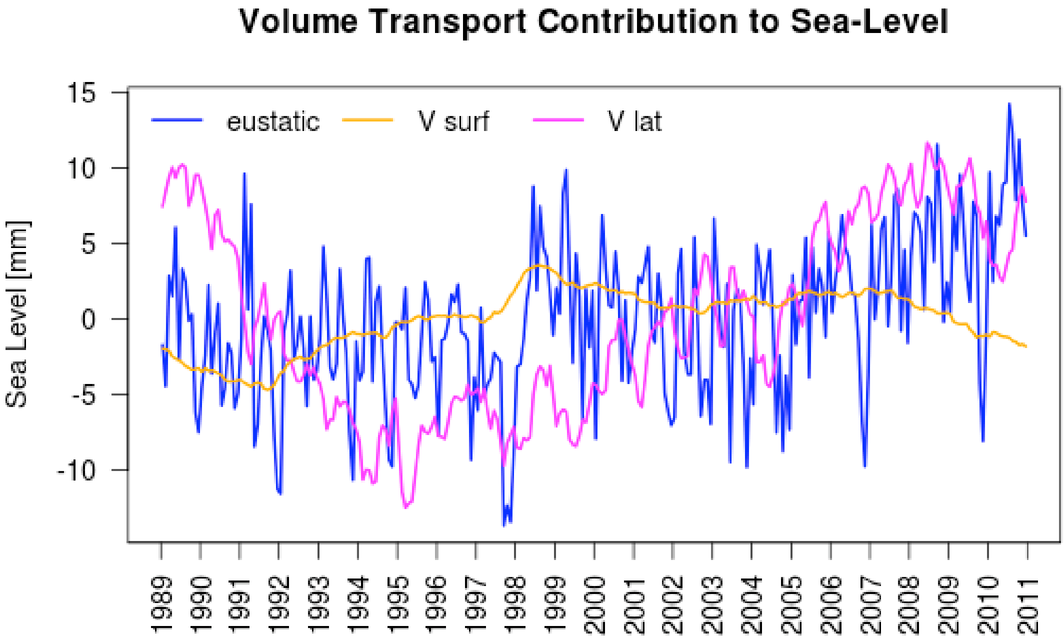

Figure 16- Eustatic contribution to sea level in the Small Islands region: lateral (magenta line) and surface (orange line) volume transport in the regional domain. The blue line corresponds to the eustatic SSH from model simulation (the same of Figure 17).

The heat balance in the study-area, which explains the thermosteric contribution to sea level, is the sum of the heat transport at surface and the heat lateral transport. The net exchange of heat between the ocean surface and the atmosphere Q_{surf} results from the balance between net short-wave (solar) radiation Q_{SW}, net long-wave radiation Q_{LW}, latent heat flux Q_{LH} and sensible heat flux Q_{SH}. The surface heat transport has been then calculated as the area integral, over the region of interest, of the net heat flux at ocean-atmosphere interface:

$$Q_{surf}=\int_{\Omega_s}(Q_{SW}+Q_{LW}+Q_{LH}+Q_{SH})dA \qquad (18)$$

The heat transport across the lateral sections Ω_L has been calculated as:

$$Q_{lat}=\int_{\Omega_L}\vec{u}\cdot\vec{n}(\rho_0 C_p T)\,d\Omega_L \qquad (19)$$

where $\rho_0 = 1020 \frac{Kg}{m^3}$ is the reference ocean density, $C_p = 4000 \frac{J}{Kg\,°C}$ is the specific heat of the ocean and *T* is the the ocean temperature in °C. The heat transport components of equation (18) (orange line) and (19) (magenta line), in *Watt*, have been converted into the corresponding mm of sea level by using the following equation (Marshall and Plumb, 2008):

$$SSH = \frac{1}{A}\frac{1}{\rho_0}\alpha_T \int \frac{Q}{C_p \rho_0} dt$$

where *Q* indicates the surface or lateral heat transport and $\alpha_T = 0.335 \frac{Kg}{m^3\,°C}$ is the thermal expansion coefficient. In Figure 17, the surface (orange line) and lateral (magenta line) heat transports time series are plotted together with the total steric (brown) and thermosteric (red line) sea level. Comparing the time series curves of Figure 17, we can observe that the thermosteric sea level, equal to 1.4 mm/yr, is due to an increase of both the lateral heat fluxes (with a trend of 0.54 mm/yr - that explains all the seasonal variability of the thermosteric component closely following its curve) and mainly the surface heat fluxes (with a trend of 0.86 mm/yr - that gives a strong contribution to the 1999-2001 peak). In particular, the increasing temperature is concentrated between the 100-300 m depth layer (i.e. in the upper thermocline zone where the heat is stored) with a minor contribution from the upper 100m and deeper 300-700 m layers (see the histogram of Figure 19).

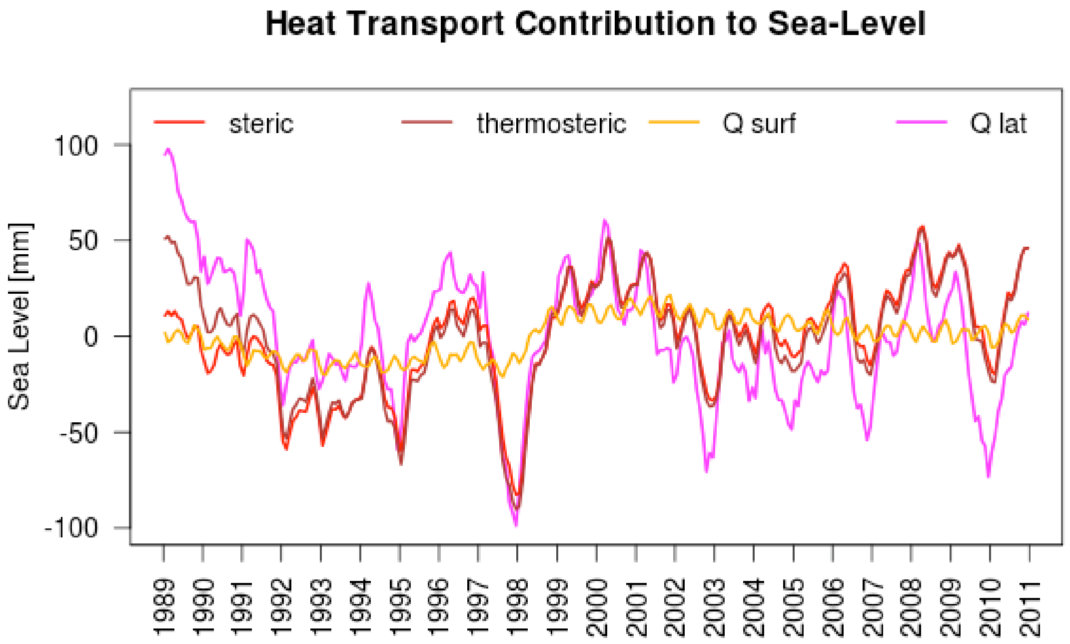

Figure 17- *Thermosteric contribution to sea level in the Small Islands region: lateral (magenta line) and surface (orange line) heat transport in the regional domain. The red and brown lines correspond to the steric SSH (the same of Figure 17) and its thermosteric component, respectively, from model simulation.*

As for the eustatic and thermosteric components, a similar approach has been adopted to understand the causes of the halosteric contribution to the steric sea level trend in this particular region. The freshwater balance at the ocean surface and at the lateral boundaries of the domain have been calculated, respectively, as:

$$FW_{surf}=\int_{\Omega_S} SSS\frac{(P-E+R)}{\rho_{fw}}dA \tag{20}$$

$$FW_{lat}=\int_{\Omega_L}(\vec{u}\cdot\vec{n})\frac{(S_0-S)}{S_0}d\Omega_L \tag{21}$$

where *SSS* is the sea surface salinity, $S_0=34.9\,PSU$ is a reference salinity and *S* is the ocean salinity. The two freshwater transports have been then converted into the correspondent mm of sea level by using the following equation (Marshall and Plumb, 2008):

$$SSH=\frac{1}{A}\int\frac{(\beta\, FW)}{\rho_0}dt$$

where FW is the surface or lateral freshwater flux and $\beta = 0.75 \frac{Kg}{m^3\,PSU}$ is the haline expansion coefficient. Time series of the simulated halosteric sea level component (cyan line) and of the lateral (magenta line) and surface (orange line) freshwater transports, are shown in Figure 18. Similarly to the eustatic component, the increasing halosteric trend (0.87 mm/yr - that contributes to the 2.3 mm/yr steric sea level rise) has to be attributed to an increase in the lateral freshwater transport within the region (with a trend of 0.6 mm/yr) and to a less extent to fluxes at the surface (0.27 mm/yr). In particular, the decrease of salt content occurs in the superficial 100 m of the water column (Figure 19).

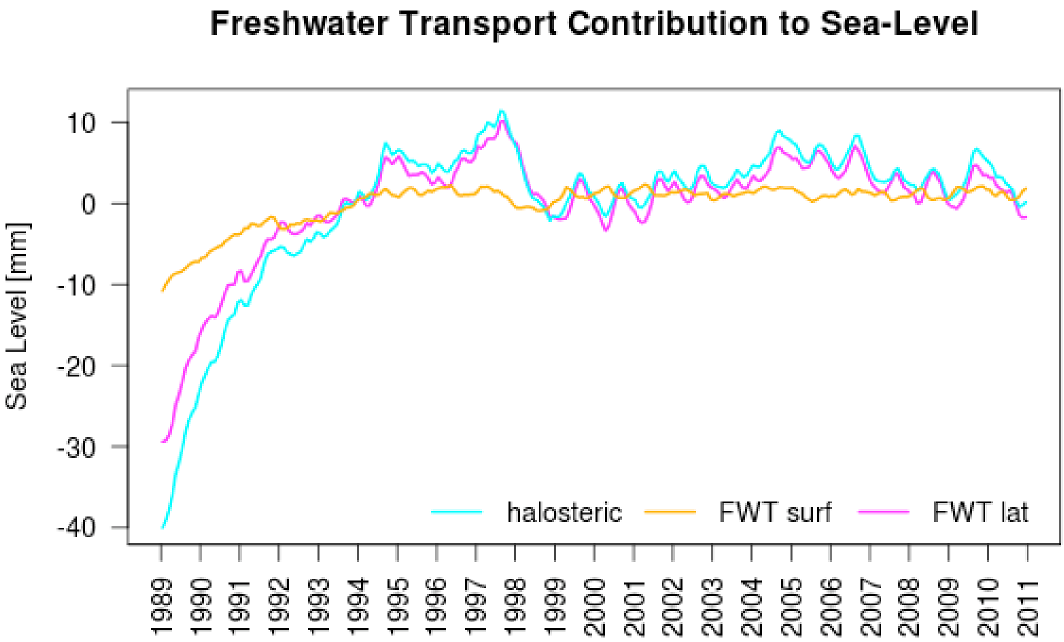

Figure 18- *Halosteric contribution to sea level in the Small Islands region: lateral (magenta line) and surface (orange line) freshwater transport in the regional domain. The cyan line correspond to the halosteric sea level component from model simulation.*

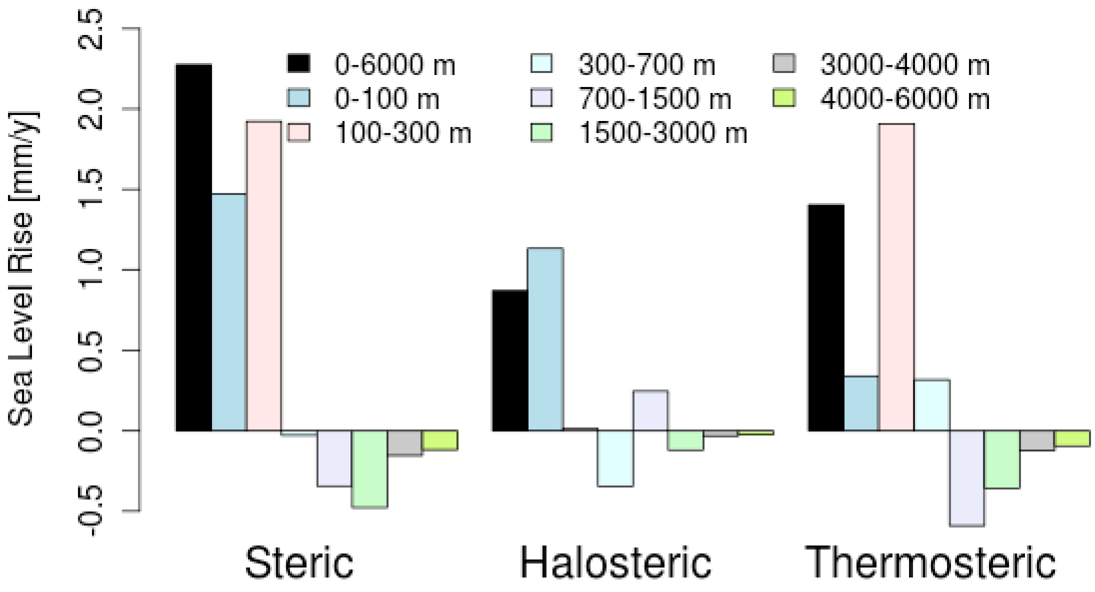

Figure 19- *Steric, halosteric and thermosteric contribution to sea level rise in the Small Islands of Pacific region (see the black rectangle in Figure 16), from different ranges of depth.*

The estimates of the different contributions in terms of sea level rise have been summarised in Table 1.

Contribution to Sea Level rise (mm/yr)	**Thermosteric**	**Halosteric**	**Eustatic**
Surface	0,86	0,27	0,09
Lateral	0,54	0,6	0,24
Total	1,4	0,87	0,33

Table 1- *Contribution of the thermosteric, halosteric and eustatic components to sea level rise (in mm/yr), calculated from the surface and lateral balance of heat, freshwater and volume transport, respectively.*

The volume, heat and freshwater transports and their corresponding trends over the 1989-2010 period, across the four boundaries of the regional domain, are summarised in Figure 20. The volume transport in the Small Islands region is characterised by an incoming flux of warm water from the eastern boundary (advected by the South Pacific gyre) and outgoing fluxes across the northern, southern and western boundaries. The outgoing volume transport at the southern boundary of the domain has decreased over 1989-2010, showing a negative trend of -0.13 Sv/yr. This deceleration of the outflow water is only partially balanced by the acceleration of the outgoing fluxes at the northern (0.01 Sv/yr) and western boundaries (0.10 Sv/yr) of the domain. The positive imbalance thus shows that an accumulation of water inside the Small Islands region has occurred, causing the small eustatic sea level rise of 0.24 mm/yr previously discussed. The positive halosteric trend is due to an increase of incoming freshwater transport (17.9 mSv/yr) that enters across the eastern boundary, together with a deceleration of the outgoing freshwater from the southern boundary (-3.99 mSv/yr), which are not balanced by the increasing freshwater outgoing transports from the northern and western boundaries. Finally, the increasing thermosteric trend is found to be due to an increase of the heat transport (40.89 TW/yr) across the eastern boundary, due to the warming of the incoming equatorial waters, which is not compensated by the heat loss from the other boundaries in our simulation. It is worthy to note that the heat flux increase is solely due to an increase of the incoming waters temperature, since the volume transport remains quite stable (0.005 Sv/yr) over the all period.

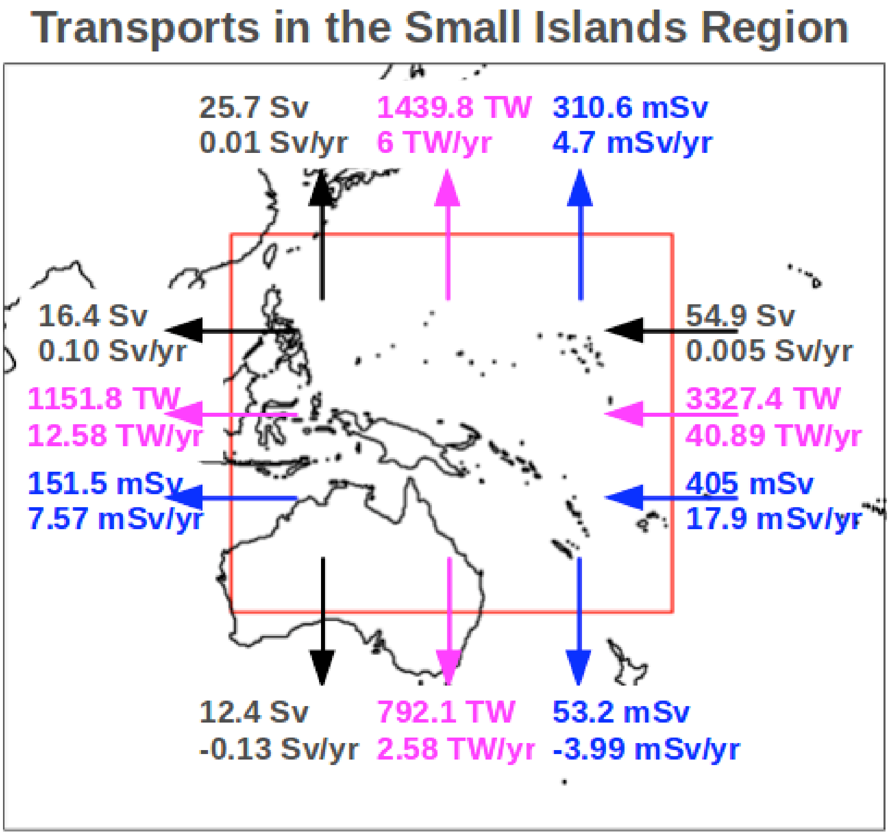

Figure 20- *Volume (in black), heat (in pink) and freshwater (in blue) transports and trends (over 1989-2010 period) across the vertical boundaries of the Small Islands region (delimited by the red rectangle). The arrows indicate the direction of the transport across the four boundaries. Units of the transports are Sverdrup (Sv), Terawatt* $(1\mathrm{TW}=10^{12}\,Watt)$ *and milli-Sverdrup* $(1\mathrm{mSv}=10^{3}\frac{m^{3}}{s})$.

To finalize our analysis, we have looked at the simulated SSH time series (displayed in Figure 22) in correspondence of nine selected Small Islands Developing States (SIDS) where tide gauges data are available, taken as reference islands for a local study of sea level change over the 2001-2010 period. The selected SIDS have been reported in Figure 21, from North to South the states are: Palau, Federated States of Micronesia, Marshall Islands, Kiribati, Nauru, Tuvalu, Samoa, Fiji and Tonga. At these particular locations we have compared the simulated sea level trends with tide gauges measurements from the Permanent Service for Mean Sea Level (PSMSL).

The PSMSL provides a dataset of historical quality-checked records of sea level from almost 2000 coastal and non-coastal tide gauges (Woodworth and Player, 2003). I t is worthy to mention that care should be paid in the comparison of our results with PSMSL records, since tide gauges data are affected by the ground vertical motions, not included in the model sea level representation, especially in active tectonic regions, in areas subject to GIA and to strong subsidence. Note also that tide gauge observations may not be fully representative of the simulated sea level, since a single model grid cell represents the average ocean state of $\sim 500\,Km^2$ while the tide gauges provide punctual observations. For these reasons we consider the comparison in a qualitative sense only.

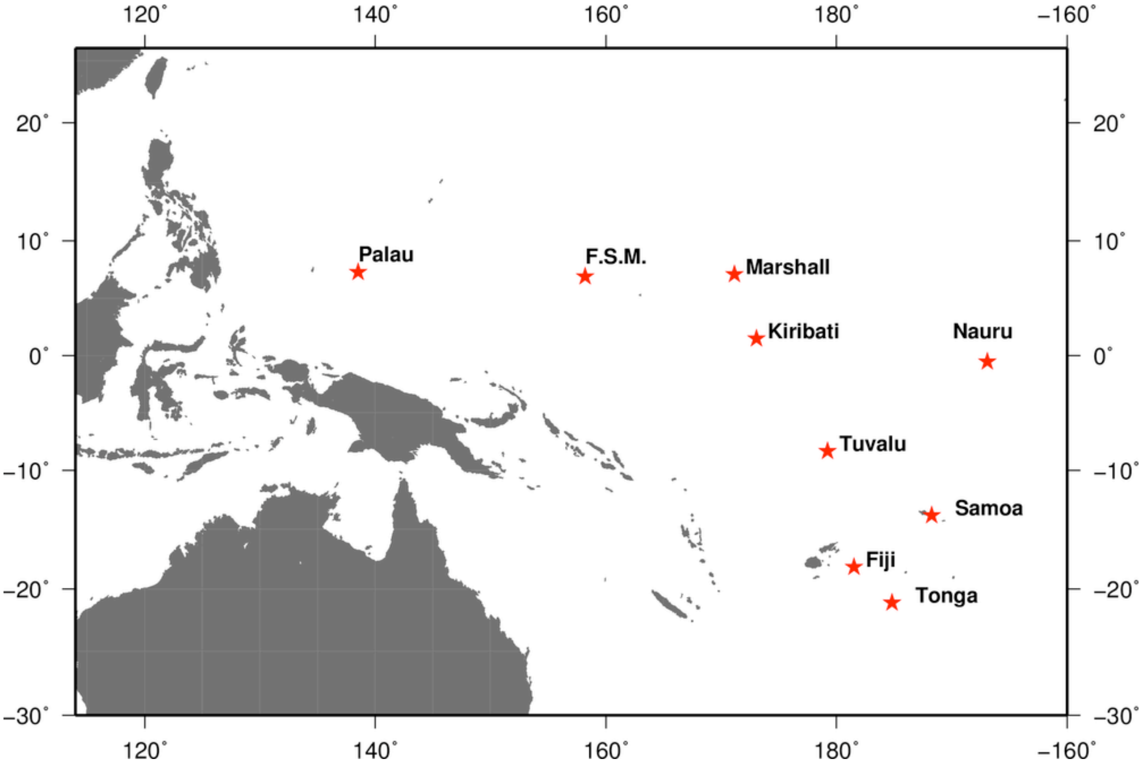

Figure 21- *Western tropical Pacific region considered in our study. Red stars corresponds to the Small Pacific Islands Developing States selected for a local study on sea level change over 2001-2010 period (Figure 22). From North to South: Palau, Marshall Islands, Federated States of Micronesia, Kiribati, Nauru, Tuvalu, Samoa, Fiji and Tonga.*

In our simulation only Kiribati, Nauru and Tuvalu exhibit a negative trend of -5.07 mm/yr, -7.88 mm/yr and -0.95 mm/yr, respectively, and thus show a sea level drop over the last 10 years. The other islands exhibit positive sea level trends confirming that, in our simulation and in accordance with tide gauges measurements, the majority of the western Tropical Pacific islands have suffered from sea level rise during the past 10 years. Except for Marshall Island and Samoa (which show weak trends of 1.84 mm/yr and 0.21 mm/yr, respectively) all the other sites exhibit a sea level rise larger than 4.24 mm/yr that peaks to 15.06 mm/yr in Palau, located in the area of higher SSH trend values (see Figure 14). The signs of the simulated sea level trends agree with the observed ones at every locations, although the former generally overestimates the magnitude of the trends with respect to the tide gauges.

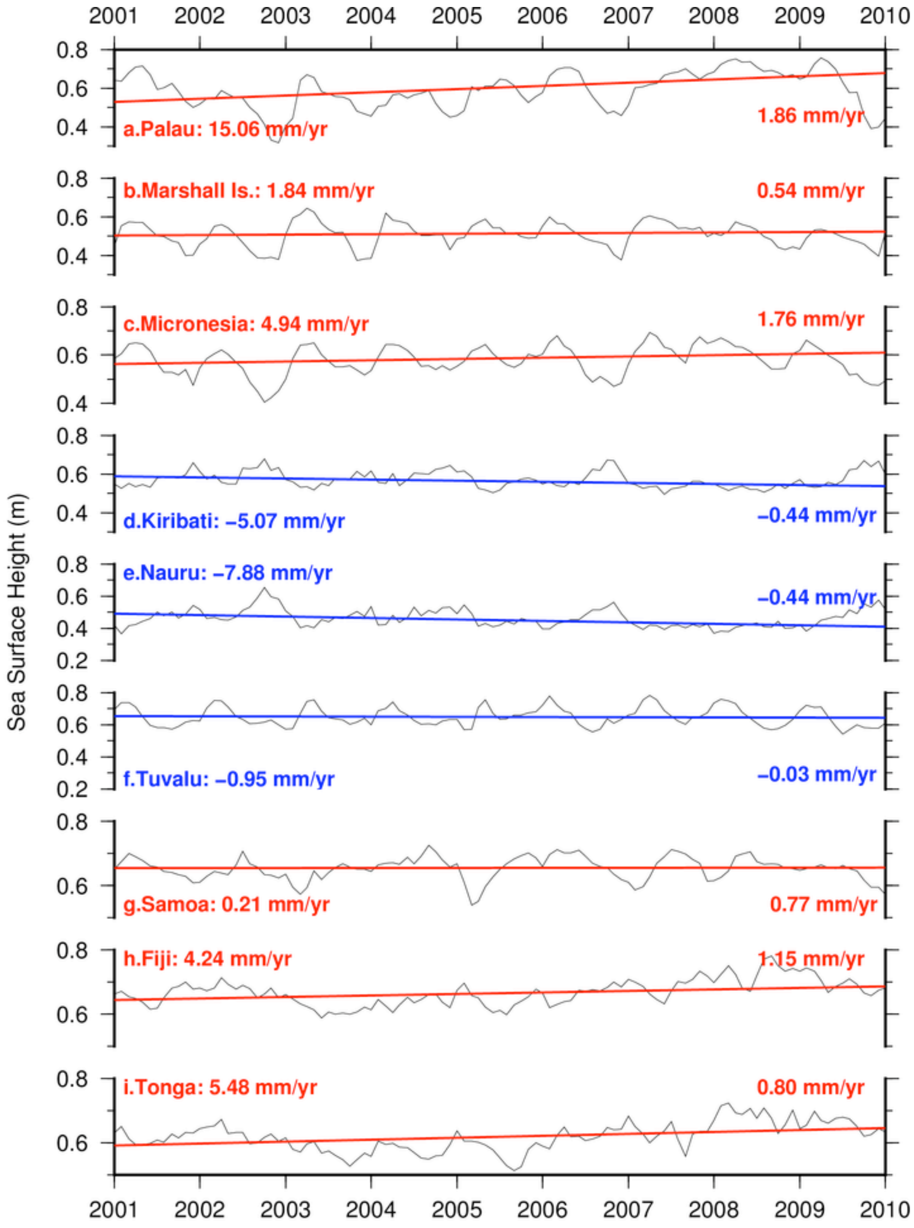

Figure 22- *Simulated sea surface height change for the 2001-2010 period at the selected Small Islands Developing States of Figure 21 (States are shown from North to South). Linear trends have been superimposed on the time series, in red for positive trend and in blue for negative trend. Mean trend values from model and tide gauges are shown in the top left and right corner, respectively, of each frame.*

3.4- Summary and conclusions

In this study we have used a global ocean model at 1/4° resolution, driven by corrected ERA-Interim atmospheric forcing in order to examine spatial patterns of sea level change. Most of previous works focused on the use of data assimilation to investigate the sea level variability (e.g. Wenzel and Schroter, 2007; Kohl and Stammer, 2008). In the comparison with altimetric observations we have shown that, even without data assimilation, our model is able to reproduce correctly both the spatial geographical patterns and temporal variability of sea level, also due to an optimization of the forcing fields that we have performed (Chapter 2). The highest values of SLA RMSE (~30 cm) and low temporal correlation are found in regions with strong mesoscale dynamics such as the western boundary currents and the ACC, while the RMSE values are generally low (~5 cm) and the correlation high in the rest of the ocean. The model ability in simulating past global and regional sea level change and its driving physical mechanisms, suggests that our configuration might be an useful tool to study sea level change in the future.

In accordance with previous works where an eddy-permitting OGCM has been used to study spatial patterns of sea level change (Lombard et al., 2009; Penduff et al. 2010; Song and Colberg, 2011), we have decomposed the total sea level signal in the steric and eustatic components. We have validated both the steric and, differently from Lombard et al. (2009), the eustatic component of sea level by comparing the simulated regional trends, seasonal amplitude and phase with GRACE gravimetry observations of mass change, available over the period 2003-2010.

The SSH spatial patterns of seasonal amplitude, phase and regional trend are, in general, well captured by the model, especially in the Pacific and Indian Ocean, while the model overestimates the North Atlantic trend and underestimates the ACC trend south off Australia. The sea level signal is quasi-totally explained by its steric component, in terms of trend, amplitude and phase, except in the ACC region (especially in the South Pacific between 50 and 70°S) and north of 60°N, where the trend and mainly the seasonal variability of sea level are largely eustatic. Our conclusions are in accordance with the work of Wenzel and Schroter (2007), who studied sea-level-change contributions through a global ocean data assimilation experiment; we found very similar geographical patterns for the eustatic regional trends, although the eustatic variability at both seasonal and interannual time scale is generally underestimated by our model. The eustatic component contributes to the seasonal amplitude signal in the Indian Ocean.

Once the model representation of the sea level and its components has been extensively validated, we have extended our analysis over all the length of the simulation (1989-2010) investigating sea level trends in six ocean basins chosen according to the large-scale positive and negative patterns of SSH trend. By comparing the distinct trends of two decades, we have shown that there are regions where the sea level trends has accelerated during the last decade with respect to the previous one (passing from -5.01 to -3.2 mm/yr in the East Pacific and from -2.67 to -1.25 mm/yr in the South Atlantic), other regions where sea level is decelerating (passing from 3.37 to 2.01 mm/yr in the North Atlantic) and regions like the Indian Ocean where the trend has moved from negative during the period 1991-2000 (-1.49 mm/yr) to positive in the last decade (1.45 mm/yr). The West Pacific Ocean is the region where sea level trend has reached the maximum value, even if statistically the trend has decelerated from 7.87 to 3.63 mm/yr during the last decade, because of a drop of the 2001-2002 SSH.

To further go into the analysis, the steric sea level has been divided into its thermosteric and halosteric contributions from different ranges of depth in order to quantify the contributions of different depth range and identify the layer playing a major role on sea level trend and its variability. Results from model simulation indicate that most of sea level change is due to the temperature change in the upper 300 m of the ocean for the Pacific and Indian Ocean. In the Atlantic Ocean, the halosteric effect is significant. While the positive halosteric trend is almost compensated by the negative thermosteric trend in the northern sector, the 0-300m halosteric component gives a strong contribution and dominates over the termosteric one in the south. In the Southern Ocean, the thermosteric and halosteric effects are comparable, while in the Arctic Ocean the steric sea level change is driven by halosteric changes. Our results agree with previous work (e.g. Lombard et al., 2009), but we have used a finer decomposition of the water column demonstrating that all the annual cycle and the majority of the steric signal is contained in the upper 300 m layer for both the thermo- and the halo- steric components.

A case study has been performed in the critical region of the Pacific Small Islands region in order to understand the causes that there drive sea level rise. In accordance with tide gauges measurements in correspondence of nine selected SIDS, the majority of the islands have suffered from sea level rise during the past 10 years. The model results of our study show that, for the period 1989-2010, the local sea level trend (2.6 mm/yr) is almost totally explained by its steric component in terms of both trend (~2.3 mm/yr) and annual cycle, while only 0.3 mm/yr of the trend is explained by the eustatic sea level component (due to an increase in the lateral inflow mass transport equal to 0.24 mm/yr). Regarding the steric trend, 1.4 mm/yr is due to the thermosteric effect, with the main contribution between 100 and 300 m of depth, while the halosteric component contributes with a positive trend of 0.87 mm/yr from the 100 m surface layer. Results of freshwater balance show that the main cause of the increasing halosteric trend is an increase in the lateral transport of the incoming freshwater that enters across the eastern boundary, together with a deceleration of the outgoing freshwater from the southern boundary, generating a rise of 0.6 mm/yr. The thermosteric sea level trend is mainly caused by an increase in the surface heat transport (0.86 mm/yr). Nevertheless, the lateral heat transport also gives an important contribution (0.54 mm/yr) and explains all the seasonal variability of sea level. The increasing thermosteric trend, mainly concentrated between 100 and 300m of depth, is due to an increase of heat transport (40.89 TW/yr) across the eastern boundary due to the warming of the incoming equatorial water, which we found not compensated by the heat loss from the other boundaries.

References

Ablain M., Cazenave A., Guinehut S., Valladeau G., 2009. A new assessment of global mean sea level from altimeters highlights a reduction of global slope from 2005 to 2008 in agreement with in-situ measurements. *Ocean Sciences,* 5, 193-201.

Antonov J.I., Levitus S., Boyer T.P., 2002. Steric sea level variations during 1957–1994: importance of salinity. *J Geophys Res* 107 (C12):8013, doi:10.1029/2001JC000964.

Barnier B., Madec G., Penduff T., Molines J.-M., Treguier A.-M. et al., 2006. Impact of partial steps and momentum advection schemes in a global circulation model at eddy permitting resolution. Ocean Dynam., 56(5-6), 543–567. doi:10.1007/s10236-006-0082-1.

Becker M., Meyssignac B., Llovel W., Cazenave A. and Delcroix T., 2012. Sea level variations at tropical Pacific islands since 1950. *Global and Planetary Change*, 80-81, 85-98.

Bindoff N., Willebrand J., Artale V. , Cazenave A., Gregory J. , Gulev S., Hanawa K., Le Quéré C., Levitus S., Nojiri Y., Shum C.K., Talley L., Unnikrishnan A., 2007. Observations: oceanic climate and sea level. In: *Climate change 2007: The physical Science Basis. Contribution of Working Group I to the Fourth Assessment report of the Intergouvernmental Panel on Climate Change* [Solomon S., D. Qin, M. Manning, Z. Chen, M. Marquis, K.B. Averyt, M. Tignor and H.L. Miller (eds.)]. Cambridge University Press, Cambridge, UK, and New York, USA.

Cabanes C., Cazenave A., Le Provost C., 2001. Sea level change from Topex/Poseidon altimetry for 1993–1999 and possible warming of the southern oceans. *Geophys Res Lett* 28(1):9–12, doi:10.1029/2000GL011962.

Carton J.A., Giese B.S., Grodsky S.A., 2005. Sea level rise and the warming of the oceans in the Simple Ocean Data Assimilation (SODA) ocean reanalysis. J Geophys Res 110:C09006, doi:10.1029/2004JC002817.

Cazenave A. and Llovel W., 2010. Contemporary sea level rise. Annu. Rev. Mar. Sci., 2(1), 145–173, doi:10.1146/annurev-marine-120308-081105.

Chambers D. and Schröter J., 2011. Measuring ocean mass variability from satellite gravimetry. *Journal of Geodynamics*, 52, 333-343.

Chowdhury M.R., Chu P.-S., Schroeder T., 2007. ENSO and seasonal sea-level variability – A diagnostic discussion for the US-affiliated Pacific Islands. *Theor. Appl. Climatol.* 88: 213–224.

Church J.A. and White N.J., 2006. A 20th century acceleration in global sea-level rise. *Geophys. Res. Lett. 33,* doi:10.1029/2005GL024826.

Delcroix T., Cravatte S., McPhaden M.J., 2007. Decadal variations and trends in tropical Pacific sea surface salinity since 1970. *J Geophys Res* 12:C03012, doi:10.1029/2006JC003801.

Ezer T., and Mellor G.L., 1994. Diagnostic and prognostic calculations of the North Atlantic circulation and sea level using a sigma coordinate ocean model. *J. Geophys. Res.*, 99, 14, 159-14, 171.

Gill A.E., 1982. Atmosphere-ocean dynamics. Academic Press, San Diego, Calif., 662 pp.

Greatbatch R. J., 1994. A note on the representation of steric sea level in models that conserve volume rather than mass. *J. Geophys. Res.,* 99, 12, 767-12, 771.

Guinehut S., Le Traon P.Y., Larnicol G., Philipps S., 2004. Combining Argo and remote-sensing data to estimate the ocean three dimensional temperature fields—a first approach based on simulated observations. J Mar Syst 46:85–98, doi:10.1016/j.jmarsys.2003.11.022.

Ishii M., Kimoto M., Sakamoto K., Iwasaki S.I., 2006. Steric sea level changes estimated from historical ocean subsurface temperature and salinity analyses. *J Oceanogr* 62(2):155–170, doi:10.1007/ s10872-006-0041-y.

IPCC, 2007: Climate Change 2007: The Physical Science Basis. Contribution of Working Group I to the Fourth Assessment Report of the Intergovernmental Panel on Climate Change [Solomon, S., D. Qin, M. Manning, Z. Chen, M. Marquis, K.B. Averyt, M.Tignor and H.L. Miller (eds.)]. Cambridge University Press, Cambridge, United Kingdom and New York, NY, USA.

Köhl A., Stammer D., Cornuelle B., 2007. Interannual to decadal changes in the ECCO global synthesis. J Phys Oceanogr 37(2):313–337, doi:10.1175/JPO3014.1.

Köhl A. and Stammer D., 2008. Decadal Sea Level Changes in the 50-Year GECCO Ocean Synthesis. *J Clim* 21:1876–1890, doi:10.1175/2007JCLI2081.1.

Le Traon P., Nadal F., Ducet N., 1998. An improved mapping method of multisatellite altimeter data. *J. Atmos. Ocean. Technol.*, 15, pp. 522–534.

Levitus S., Antonov J., Boyer T., 2005. Warming of the World Ocean, 1955–2003. *Geophys Res Lett* 32:L02604, doi:10.1029/2004GL021592.

Lombard A., Cazenave A., Le Traon P.Y., Guinehut S., Cabanes C., 2006. Perspectives on present-day sea level change: a tribute to Christian Le Provost. *Ocean Dyn* 56:445–451, doi:10.1007/s10236-005-0046-x.

Lombard A., Garric G., Penduff T., 2009. Regional patterns of observed sea level change: insights from a 1/4 global ocean/sea-ice hindcast. Ocean Dynam., 59, 3, 433–449, doi:10.1007/s10236-008-0161-6.

Lowe J. A. and Gregory J. M., 2006. Understanding projections of sea level rise in a Hadley centre coupled climate model. *J. Geophys. Res.* 111, C11014. doi:10.1029/2005JC003421.

Marshall J. and Plumb R.A., 2008. Atmosphere, Ocean and Climate Dynamics: An Introductory Text. *International Geophysical Series*, Vol. 93, Academic Press, 319 pp.

Mellor G. L. and Ezer, T. 1995. Sea level variations induced by heating and cooling: an evaluation of the boussinesq approximation in ocean models. *Journal of Geophysical Research*, 100, 20 565–20 577.

Milne G., Gehrels W.R., Hughes C., Tamisiea M., 2009. Identyfying the causes of sea level changes. *Nature Geoscience*, vol 2, 471-478.

Mimura N. and Plesikoti N., 1997. Vulnerability of Tonga to future sea-level rise. *J Coastal Res* Spec Issue 24:117–132.

Mitrovica J.X., Gomez N., Clark P.U., 2009. The sea-level fingerprint of West Antarctic collapse. *Science*, Vol. 323, p. 753.

Peltier W. R., 2004. Global Glacial Isostasy and the Surface Ot the Ice- Age Earth: The Ice-5g(Vm2) Model and GRACE. *Annual Review of Earth and Planetary Sciences*, 32, 111–149.

Penduff T., Juza M., Brodeau L., Smith G. C., Barnier B., Molines J.-M., Treguier A.-M., Madec G., 2010. Impact of global ocean model resolution on sea-level variability with emphasis on interannual time scales. *Ocean Sci.*, 6, 269–284, doi:10.5194/os-6-269-2010.

Pinardi N., Rosati A., Pacanowski R.C., 1995. The sea surface pressure formulation of rigid lid models: Implications for altimetric data assimilation studies, *J. Mar. Res.*, 6, 109– 119.

Plag H.P., 2006. Recent relative sea level trends; An attempt to quantify forcing factors. *Phil. Trans. Roy, Soc. Lond*, A, 364, 1841-1869.

Ponte R. M., Quinn K. J., Wunsch C., Heimbach P., 2007. A comparison of model and GRACE estimates of the large-scale seasonal cycle in ocean bottom pressure. *Geophys. Res. Lett.*, 34, L09603, doi:10.1029/2007GL029599.

Rio M. H., Guinehut S., Larnicol G., 2011. New CNES-CLS09 global mean dynamic topography computed from the combination of GRACE data, altimetry, and in situ measurements, *J. Geophys. Res.*, 116, C07018, doi:10.1029/2010JC006505.

Song Y. T. and Colberg R., 2011. Deep ocean warming assessed from altimeters, gravity recovery and climate experiment, in situ measurements, and a non-Boussinesq ocean general circulation model. *J. Geophys. Res.* 116, C02020.

Stammer D., Wunsch C., Ponte R. M., 2000. De-aliasing of global high frequency barotropic motions in altimeter observations. *Geophys. Res. Lett.*, 27, 1175– 1178.

Vinogradov S. V., Ponte R. M, Heimbach P., Wunsch C., 2008. The mean seasonal cycle in sea level estimated from a dataconstrained general circulation model, J. Geophys. Res., 113,C03032, doi:10.1029/2007JC004496.

Watkins M. M., Yuan D., Bertiger W., Kruizinga G., Romans L., Wu S., 2002. GRACE gravity field results from JPL. EOS, Transactions, American Geophysical Union 83 .

Wenzel M. and Schröter J., 2007. The global ocean mass budget in 1993–2003 estimated from sea level change. *J. Phys. Oceanogr.,* **37,** 203–213.

Willis J.K., Roemmich D., Cornuelle B., 2004. Interannual variability in upper-ocean heat content, temperature and thermosteric expansion on global scales. *J Geophys Res* 109:C12036, doi:10.1029/2003JC002260.

Woodworth P.L. and Player R., 2003. The Permanent Service for Mean Sea Level: an update to the 21st century. *Journal of Coastal Research*, 19, 287-295.

Wunsch C., Ponte R.M., Heimbach P., 2007. Decadal trends in sea level patterns:1993–2004. J Clim 20:5889–5911, doi:10.1175/2007JCLI1840.1.

Chapter 4

Short-term impact of ice sheets runoff estimated from gravimetry data on ocean model simulations

Abstract

We have investigated the response of an eddy-permitting sea-ice/ocean general circulation model to realistic estimates of freshwater fluxes from Greenland and Antarctica ice sheets, with the aim of quantifying and studying the impact of the water exchange between the ocean and the ice-sheets, which is one of the major causes of sea level change. We have constructed a 2003-2010 monthly-mean ice sheets runoff through a combination of GRACE satellite gravimetry and atmospheric model data. In particular, the runoff has been calculated as a 8-member ensemble mean obtained by combining the four existing GRACE solutions, each of them balanced with both RACMO atmospheric regional model and ERA-Interim atmospheric reanalysis fields. The estimated runoff has been then redistributed on the ice sheets coasts, according to the main drainage basin systems, and at last used as input in our simulation. Our estimates are 20-30 times higher than the climatological runoff used in our previous simulation. Such experiments are generally carried out using rough estimates of freshwater fluxes from ice sheets in global model having typically 1° horizontal resolution. A precise advection of freshwater requires eddy-resolving configuration, necessary to simulate the coastal currents involved in the transport of the runoff from the ice sheets coasts. To some extent, we gain better insight into this issue using an eddy-permitting model (1/4°) and we explore the short-term impact of ice sheet melting on sea level and on the main ocean parameters. In response of the enhanced runoff the sea level rises generally everywhere around Greenland due to an increase in its eustatic component, although the halosteric contribution has important local effects particularly in the Baffin Bay. In addition to a freshening of surface and subsurface waters around Greenland (especially Baffin Bay, Nordic Seas and North Atlantic subpolar gyre), in agreement with observations, the enhanced runoff results in a displacement of the warm core of Greenland rim currents offshore; this in turn modifies the surface and subsurface temperature field. Furthermore, the decrease of salinity brings to a reduction of deep convection, even if small, in the Labrador Sea, and the consequent reduction of mixed layer depth agrees well with independent estimates.

4.1- Introduction and motivations

The freshwater input into the ocean as a result of land-ice loss and water exchange with terrestrial reservoirs is, together with the thermal expansion of the sea waters, one of the two major causes of global sea level change on short time-scale.

Antarctica and Greenland, the world's largest ice sheets, make up the vast majority of the Earth's ice. A complete collapse of the sheets would rise sea level by ~70 m (about 90% from Antarctica). However, current estimates indicate that mass balance for the Antarctica ice sheet is in approximate equilibrium and may represent only about 10% of the current contribution to sea level rise coming from glaciers, although some localized areas of the Antarctica have recently shown significant negative balance. The Greenland ice sheet may be contributing about 30% of all glaciers melt for rising sea level. In terms of sea level rise, estimates of Greenland and Antarctica contributions are equal to 0.7 ± 0.5 mm/yr in 1993-2003 decade and 1.0 ± 0.4 mm/yr during 2003-2008 period, which means that a 40% increase in mass loss compared to 1993-2003 period occurs (Cazenave et al., 2009; Van den Broeke et al., 2011). It is worthy to note that the network of lower latitude small glaciers and ice caps, although making up only about 4% of the total land-ice area, may have provided as much as 60% of the total glacier contribution to sea level change since 1990s (Meier et al., 2007).

Satellite-derived observations over the past two decades show rapid acceleration of flow speed of some Greenland and large West Antarctica outlet glaciers system (Howat et al. 2007, Rignot et al., 2008). Furthermore, recent observations suggest that ice dynamics may be a key factor in the response of coastal glaciers and ice sheets to recent warming (Alley et al., 2008). In Greenland, altimetry observations indicate a thickening of the high central ice sheet, but also a significant increased loss near the coast has occurred (Johannessen et al. 2005; Krabill et al. 2004). The Antarctic ice sheet system is more complex, and presents large regional differences. While surface temperatures are well below the freezing point over most of East Antarctica, and a small increase in temperature cannot initiate melt, ice loss by melting in West Antarctica is a direct result of warming air temperature. The cause of acceleration of other large outlet glaciers in West Antarctica is not fully understood, but may be related to sea-ice shelf instability (Holland et al. 2008).

Since the early 1990s, different remote-sensing techniques have offered new insight on contemporary mass change of the ice sheets (e.g., Wingham et al. 2006). Airborne and satellite laser altimetry (ICESat satellite since 2003), and radar interferometry (InSAR) permit to monitor changes in the ice sheet elevation and to quantify variations in ice discharge. Observations from the Gravity Recovery and Climate Experiment (GRACE) satellite mission (Tapley et al., 2004) provides monthly estimates of Earth's global gravity field at scales of a few hundred kilometers and larger. Those allow accurate estimates of large-scale ice sheet mass changes (with nearly complete coverage of polar regions, up to 89°N/S). Comparing results from different techniques is not easy, because each technique has its own bias and limitations: GRACE gravimetry is sensitive to solid mass change associated with Glacial Isostatic Adjustment (GIA). Over Antarctica, where the GIA effect is of the same order of magnitude as the ice mass change, the poorly-known GIA correction is a source of significant uncertainty (Peltier 2009) - GRACE results over Antarctica are more uncertain than over Greenland. However, GRACE is in good agreement with other observations showing a quasi-balance over East Antarctica, but a significant widespread ice-mass loss over West Antarctica during the past few years (Velicogna and Wahr, 2006; Ramillien et al., 2006b; Chen et al., 2006; Cazenave et al., 2009), confirmed also by regional climate models (Rignot et al., 2008).

Due to the strong link between ice sheet melting and climate variability, big effort is focused on improving modeling of ice sheet dynamics and ice shelf/ocean interactions in order to accurately and realistically simulate the impact of land-ice-melting on the ocean and, in particular, on sea level change.

Prescribed runoff, generally used in OGCMs, only includes a climatological estimate of river runoff from largest rivers and does not take into account the ice sheets contribution and its variability. (e.g. see Bourdallé-Badie and Treguier (2006) for a version of ORCA025 river runoff). Estimates of solid-ice fluxes from satellite observations can be used to provide the spatial distribution of freshwater fluxes, which can be prescribed as forcing in ocean circulation models.

The objective of this Chapter is firstly to present and discuss a novel method for the estimation of runoff from the ice-sheets by combining gravimetric data with atmospheric model data. Then, we investigate the extent to which changes in ice sheets runoff can impact the sea level, the ocean freshening and consequently the thermohaline circulation. Furthermore, some model performance improvements given by an observation-base runoff estimation are discussed. For this purpose, we have constructed a realistic interannual dataset of ice sheets runoff by using 2003-2010 GRACE gravimetry observations of ice sheets mass loss and atmospheric model results of precipitation and sublimation. The freshwater fluxes estimates have been redistributed on the coasts according to the main drainage basin systems of the ice sheets, in order to realistically describe the ocean reaction to an increased melting, and at last used to force our eddy-permitting OGCM in order to study the response of the ocean water mass properties and ocean circulation (on basin-scales) to a more realistic freshwater input.

Many studies have investigated by means of ideal experiments the impact of an enhanced freshwater input using coarse-resolution ocean models. For example, Gerdes et al. (2005) studied the reaction of a global 2° resolution ocean model by assuming a time-constant melt water flux from Greenland for the next 100 years; Yin et al. (2010) used a 2° horizontal resolution model by perturbing two multi-century simulations with a constant amount of 0.1 an 1.0 Sv; Stammer (2008) applied a constant freshwater flux for 50 years and simulated the response of the ocean with a 1°x1° configuration; Hu et al. (2011) added a constant annual mean melting rate redistributed uniformly on the southern coasts of Greenland, and they studied the impact on the ocean over the next two centuries using a 1° resolution model. Marsh et al. (2010) demonstrated the higher efficiency of an eddy-permitting model configuration in reproducing the dynamics of Greenland boundary currents and eddies, and the spreading of the land-ice freshwater (from a mass balance model and atmospheric reanalyses) into the ocean. Although our configuration is still somewhat idealized (eddy-resolving configuration would be more adequate to well simulate the freshwater advection), the experiment is a step towards understanding the fate of additional freshwater fluxes from ice sheets and its short-term impact on climate.

The Chapter is structured as follows: we firstly introduce the methods (Section 4.2) and data sets used for the runoff calculation (Section 4.3); in Section 4.4 we show the comparison among the different GRACE solutions; in Section 4.5 we present the results of the runoff calculation and in Section 4.6 the use of different precipitation datasets to calculated the ice sheets runoff is performed and discussed; we finally discuss the sensitivity of our ocean model simulation to the newly estimated runoff and its short-time impact on the main ocean parameters (Section 4.7); in Section 4.8 the main conclusions are summarized followed by a scientific discussion.

4.2- Methods of runoff calculation

Freshwater discharge along continental margins is a key component of the Earth's water cycle. It plays a major role in a wide range of climatic processes (Famiglietti, 2004) and modification of the land hydrological cycle due to climate variability and direct anthropogenic forcing may also affect sea level. Hence the monitoring of this parameter is of central importance to understand changes in the Earth system. However, there exists no comprehensive global network for the monitoring of freshwater discharge into the world oceans (Alsdorf and Lettenmaier 2003; Brakenridge et al. 2005), based on tide gauges observations that cover varying and discontinuous time periods and with variable accuracies. To overcome to this lack, Fekete et al. (2000, 2002) followed a data-merging approach by using observed discharge data from the Global Runoff Data Center (GRDC; http://grdc.bafg.de) to constrain modeled estimates of runoff. Later, Dai and Trenberth (2002) improved the previous work by incorporating a river-routing scheme for the appropriate transport of the runoff into the ocean. Alternatively, terrestrial water storage observations from

GRACE satellite mission combined with precipitation and evaporation data (or similarly, with the atmospheric moisture storage change and divergence) has been used to solve a water balance for the terrestrial freshwater discharge (Syed et al., 2007; Syed et al., 2009; Llovel et al., 2011).

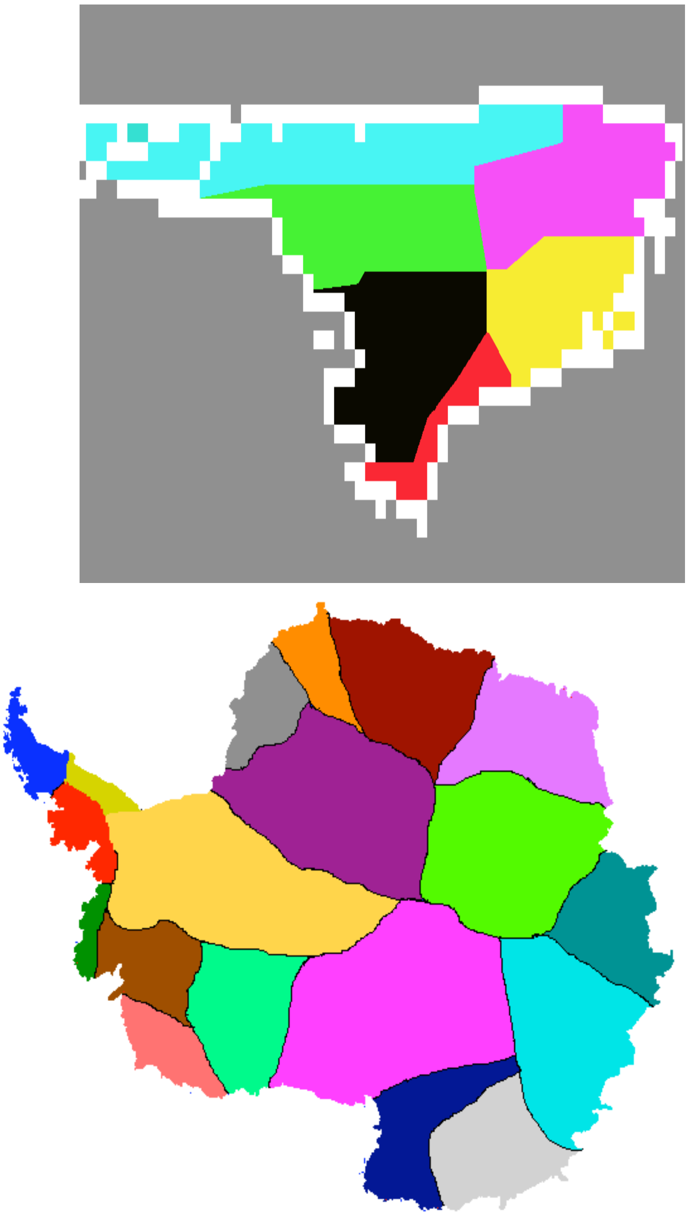

Figure 1– *Greenland (top) and Antarctica (bottom) drainage system regions based on surface slopes analyses proposed by Luthcke et al. (2006) and by Rignot et al. (2008), respectively.*

By following the same method, in our study we present monthly estimates of runoff (for the 2003-2010 period) from Greenland and Antarctica ice sheets, calculated by combining GRACE equivalent water height (EWH) measurements with atmospheric fluxes in a water mass balance equation. Note that this is the first time that such a calculation is made over the ice sheets regions giving a tone of innovation to the present study. In particular, ice sheets runoff estimates are calculated by following two approaches, as proposed respectively by Llovel et al. 2011 and Syed et al. 2009. The latter expands upon the previous work of Syed et al. (2005, 2007) to estimate freshwater discharge for several large river basins, from continents and drainage regions.

In the first approach, the runoff has been calculated from the use of the ice sheets water mass balance equation given by:

$$\frac{\partial M}{\partial t} = SMB - D \tag{1}$$

where $\frac{\partial M}{\partial t}$ is the variation of mass in time over the ice sheet; SMB = P – E - R is the surface mass balance, equal to the sum of solid and liquid precipitation (P), evaporation and sublimation (E) and liquid runoff from the surface water melting (R, note that this term is negligible in Antarctica); D is the ice discharge (iceberg calving) that is the main process through which the ice sheets are loosing mass. The estimate of the total (liquid and solid) runoff leaving the ice sheet is therefore equal to:

$$R + D = P - E - \frac{\partial M}{\partial t} \tag{2}$$

We have performed the calculation by firstly estimating the total volume of M, P and E of every drainage basins of the two ice sheets :

$$V_M^k(t) = \sum_{i,j\in k} M(i,j,t) * dx * dy$$

$$V_P^k(t) = \sum_{i,j\in k} P(i,j,t) * dx * dy$$

$$V_E^k(t) = \sum_{i,j\in k} E(i,j,t) * dx * dy$$

where *dx* and *dy* are respectively the zonal and meridional grid size and *k* indicates each drainage basin. Note that while M is given in meters of equivalent water, P and

E are water fluxes. For Greenland we have schematized the geographical boundaries according to the ice sheets drainage system regions based on surface slopes analyses proposed by Luthcke et al. (2006), dividing Greenland surface in 6 different drainage systems (Figure 1 top panel), and for Antarctica using the one proposed by Rignot et al. (2008) that subdivides the ice sheets in 18 drainage basins (Figure 1 bottom panel).

Since GRACE data are given as monthly means centered on the 15th day of each month, compatible estimates of P and E were computed by integrating daily averages between the 15th day of consecutive months as follows:

$$\int_{N_m/2}^{N_{m+1}/2} V_{R+D}^{k} dt = \int_{N_m/2}^{N_{m+1}/2} V_{P-E}^{k} dt - [(V_M^k)_{m+1} - (V_M^k)_m]$$

where N_m is the number of days in the month m and $(V_M^k)_m$ is the total volume of M over a certain drainage basin of Greenland/Antarctica expressed in equivalent water mass anomaly of the month m.

The total runoff volume of every drainage basins of the two ice sheets V_{R+D}^{k} thus computed has been then re-located at the nearest ocean grid cell, around the coasts of Greenland and Antarctica, by dividing the volume for the coastal grid cells area. Figure 2 shows the freshwater flux (in $\frac{Kg}{m^2 * s}$) per model grid point for Greenland (top panel) and Antarctica (bottom panel); we can see the strongest fluxes are located along the south east coast of Greenland.

In the second approach, the ice sheets runoff is calculated by the use of the combined land-atmosphere water mass balance equation, obtained from equation (1) and the atmospheric moisture budget expressed as:

$$\frac{\partial W}{\partial t} = E - P - \vec{\nabla} \cdot \vec{Q} \qquad (3)$$

where W is the total column water vapor and the last term on the right hand side is the horizontal divergence of the vertically integrated vapor flux.

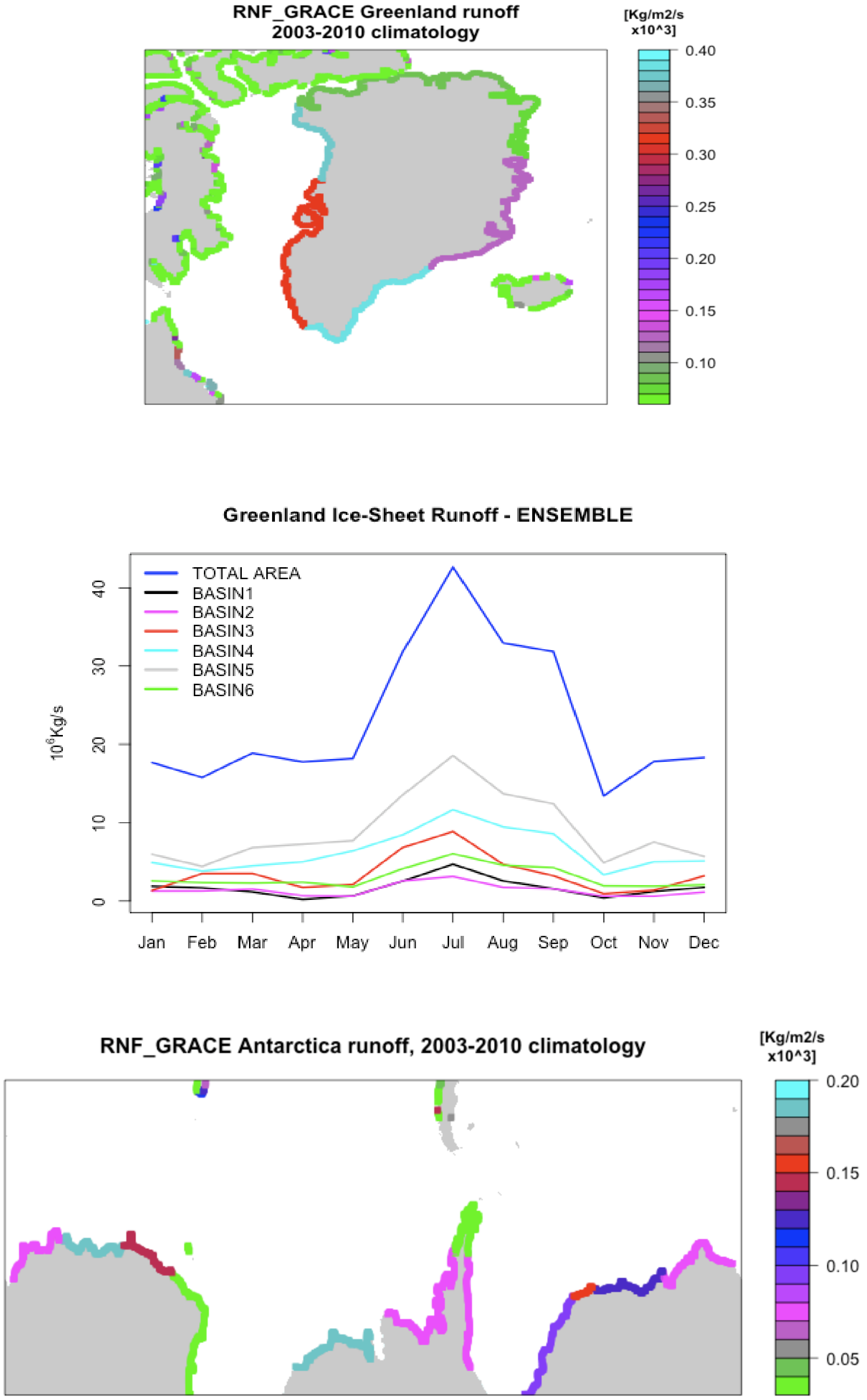

Figure 2– *Climatology (2003-2010) of RNF_GRACE experiment freshwater flux at every model grid cell from Greenland (top panel) and Antarctica (bottom panel). Middle panel: monthly climatology (2003-2010) of Greenland RNF_GRACE experiment freshwater flux; the plot shows the contribution from the total ice sheet area (blue line) and from the individual drainage system basins.*

By combining equations (1) and (3) we therefore obtain the total runoff now expressed as:

$$R+D=-\frac{\partial M}{\partial t}-\frac{\partial W}{\partial t}-\vec{\nabla}\cdot Q \qquad (4)$$

On land, the method of equation (4) has been proved more accurate than equation (3) due to the large uncertainty in the atmospheric models evapotranspiration that is bypassed by the use of the combined land-atmosphere water mass balance equation (Syed et al. 2009). This is however questionable on land-ice, where the contribution of evaporation is negligible and large uncertainties on atmospheric moisture remain due to lack of a proper observational network.

Finally, we have tested the use of 8 members ensemble mean that has been calculated by using the four existing GRACE solutions balanced, in water mass balance equation (2), once with RACMO atmospheric regional model data and once with ERA-Interim atmospheric variables.

4.3- Data sets

The GRACE space mission, sponsored by National Aeronautics and Space Administration (NASA) and Deutsches Zentrum fur Luft- und Raumfahrt (DLR), has been collecting data since March 2002. It provides, at regular time intervals, global solutions of the Earth gravity field (e.g. Wahr et al., 1998; Tapley et al., 2004; Schmidt et al., 2006). These solutions consist of spherical harmonics coefficients (up to a certain degree) of the gravity field. Changes in the gravity field are largely caused by the redistribution of water mass in the hydrological cycle (Wahr et al., 1998, 2004). Hence, for the very first time satellite-based global maps of terrestrial water storage variations can be derived from GRACE measurements. In fact the gravity fields coefficients (or geoid coefficients) are later converted into units of surface mass density or mm of equivalent water height (Ramillien et al., 2006b). The solutions will be later called “equivalent water height differences” since they are expressed as differences between the time-variable solution and a static gravity field. In the present work we have tested the use of all the existing GRACE solutions, released by different research groups: Deutsches Geo Forschungs Zentrum (GFZ - Postdam, Germany), NASA Jet Propulsion Laboratory (JPL - US), Center for Space Research (CSR - US) and Groupe de Recherche de Geodesie Spatiale (GRGS) at the Center National d'Etudes Spatiales (CNES - Toulouse, France). These are monthly solutions at 330 km of resolution (i.e. up to degree 60 of the spherical harmonics); for the CNES/GRGS we have also used a 10-day interval solutions released at 400 km of spatial resolution (i.e. up to degree 50 of the spherical harmonics). In addition to the different spatial resolution, the solutions also differ because of the different pre-processing methods used to filter out the high frequencies from the signal in order to extract realistic hydrological signals on continents from noisy GRACE solutions: stabilitation method applied to Level-1 of GRGS solutions and gaussian filter applied to Level-2 of CSR, GFZ, JPL solutions. Another significant difference, is the application of the Independent Component Analysis (ICA) method to further filter the CSR, GFZ and JPL solutions (later called ICA-based solutions); the ICA method has not been applied to the GRGS solution. This post-processing technique has been used in order to reduce the presence of north-south striping due to orbit resonance that limits geophysical interpretation of the signal (Frappart et al., 2010, 2011). The reader is referred to Whar et al. (1998) for further details on GRACE data processing. Moreover, differences in the static gravity field removed to the time-varying solution and differences in the oceanic/atmospheric models used to dealiasing the GRACE solutions (in order to remove the atmospheric pressure influence on satellite orbits and on the ocean state) can be other possible causes. The accuracy of water storage change estimates observed by GRACE ranges from 1.5 cm to less than a millimeter depending on the geographic domain over which the data are averaged (Wahr et al., 2004; Ramillien et al., 2006a). In general, errors in GRACE data are representative of a combination of instrument and processing errors, which include truncation errors, leakage errors due to contaminating signals from neighboring regions, and separation errors due to the inexact removal of mass variations in the atmospheric column and in the solid earth below.

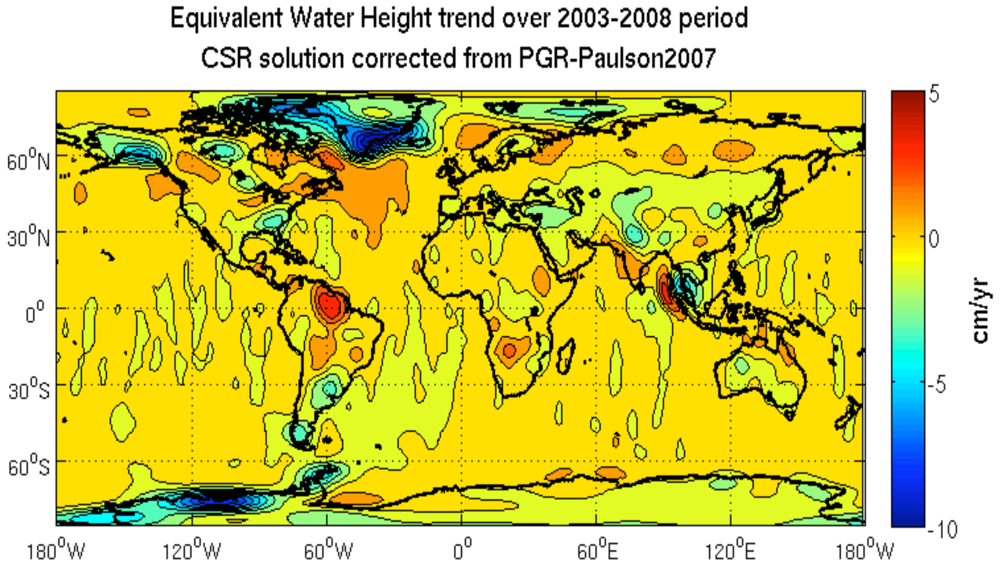

Figure 3 – *Equivalent water height trend over the 2003-2008 period calculated from CSR GRACE solution. The trend has been corrected from the PGR estimate from the ICE-5G ice deglaciation model (Paulson et al., 2007).*

To have an idea of the mass variations of the two ice sheets, Figure 3 shows the linear trend map (over 2003-2008 period) of equivalent water height for the CSR solution. We observe a strong decrease of mass over the West Antarctica (more than 10 cm/yr equivalent water height) and a slight decreasing trend over the Antarctic Peninsula.

The East Antarctica shows neither loss nor accumulation of mass. Most of the Greenland ice sheet is characterized by ice mass loss mostly concentrated in the south-east part. Since GRACE is not able to separate the equivalent water height change from the solid Earth response, we have corrected GRACE data from the effect of the Post Glacial Rebound (PGR, i.e. the vertical displacement of the solid Earth in response to the last deglaciation and present-day land ice melt) on the geoid. The PGR trend has been computed using the global ICE-5G ice deglaciation model (Peltier, 2004; Paulson et al., 2007). Note that removing the PGR effect from GRACE adds further uncertainties in the mass balance estimates, due to the inaccuracy of the PGR trend that still can not be modelled accurately. Note also that while the PGR effect is negligible on Greenland ice sheet, it is significant on Antarctica. In fact, the mass balance of Antarctica appears to be close to zero when GRACE estimates are not corrected for long-term PGR.

For precipitation and sublimation (terms P and E in equation (2)), we considered two different datasets: i) ERA-Interim (Simmons et al., 2007; Dee et al., 2011) global atmospheric reanalyses data from the European Center for Medium-range Weather Forecasts (ECMWF), at 0.75° of resolution and ii) data from the RACMO2 regional atmospheric climate model (van Meijgaard et al., 2008; Ettema et al., 2009) developed at Koninklijk Nederlands Meteorologisch Instituut , at 55 km of resolution for Antarctica and 11 km for Greenland. Regarding the total column water vapor and the horizontal divergence of the vertically integrated vapor flux, required for the coupled land–atmosphere water balance of equation (4) we used only ERA-Interim data product.

4.4- Comparison of GRACE solutions

In Figure 4 the comparison between the time series of equivalent water height difference among all the GRACE solutions, over Greenland, East and West Antarctica, is shown.

Equivalent Water Height - GREENLAND

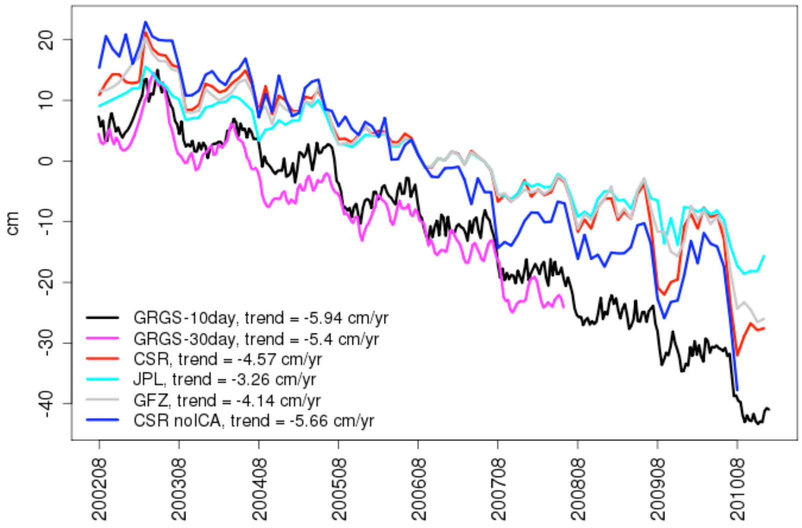

Equivalent Water Height difference - EAST ANTARCTICA

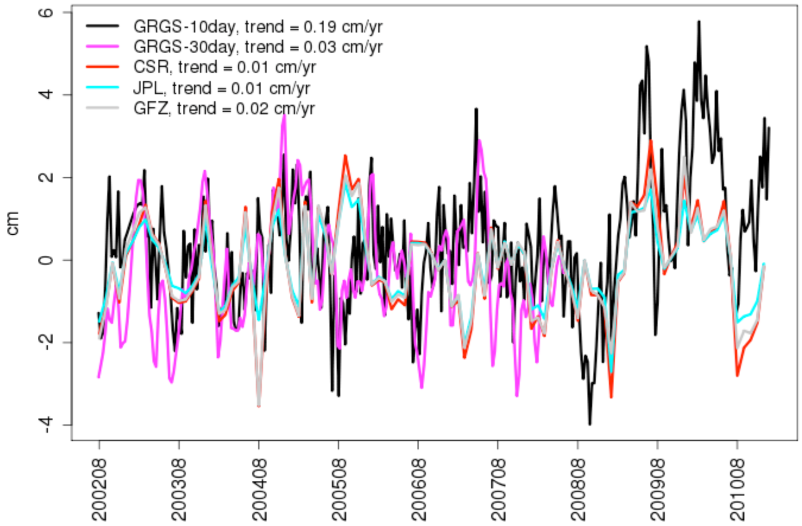

Equivalent Water Height difference - WEST ANTARCTICA

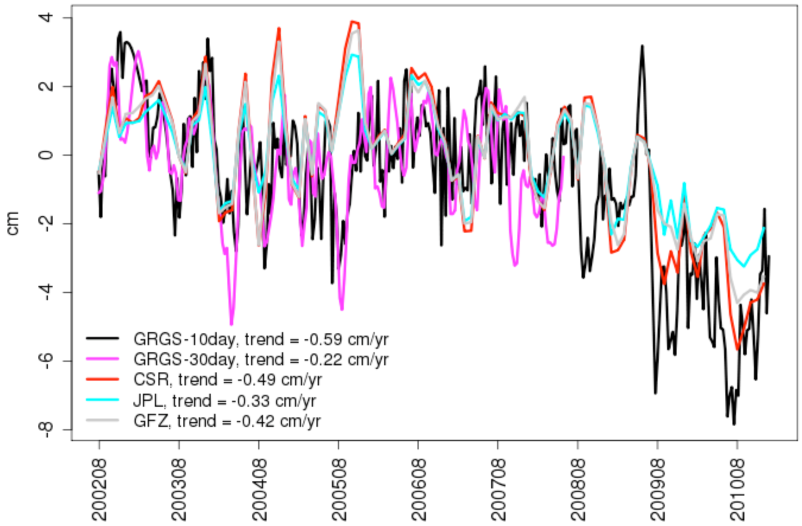

Figure 4– *Time series of equivalent water height over Greenland (top), East and West Antarctica (middle and bottom, respectively) from the all GRACE solutions. The blue line represent the EWH time series of the CSR solution before the application of the ICA post-processing technique.*

To make an exhaustive comparison we have also over-plotted the GRGS solutions at 30-day temporal frequency, which has not been used in the calculation of the ensemble runoff due to its limited time availability (August 2002 – May 2008). While East Antarctica is close to a state of net mass balance, the West Antarctica and Greenland are losing mass. The former shows a mass loss acceleration in correspondence of August 2007, while the latter shows a pronounced negative trend through the whole time span. It is evident that the two groups of GRACE solutions, the GRGS and the ICA-based solutions, show a different behavior, namely the GRGS solutions show a faster mass loss acceleration with respect to the ICA-based. This is particularly evident in Greenland in correspondence of August 2007. For example, the GRGS-10day solution shows a trend almost twice higher than the JPL solution, which in terms of equivalent sea level means a contribution from Greenland ice sheet equal to 0.28 mm/yr (GRGS-10day) and 0.15 mm/yr (JPL). The difference in the equivalent water height trends is a consequence of the differences in the spatial resolution and in the pre- and post- processing techniques (discussed in the previous Section) applied to the GRACE solutions. By overplotting one of the ICA-based solution (in this case the CSR) on EWH time series over Greenland before the application of the ICA method (the blue line in Figure 4, top panel), we can see that it is closest to the GRGS solution tendency. This suggest that the application of the ICA method may be one of the possible causes of the differences in the trends.

4.5- Runoff results

In order to validate the runoff estimates from Greenland and Antarctica ice sheets, calculated as previously explained, we have compared the results obtained from equations (2) and (4) with measurements of ice discharge, obtained by combining maps of surface velocities along ice sheet coasts from InSAR and ice thickness from

Digital Elevation Model (DEM, Rignot et al., 2011). The comparison is made by subtracting the liquid runoff from the total runoff (liquid + solid) in order to have consistent data. For Antarctica we could make a direct comparison since liquid runoff is negligible and the ice discharge is the only process that contribute to mass loss from the ice sheet. Note that InSAR data can not be used for runoff estimation since their availability is discontinuous and they are given as yearly means.

The runoff values obtained by using the ice sheets water mass balance equation (2) are found consistent with the InSAR observations, both for Greenland (Figure 5 top panel) and Antarctica (Figure 5 bottom panel), in particular we found that the use of precipitation and sublimation fields from the RACMO regional model (green line) slightly overestimates observation values while the use of ERA-Interim (cyan line) slightly underestimates; on the other hand the runoff values obtained by using the combined land-atmosphere water mass balance equation (4) (blue line) strongly underestimates InSAR data. The ensemble mean solution is the red line in Figure 5 and it is evident that this is the curve that better fits with ice discharge observations and it is hence the solution used in our sensitivity run.

Figure 6 and Figure 7 show the climatological seasonal cycles of Greenland and Antarctica runoff computed from GRACE data (red line).

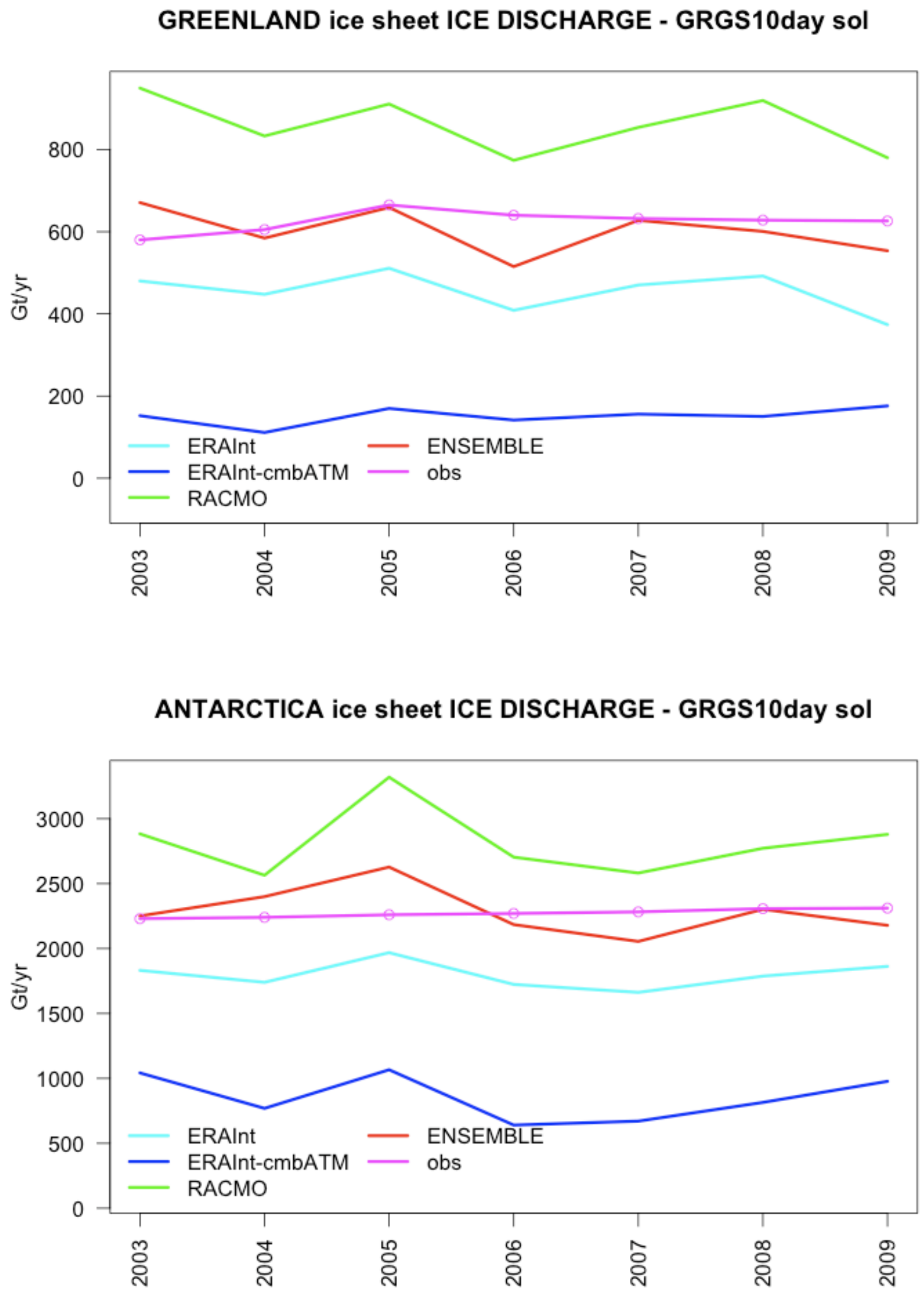

Figure 5– *Comparison of Greenland (top panel) and Antarctica (bottom panel) ice discharge estimated from the different methods of runoff calculation with InSAR observations (magenta line).*

For comparison, the Figures also report the climatological runoff from Bourdallé-Badie and Treguier (2006) that is used as default runoff in NEMO model (grey line). The GRACE derived runoff in Greenland is significantly higher than the climatological one by a factor of 20, during winter, and 30, during summer. In addition the summer peak shifts from June to July. In Antarctica the estimated runoff has values generally comparable with those from Bourdallé-Badie and Treguier (2006), but differently from the climatological runoff (grey line) it does not show any seasonal cycle (red line). The anomalous behavior of the GRACE-derived runoff in Antarctica can be attributed to uncertainties and inaccuracies, over the ice sheet, in the precipitation data (from ERA-Interim reanalysis and RACMO model) and in GRACE observations. In the next Section we will deepen this aspect.

4.6- Runoff derived from ice sheets water mass balance with different precipitation datasets

We have estimated the ice sheet mass balance derived runoff by using different datasets of precipitation, in order to asses, in the comparison with other datasets, the reliability of the RACMO model and ERA-Interim precipitation data over the two ice sheets and to further investigate the anomalous behavior of the Antarctica runoff, discussed in the previous Section.

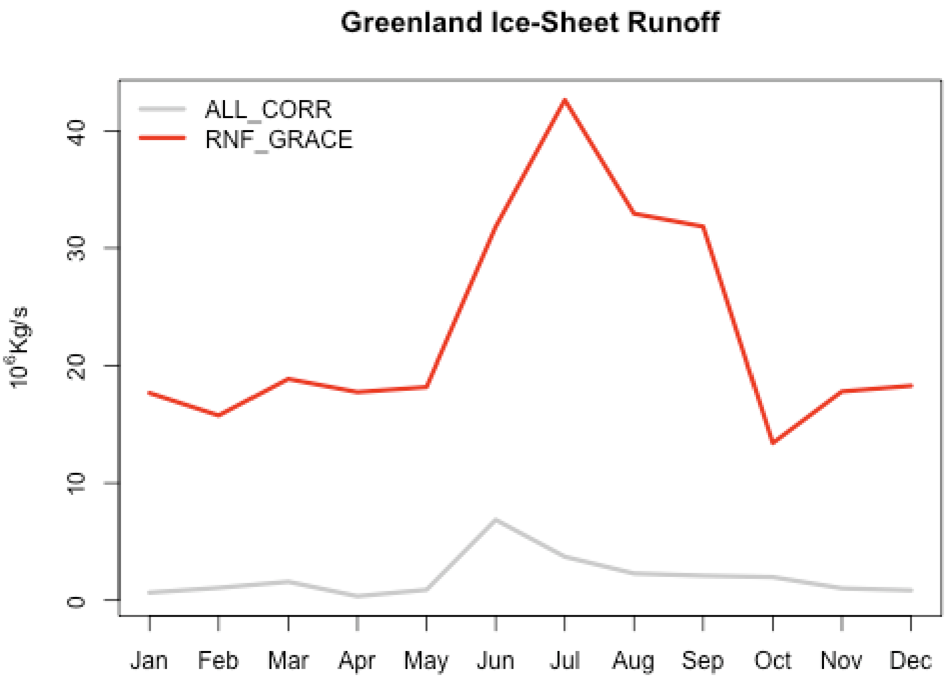

Figure 6– *Monthly climatology (2003-2010) of Greenland ice sheet runoff used in ALL_CORR (grey curve) and RNF_GRACE (red line) experiments.*

RACMO and ERA-Interim precipitations have been compared with CMAP, GPCP and Sheffield precipitation datasets. The CPC Merged Analysis of Precipitation (CMAP) is a technique which produces pentad and monthly analyses of global precipitation in which observations from raingauges are merged with precipitation estimates from several satellite-based algorithms (infrared and microwave). The analyses are on a 2.5° x 2.5° degree latitude/longitude grid and extend back to 1979 (Xie and Arkin, 1997).

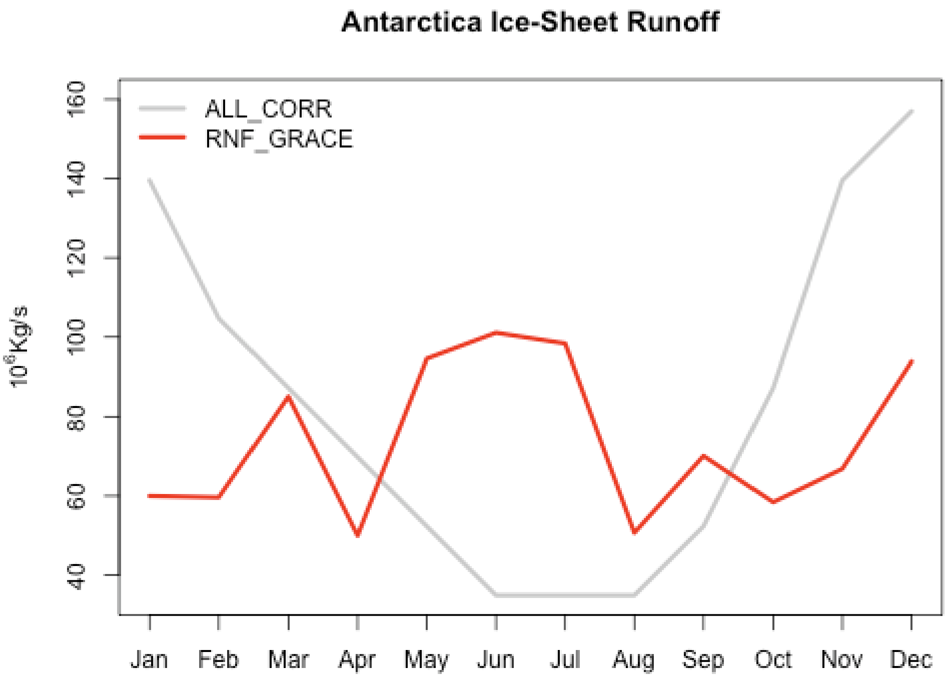

Figure 7– *Monthly climatology (2003-2010) of Antarctica ice sheet runoff used in ALL_CORR (grey curve) and RNF_GRACE (red line) experiments.*

The Global Precipitation Climatology Project (GPCP) was established by the World Climate Research Program to quantify the distribution of precipitation around the globe over many years. The precipitation product is produced by optimally merging estimates computed from microwave, infrared, and sounder data observed by the international constellation of precipitation-related satellites, and precipitation gauge analyses. The product used is available since 1979 with horizontal resolution of 2.5° x 2.5° (Adler et al., 2003).

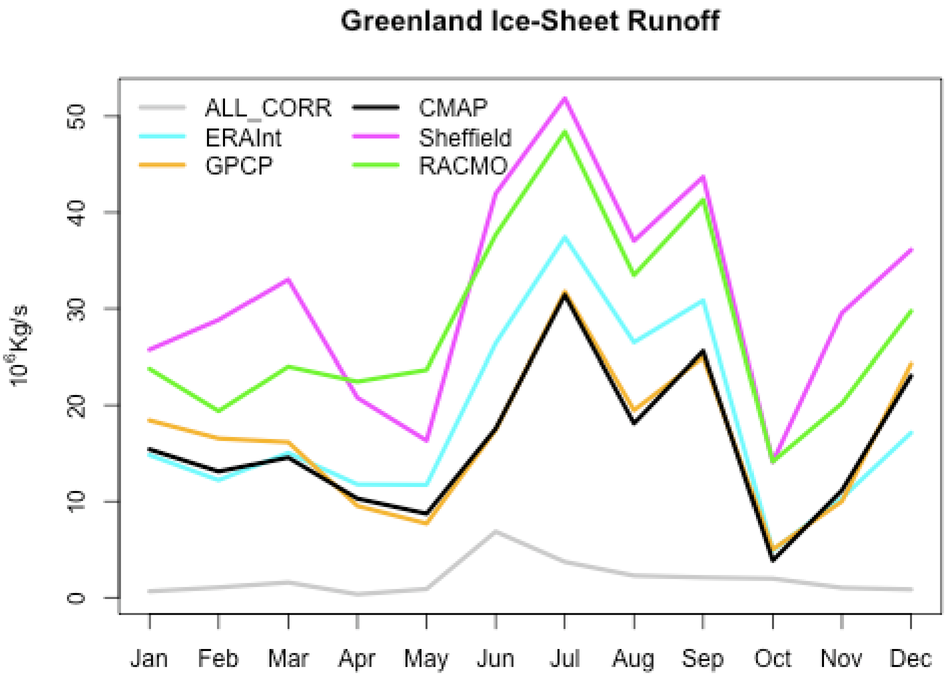

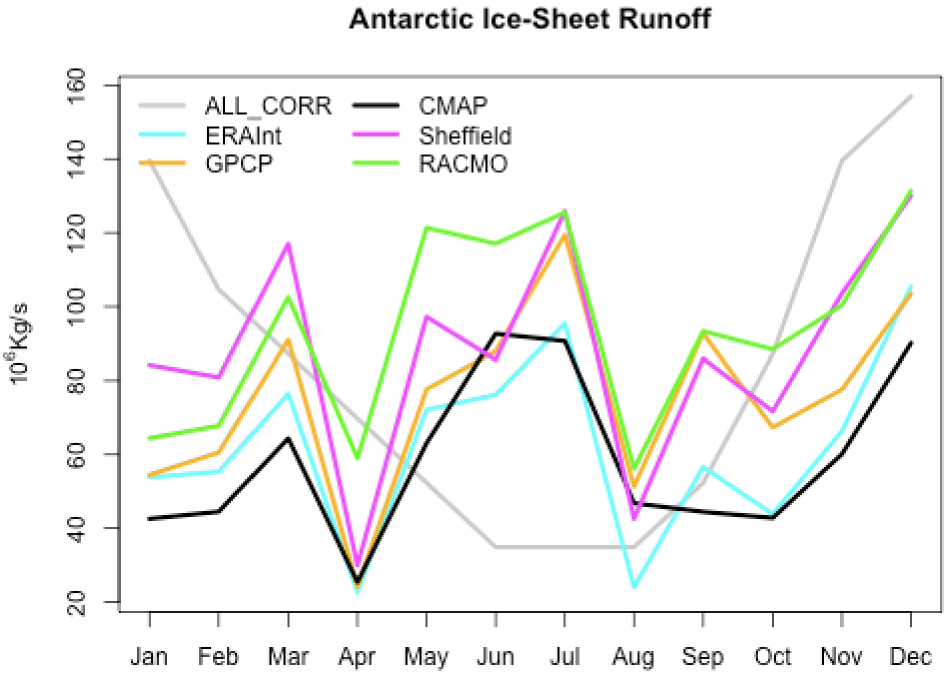

Figure 8– *Ice sheet water mass balance derived runoff (2003-2008 climatologies) by using different datasets of precipitation from Greenland (top) and Antarctica (bottom). For comparison, the ALL_CORR runoff is also plotted (grey line).*

The Sheffield dataset of precipitation (Sheffield et al., 2006) is a global, 60-yr (1948-2008), 3-hourly, 1.0° dataset of land surface hydrology fields. The dataset is constructed by combining a suite of global observation-based datasets (GPCP, TRMM, GSWP-2) with the National Centers for Environmental Prediction–National Center for Atmospheric Research (NCEP–NCAR) reanalysis.

In Figure 8 we show the comparison among the ice sheets runoff calculated with mass balance equation (2) by using the different precipitation datasets: ERA-Interim (cyan line), RACMO (green line), CMAP (black line), GPCP (orange line) and Sheffield (magenta line). The comparison among the datasets is also shown (Figure 9). The different estimated runoff are of the same order of magnitude on both Greenland (top) and Antarctica (bottom), with RACMO-derived and Sheffield-derived runoff presenting the highest values of precipitation and hence of runoff, and they also show the same seasonal cycle peaks. The similarity of the different GRACE-derived runoff confirms the robustness of our method and the reliability of the precipitation data used (ERA-Interim and RACMO). On Antarctica, the agreement in the seasonal cycle among the estimated runoff suggest that, despite the uncertainties in the precipitation data, GRACE measurements over Antarctica might be the main cause for the anomalous runoff behavior. Uncertainties in GRACE data are mostly derived from measurements errors and loss of signals by low-pass filtering. Furthermore, we have corrected GRACE data from the PGR effect that represents a major source of error in the ice sheet mass balance estimates since it is not well-modelled, especially over Antarctica where available long-term observational constraints are rare (Frappart and Ramillien, 2012). It is however worthy to underline that several uncertainties also affect the precipitation reanalyses and caution has to be taken when reanalyses data are used for a study of Antarctica mass balance (Bromwich et al., 2011). In fact, data assimilation is still challenging in this region as reanalyses rely heavily upon a small number of ground-based and upper-air observations in Antarctica, especially in the interior of the ice sheet.

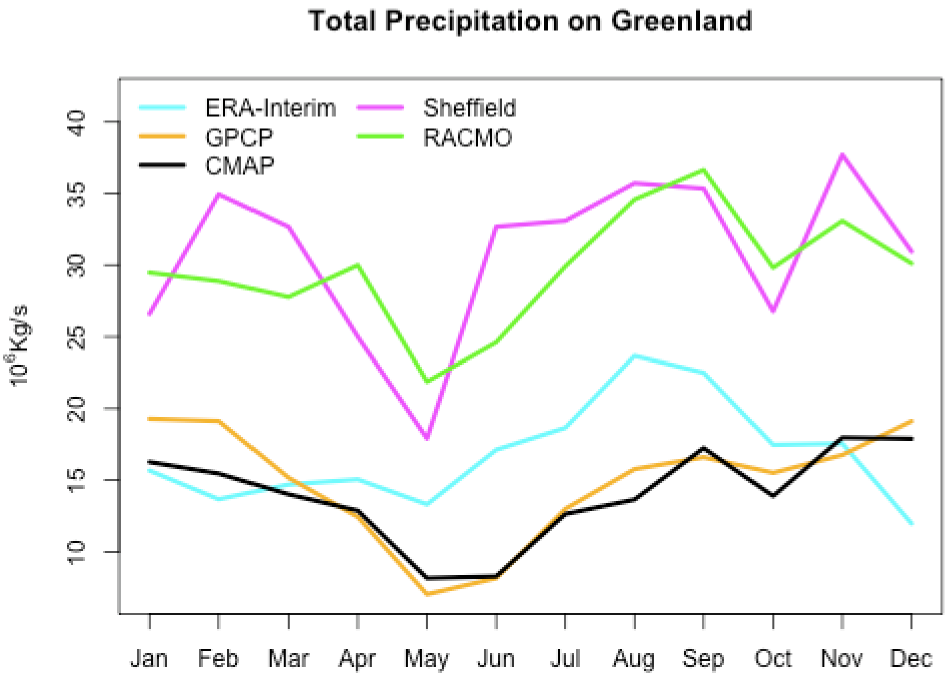

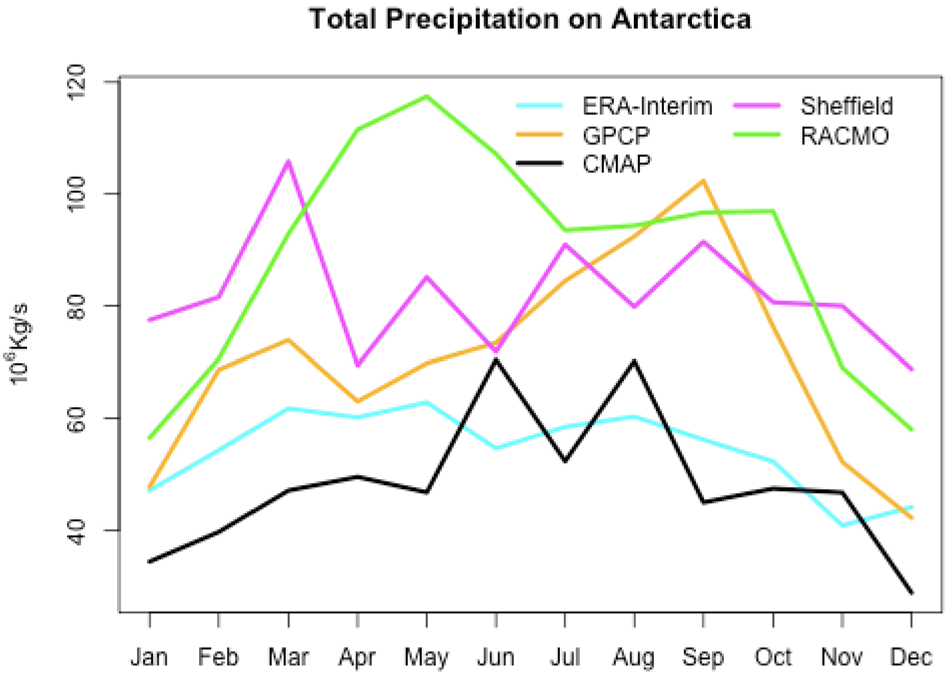

Figure 9– *Comparison among the different precipitation datasets (2003-2008 climatologies) over Greenland (top) and Antarctica (bottom).*

Moreover, the wind-blown snow (or wind-driven ablation), which greatly affects the surface mass balance over Antarctica due to the presence of katabatic winds (Rémy and Frezzotti, 2006), is an important process that is not taken into account in ERA-Interim reanalysis.

Due to the unreliability of the Antarctica estimated runoff, in the next Sections we will concentrate our analysis on the impact that the estimated runoff has around Greenland only; furthermore, the differences between the climatological and the GRACE-derived runoff in Antarctica is smaller, leading to a less appreciable impact on the ocean.

4.7- Results

Our experiment (hereafter called RNF_GRACE) consists of a 8-year (2003-2010) eddy-permitting (1/4° of horizontal resolution) ocean/sea-ice simulation performed with NEMO_LIM2 OGCM, forced by 3-hourly turbulent fluxes and daily radiative and freshwater fluxes from ERA-Interim reanalysis. The simulation shares the same model physics and forcing field corrections of the ALL_CORR experiment (described in Chapter 2), as well as the same ocean initial conditions. The difference between ALL_CORR and RNF_GRACE is the ice sheets runoff prescribed in the simulation: the reference runoff from Bourdallé-Badie and Treguier (2006) for the former while for the latter we used the GRACE derived runoff, redistributed on the ice sheet coasts according to the main drainage basin systems. To investigate the response of the ocean to the new ice sheet freshwater flux, in the following Sections we will analyze the differences between the two runs (RNF_GRACE minus ALL_CORR).

4.7.1- Impact on salinity and temperature

The response of the ocean to the enhanced runoff is appreciable after 6 months (not shown) in correspondence with the summer peak of runoff (Figure 6); the maximum differences occur in October and are located on the southern and western coasts (not shown), where the runoff flux has the highest values (see Figure 2).

After 1 year, the freshwater input stays confined along Greenland coast, with negative sea surface salinity (SSS) anomalies of more than -0.5 psu and offshore sea surface anomalies in the Labrador Sea at Davis Strait and just south of Nares Strait (Figure 10).

After 2 years fresh surface waters spread off the Greenland coasts and after 3 years the negative anomalies reach the Nordic Seas and are advected into the Labrador Sea by the Western Greenland current system (Figure 10). For details about the current system around Greenland, see Figure 16 and refer to Section 4.7.3. Weak positive SSS anomalies are visible on the west side of the Baffin Bay in 2003 and they become more pronounced in 2004, when the anomalies start to be advected by the Labrador Current in the subpolar gyre; in 2007 the Baffin Bay positive anomalies increase up to 0.5 psu and a weak signal is also visible in the Canadian Archipelago (Figure 10). In the subsequent years more extensive annual mean anomalies develop and at the end of the simulation the negative and positive SSS anomalies cover, respectively, the whole Nordic Seas and the Canadian Archipelago; due to the weak runoff enhance off the north coast of Greenland, the signal in the Arctic Ocean remains small (Figure 10).

The fresh salinity anomaly initially stays in the surface layer and is then propagated, after 2 years, down to 300 m of depth in the eastern Baffin Bay (Figure 11, top left panel). At the end of simulation (Figure 11, top right panel) the subsurface negative salinity anomalies, up to -0.3 psu, cover the whole Baffin Bay where they propagate up to -540 m (Figure 11, bottom panel); a weak signal is also visible in the Nordic Seas and in the subpolar gyre. The highest values in the Baffin Bay are due to the local cyclonic recirculation that increases the residence time of the anomalies (Marsh et al., 2010).

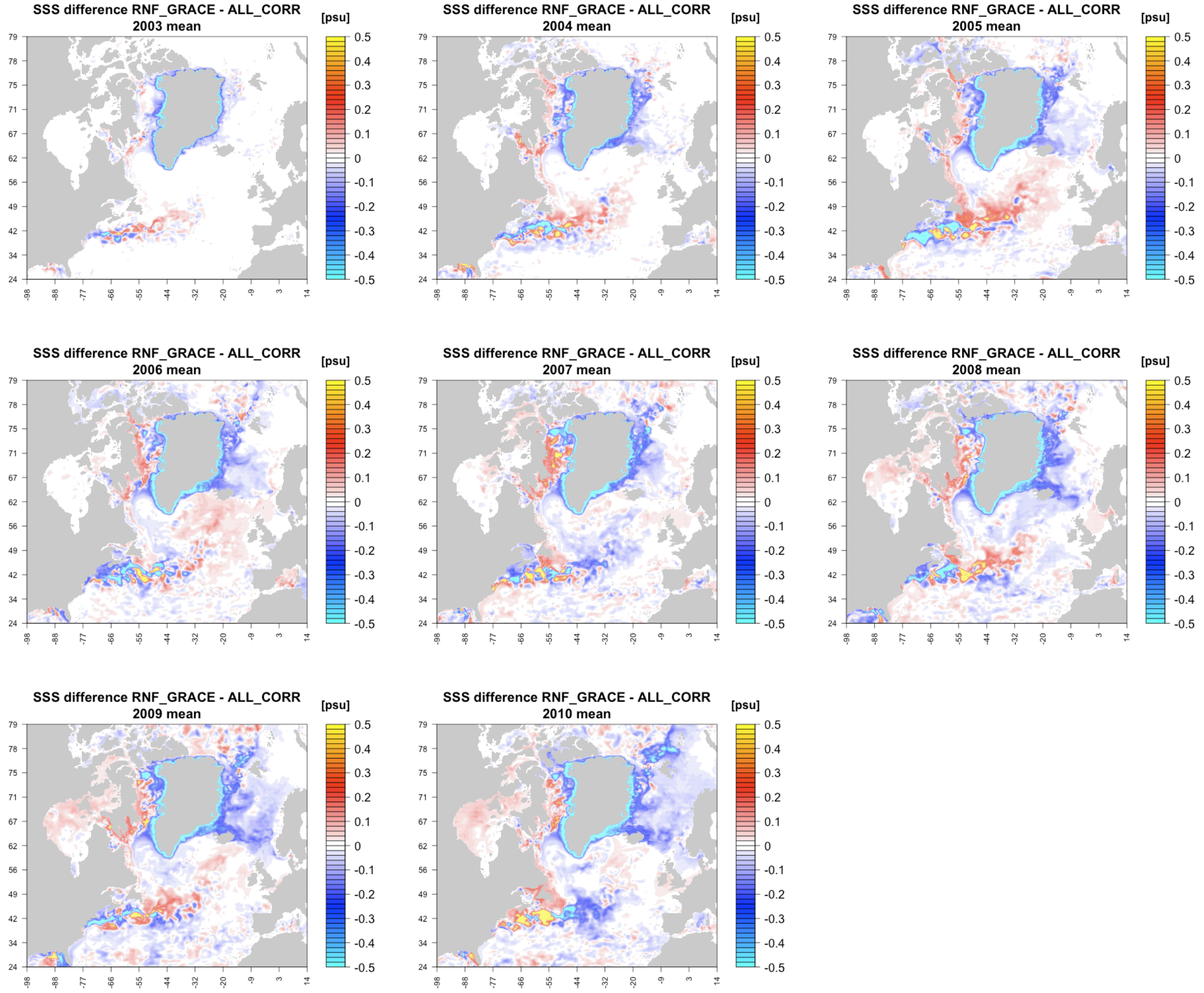

Figure 10– *Annual mean SSS differences between RNF_GRACE and ALL_CORR experiments for all the simulation period (2003-2010*).

Figure 12 (left panel) depicts the model salinity biases at 110 m of depth, averaged over the last year of simulation, with respect to ENACT (EN3) objective analysis. The decrease of surface and subsurface salinity in the Baffin Bay have a positive impact in the attenuation of the salty biases in this area, especially in the southern part of the bay (Figure 12, right panel). SSS bias also decreases, in particular in the Davis Strait, passing from more than 1 psu to 0.7 psu (not shown).

In the absence of any additional surface heat fluxes, variations in temperature only result from the redistribution of heat by the changing circulation and the altered convection (Stammer et al., 2011). Adding fresh water to the model, in fact, changes the ocean circulation around Greenland resulting in variations in atmosphere-ocean fluxes (Brunnabend et al., 2012). Positive anomalies of SST in the range of ±1°C start to develop in the boundary current locations after 6 months (Figure 13, top left panel).

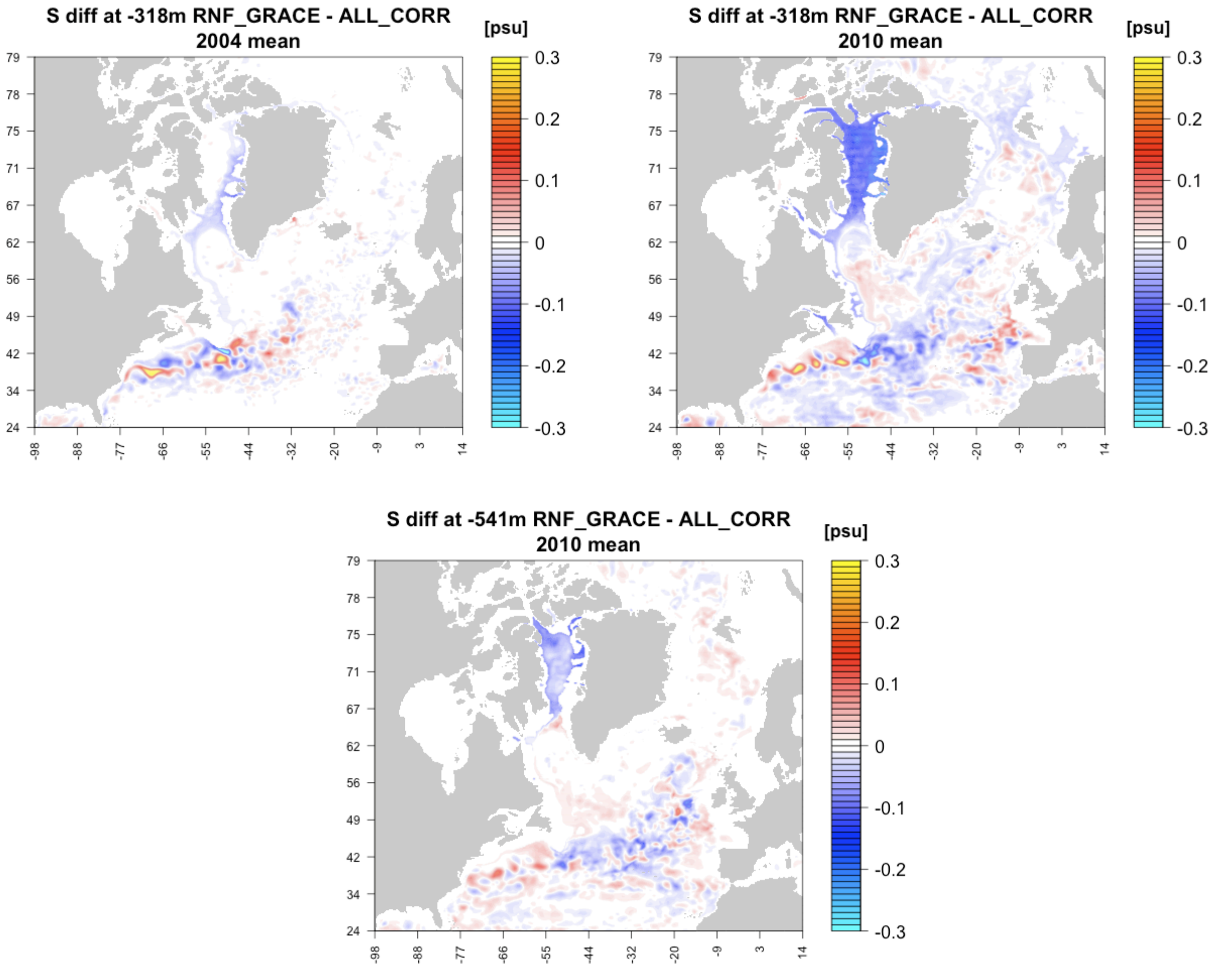

Figure 11– *Top panels: differences between RNF_GRACE and ALL_CORR experiments of 2004 (left) and 2010 (right) mean salinity at -318 m. Bottom panel: salinity difference at -541 m (2010 mean) between RNF_GRACE and ALL_CORR experiments.*

After 8 years the warm anomalies cover also the west part of Baffin Bay, the Davis Strait and some locations in the Labrador Sea, while cold SST anomalies off southern Greenland, with highest values on the southeast coast, are visible. The large positive and negative anomalies present in the Gulf Stream region are due to the strong mesoscale dynamics characteristics of this area (Figure 13, top right panel).

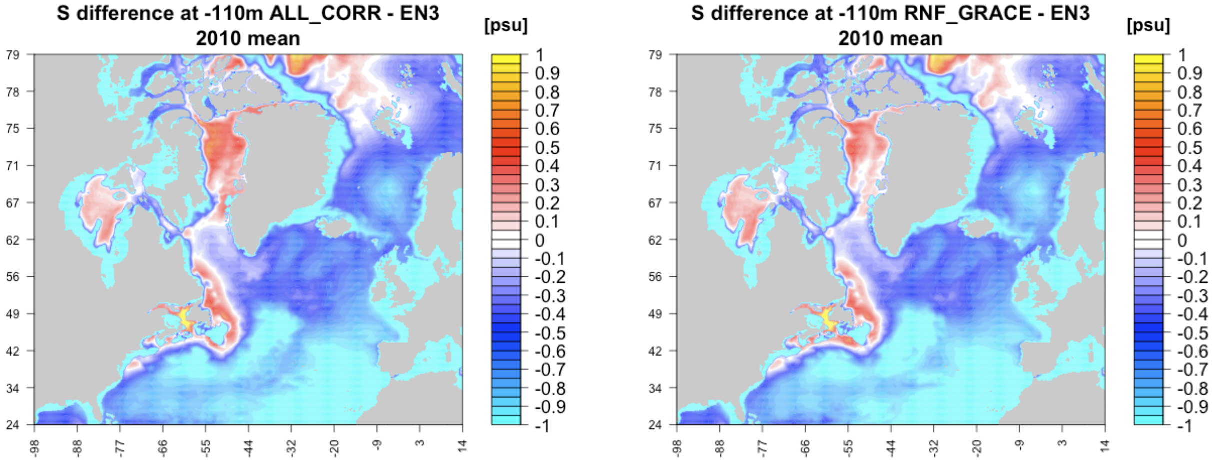

Figure 12– *Salinity differences at -110 m (2010 mean) between ALL_CORR and EN3 dataset (left) and RNF_GRACE and EN3 dataset (right).*

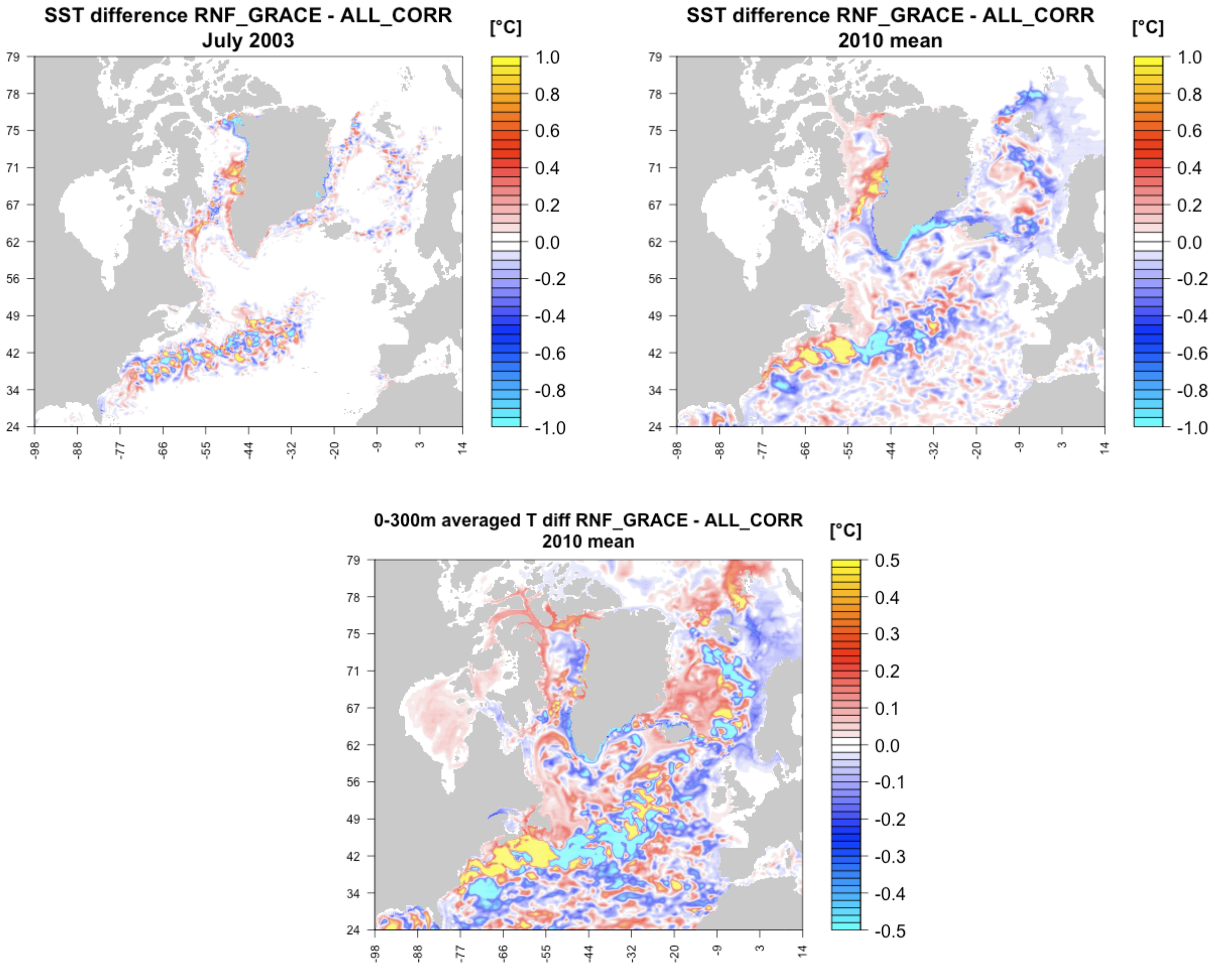

Figure 13– *Differences between RNF_GRACE and ALL_CORR experiments of: SST monthly mean for July 2003 (top left), SST 2010 annual mean (top right) and 2010 mean temperature averaged over the upper 300 m (bottom).*

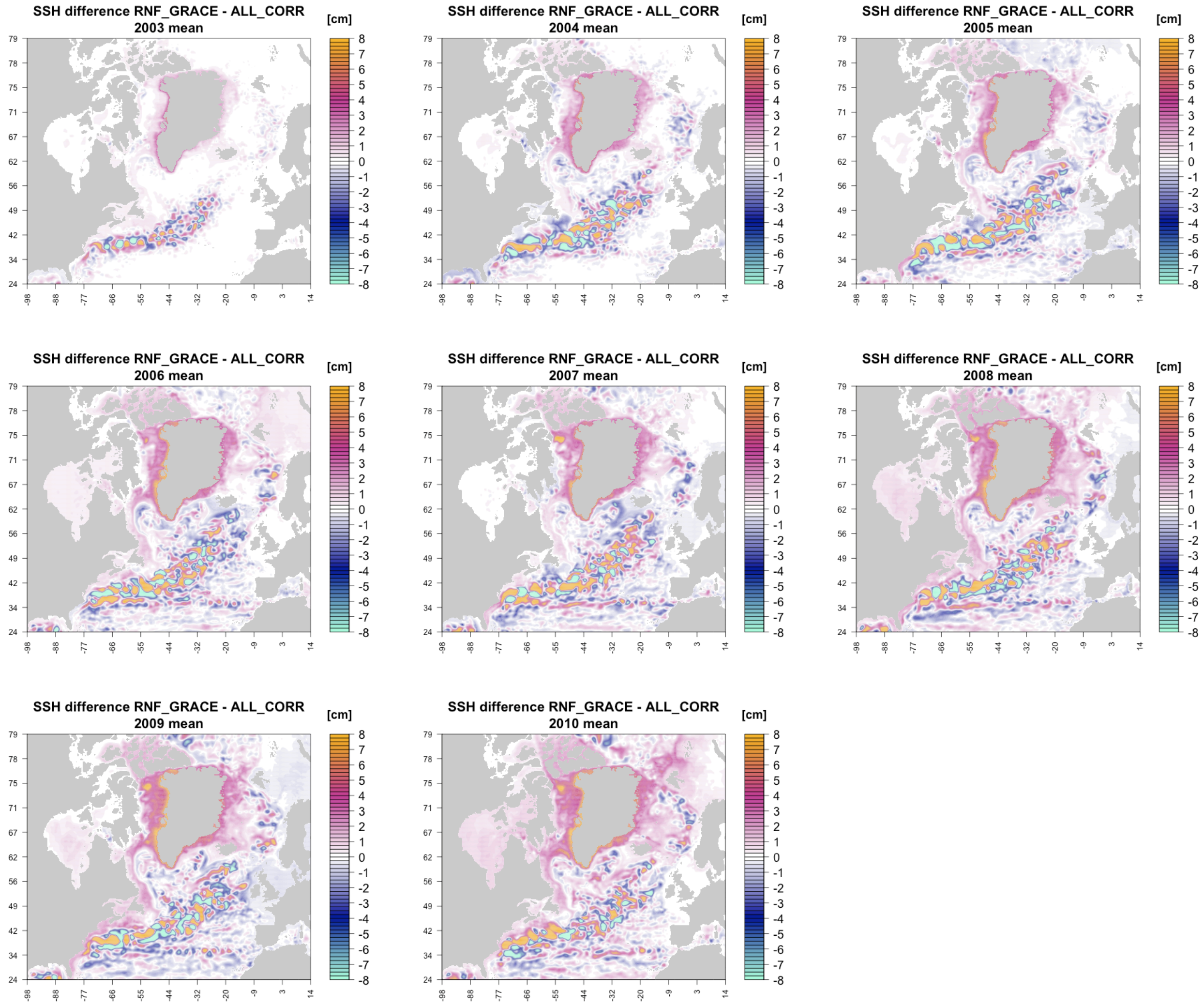

Figure 14– *Annual mean SSH differences between RNF_GRACE and ALL_CORR experiments for all the simulation period (2003-2010).*

4.7.2- Impact on Sea Surface Height

The SSH increases in the RNF_GRACE experiment, with respect to ALL_CORR, during all the length of the simulation (Figure 14). In particular, the mean sea level trend around Greenland (60°N-90°N) increases of 1 mm/yr, passing from 4.03 mm/yr (ALL_CORR) to 5.32 mm/yr (RNF_GRACE). The sea level change is not uniform. At the end of the first year, the sea level slightly increases, up to ~4 cm, near Greenland coasts and after 6 years of simulation it reaches peak of ~8 cm off South and West Greenland, where runoff input has its highest values; at that time the positive anomalies cover also the Canadian Archipelago and the positive anomalies in

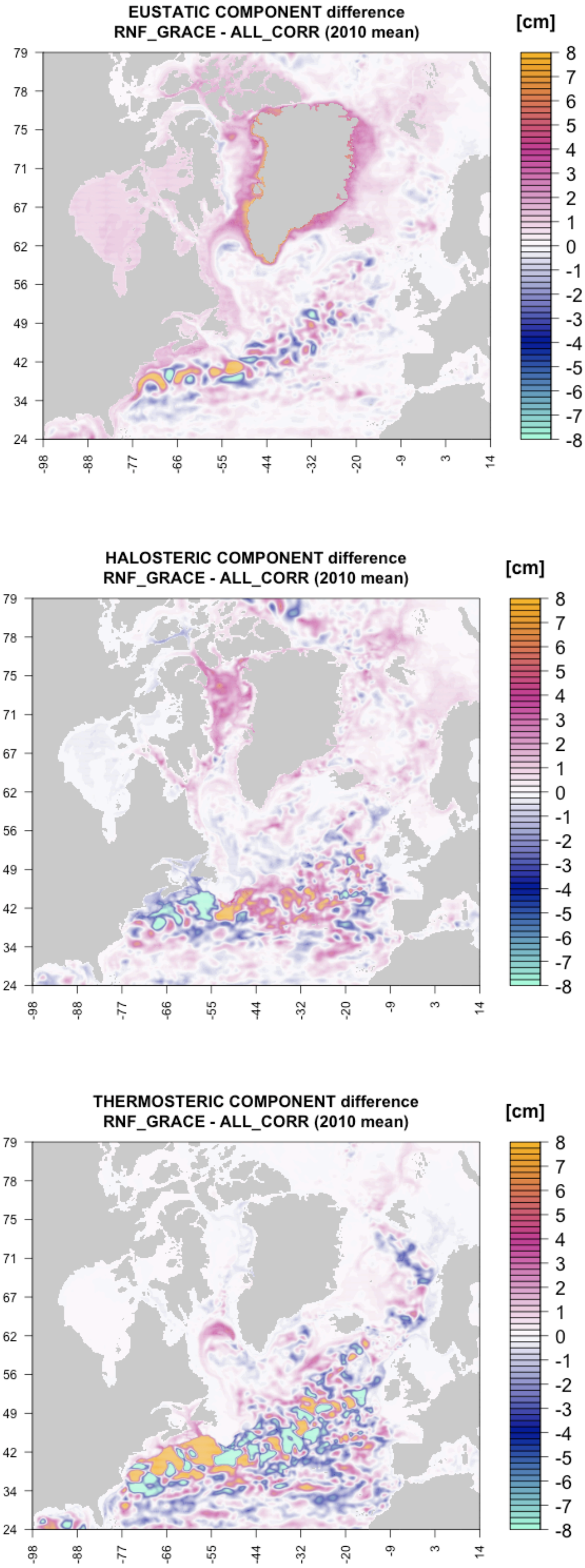

Figure 15– *Eustatic (top), halosteric (middle) and thermosteric (bottom) sea level component differences (2010 mean) between RNF_GRACE and ALL_CORR runs.*

the Labrador Sea boundary current are more pronounced. At the end of simulation high positive SSH anomalies are also visible north of Fram Strait. The presence of eddies in the Gulf Stream, characteristics of mesoscale dynamics areas, generates high values of positive and negative SSH anomalies shown in Figure 14.

With the aim of identifying the causes of local SSH increase in RNF_GRACE experiment, we present in Figure 15 (top panel) the 2010 eustatic SSH anomaly with respect to ALL_CORR simulation (calculated as the difference between the total and steric SSH) and the halosteric and thermosteric SSH anomalies (middle and bottom panels, respectively). The pattern of the spatial variability of sea level mostly results from eustatic sea level change. In particular the eustatic SSH increase, caused in turn by the enhanced freshwater input of the RNF_GRACE experiment, is responsible for sea level rise around the Greenland coasts, in the Canadian Archipelago, in the western Labrador Sea and partly in the Nordic Seas; Figure 14 shows indeed the same patterns of the eustatic sea level anomaly in those areas. On the other hand the strong SSH increase in the Baffin Bay appears to be caused by the halosteric expansion of water column, due to the local decrease of salinity (see Figure 10 and 12); the halosteric component gives also a contribution to the positive SSH anomalies in the Nordic Seas and Labrador Sea. The thermosteric component (Figure 15 bottom panel) plays a negligible role in the increase of SSH, except for a small region in the northern Labrador Sea just south of Davis Strait, where the rim current surface height increases sterically due to local warming of subsurface water (visible in Figure 13 bottom panel).

4.7.3- Impact on boundary currents and deep water formation

In this Section we have analyzed how the input of freshwater modifies the coastal circulation around Greenland. The near-surface circulation around Greenland consists of 4 major boundary currents: the East Greenland Current (EGC), the West Greenland Current (WGC), the Baffin Island Current and the Labrador Current (LC) (Figure 16). The EGC flows southward from Fram Strait (about 80°N) to Cape Farewell (about

60°N), mixing on the way with the Irminger Sea Current, along the eastern coast of Greenland with high velocity core ranging from 50 to 100 cm/s (Sutherland and Pickart, 2008).

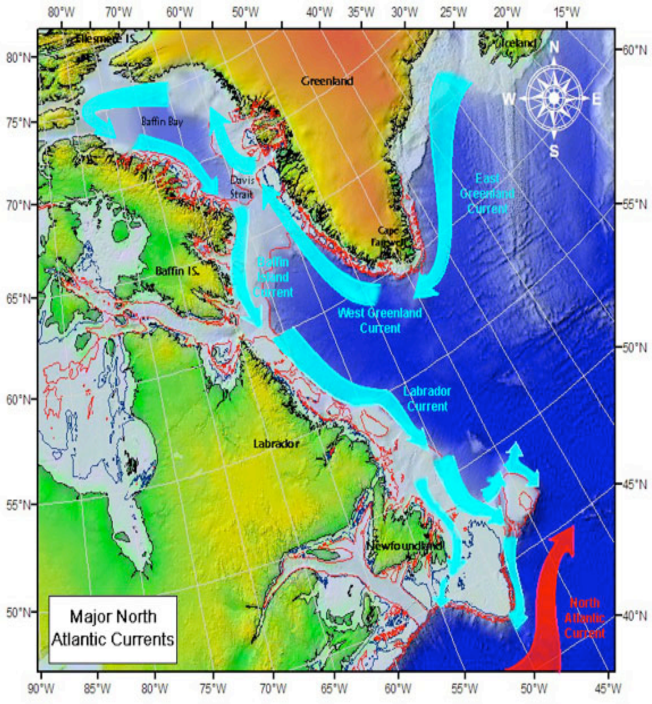

Figure 16– *Depiction of the mean circulation around Greenland (from United States Coast Guard: www.uscg.mil).*

The WGC flows northward from Cape Farwell along the west coast of Greenland and bifurcates near 61°N where the cyclonic boundary current encounters shoaling depths; a fraction of the flow follows the Greenland cost, the rest head southwestward and joins the outflow from Davis Strait forming the LC (Pickart et al. 2007). The LC is a combination of the WGC, the Baffin Island Current and the arctic inflow from Hudson Bay. It flows southwestward from Hudson Strait (60°N) along the continental slope and passes around Newfoundland where it meets the Gulf Stream. The Baffin Island Current is a near-surface current that moves south down the western side of Baffin Bay, along Baffin Island, with a mean velocity of ~30 cm/s (Munchow et al., 2011).

We have analyzed the short-term impact of the enhanced runoff on three vertical velocity sections in correspondence of Baffin Bay, in the WGC and in the Labrador Current.

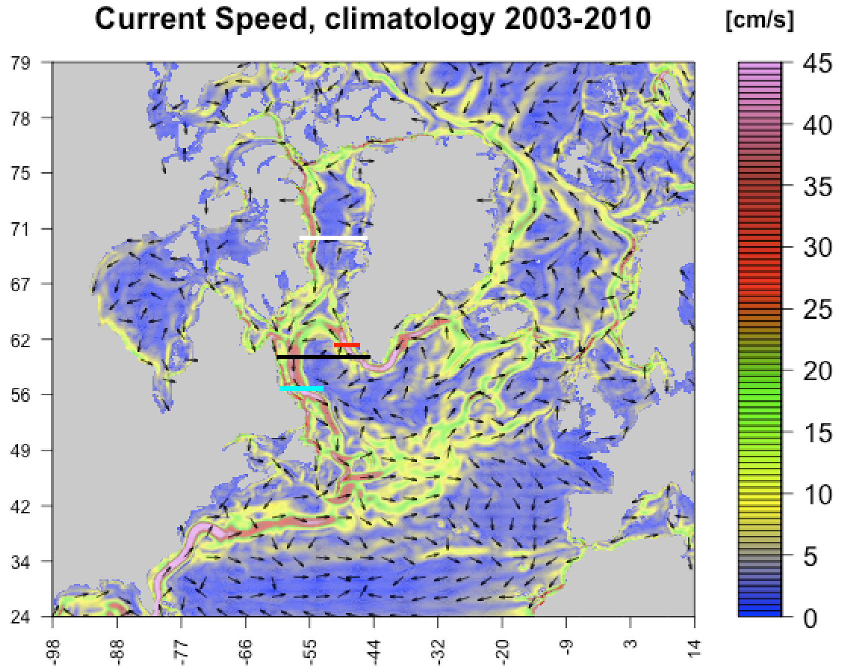

Figure 17– *Current speed climatology (2003-2010) simulated by the model (ALL_CORR experiment); the figure also reports four lines in correspondence of the cross-sections discussed in paragraph 4.6.3. In particular, the white line refers to the Baffin Bay section, the red line to the West Greenland Current section; the cyan line to the Labrador Current section and the black line to the section at the site of deep water formation in the Labrador Sea.*

The vertical velocity fields are annual averages of the last year of simulation and their location is shown in Figure 17, which depicts the current speed climatology (2003-2010) simulated by the model in the ALL_CORR run (the velocity field climatologies are similar in both the ALL_CORR and RNF_GRACE experiments). Thanks to the eddy-permitting resolution of our model configuration we have a more realistic representation of the Greenland boundary currents, directly involved in the freshwater transport along the coasts, with respect to model resolution generally used in this kind of simulation (~1°); nevertheless an eddy-resolving configuration is required to fully resolve the boundary currents dynamics. The simulated currents mean velocities are in good agreement with previous studies (see Section 4.5), with maximum speed of ~45 cm/s in the Labrador Current and in the proximity of Cape Farwell and ~15 cm/s in the EGC.

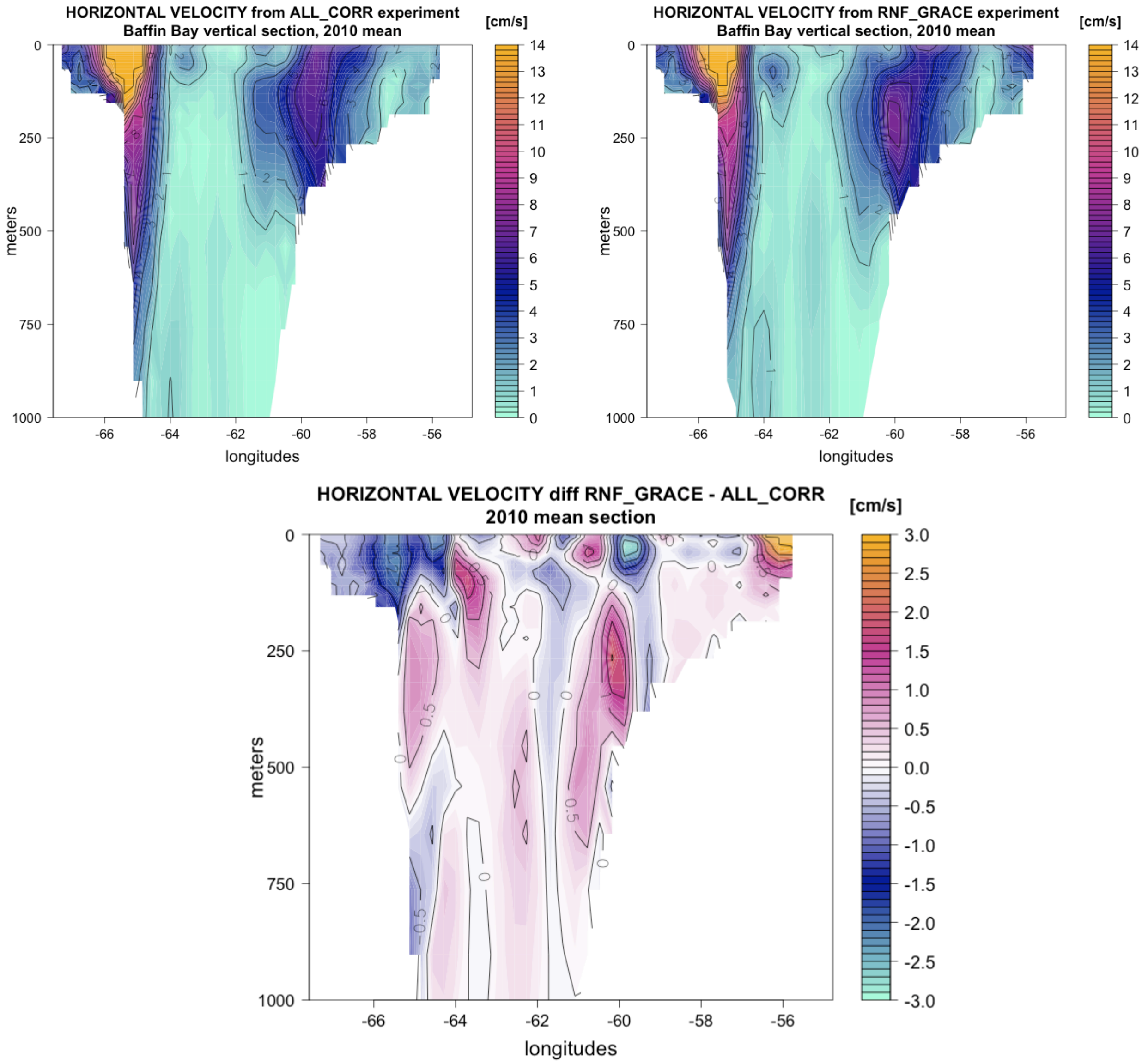

Figure 18– *Top panels: horizontal current speed vertical section (2010 mean) in correspondence of the Baffin Bay from ALL_CORR (left) and RNF_GRACE (right) experiments. Bottom: difference between the two sections (RNF_GRACE minus ALL_CORR).*

Figure 18 shows the horizontal velocity module across a Baffin Bay latitudinal cross-section (white line in Figure 17). We can see the Baffin Island Current on the west side and the West Greenland Current (WGC) on the east side of the bay with the core of 7 cm/s located in the upper 150 m layer in ALL_CORR simulation. The stronger input of freshwater prescribed in RNF_GRACE experiment changes structure (and location) of the WGC offshore, deeply creating a negative velocity anomaly in the near-surface and a positive velocity anomaly between 200 m and 500 m.

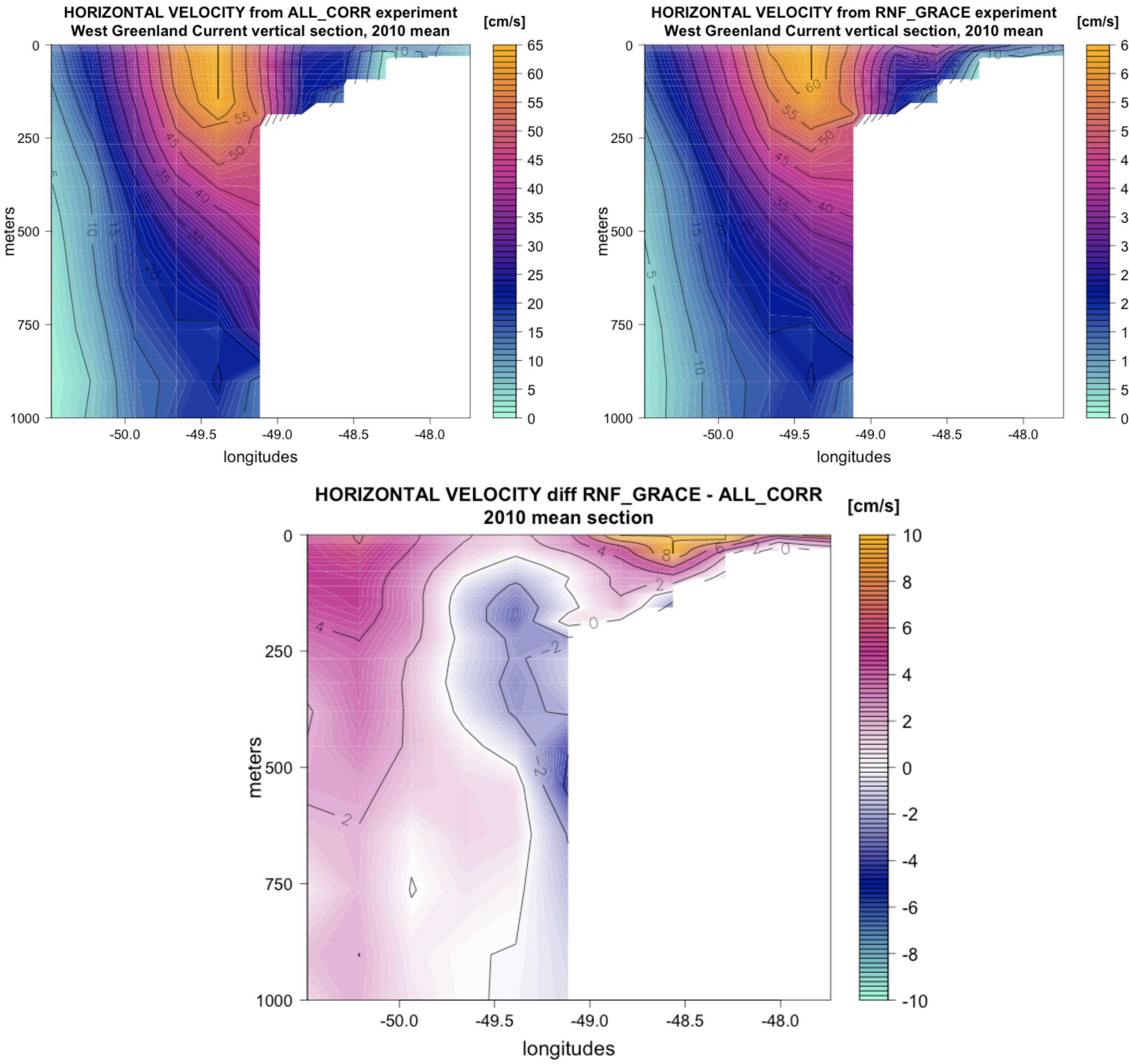

Figure 19– *Top panels: horizontal current speed vertical section (2010 mean) in correspondence of the West Greenland Current from ALL_CORR (left) and RNF_GRACE (right) experiments. Bottom: difference between the two sections (RNF_GRACE minus ALL_CORR).*

A similar mechanism is visible in the WGC cross-section of Figure 19 (red line in Figure 17); it is visible the northwards current with a surface core of about 60 cm/s that extends up to 300 m of depth. As for the case of Baffin Bay, the enhanced input of freshwater of RNF_GRACE simulation displaces the rim current offshore generating a positive velocity anomaly offshore, west of -50°, and a negative anomaly between -49° and -49.5° of longitude below 100 m of depth; furthermore the freshwater inflow at the coast perturbs the water column, generating an instability in the velocity field visible in the positive velocity anomaly on the continental shelf.

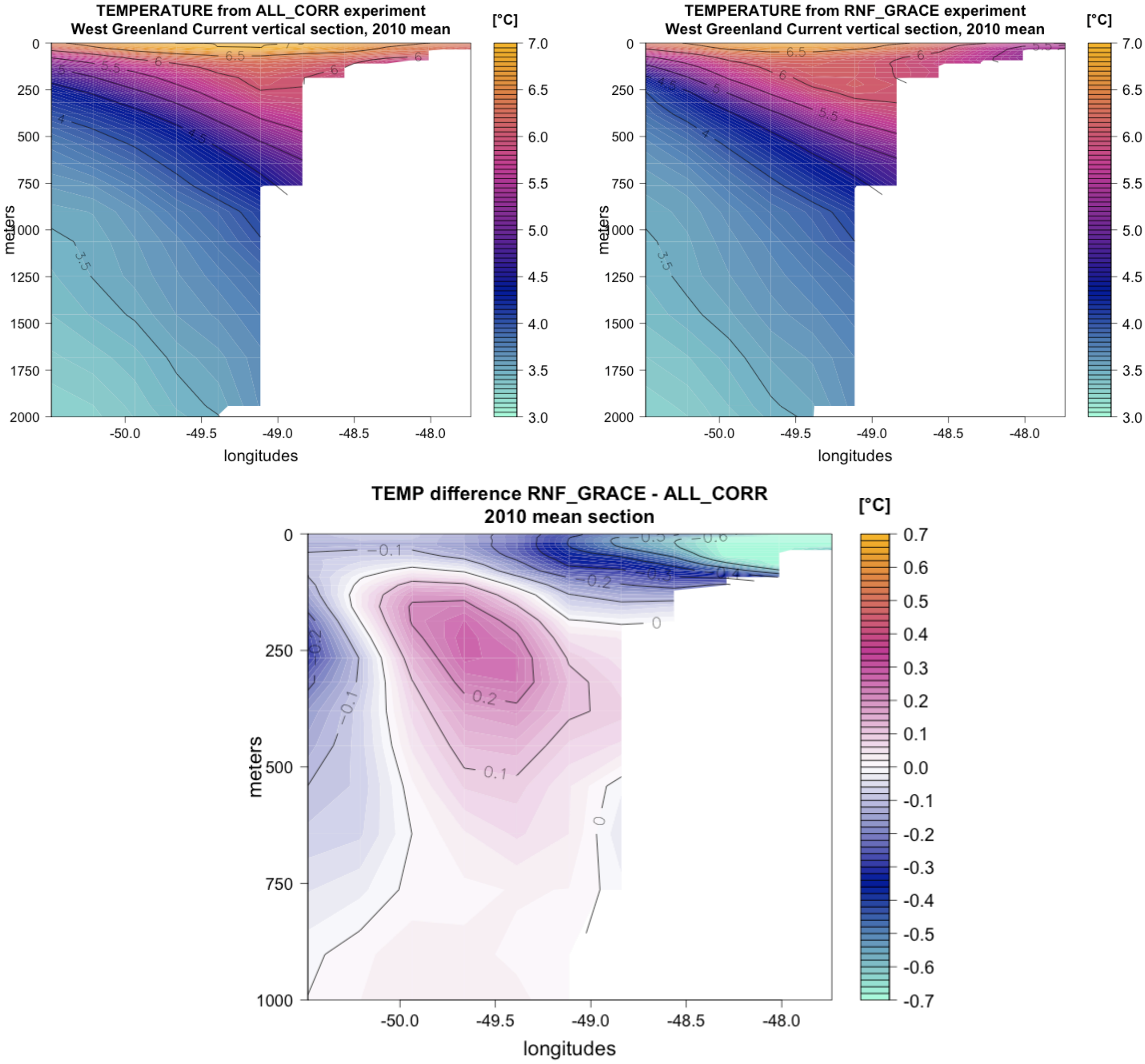

Figure 20– *Top panels: vertical temperature section (2010 mean) in correspondence of the West Greenland Current from ALL_CORR (left) and RNF_GRACE (right) experiments. Bottom: difference between the two sections (RNF_GRACE minus ALL_CORR).*

The displacement of the rim current moves the warm core of ~7°C westward, creating a subsurface positive temperature anomaly offshore (Figure 20), also visible in the anomalies map of temperature, integrated between the surface and 300 m of

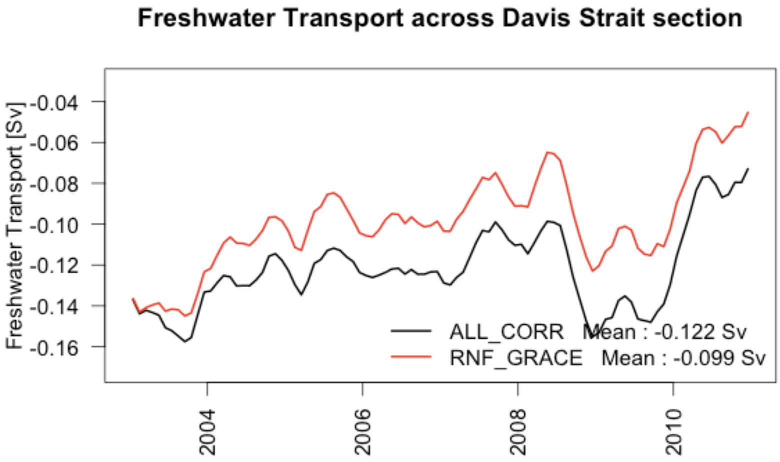

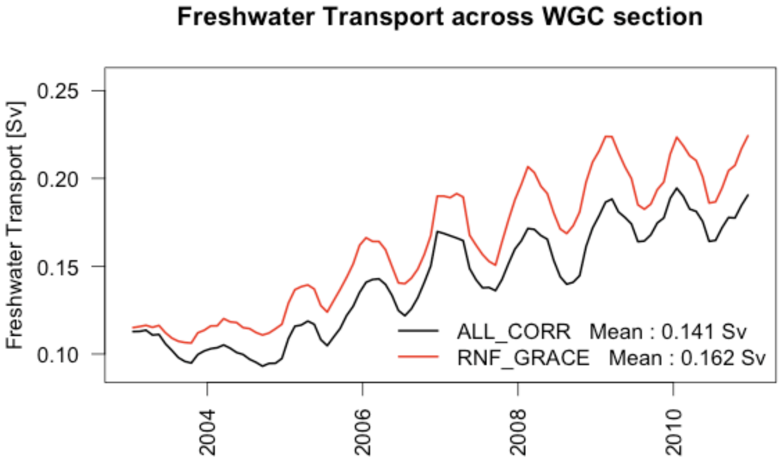

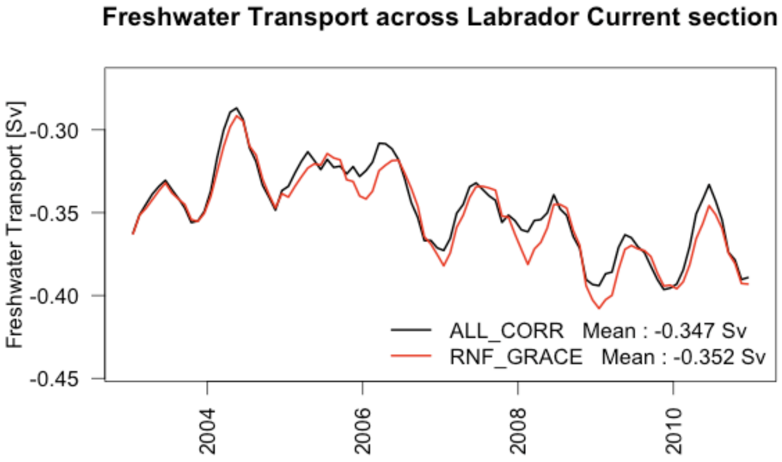

Figure 21– *Time series of the northward freshwater transport across Davis Strait (top), West Greenland Current (middle) and Labrador Current sections (bottom).*

depth (Figure 13, bottom panel); the cold temperature anomaly close to the ice sheet coast (Figure 20) is caused by the cooling that the freshwater inflow experiences in the exchange of heat with the surrounding atmosphere.

The enhanced freshwater at Greenland coasts increases the northward freshwater transport (FWT) in the RNF_GRACE run, across WGC section and Davis Strait, while in the Labrador Current section the signal of the enhanced runoff is almost lost (Figure21). Even if not appreciable in the FWT, the impact of fresher waters advected by the branch of WGC is still visible in the Labrador Current and Labrador Sea sections (cyan and black lines in Figure 17, respectively) slightly decreasing the water density at these locations (Figure 22 and 23, bottom panels). The Labrador Sea is the other major location of deep/intermediate water formation in the North Atlantic, cold air blowing off the Canadian landmass during winter chills the surface waters, which destabilizes the water column and causes deep convection. This sinking of dense water – which can extend as deep as 2 km – forms a water mass known as Labrador Sea Water, which then spreads into the North Atlantic Ocean and contributes to the global Atlantic Meridional Overturning Circulation (AMOC) (Pickart et al. 2002). Water density decrease in the area of deep water formation in the Labrador Sea (Figure 10 and Figure 23 top panel) leads to reduced convection there and suppresses the sink of water masses. As a consequence the Mixed Layer Depth (MLD) is shallower in RNF_GRACE simulation. This is shown in Figure 24 where the overestimation of MLD, visible in the difference between observations and ALL_CORR run (Figure 24, left panel), is mitigated in RNF_GRACE experiment (Figure 24, right panel). As a consequence of reduced convection, near-surface water gets anomalously cold through surface cooling and subsurface waters become warmer as evident in the vertical temperature anomaly section of Figure 23 (middle panel). The difference in the MLD demonstrates the ability of the gravimetry derived freshwater input in better capturing the deep convection characteristics in the Labrador Sea. The reduced convection and formation of deep water has some impact on the AMOC that is slightly reduced, up to 1 Sv, in the RNF_GRACE experiment

(Figure 25).

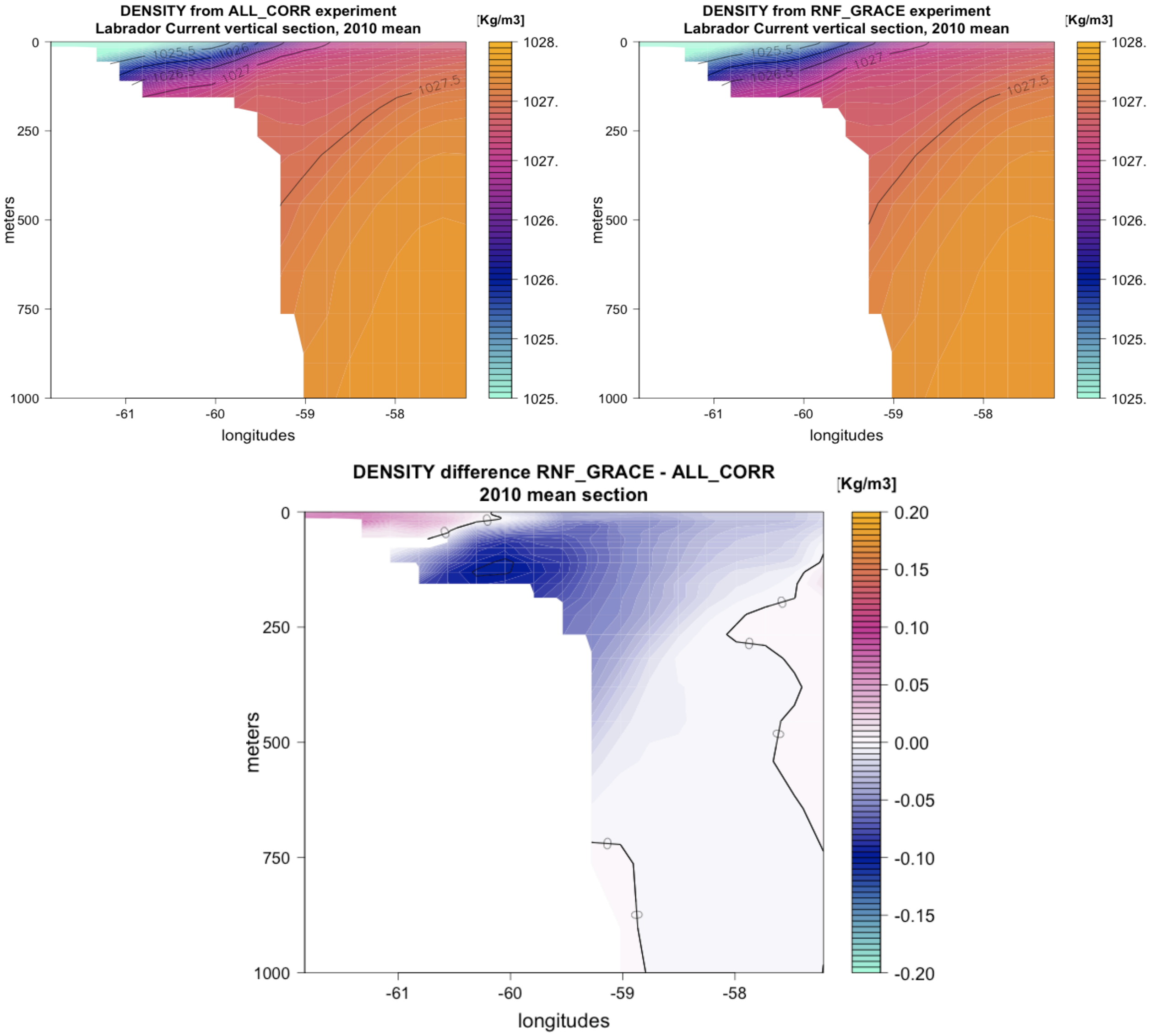

Figure 22– *Top panels: vertical density section (2010 mean) in correspondence of the Labrador Current, from ALL_CORR (left) and RNF_GRACE (right) experiments. Bottom: difference between the two sections (RNF_GRACE minus ALL_CORR).*

4.8- Conclusions and discussion

In this Chapter we have demonstrated the possibility of creating an ice sheets runoff dataset by combining GRACE gravimetry data of water mass variation on land-ice with atmospheric model data of precipitation and sublimation. We have tested the use of atmospheric variables from both an high resolution regional model, RACMO, and

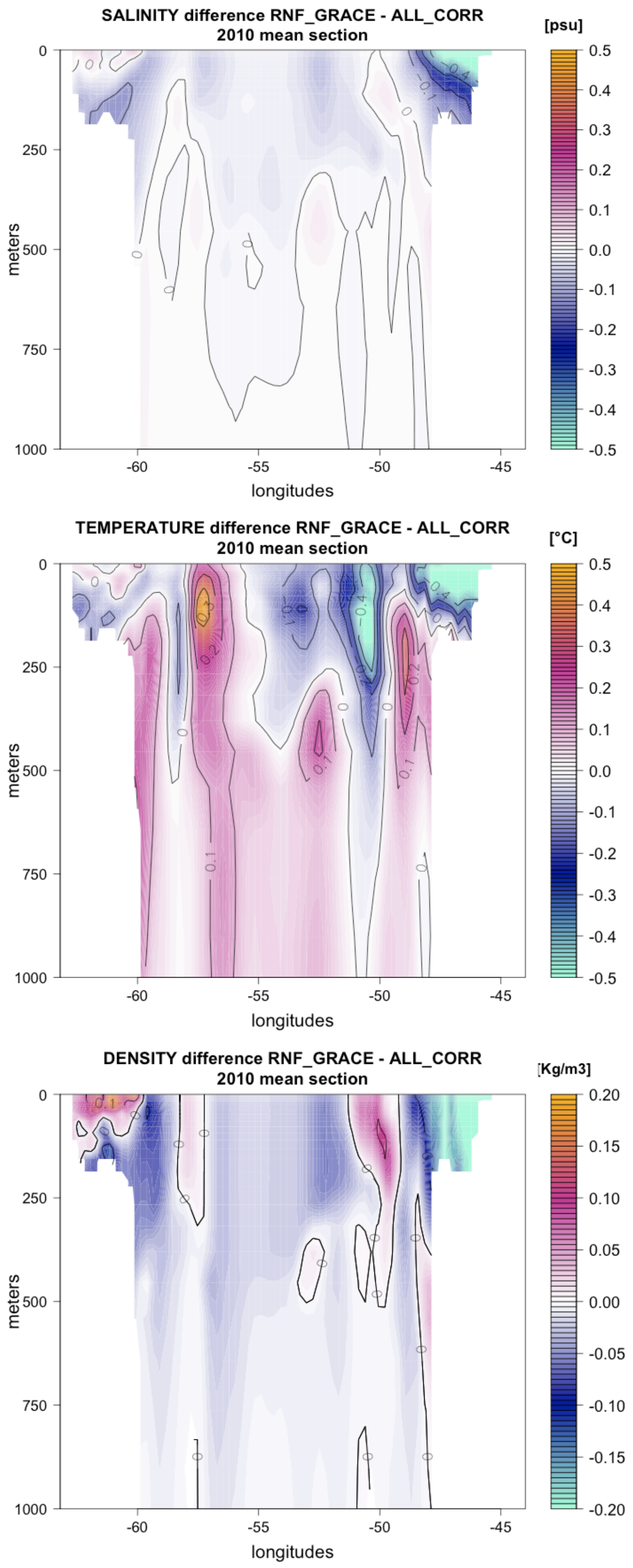

Figure 23– *Difference (RNF_GRACE minus ALL_CORR) of 2010 mean vertical salinity (top), temperature (middle) and density (bottom) section in correspondence of the deep water formation area in the Labrador Sea.*

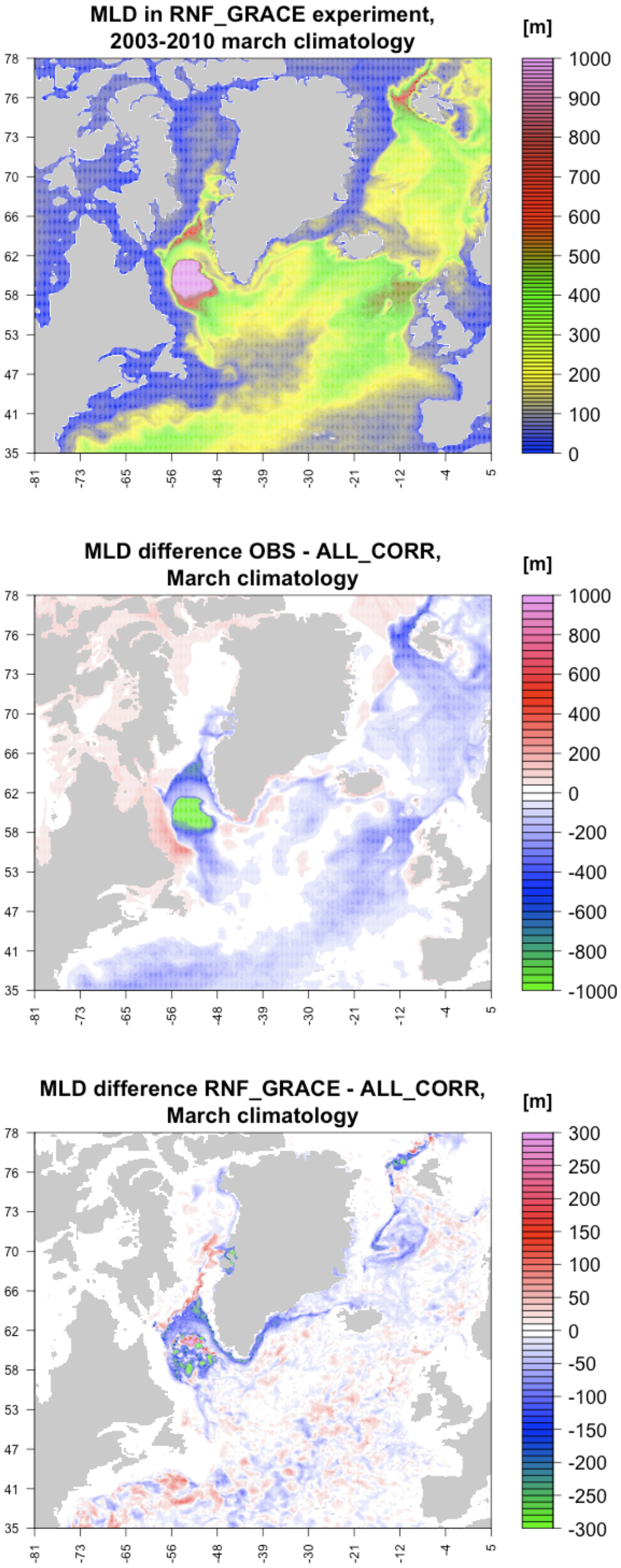

Figure 24– *Top: Mixed Layer Depth from RNF_GRACE experiment (2003-2010 March climatology). Bottom: Mixed Layer Depth difference (March climatology) between observations and ALL_CORR (left) and RNF_GRACE and ALL_CORR (right) experiments.*

ERA-Interim reanalysis. In the comparison with InSAR satellite observations of ice discharge, it turned out that the best fit with observations is achieved with an ensemble of all the existing GRACE solutions balanced with the two atmospheric model datasets. This balance has been performed through the use of the ice sheets water mass balance equation. This is the first time that such a balance is applied on land-ice. We have also tested the use of the combined land-atmosphere water mass balance, which however led to a large underestimation of the runoff and has not been considered further. The resulting runoff is significantly higher, by a factor of 20 to 30, than the climatological runoff from Bourdallé-Badie and Treguier (2006) that is used as default runoff in NEMO model. We have used the newly estimated runoff in our ocean model simulation and hence investigated its short-term impact on the main ocean parameters.

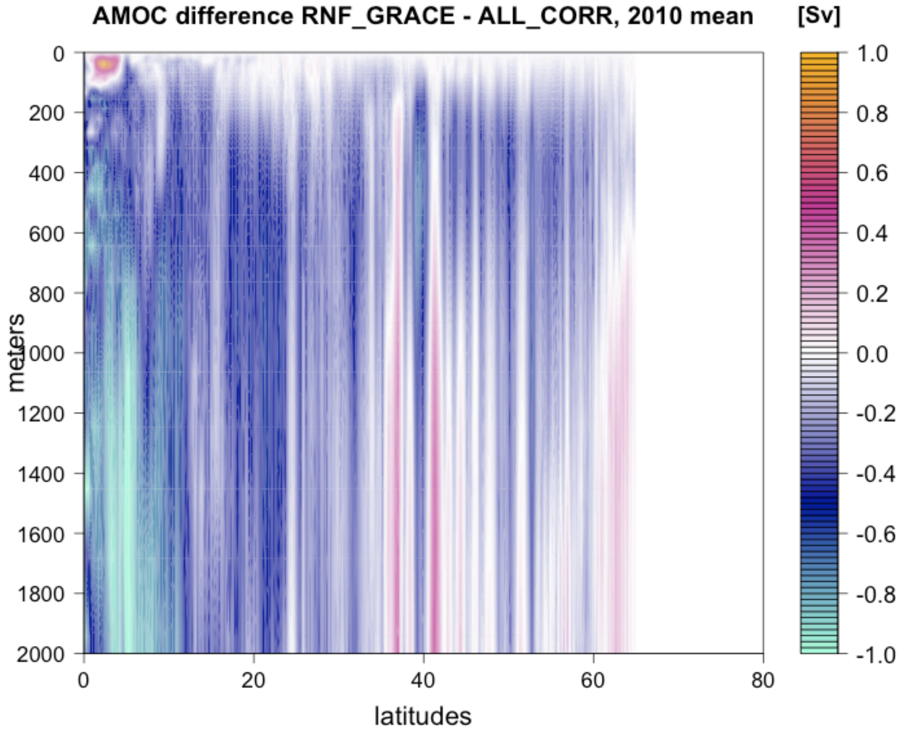

Figure 25– *Difference of the mean 2010 Atlantic Meridional Overturning Circulation (AMOC) between the RNF_GRACE and ALL_CORR experiments.*

The response of the ocean to an enhanced and time-varying ice sheets runoff is appreciable on regional scale while its impact results negligible on large scale. Around Antarctica coasts the impact is low and does not show a clear effect, probably due to the large extension of the Antarctica continent as well as to the strong influence that the ACC has in redistributing the incoming runoff around the coasts. Furthermore, in Antarctica the estimated runoff does not show any seasonal cycle. This anomalous behavior is attributable to uncertainties in both the precipitation data and GRACE observations. However, similarities in the seasonal cycle among the estimated runoff by using different precipitation datasets, suggest that GRACE measurements over Antarctica might be the main cause for the anomalous runoff behavior.

The enhanced input of freshwater into the ocean produces an eustatic sea level rise that subsequently increases during the simulation. The positive SSH anomalies initially stay around Greenland coasts and cover, after 6 years, the Canadian Archipelago, the western part of the Labrador Sea and the Nordic Seas. The highest values of SSH anomalies, up to 8 cm, are found around South and West Greenland, where runoff input has its highest values. A strong increase of SSH is also visible in the Baffin Bay, where the cause of sea level rise has to be attributed not only to the increase of its eustatic component but also to the halosteric expansion of the water column. The increase in the halosteric sea level gives also a non-negligible contribution in the Nordic Seas and in the Labrador Sea.

The enhanced income of freshwater and ice discharge from Greenland coasts induces a freshening of sea water already appreciable, close to the coasts, after 6 months of simulation. At the end of the simulation fresh SSS anomalies, with peak of more than -0.5 psu, are visible all around the Greenland coasts, in the Nordic Seas and in the Labrador Sea, advected there by the two branches of the WGC and further spread into the subpolar gyre region. The fresher waters propagate, after 2 years, up to 300 m with highest values in the Baffin Bay, where the anomalies are also visible at 540 m of depth, due to the local recirculation that increases the residence time of the anomalies. The use of the newly runoff dataset, with respect to the climatological previous one, has positive impacts in reducing the positive salinity model biases in Baffin Bay and Davis Strait for the subsurface and surface waters, respectively. It is worthy to note that the freshwater inflow from sea-ice melting during summer is not significant with respect to the ice sheet runoff. Furthermore sea-ice melting is slightly decreased, during summer, in the RNF_GRACE experiment with respect to the ALL_CORR (not shown), hence sea-ice does not have a positive feedback on the ocean freshening and the negative SSS anomalies are totally due to the enhanced runoff from Greenland coasts.

The sensitivity of the AMOC to high-latitude freshwater input is one of the key uncertainties in the climate system. Considering the importance of the meridional overturning for global transport of heat, and the vulnerability of the Greenland ice sheet to global warming, evaluating this sensitivity is crucial for climate change projections. In contrast to traditional "hosing" experiments, where additional freshwater input is applied over a broad belt of the subpolar North Atlantic and the hosing prescription directly affects the areas where deep convection occurs (e.g. Stouffer et al., 2006), we have applied additional runoff, non-uniformly, in a narrow strip around the Greenland coast. Only sufficiently high resolution can explicitly resolve dynamics required to transport the freshwater to the deep convection sites. The ability of the model in reproducing the transports by western boundary currents and meso-scale eddies is hence a key issue. In agreement with Marsh et al. (2010), we address that eddy-permitting systems are able to show how the presence of narrow boundary currents around Greenland limit the access of the anomalous freshwater into the deep convection sites. In the Labrador Sea, downstream the strongest discharges from the Greenland ice sheet and associated surface freshening, there is no dramatic drop of density after 8 years in the perturbed experiment: the freshwater signal can be traced along the boundary current (the FWT increases across the WGC and Davis Strait), while relatively little additional freshwater reaches the interior of the Labrador Sea (the FWT in the Labrador Current remains almost unchanged in the RNF_GRACE experiment). Nevertheless, the enhanced input of freshwater has an impact, even if small, in reducing the convection at the site of deep water formation in the Labrador Sea, due to a decrease in the sea water density therein. The reduced convection in turn improves the MLD representation, especially in winter time, which is usually overestimated by the model, demonstrating the positive impact that the use of the gravimetry derived freshwater runoff has in better capturing the deep convection in the Labrador Sea. In the Nordic Seas, with the freshwater discharges on the eastern and northern sides of Greenland being much weaker than those influencing the Labrador Sea, there is no evidence of decline in convective activity within the Greenland Sea Gyre. The small decline in convective activity in the Labrador Sea is reflected by a small reduction of the AMOC (up to 1 Sv). It is worth noting that a time-scale of 8 years does not allow us to investigate the adjustment of the AMOC to enhanced melt water under present-day conditions - no conclusion can be drawn on the longer-term response of the large-scale circulation. We expect a gradual adjustment of AMOC to freshwater fluxes on decadal time-scales (Weijer et al., 2012).

References

Adler R.F., Huffman G.J., Chang A., Ferraro R., Xie P., Janowiak J., Rudolf B., Schneider U., Curtis S., Bolvin D., Gruber A., Susskind J., Arkin P., 2003. The Version 2 Global Precipitation Climatology Project (GPCP) Monthly Precipitation Analysis (1979-Present). *J. Hydrometeor.*, 4,1147-1167.

Alley R., Fahnestock M., Joughin I., 2008. Understanding glacier flow in changing time. *Science* 322:1061-62.

Alsdorf D.E. And Lettenmaier D.P., 2003. Tracking fresh water from space. *Science,* 301, 1491-1494.

Bourdallé-Badie R. and Treguier A.M., 2006. A climatology of runoff for the global ocean-ice model ORCA025. Mercator-Ocean reference : MOO-RP-425-365-MER.

Brakenridge G.R., Nghiem S.V., Anderson E. and Chien S., 2005. Space-based measurement of river runoff. *Eos, Trans. Amer. Geophys. Union*, 86, 185-188.

Bromwich D., Nicolas J., Monaghan A., 2011. An assessment of precipitation changes over Antarctica and the Southern Ocean since 1989 in contemporary global renalyses. *Journal of Climate*, 24, 4189-4209.

Brunnabend S.-E., Schröter J., Timmermann R., Rietbroek R., Kusche J., 2012. Modeled steric and mass-driven sea level change caused by Greenland Ice Sheet melting. *Journal of Geodynamics*, vol. 59-60, pp. 219-225.

Cazenave A., Dominh K., Guinehut S., Berthier E., Llovel W., et al., 2009. Sea Level budget over 2003-2008: A reevaluation from GRACE space gravimetry, satellite altimetry and Argo. *Glob. Planet. Change* 65:83-88, doi:10.1016/j/gloplacha.2008.10.004.

Chen J.L., Wilson C.R., Tapley B.D., 2006a. Satellite gravity measurements confirm accelerated melting of the Greenland ice sheet. *Science* 313:1958.

Chen J.L., Wilson C.R., Blankenship D.D., Tapley B.D., 2006b. Antarctic mass change rates from GRACE. *Geophys. Res. Lett.* 33:L11502, doi:10.1029/2006GL026369.

Chen J.L., Wilson C.R., Tapley B.D., 2011. Interannual variability of Greenland ice losses from satellite gravimetry. *J. Geophys. Res.,* VOL. 116, B07406, doi:10.1029/2010JB007789.

Dai A. and Trenberth K.E., 2002. Estimates of freshwater discharge from continents: latitudinal and seasonal variations. *Journal of hydrometeorology*, 3, 660-687.

Dee D. P., Uppala S. M., Simmons A. J., Berrisford P., Poli P. et al., 2011. The ERA-Interim reanalysis: configuration and performance of the data assimilation system. *Quarterly Journal of the Royal Meteorological Society,* Volume 137, pages 553-597.

Ettema J., van den Broeke M.R., van Meijgaard E., van de Berg W.J., Bamber J.L., Box J.E., Bales R.C., 2009. Higher surface mass balance of the Greenland ice sheet revealed by high-resolution climate modeling. *Geophys. Res. Lett.*, Vol. 36, L12501, doi:10.1029/2009GL038110.

Famiglietti J.S., 2004. Remote sensing of terrestrial water storage, soil moisture and surface waters. In *The State of the Planet: Frontiers and Challenges in Geophysics,* *Geophys. Monogr. Ser.*, 150, edited by R. S. J. Sparks and C. J. Hawkesworth, pp. 197–207, AGU, Washington D.C.

Fekete B.M., Vörösmarty C.J., Grabs W., 2000. Global composite runoff fields based on observed data and simulated water balance. Global Runoff Data Centre Tech. Rep. 22, Koblenz, Germany, 108 pp.

Fekete B.M., Vörösmarty C.J., Grabs W., 2002. High-resolution fields of global runoff combining observed river discharge and simulated water balances. *Global Biogeochem. Cycles*, 16, 1042, doi:10.1029/1999GB001254.

Frappart F. and Ramillien G., 2012. Contribution of GRACE Satellite Gravimetry in Global and Regional Hydrology, and in Ice Sheets Mass Balance. In the book "Water Resources Management and Modeling", edited by Purna Nayak, ISBN 978-953-51-0246-5, InTech, March 3, 2012.

Frappart F., Ramillien G., Maisongrande P., Bonnet M.-P., 2010. Denoising satellite gravity signals by Independent Component Analysis. *IEEE Geosci. Remote Sens. Lett.* 7 421–5.

Frappart F., Ramillien G., Leblanc M., Tweed S.O., Bonnet M.-P., Maisongrande P., 2011. An independent component analysis approach for filtering continental hydrology in the GRACE gravity data. *Remote Sens. Environ.* 115 187–204.

Gerdes R., Hurlin W., and Griffies S. M., 2006. Sensitivity of a global ocean model to increased run-off from Greenland. *Ocean Modell.,* 12, 416–435.

Holland D., Thomas R.H., De Young B., Ribergaard M.H., Lyberth B., 2008. Acceleration of Jakobshawn Isbraetriggered by warm subsurface ocean waters. *Nat.*

Geosci.

Howat I.M., Joughin I.R., Scambos T.A., 2007. Rapid changes in ice discharge from Greenland outlet glaciers. *Science* 315:1559-61, doi:10.1126/science.1138478.

Hu A., Meehl G. A., Han W., and Yin J., 2011. Effect of the potential melting of the Greenland Ice Sheet on the Meridional Overturning Circulation and global climate in the future, *Deep Sea Res. Part II,* 58,1914-1926.

Krabill W., Hanna E., Huybrechts P., Abdalati W., Cappelen J., et al., 2004. Greenland Ice Sheet: Increased coastal thinning. *Geophys. Res. Lett.* 31:L24402, doi:10.1029/2004GL021533.

Johannessen O.M., Khvorostovsky K., Miles M.W., Bobylev L.P., 2005. Recent ice-sheet growth in the interior of Greenland. *Science.*

Large W. G., Yeager S. G., 2008. The global climatology of an interannually varying air-sea flux data set. *Climate Dynamics*, doi: 10.1007/s00382–008–0441–3.

Llovel W., Becker M., Cazenave A., Jevrejeva S., Alkama R., Decharme B., Douville H., Ablain M., Beckley B., 2011. Terrestrial waters and sea level variations on interannual time scale. *Glob. Planet. Change* 75(1–2):76–82.

Llyod J., Kuijpers A., Long A., Moros M., and Park L., 2007. Foraminiferal reconstruction of mid- to late Holocene ocean circulation and climate variability in Disko, Bugt, West Greenland. The Holocene: 17: 1079-1091.

Luthcke S.B., Zwally H.J., Abdalati W., Rowlands D.D., Ray R.D., et al., 2006. Recent Greenland ice mass loss by drainage system from satellite gravimetry observations. *Sciencexpress* 314:1286-89, doi:10.1126/science.1130776.

Marsh R., Desbruyères D., Bamber J. L., De Cuevas B. A., Coward A. C., and Aksenov Y., 2010. Short-term impacts of enhanced Greenland freshwater fluxes in an eddy-permitting ocean model, *Ocean Sci., 6, 749-760.*

Meier W. N., Stroeve J., Fetterer F., 2007. Whither Arctic sea ice?: A clear signal of decline regionally, seasonally, and extending beyond the satellite record. *Ann. Glaciol.*, 46.

Munchow, A., Falkner K., Melling H., 2011. Baffin Island and West Greenland Current systems in northern Baffin Bay: Synoptic observations and climatological context. *J.Phys. Oceanogr.*

Paulson A., Zhong S., Wahr J, 2007. Inference of mantle viscosity from GRACE and relative sea level data. *Geophys. J. Int.* 171, 497–508. doi: 10.1111/j.1365-246X.2007.03556.x

Peltier W. R., 2004. Global glacial isostasy and the surface of the Ice-Age Earth: The ICE-5G (VM2) model and GRACE. *Annu. Rev. Earth Planet. Sci.*, 32, 111– 149.

Pickard R. S. and Spall M. A., 2007. Impact of Labrador Sea convection on the North Atlantic meridional overturning circulation. *J. Phys. Oceanogr.,* 37, 2207–2227.

Pickard R. S., Torres D. J., Clarke R. A., 2002. Hydrography of the Labrador Sea during active convection. *J. Phys. Oceanogr.,* 32, 428-457.

Ramillien G., Frappart F., Güntner A., Ngo-Duc T., Cazenave A., Laval K., 2006a.

Time variations of the regional evapotranspiration rate from Gravity Recovery and Climate Experiment (GRACE) satellite gravimetry. Water Resour. Res., 42, W10403, doi:10.1029/2005WR004331.

Ramillien G., Lombard A., Cazenave A., Ivins E., Llubes M., et al., 2006b. Interannual variations of ice sheets mass balance from GRACE and sea level. *Glob. Planet. Change* 53:198-208.

Remy F. and Frezzotti M, 2006. Antarctica ice sheet mass balance. *C. R. Geosci.*, 338, 1084-1097.

Rignot E. and Kanagaratnam P., 2006. Changes in the Velocity Structure of the Greenland Ice Sheet. *Science.*

Rignot E., Bamber J.L., Van den Broeke M.R., Davis C., Li Y., et al., 2008. Recent Antarctic ice mass loss from radar interferometry and regional climate modelling. Nat. Geosci. 1:106-10.

Rignot E., Velicogna I., van den Broeke M.R., Monaghan A., Lenaerts J., 2011. Acceleration of the contribution of the Greenland and Antarctic ice sheets to sea level rise. Geophys. Res. Lett. 38:L05503. doi:10.1029/2011GL046583.

Schmidt R., Flechtner F., Reigber Ch., Schwintzer P., Günter A., Doll P., Ramillien G., Cazenave A., Petrovic S., Jochman H., Wunsch J., 2006. GRACE observations of changes in continental water storage. *Glob. Planet. Change* 50/1–2, 112–126. doi:10.1016/j.gloplacha.2004.11.018.

Sheffield J., Goteti G., Wood E.F., 2006. Development of a 50-yr high-resolution global dataset of meteorological forcings for land surface modeling. *J. Clim.*

19:3088–3111.

Simmons A., Uppala S., Dee D., Kobayashi S., 2007. ERA-Interim: New ECMWF reanalysis products from 1989 onwards. In Newsletter 110. ECMWF.

Slobbe D.G., Ditmar P., Linderbergh R.C., 2009. Estimating the rates of mass change, ice volume change ad snow volume change in Greenland from ICESat and GRACE data. *Geophys. J. Int.* 176:95-106.

Stammer D., 2008: Response of the global ocean to Greenland and Antarctica ice melting. *J. Geophys. Res.*, 113, C06022, doi:10.1029/2006JC004079.

Stammer D., Agarwal N., Herrmann P., Kohl A., Mechoso C. R., 2011. Response of a coupled ocean-atmosphere model to Greenland ice melting. *Surv. Geophys.* 32, 621–642.

Stouffer R.J., Yin J., Gregory J.M., Dixon K.W., Spelman M.J., Hurlin W., Weaver A.J. et al., 2006. Investigating the Causes of the Response of the Thermohaline Circulation to Past and Future Climate Changes. *Journal of Climate*, Vol. 19.

Sutherland D.A. and Pickart R.S., 2008. The East Greenland Coastal Current: Structure, variability, and forcing. *Prog. Oceanogr.*, 78, 58–77.

Syed T.H., Famiglietti J.S., Chen J., Rodell M., Seneviratne S.I., Viterbo P., Wilson C.R., 2005. Total basin discharge for the Amazon and Mississippi River basins from GRACE and a land-atmosphere water balance. *Geophys. Res. Lett.*, 32, L24404, doi:10.1029/2005GL024851.

Syed T.H., Zlotnicki V. and Rodell M., 2007. Contemporary estimates of Arctic freshwater discharge frno gRACE and reanalyses. *Geophys. Res. Lett.*, 34, L19404, doi:10.1029/2007GL031254.

Syed T.H., Famiglietti J.S., Chambers D.P., 2009. GRACE-based estimates of terrestrial freshwater discharge from basin to continental scales. *J Hydrometeorol* 10:22–40.

Tapley B.D., Bettadpur S., Watkins M., Reigber C., 2004. The gravity recovery and climate experiment : mission overview and Early results. *Geophys. Res. Lett.* 31, L09607. doi:10.1029/2004GL019920.

Van den Broeke M.R., Bamber J., Lenaerts J., Rignot E., 2011. Ice sheets and sea level: thinking outside the box. *Sur. Geophys.* 32 495–505, doi 10.1007/s10712-011-9137-z.

Van Meijgaard E., van Ulft L.H., van de Berg W.J., Bosveld F.C., van den Hurk B.J.J.M., Lenderink G., Siebesma A.P., 2008. The KNMI regional atmospheric climate model RACMO version 2.1. Technical report ; TR – 302.

Velicogna I., Wahr J., 2006a. Revised Greenland mass balance from GRACE. *Nature* 443:329.

Velicogna I., Wahr J., 2006b. Measurements of time-variable gravity show mass loss in Antarctica. *Sciencexpress* 311:1754-56, doi:10.1126/science.1123785.

Wahr J., Molenaar M., and Bryan F., 1998. Time-variability of the Earth's gravity field: Hydrological and oceanic effects and their possible detection using GRACE. *J. Geophys. Res.*, 103, 32,20530,229.

Wahr J., Swenson S., Zlotnicki V., Velicogna I., 2004. Time-variable gravity from GRACE: First results. *Geophys. Res. Lett.*, 31, L11501, doi:10.1029/2004GL019779.

Weijer W., Maltrud M.E., Hecht M.W., Dijkstra H.A., Kliphuis M.A., 2012. Response of the Atlantic Ocean circulation to Greenland Ice Sheet melting in a strongly-eddying ocean model. GRL, vol. 39.

Witze A., 2008. Loosing Greenland. Science 452:798-802.

Xie P. and Arkin P.A., 1997. Global precipitation: A 17-year monthly analysis based on gauge observations, satellite estimates, and numerical model outputs. *Bull. Amer. Meteor. Soc.*, 78, 2539-2558.

Yin J., Stouffer R. J., Spelman M. J., Griffies S. M., 2010. Evaluating the uncertainty induced by the virtual salt flux assumption in climate simulations and future projections. *J. Clim.* 23, 80-96. doi:10.1175/2009JCLI3084.1.

Chapter 5

Sea Level projections over the next 20 years

Abstract

As a major effect of future climate change, sea level rise is a topic of crucial interest among the climate community. Over the 21st century, in fact, global-mean sea level is expected to rise at an even larger rate with respect to the last century, as a result of anthropogenic greenhouse gases (GHG) induced global warming, with potential impacts on the environment and on coastal communities. Clearly, detecting and predicting sea level change is an important issue in the frame of climate change investigation.

The objective of this Chapter is to project global and regional sea level change over the next 20 years (2011-2030) by using the NEMO Ocean General Circulation Model (OGCM) and to understand the main causes of future sea level variations as well as the uncertainties linked to our projections. The OGCM is forced with two different sets of atmospheric fluxes provided by the Centro Euro-Mediterraneo per i Cambiamenti Climatici Climate Model (CMCC-CM) under the medium-low RCP4.5 GHG stabilisation scenario. The simulations are performed at an unprecedented resolution of 0.25°, which is a major novelty in our approach with respect to most of the currently available projections performed by means of coupled models whose ocean component has a coarse horizontal resolution (1° to 2°).

In order to assess the reliability of our approach, the model forced by the CMCC-CM air-sea fluxes has been firstly validated over the last decade. In the comparison with satellite data the main sea level trend patterns are correctly captured by the model simulation. The results of our projections show that the global-mean sea level will increase by ~1.7 cm at the end of 2030 and that future regional sea level changes will exhibit a non-uniform spatial distribution. According to our projections and in agreement with previous 21st century projections, sea level is expected to rise in the North Atlantic (north of 40°N), in the Kuroshio Current region and in the Arctic Ocean. The ocean freshening is foreseen to be the responsible of such a sea level rise, induced by an increase of precipitation in the Tropical Pacific and sea-ice melting in the Arctic region. In the North Atlantic a decrease of the Westerlies speed will induce a slowdown of the subtropical gyre, which in turn will reduce the transport of salty water to high latitudes, with a consequent increase of the halosteric sea level trend. Nevertheless, caution should be paid in the interpretation of future sea level change in areas where the two projections differ significantly, namely in the western Tropical Pacific and in areas of strong mesoscale dynamics.

The tropical western Pacific islands are particularly concerned about future sea level change due to their low-lying position above the mean sea level; therefore, we have focussed our analysis on this vulnerable area. Such a regional study suggests that

most of the Pacific Small Islands will not suffer from the impacts of future sea level change, while the most vulnerable territories will be the islands located north of 18°N where the two projections agree on a future sea level rise up to 7-8 mm/yr.

As a final remark, we found that regional sea level increase in the next 20 years are comparable in magnitude to 2001-2010 sea level trends, suggesting that GHG mitigation strategies implicit in the RCP4.5 scenario may be effective in containing future sea level rise and hence in partially reducing its potential impacts.

5.1- Introduction and motivations

On times scales of decades to tens of thousands of years, sea level change results from exchange of mass between glaciers, ice sheets and terrestrial water storage with the ocean. Sea level also changes if the density of the ocean changes (mainly as a result of temperature variations) even though there is no variation in mass. During the last century, sea level is estimated to have risen by 10-20 cm, as a result of a combination of the thermal expansion of the ocean and the increased mass of the ocean from melting glaciers and ice sheets (IPCC AR4, 2007). Over the 21st century, sea level is expected to rise at an even larger rate with respect to the last century as a result of anthropogenic climate change, with impacts on both the environment and the human society. Hence, a common concern is to implement powerful observational and modeling tools, such as the coupled Atmosphere-Ocean General Circulation Models (AOGCMs), for predicting the future sea level rise and understanding its causes under different greenhouse gases (GHG) emission scenarios. The Intergovernmental Panel on Climate Change (IPCC) has devoted many efforts in collecting and summarizing the sea level projections from different AOGCMs. In the Fourth IPCC Assessment Report (IPCC AR4, 2007), the sea level rise due to ocean thermal expansion, glaciers, ice caps and ice sheets contribution, is projected to be in the range of 18 and 59 cm by the end of 2095 (Figure 1, magenta bar). Furthermore, an additional 10-20 cm of sea level rise (red bar) may be accounted for in case of a rapid dynamic response of Greenland and West Antarctica ice sheets. Landerer et al. (2007) found a global-mean sea level rise from an AOGCM projection, under the IPCC-A1B scenario, equal to 26 cm by 2100, due in particular to an increase of the net heat flux into the ocean. Very recently, Yin (2012) used an ensemble of 34 AOGCMs to estimate the sea level rise under three different Representative Concentration Pathway (RCP, Moss et al. 2010) scenarios (i.e. RCP2.6, RCP4.5 and RCP8.5, which stabilize radiative forcing at 2.6, 4.5 and 8.5 $\frac{W}{m^2}$ by the year 2100), finding that by the end of this century the global-ocean sea level rise, due to thermal expansion only, can reach 13 ± 0.3 cm, 18 ± 0.3 cm and 28 ± 0.3 cm, respectively. A word of caution should be addressed on the interpretation of those sea level projections. Indeed, current coupled models do not account for or have no accurate representation of the land-ice melting and its contribution to sea level change. However, empirical methods based on the extrapolation of the ice sheets induced sea level rise from AOGCMs projections, suggest that such a contribution will be increasingly positive (Gregory and Huybrechts, 2006).

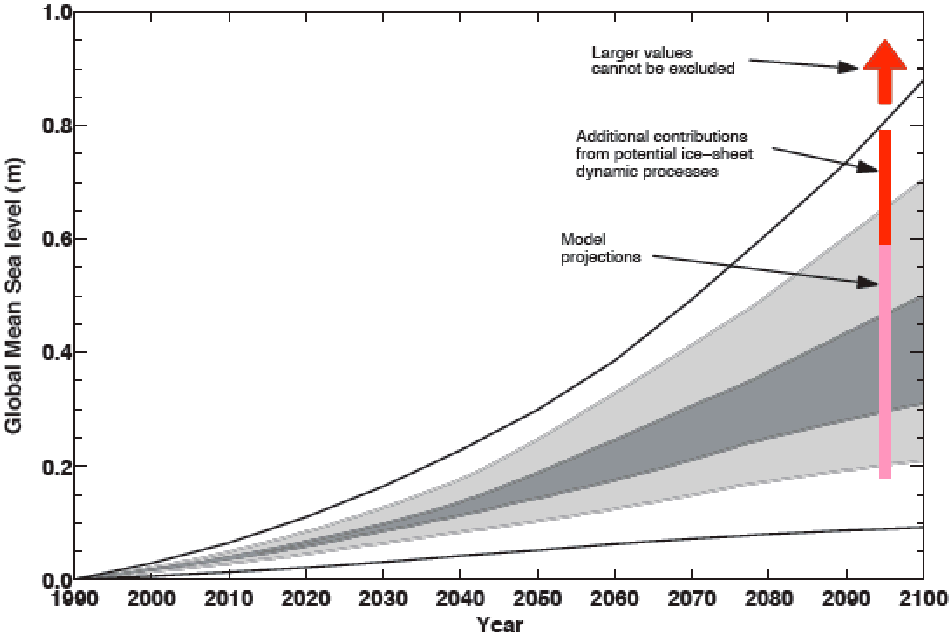

Figure 1– *IPCC projected global averaged sea level rise for the 21st century. The bars plotted at 2095 represent the IPCC AR4 (2007) projections (90% confidence limits). The magenta bar is the range of model projections, and the red bar is the extended range to allow for the potential contribution from a dynamic response of the Greenland and Antarctic Ice Sheets to global warming. The shading represent the projected range of global averaged sea level rise from the IPCC TAR (2001) and the outer lines include an allowance for an additional land-ice uncertainty.*

The future regional sea level changes exhibit a non-uniform spatial distribution in AOGCMs projections. The sea change patterns are mainly attributed to variations in ocean density, caused by a combination of wind, heat and freshwater fluxes changes (Banks et al., 2002; Lowe and Gregory 2006; Suzuki and Ishii, 2011). While the baroclinic component dominates the regional sea level change, the barotropic contribution remains confined in the Southern Ocean and partly in the Arctic region (Lowe and Gregory, 2006; Suzuki and Ishii, 2011). Several regional sea level variation patterns, common to all AOGCMs projections, have been identified: i) a strong sea level increase in the Arctic Ocean, caused by a freshening of the surface layers from enhanced precipitation and continental runoff (Landerer et al., 2007; Yin, 2012); ii) a dipole sea level pattern in the North Atlantic, with an halosteric driven sea level rise in the northern part, due to an increased atmospheric moisture transport from low to high latitudes and the consequent ocean freshening (Landerer et al., 2007), and a sea level fall in the southern part, possibly caused by the weakening of the Atlantic Meridional Overturning Circulation (AMOC) that induces a salinification therein (Yin et al., 2010); iii) a dipole pattern of sea level change in the North Pacific, which consists in a sea level rise in the Kuroshio Current region and its eastward extension and a sea level fall north of it; the increasing sea level has been attributed to a stronger horizontal mass transport in the region (Landerer et al., 2007) and to an increased precipitation (Yin et al., 2010); iv) a sea level fall in the ACC, generally induced by a strengthening of the wind stress, which in turn increases the ACC transport and hence lowers the SSH (Lowe and Gregory, 2006; Landerer et al., 2007; Suzuki and Ishii, 2011; Yin, 2012).

Future sea level variations will have significant impact on the coastal communities, especially in low-lying areas where sea level is rising (Strauss et al. 2012), further strengthened by the foreseen increase in the frequency of storm surge events (Lowe and Gregory, 2005). The tropical western Pacific islands region is particularly concerned about these projections since most of the coastal areas do not exceed 10 meters of elevation above mean sea level. In addition, a large amount of the population of many Small Islands Developing States (SIDS) lives in coastal areas, which makes them extremely vulnerable to sea level rise, storm surges, floods and other climate change-induced hazards.

The majority of sea level change projections previously described are performed with coupled models whose ocean component has a coarse horizontal resolution (1° to 2°). Such a resolution might be not adequate to represent the mesoscale sea level variability and the details of ocean structures, such as western boundary currents and fronts with pronounced horizontal gradients of water properties, important for estimating the geographical pattern of future sea level change. Indeed, Suzuki et al. (2005) showed that the use of an eddy-permitting resolution for the ocean component of their coupled model provides much more detailed ocean structure changes under global warming, with respect to a coarser resolution ocean component.

In light of the above discussion it is now clear that sea level is a key climate parameter, whose change and possible rise should be monitored and predicted for the future. In Chapter 3, we have investigated sea level changes during the last 20 years and we have proved that NEMO-ORCA025 OGCM is an effective tool for detecting and quantifying the sea level spatial and temporal variability. The objective of this Chapter is to extend the sea level investigation in the future, by further using our OGCM for projecting sea level change over the two forthcoming decades and analyzing the global and regional causes of sea level variations. Unlike most of the currently available projections performed by means of coarse resolution coupled model, our projections are performed with an uncoupled ocean model at eddy-permitting resolution, which will represent the added value of our projections with respect to the existing works. The OGCM is forced with atmospheric fluxes provided by the Centro Euro-Mediterraneo per i Cambiamenti Climatici Climate Model (CMCC-CM; Scoccimarro et al., 2011) under the RCP4.5 emission scenario, which is a medium-low stabilization scenario where the total radiative forcing is stabilized before 2100 by a range of strategies for reducing GHG emissions (Clarke et al., 2007). Furthermore, we use two sets of atmospheric forcing, from CMCC-CM simulations, with different ocean initializations. This implies that we are also able to appreciate possible impact of different future atmospheric forcing and, thus, provide an estimate of the uncertainty of sea level projection.

The Chapter is structured as follows: we firstly review the coupled model simulations that provide the atmospheric forcing (Section 5.2) and we give a description of our experiments set up (Section 5.3); in Section 5.4 we show the comparison of model outputs simulation with observational datasets, for the period 2001-2010, in order to validate the use of NEMO-ORCA025 forced by the CMCC-CM atmospheric fluxes. Finally we show and discuss the results of future sea level projections over the period 2011-2030, with focus on the Pacific Small Islands region; differences and similarities between the two simulations will also be highlighted.

5.2- Atmospheric forcing from the CMCC-CM

The atmospheric forcing used in this work consist in a set of decadal predictions performed with the global coupled AOGCM developed at the Centro Euro-Mediterraneo per i Cambiamenti Climatici. These simulations have been produced in the frame of the EU COMBINE Project and further information is detailed in Bellucci et al. (2012). The atmospheric component is ECHAM5 (Roeckner et al., 2003) with a T159 horizontal resolution (about 80 Km) and 31 hybrid vertical levels. OPA8.2 model (Madec et al., 1998) in the ORCA2 configuration is the ocean component. The model makes use of a tripolar grid domain, it has 31 vertical levels and 2° of horizontal resolution that increases equatorward where it reaches a value of 0.5°. The ocean model is also coupled with the Louvain-La-Neuve (LIM) sea-ice model (Fichefet and Morales-Maqueda, 1999).

For our simulations we have used CMCC-CM atmospheric forcing with 3-hourly temporal frequency. Following the CMIP5 protocol the simulations started the 1st of November at 5-year intervals from 1960 to 2005, using CMIP5 radiative forcing conditions for the 1960–2005 period and the RCP4.5 emission scenario for the 2006–2030 period. They consist in a set of 3-member ensemble of 30-year simulations for the starting dates 1960, 1980, 2005 and of 10-year simulations for the remaining dates. The ocean initial conditions are provided by three different ocean reanalyses produced with the same OGCM (OPA8.2) at 2° of horizontal resolution but with different data assimilation system: an Optimal Interpolation (OI, Bellucci et al., 2007) scheme for one of the three reanalyses and a three-dimensional variational data assimilation system (3DVAR1 and 3DVAR2, Dobricic and Pinardi, 2008; Storto et al., 2011) for the other two. The latter two reanalyses differ for the method used to estimate the model error covariances. The use of different ocean reanalyses was found to lead to a sufficiently large spread of the uncertainties of the ocean initial conditions (Bellucci et al., 2012). More details on these ocean reanalyses are explained in Bellucci et al. (2012).

5.3- Experiments set up

Our study consists in three simulations all performed with NEMO-ORCA025 OGCM forced by CMCC-CM atmospheric forcing and initialized with the ocean state of the ALL_CORR simulation described in Chapter 2 (see Table 1 for details). With the ALL_CORR simulation our experiments also share the same ocean model configuration and physical parameterizations. The first experiment is a 10-year (2001-2010) simulation (later called ORCA025-3DVAR1_XX) aiming at validating our configuration through the comparison with independent datasets; the simulation has been performed by using the atmospheric forcing of the CMCC-CM experiment started from the 3DVAR1 reanalysis ocean initial state. Then, two "future" 20-year simulations have been produced for the period 2011-2030; the two projections differ for the CMCC-CM atmospheric forcing used. According to the ocean initial state of the decadal prediction used to force our model, the experiments will be named ORCA025-OI and ORCA025-3DVAR1. This in turn allows us to have a range of uncertainty in our future sea level projections implicit in the uncertainties of the different coupled model simulations.

5.4- Results

5.4.1- Validation and comparison with ALL_CORR simulation

A necessary step before performing future sea level projections is to asses whether the model realistically responds to the coupled model atmospheric forcing, in particular in correctly reproducing sea surface height (SSH) field. Since the sea water temperature is the primary ocean parameter affecting the baroclinic sea level evolution, we have compared the simulated sea surface temperature (SST) and the vertically averaged temperature with observations such as Reynolds SST and EN3 subsurface temperatures, respectively. In the comparison between the simulated and observed time mean SST (Figure 2), we can see that the model presents the same spatial patterns of the SST biases already observed in the CTRL simulation of Chapter 2 (see therein Figure 5), but more pronounced. The reason can be understood by looking at the comparison of downward long-wave (LW) and short-wave (SW) radiations between the CMCC-CM coupled model and ERA-Interim (Figure 3 and 4, respectively), the latter used as atmospheric forcing in the experiment of Chapter 2 .

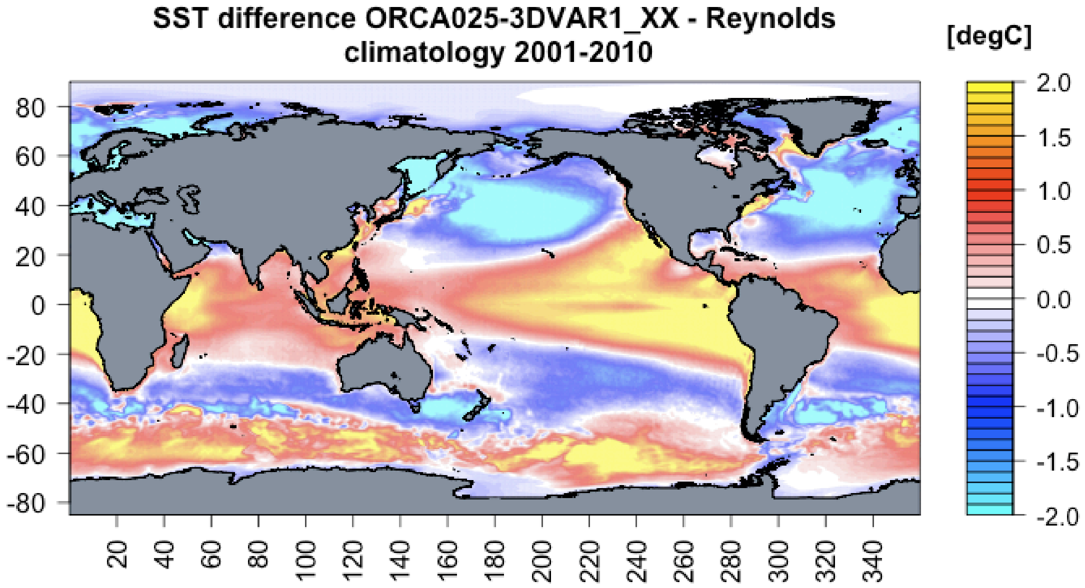

Figure 2– *Difference of SST climatology (2001-2010) between ORCA025-3DVAR1_XX experiment and Reynolds dataset.*

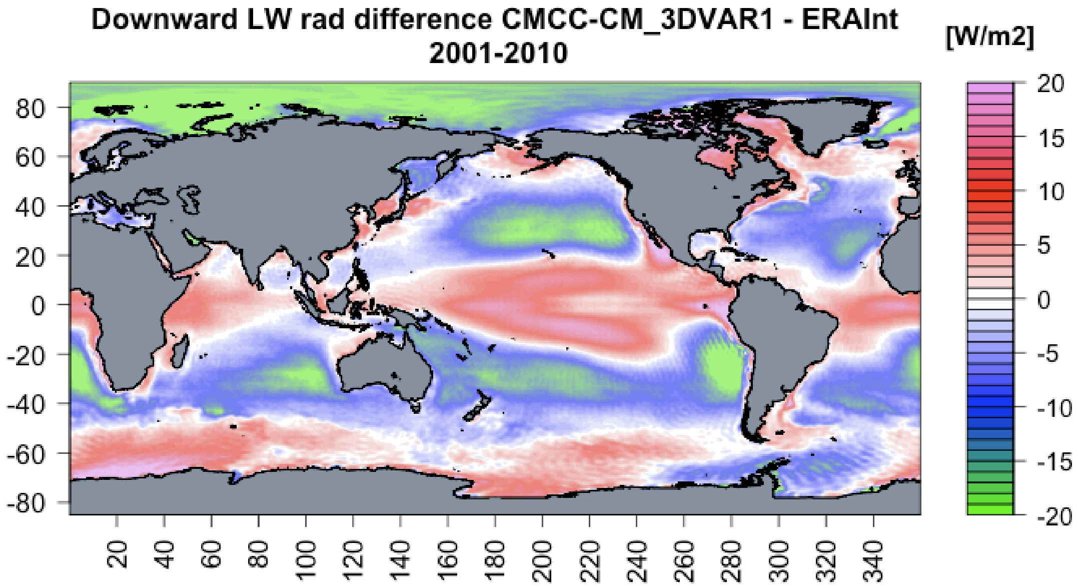

Figure 3- *Difference between CMCC-CM and ERA-Interim 2001-2010 mean downward long-wave radiation.*

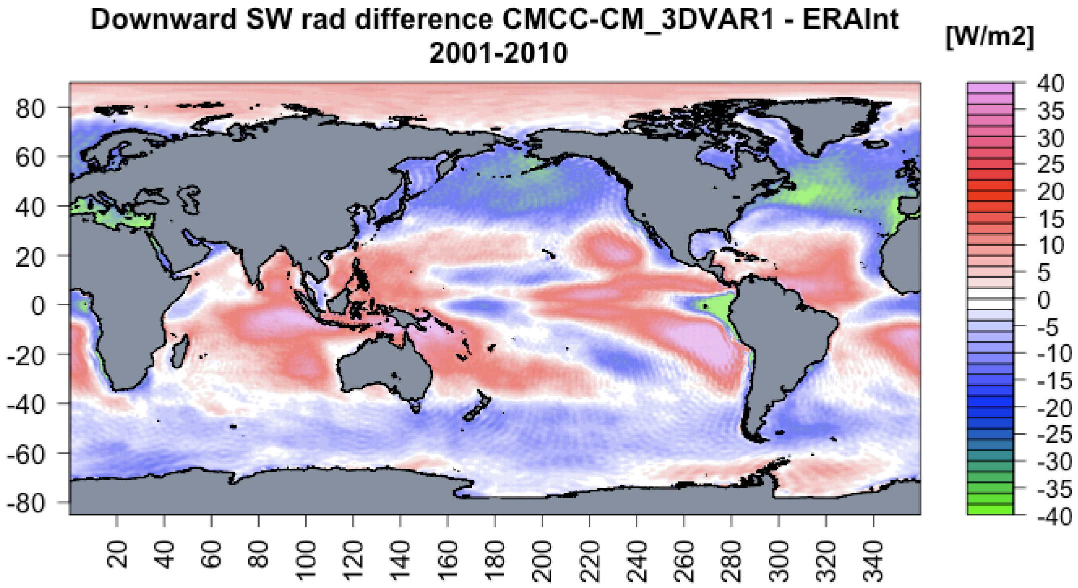

Figure 4- *Difference between CMCC-CM and ERA-Interim 2001-2010 mean downward short-wave radiation.*

We can notice that the larger warm tropical SST biases might be attributed to the higher values of downward LW and SW radiations that the CMCC-CM model exhibits with respect to the ERA-Interim ones. Conversely, the lower values of SW and LW radiations at mid-latitudes lead cold biases, also visible in the CTRL simulation (Chapter 2), although weaker in intensity. The LW radiation also contributes to the warmer ACC bias. Nevertheless the high biases of the model remain steady over the simulation period and do not increase in time. This is true for both the bias and the root mean square error (RMSE) against Reynolds SST for which we show the global (60°S-60°N) monthly means time series (Figure 5).

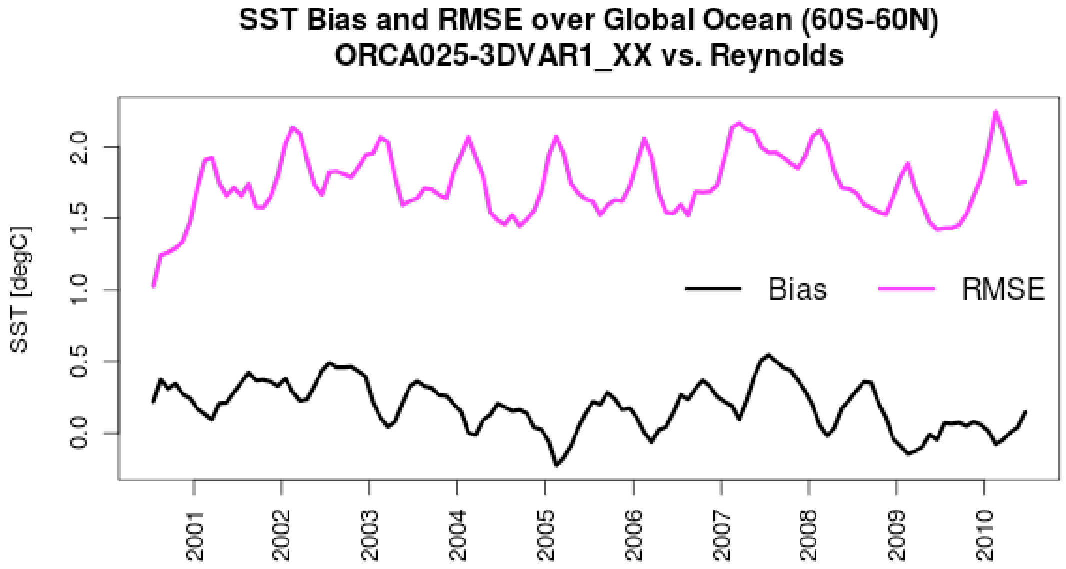

Figure 5- *Time series of monthly SST bias (black) and RMSE (magenta) against Reynolds data (model – observations), averaged between 60S-60N.*

This is a crucial point, since an error increasing with time for the 2001-2010 could compromise the reliability of the future projections; Figure 5 thus suggests that the use of the coupled model forcing causes systematic errors that however remain stable over the time period. Furthermore it is important to underline that not the SST but rather the vertically integrated temperature affects the sea level variability. For this reason we have validated the mean 2001-2010 vertically averaged temperature (only up to 1200 m of depth for scarcity of observations below) with the EN3 objective analyses (Figure 6).

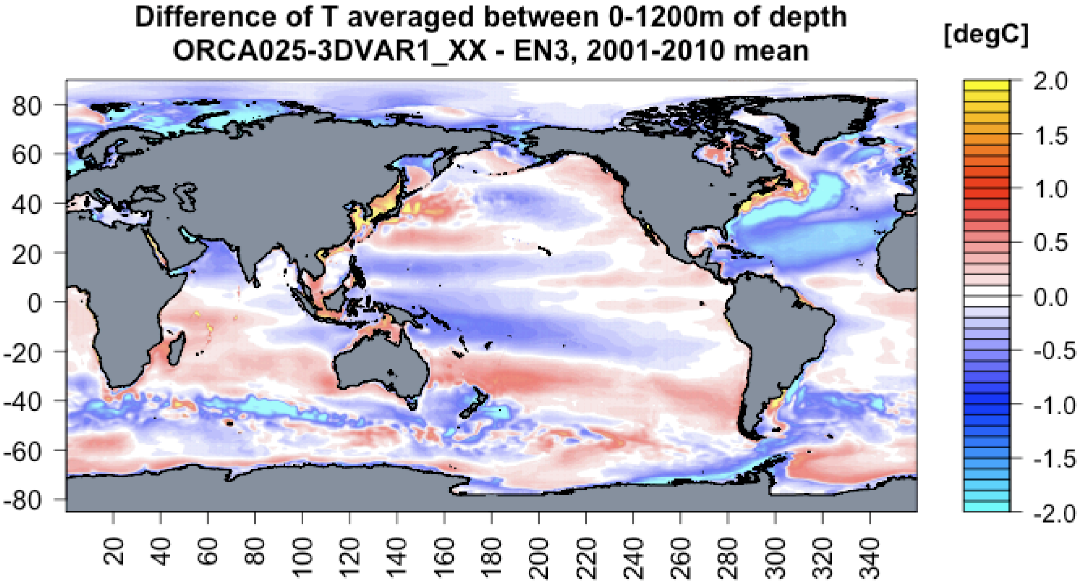

Figure 6- *Difference of 2001-2010 mean temperature averaged from sea surface to 1200 m of depth, between ORCA025-3DVAR1_XX experiment and EN3 objective analysis data.*

Except for the North Atlantic the 0-1200m temperature shows significant lower biases with respect to the SST, which means that possible inconsistencies between the CMCC-CM radiations and our model configuration, even if important at the sea surface, do not have a strong impact at depth, resulting in an averaged temperature in good agreement with observations. This suggests that reliable sea level projections may be achieved with this configuration. The 2001-2010 ORCA025-3DVAR1_XX sea level anomalies, indeed, agree well with AVISO satellite altimetric data in terms of RMSE (Figure 7). The results are highly comparable with our ALL_CORR experiment (Figure 6 of Chapter 4), showing high RMSE only in areas of strong mesoscale activity such as ACC, Gulf Stream, Kuroshio and Falkland Currents and low reasonable values (between 2 and 8 cm) in the rest of the ocean.

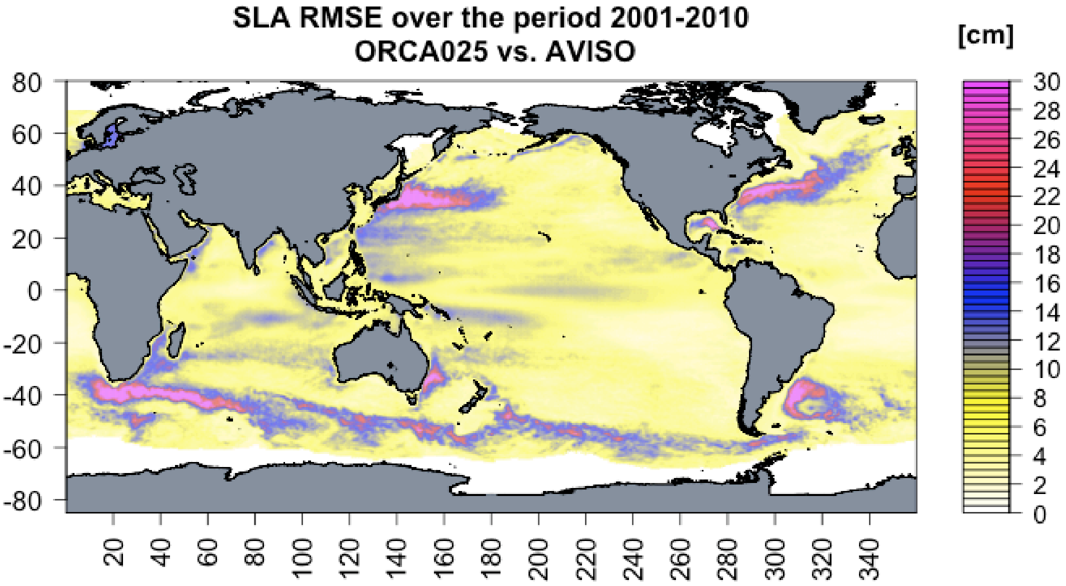

Figure 7- *Sea level anomaly RMSE over the period 2001-2010, ORCA025-3DVAR1_XX experiment against AVISO altimetry data.*

In the comparison with AVISO satellite data (Figure 8) the main sea level trend patterns, over the common period 2001-2010, are reproduced by both the ORCA025-3DVAR1_XX and ALL_CORR experiments. However, the latter simulation performs better, compared to altimetry data, in areas such as the North Atlantic and the West Tropical Pacific Oceans where ORCA025-3DVAR1_XX presents a decreasing sea level trend. Also in the ACC, especially in the South Pacific section, the two simulations present a different sea level tendency (generally, increasing in ORCA025-3DVAR1_XX and decreasing in ALL_CORR) attributable to differences in the intensity of the Westerlies over the Southern Ocean. Indeed, in the ORCA025-3DVAR1_XX experiment the Westerlies induce a weaker wind stress magnitude, with respect to ALL_CORR (Figure 10 bottom panel), in the whole South Pacific and to a lesser extent in the rest of the ACC region. Weaker wind stress results in a slower ACC. In Figure 12, which shows the time series comparison of the 0-1000 m averaged zonal current between the two experiments, we can see that in the ORCA025-3DVAR1_XX simulation the averaged ACC zonal current is slower and decreases during the 2001-2010 period from ~1.9 to 1.5 cm/s. As a consequence of the slower ACC the volume transport reduces from 144.3 Sv (ALL_CORR) to 104.5 Sv (ORCA025-3DVAR1_XX) across the Drake passage section and from 129.7 Sv (ALL_CORR) to 118.2 Sv (ORCA025-3DVAR1_XX) across the Tasmania-Antarctica section. This in turn leads to a rise in the ACC sea level.

The lower Trades wind stress of the ORCA025-3DVAR1_XX run (Figure 10 bottom panel), especially in the East Pacific, induces a slower North and South Equatorial Currents (Figure 11 bottom panel) and hence a reduced transport of near-surface warm water from East to West Tropical Pacific, responsible for the high values of SSH trend in this region. The reduced heat transport in the western Pacific produces a negative thermosteric sea level trend in ORCA025-3DVAR1_XX simulation (Figure 9 top left panel), which prevails on the positive halosteric trend (Figure 9 bottom left panel) hence resulting in a decreasing total sea level (Figure 8 upper panel) in this region. The opposite tendency of the thermosteric and halosteric sea level components is not surprising. In fact, the surface mixed layer of the ocean is often characterized by density compensation between the horizontal temperature and salinity gradients. That is, thermosteric and halosteric components of sea level change tend to compensate in their effect on density (Rudnick and Ferrari, 1999; Ferrari and Paparella, 2003; Levitus et al., 2005). The reason of the increasing halosteric trend in the western Tropical Pacific, not visible in ALL_CORR (Figure 9 bottom right panel), can be also ascribed to higher values of precipitation flux (Figure 13) in the double-Intertropical Convergence Zone (ITCZ), typical of the coupled general circulation models (e.g. Bellucci et al., 2010).

Finally, the cause of the ORCA025-3DVAR1_XX negative SSH trend in the North Atlantic (north of 30°N) is attributable to a more pronounced negative thermosteric trend, with respect to ALL_CORR, caused by the lower CMCC-CM incoming SW radiation in this region with respect to the ERA-Interim one (Figure 4).

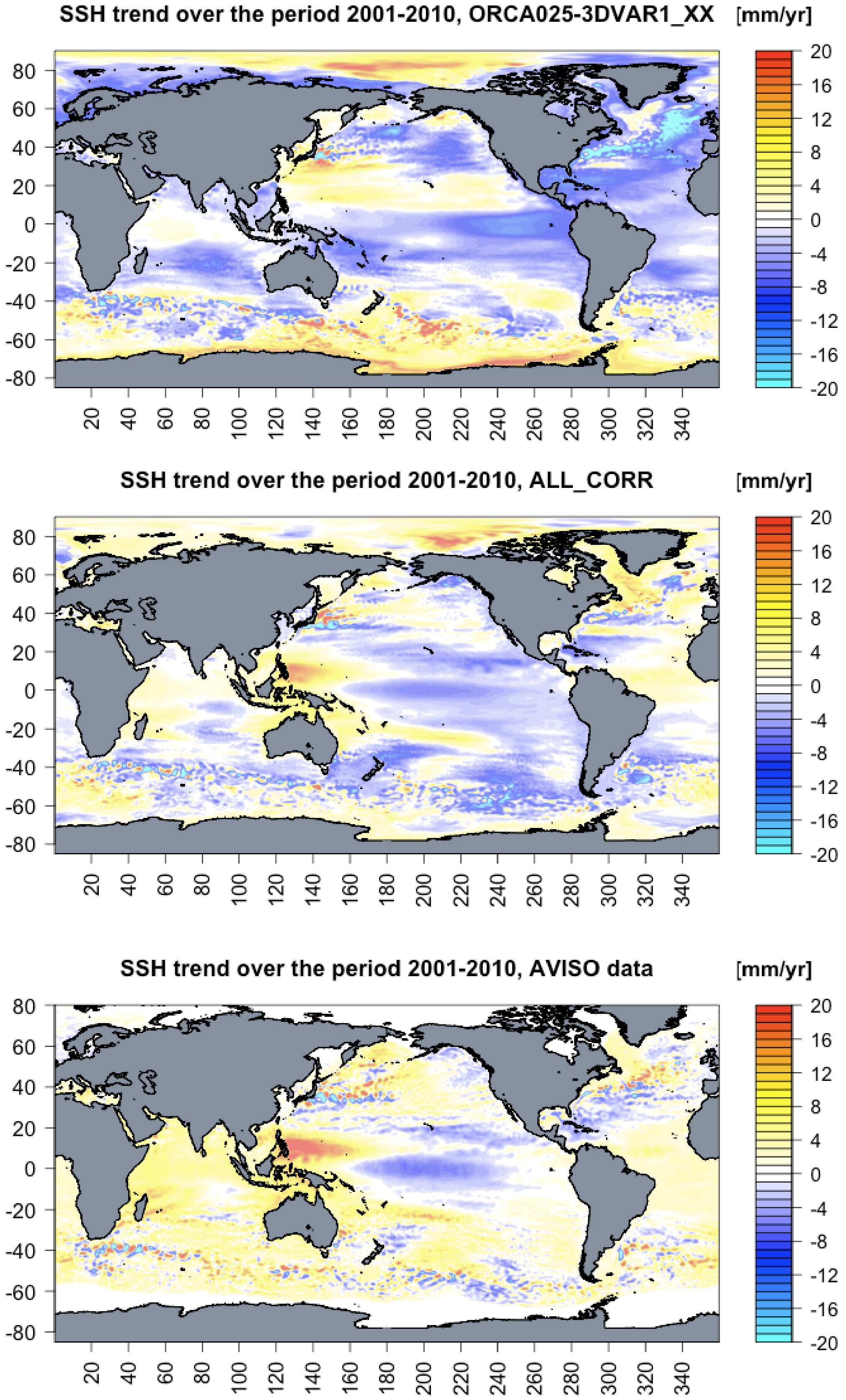
SSH trend over the period 2001-2010, ORCA025-3DVAR1_XX

SSH trend over the period 2001-2010, ALL_CORR

SSH trend over the period 2001-2010, AVISO data

Figure 8- *Maps of sea level trend over the period 2001-2010 from ORCA025-3DVAR1_XX (top) and ALL_CORR (middle) experiments and from AVISO altimetry data (bottom).*

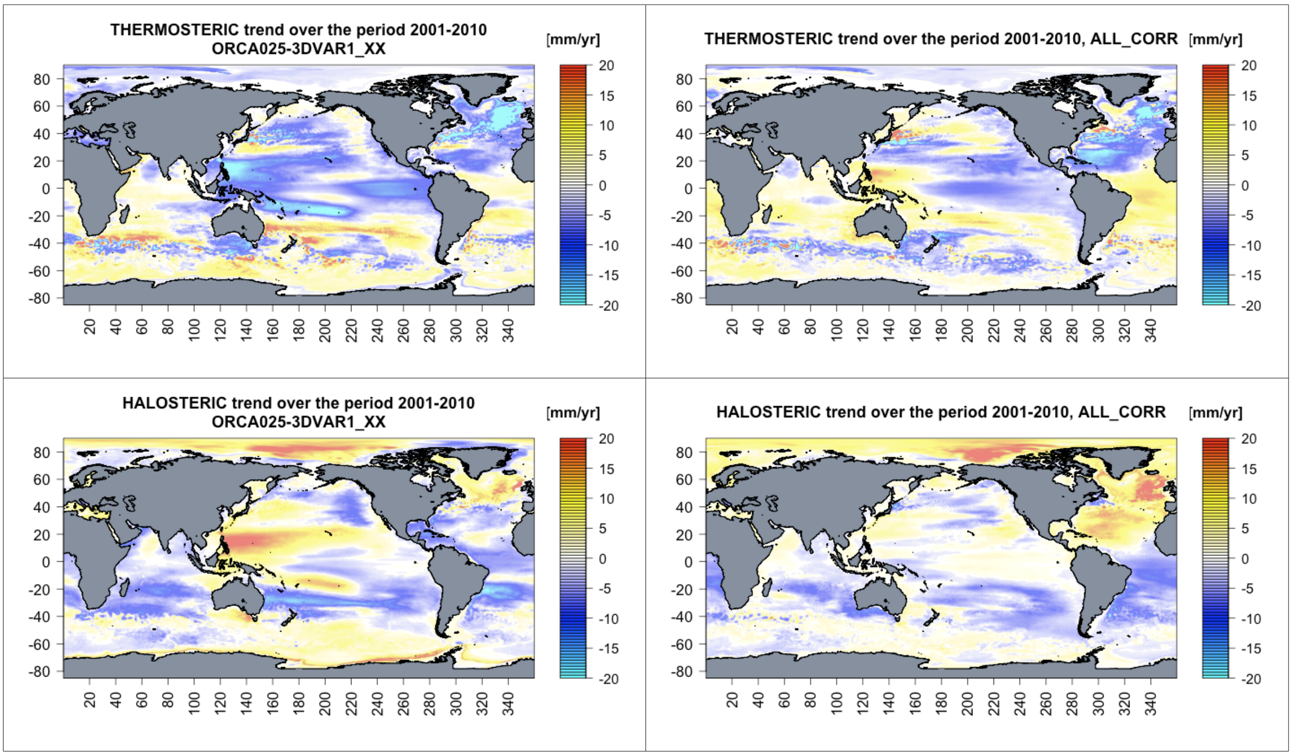

Figure 9- *Maps of thermosteric (top) and halosteric (bottom) sea level trends over the period 2001-2010 from ORCA025-3DVAR1_XX (left) and ALL_CORR (right) experiments.*

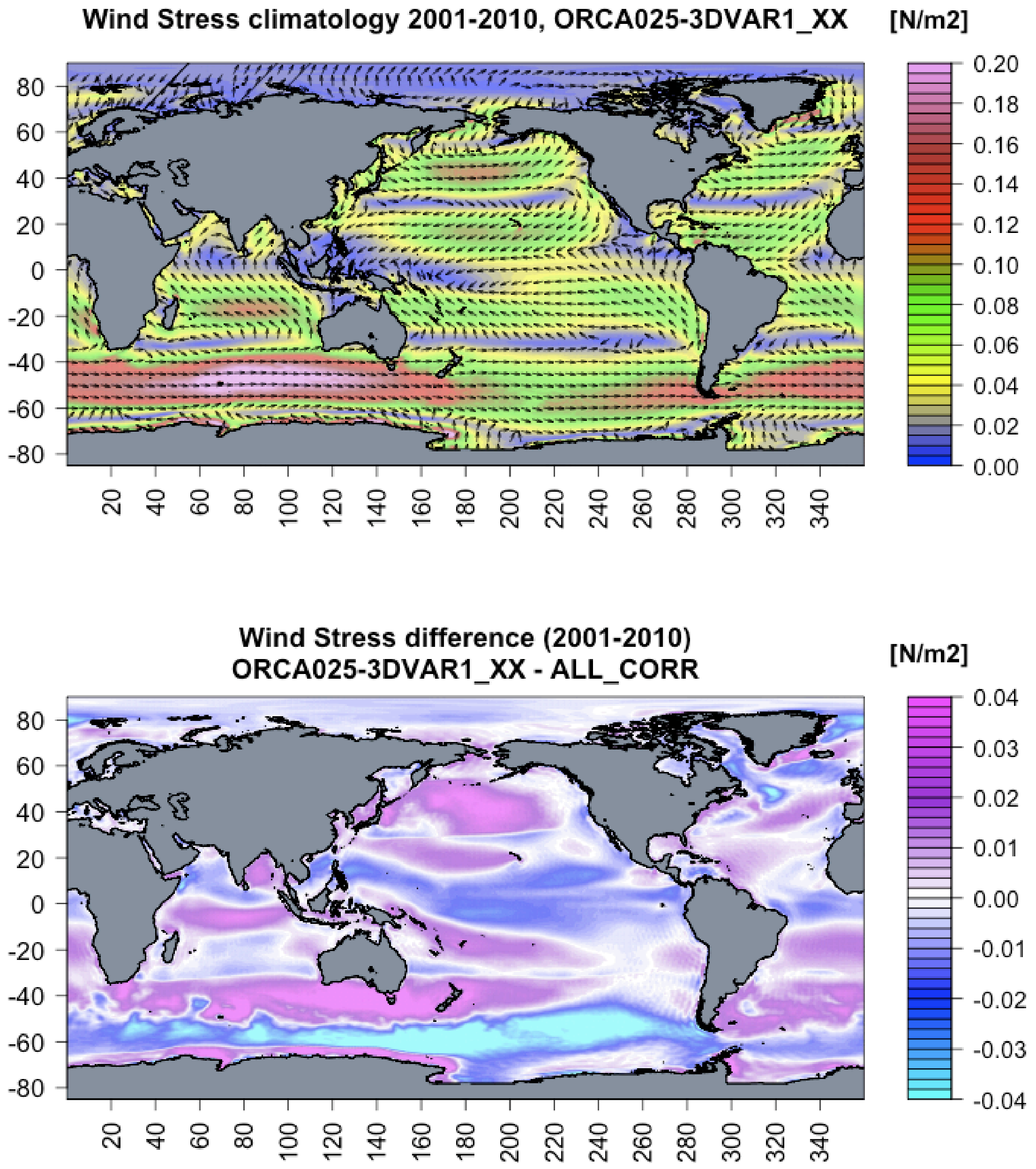

Figure 10- *Top: Wind stress field climatology (2001-2010) for ORCA025-3DVAR1_XX experiment; the colorbar indicates wind stress magnitude. Bottom: wind stress magnitude difference between ORCA025-3DVAR1_XX and ALL_CORR experiments (2001-2010 mean).*

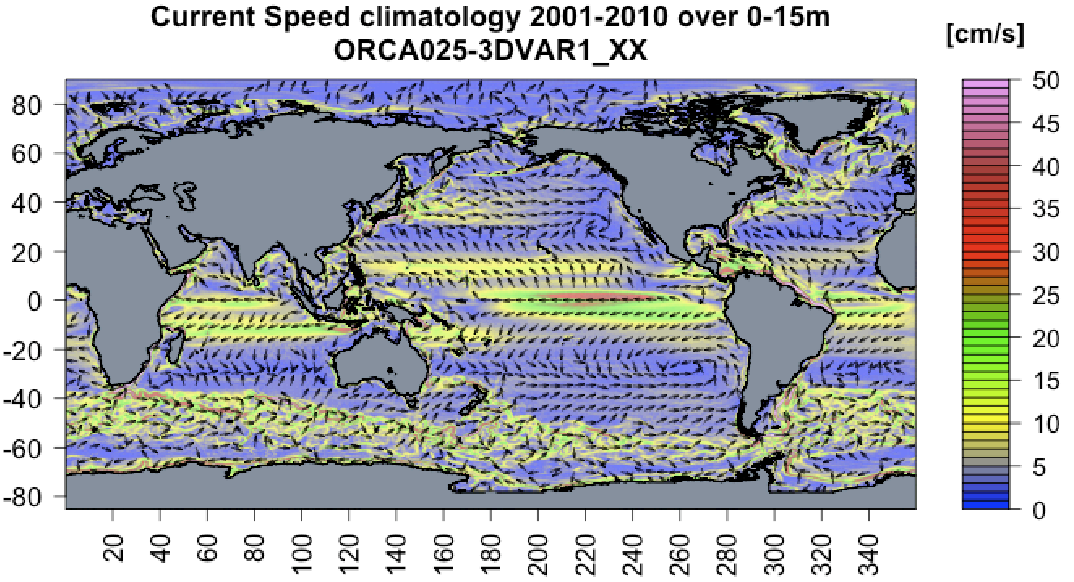

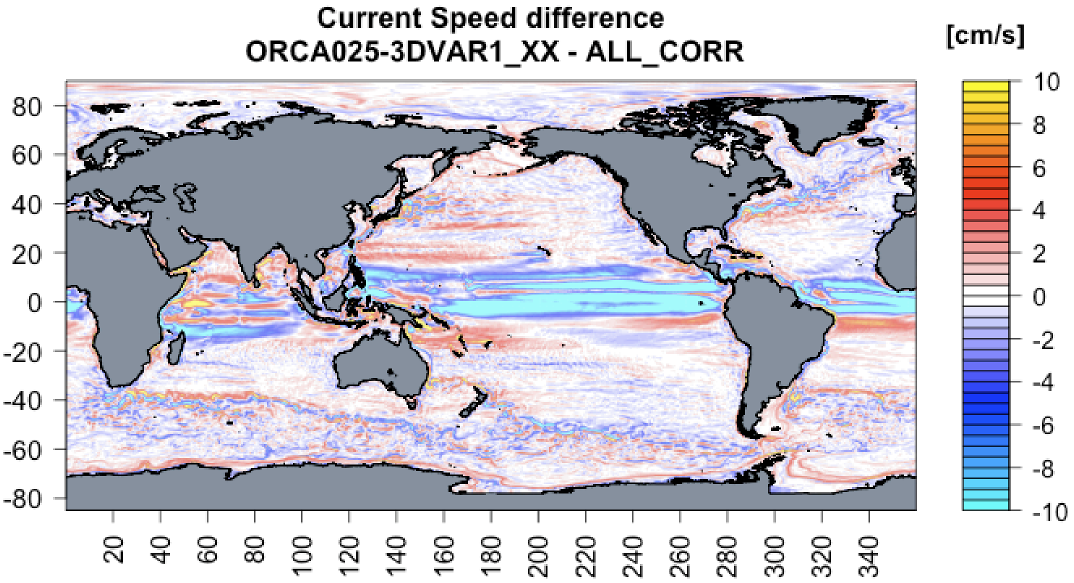

Figure 11- *Top: Velocity field climatology (2001-2010) averaged between 0-15m of depth for ORCA025-3DVAR1_XX experiment; the colorbar indicates current speed magnitude. Bottom: current speed difference between ORCA025-3DVAR1_XX and ALL_CORR experiments (2001-2010 mean).*

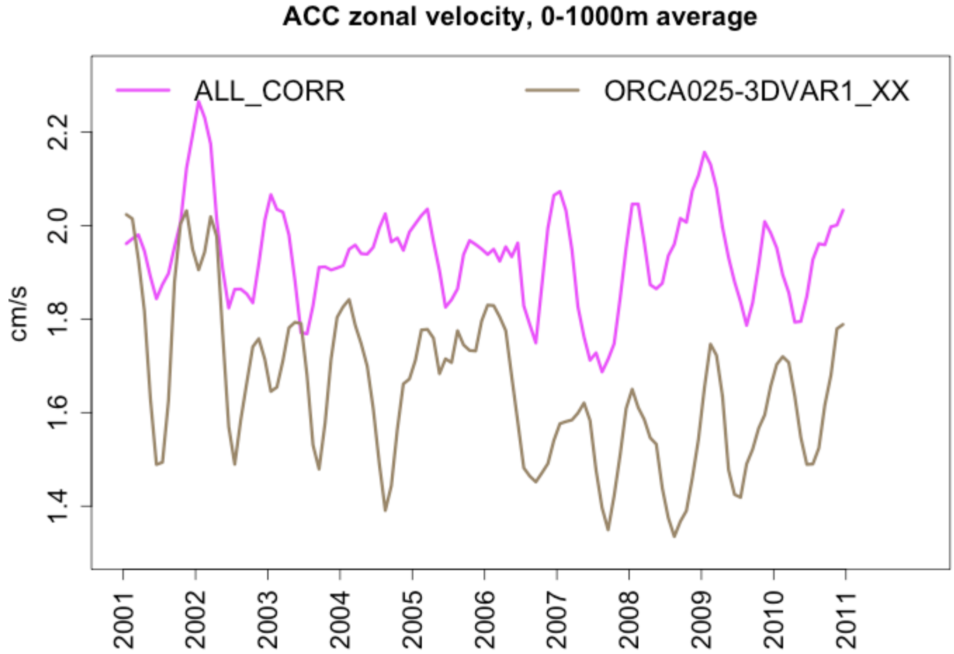

Figure 12- *Time series of the Antarctic Circumpolar Current zonal velocity averaged between 0 and 1000m, for ALL_CORR (magenta line) and ORCA025-3DVAR1_XX (grey line) experiments.*

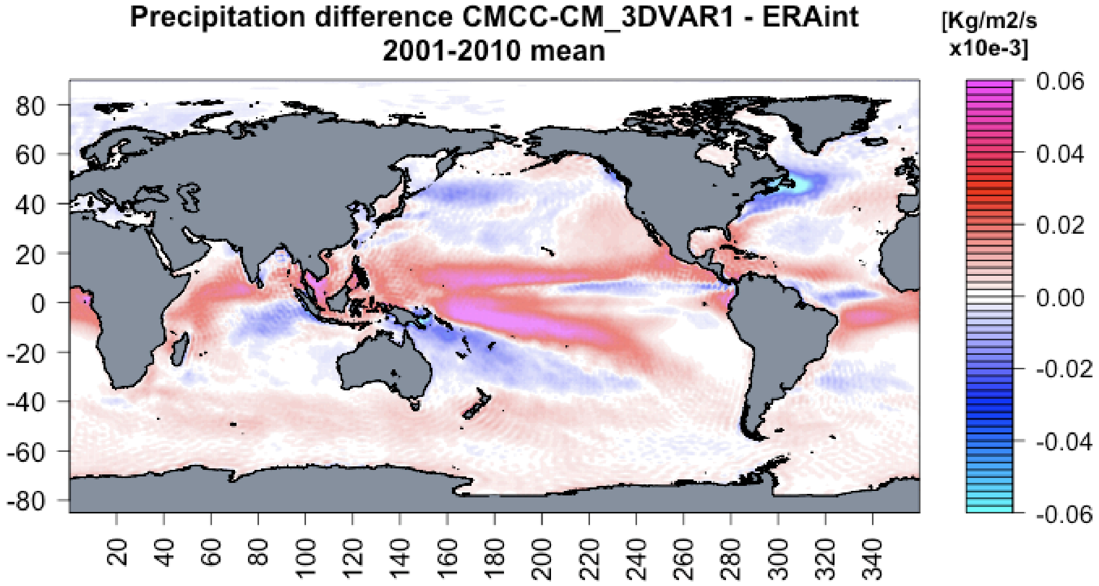

Figure 13- *Difference between CMCC-CM and ERA-Interim 2001-2010 mean precipitation.*

5.4.2- Sea level projections over the next 20 years: Global Ocean

In our simulations, the global-mean sea level due to thermal expansion of the ocean, which is the main contributor to future global-mean sea level rise (IPCC AR4, 2007), is projected to remain rather steady for the first 8 years (Figure 14). Since 2019 the globally-averaged SSH will start to grow and it is projected to rise up to ~1.7 cm by the end of 2030. This magnitude is comparable with the previous works of Suzuki et al. (2005) and Yin (2012), who projected a global ocean thermal expansion, by 2030, of ~2 and ~3 cm, respectively.

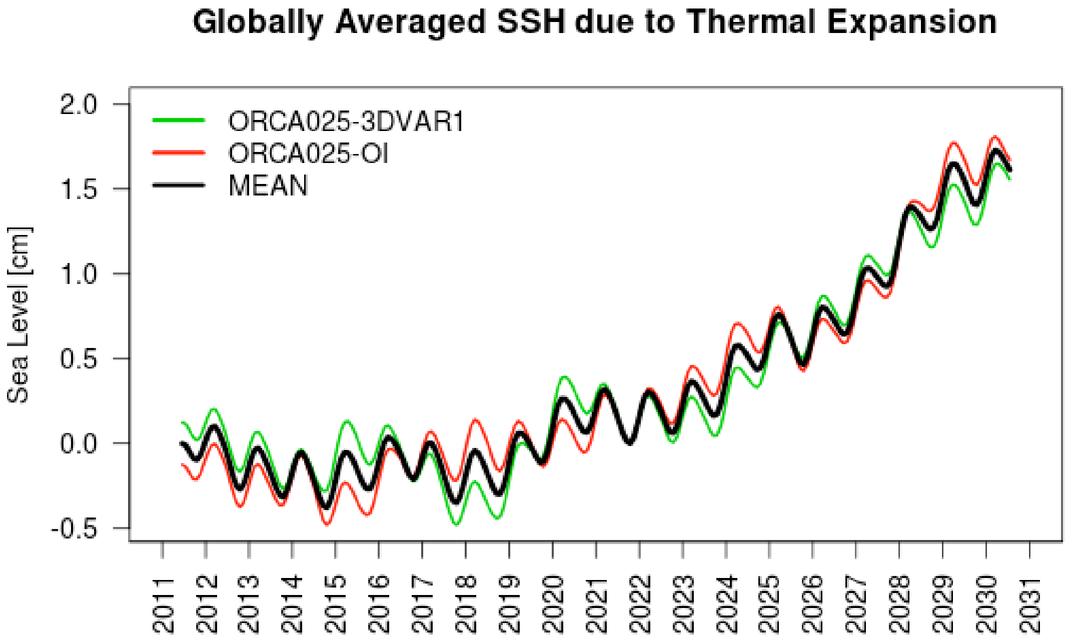

Figure 14- *Globally-averaged sea surface height due to thermal expansion as projected by ORCA025-3DVAR1 (green line) and ORCA025-OI (red line) experiments. The black line shows the mean SSH between the two simulations. An annual running-mean has been applied to the time-series in order to better appreciate the interannual variability of the global-mean SSH.*

While the global ocean thermal expansion reflects the globally-averaged density change of the ocean, this change is not spatially uniform. Similarly to the 1989-2010 period (see Chapter 3), the local SSH trend in the next 20 years will be almost totally explained by its steric component, which resembles the same regional trend features

(Figure 15, top and bottom left panel). While in the last century local sea level changes mainly result from variations in temperature, during the next 20 years the steric spatial changes will be mostly driven by variations in the salinity field (Figure 15, bottom right panel). The thermosteric (Figure 15, top right panel) and halosteric contributions have often opposite local effect on sea level and tend to compensate each other.

As Gregory et al. (2001) and Yin et al. (2010) have pointed out in their comparison between several AOGCMs simulations, there is a significant lack of agreement in the geographical pattern of sea level variations over the 21st century, reflecting the wide range of systematic uncertainties in each of the models considered. Nevertheless, all the current AOGCMs sea level projections agree on some common spatial features, previously discussed in the Introduction. These relevant common patterns appear in our 2011-2030 sea level projections as well.

Figure 15 (top left panel) shows the sea level trend over the period 2011-2030 from ORCA025-3DVAR1 experiment. In the Pacific Ocean the most prominent feature is a pronounced local sea level rise in the Kuroshio Current and its extension and a sea level fall to the north, resulting in the dipole SSH pattern common to most of the AOGCMs sea level projections (Lowe and Gregory, 2006; Landerer et al., 2007; Suzuki and Ishii, 2011; Yin, 2012); a sea level fall is also visible to the south, off the Indonesian coasts. The sea level rise in the North Pacific Ocean is consistent with an upper-ocean freshening, which results in the halosteric sea level rise in the subtropical gyre visible in Figure 15 (bottom right panel). The freshening is due to an increase of precipitation between the equator and 20°N (Figure 16), probably also caused by a northward displacement of the ITCZ, which is redistributed in the whole North Pacific by the southern branch of the subtropical gyre. On the contrary the precipitation is expected to decrease in the equatorial Indian Ocean with a consequent negative halosteric trend and hence a sea level drop therein. Another relevant feature of spatial sea level change in the next two decades is a north-south dipole pattern in

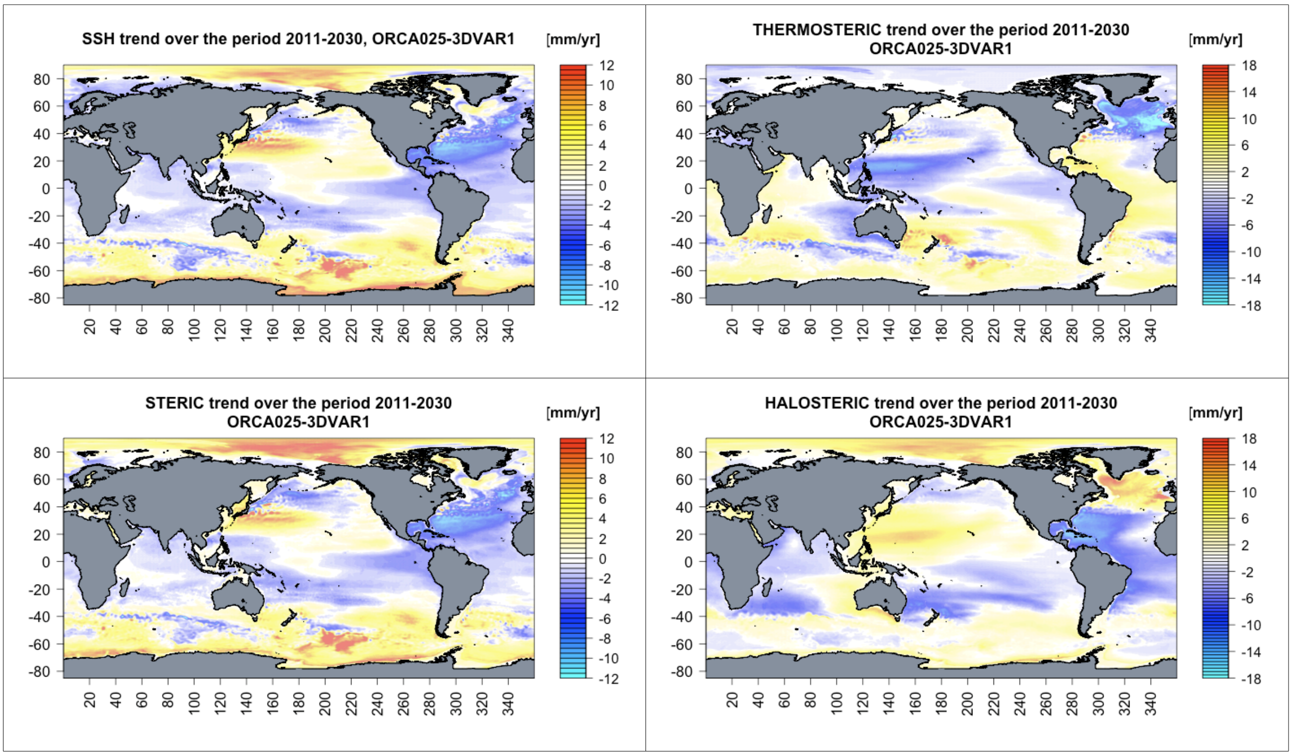

Figure 15- *Maps of projected sea level trend (top left) and its steric (bottom left), thermosteric (top right) and halosteric (bottom right) trend components for 2011-2030 period, from ORCA025-3DVAR1 experiment.*

the North Atlantic, with a rise in the subpolar gyre, north of the Gulf Stream, and a fall in the subtropical region. The dipole pattern is determined by the halosteric trend, which increases in the northern part and decreases in the southern part of the dipole (Figure 15, bottom right panel). The halosteric component tends to prevail on the thermosteric one, which shows an opposite behavior, decreasing in the north and increasing in the south (Figure 15, top right panel). The spatial patterns of the thermosteric and halosteric components in the North Atlantic, are attributable to a deceleration of the North Atlantic subtropical gyre, which is in turn induced by a projected slowdown of the westerlies in the next 20 years (Figure 17). The westward and eastward branches of the gyre show in fact a slowing down of the zonal velocities of ~ 2 cm/s in 20 years (Figure 18 top and bottom panels, respectively). The slowdown of the North Atlantic subtropical gyre results in a reduction of the northward transport of warm and salty waters. In particular, in correspondence of a zonal section taken off coasts of Florida, the northward volume transport is projected to decrease with a rate of -0.3 Sv/yr in the 2011-2030 period, with a consequent reduction of the heat transport (-12 TW/yr) and increase of the freshwater transport (0.02 Sv/yr). Unlike other sea level projections (Yin et al., 2010), in our simulations the thermohaline circulation does not significantly vary in response of future global warming; hence the North Atlantic salinification, in the southern part of the dipole, is driven by the slowdown of the subtropical gyre and not by the weakening of the AMOC, which remains constant at 10 Sv (at 26°N) and it does not show any significant trend. Probably, 20 years of simulation is a too short time span in order to appreciate the weakening of the AMOC. Differently from previous studies, in our projections the ACC region shows a general increasing sea level trend, with peaks in the Pacific sector, mainly attributable to a thermosteric sea level rise within the region. Furthermore, a freshening in the Southern Ocean leads to a positive halosteric sea level trend that strengthens the effect of the positive thermosteric contribution. A strong sea level rise (up to 12 mm/yr) is also projected, in accordance with previous studies (Lowe and Gregory, 2006; Landerer et al., 2007; Suzuki and Ishii, 2011; Yin, 2012), in the Arctic Ocean, which is caused by a surplus of freshwater in the region. In fact, during the 2011-2030 period the net surface freshwater flux (138.9 mSv) will not be balanced by the total outgoing lateral freshwater transport (-103.5 mSv) (see Table 1), resulting in a positive halosteric trend (Figure 15, bottom right panel) and a consequent steric sea level rise. In particular, the main source of the surplus of freshwater in the Arctic region (35.4 mSv) will be the sea-ice melting, which represents the 76% of the net surface freshwater flux, and will further increase at a rate of 1.27 mSv/yr during the next 20 years.

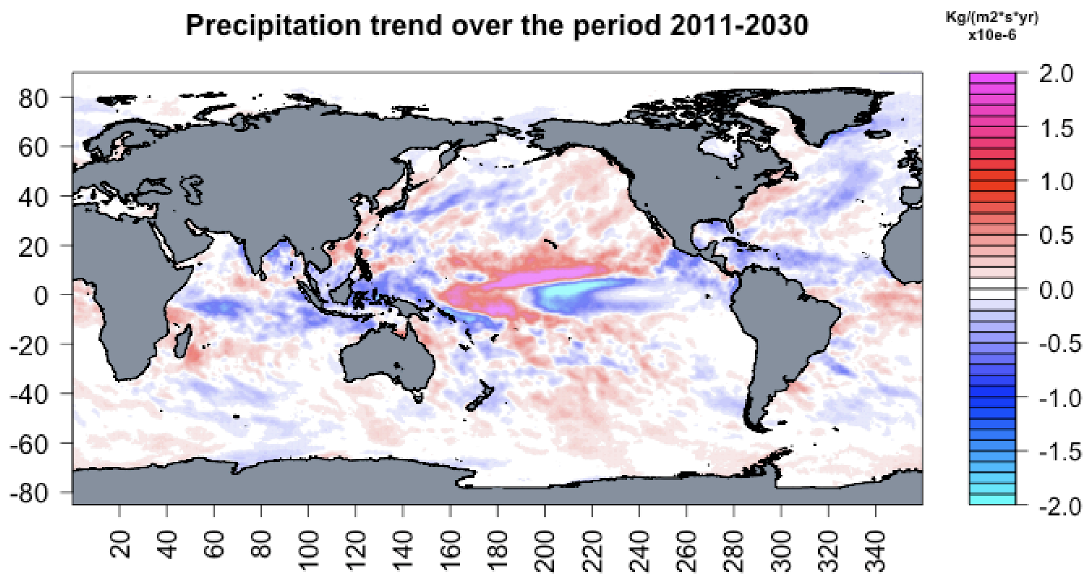

Figure 16- *Precipitation trend over 2011-2030 period from ORCA025-3DVAR1 forcing data. Units are* $Kg*m^{-2}*s^{-1}*yr^{-1}10^{-6}$

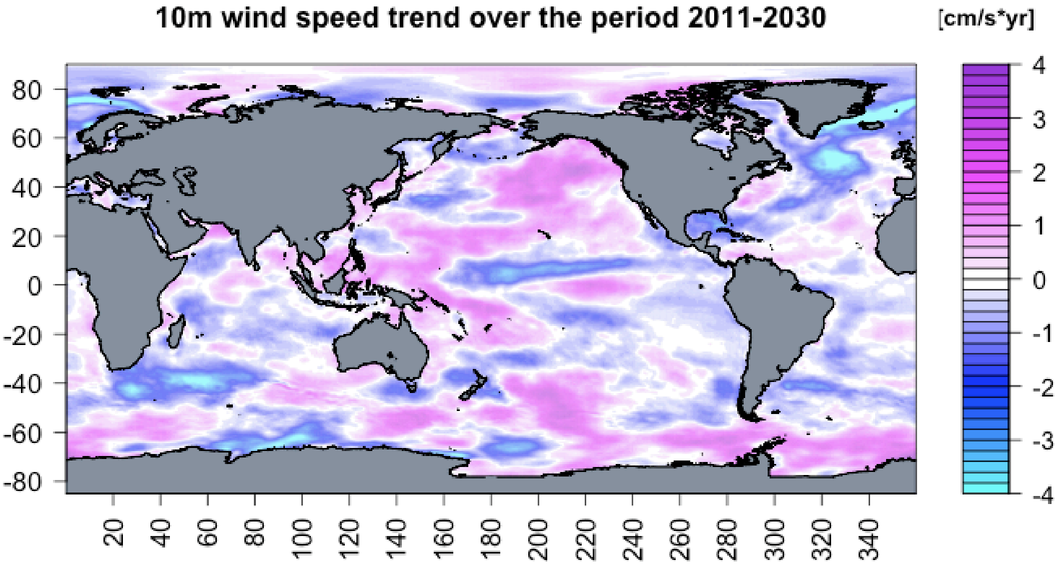

Figure 17- *Trend of wind speed at 10m over the period 2011-2030, from ORCA025-3DVAR1 forcing data.*

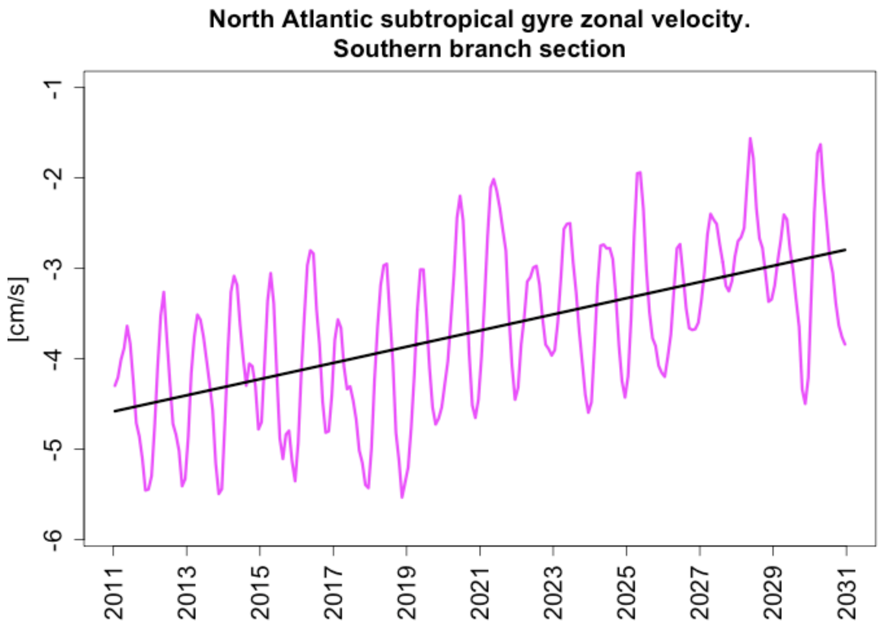

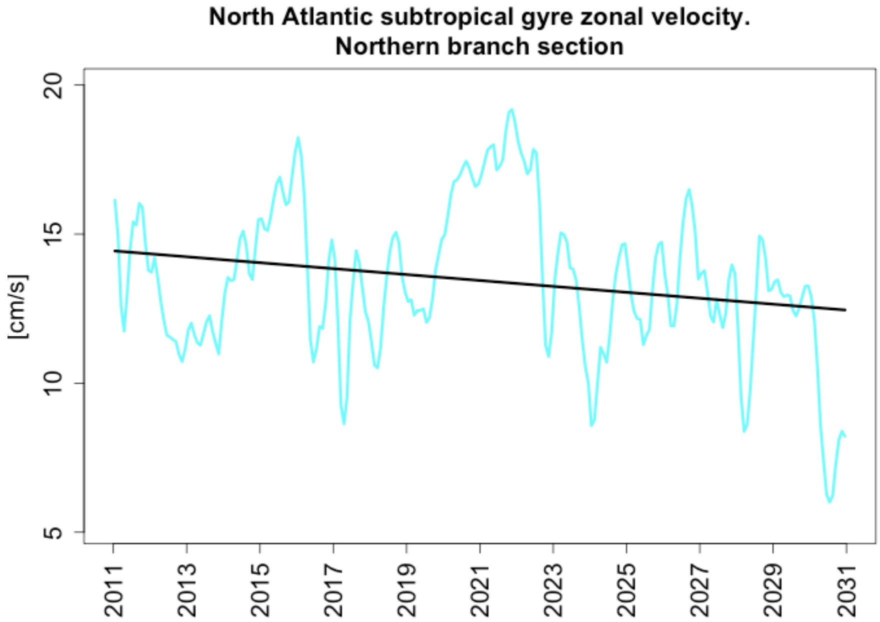

Figure 18- *North Atlantic subtropical gyre zonal velocities (0-200 m mean) averaged over a southern (top panel) and a northern (bottom panel) meridional sections. The two sections are taken in correspondence of the westward and eastward branches of the gyre, respectively.*

5.4.3- Comparison between different future projections

As a starting point for the comparison between the ORCA025-3DVAR1 and ORCA025-OI projections, we have analysed the Root Mean Square Deviation (RMSD) between them. The sea level RMSD shows generally low values, between 2 and 4 cm, in most of the global ocean, indicating a low mismatch between the two projections. However, some large differences can be noticed where sea level variability is strong, i.e. in areas of strong mesoscale dynamics (ACC, Kuroshio, Gulf Stream, Falkland Current), which present the largest values of RMSD, up to 30 cm (Figure 19, top panel). Also the Tropical Pacific presents high SSH spread values (~10 cm). This feature can be attributed to differences in the atmospheric moisture and cloudiness between the two CMCC-CM simulations, which in turn affect the radiative fluxes (especially the solar radiation) and the precipitation, the former impacting the thermosteric spread while the latter the halosteric one. In fact, we found large values of short-wave and precipitation spread in correspondence of the Tropical Pacific region (Figure 20 top and bottom panels, respectively), the former peaking at 40 $\frac{W}{m^2}$ in correspondence of the western Pacific ITCZ. However, the spatial SSH RMSD between the two projections, in the 2011-2030 period, is almost totally explained by the themosteric sea level contribution (Figure 19, middle panel), while the halosteric component spread is quite low in the whole global ocean (Figure 19, bottom panel).

Figure 21 shows the globally averaged RMSD for all the sea level components. It can be seen that in only one year from the simulations beginning the sea level spread grows broadly, moving from about 2 to 7 cm, while at the end of the projections it is grown of only another 3 cm, thus reaching 10 cm. Interestingly, the thermosteric and halosteric components reach about 8 and 3 cm, respectively, after 3 years of projections and remain constant afterwards. While the behaviour of the halosteric component spread is rather flat during the time period, the thermosteric component is slightly noisy due to the variability of the surface heat fluxes. In particular, the spread in the temperature fields is generally contained in the first 200 to 300 m of depth (not shown). The peak in the SSH RMSD during the 2021-2024 years is due to an increase of spread contained in the eustatic component, which we found to be primarily due to local increased spread of the wind forcing, especially in the Southern Ocean (not shown). These results suggest that there exist mainly two mechanisms responsible for the sea level spread variability during the projections time period: the first one linked to radiative forcing variability, which is the main responsible for the SSH spread magnitude but gets almost steady after 3 years from the beginning of the simulation and does not vary significantly afterwards, and a second one linked to the wind forcing and hence to the local circulation variability, which has a more variable behaviour due to the consequent water mass redistribution within the ocean.

In terms of sea level regional trends, the comparison between the ORCA025-3DVAR1 and ORCA025-OI experiments reveals a general agreement between the two projections. Both the experiments, in fact, reproduce the main sea level spatial features (Figure 15 top left panel and Figure 22 top panel). Differences between the two projections are visible in the Tropical Pacific: the ORCA025-OI shows a stronger thermosteric sea level fall in the eastern Tropical Pacific, while in the western Pacific the negative thermosteric trend is more pronounced in ORCA025-3DVAR1 (Figure 15 top right panel and Figure 22 bottom panel). This is likely to be due to differences in the radiative flux, mentioned above, and the consequent heat redistribution within the tropical ocean.

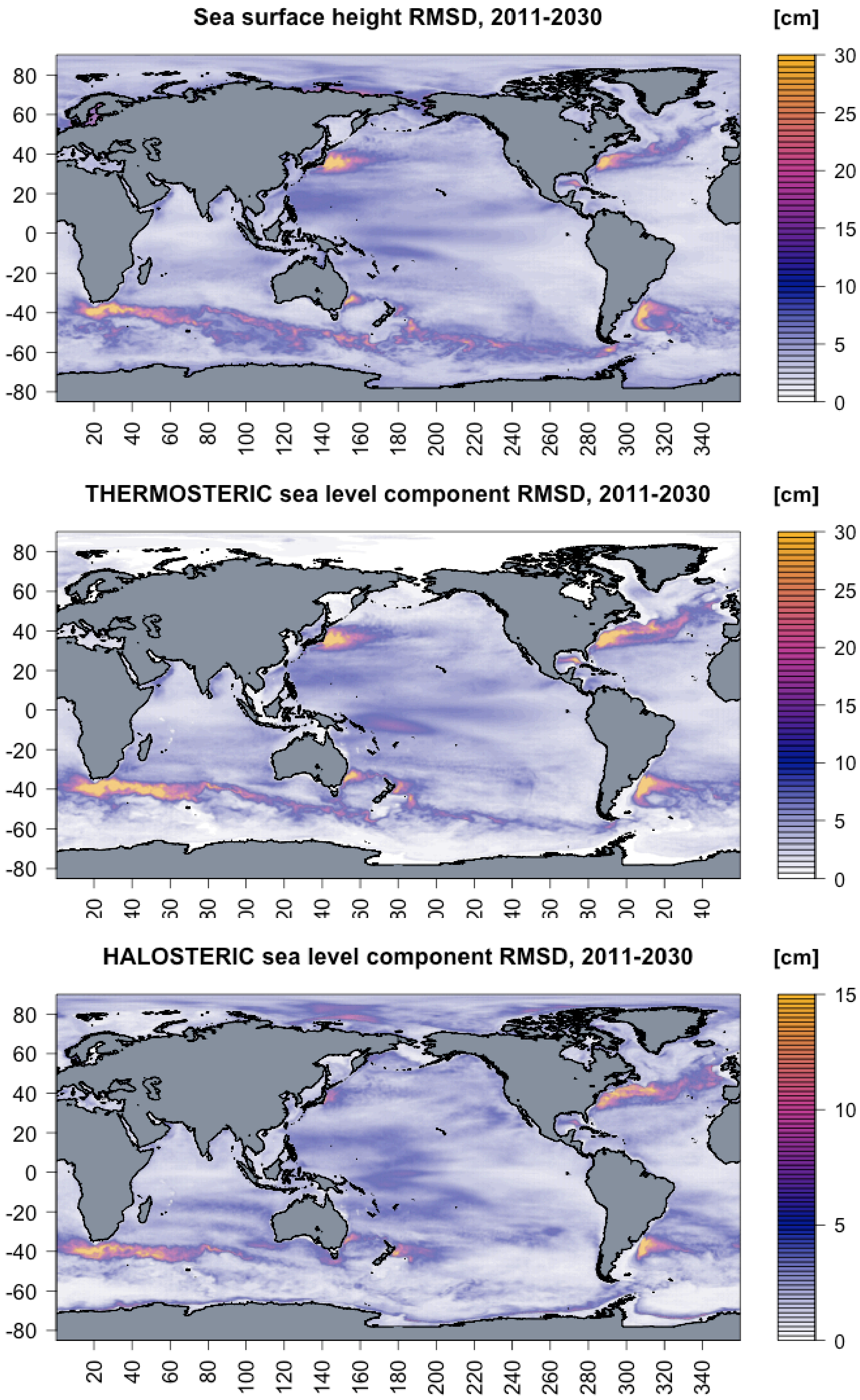

Figure 19- *SSH (top), themosteric (middle) and halosteric (bottom) Root Mean Square Difference between ORCA025-3DVAR1 and ORCA025-OI projections, for the period 2011-2030. Note the different palette in the halosteric map.*

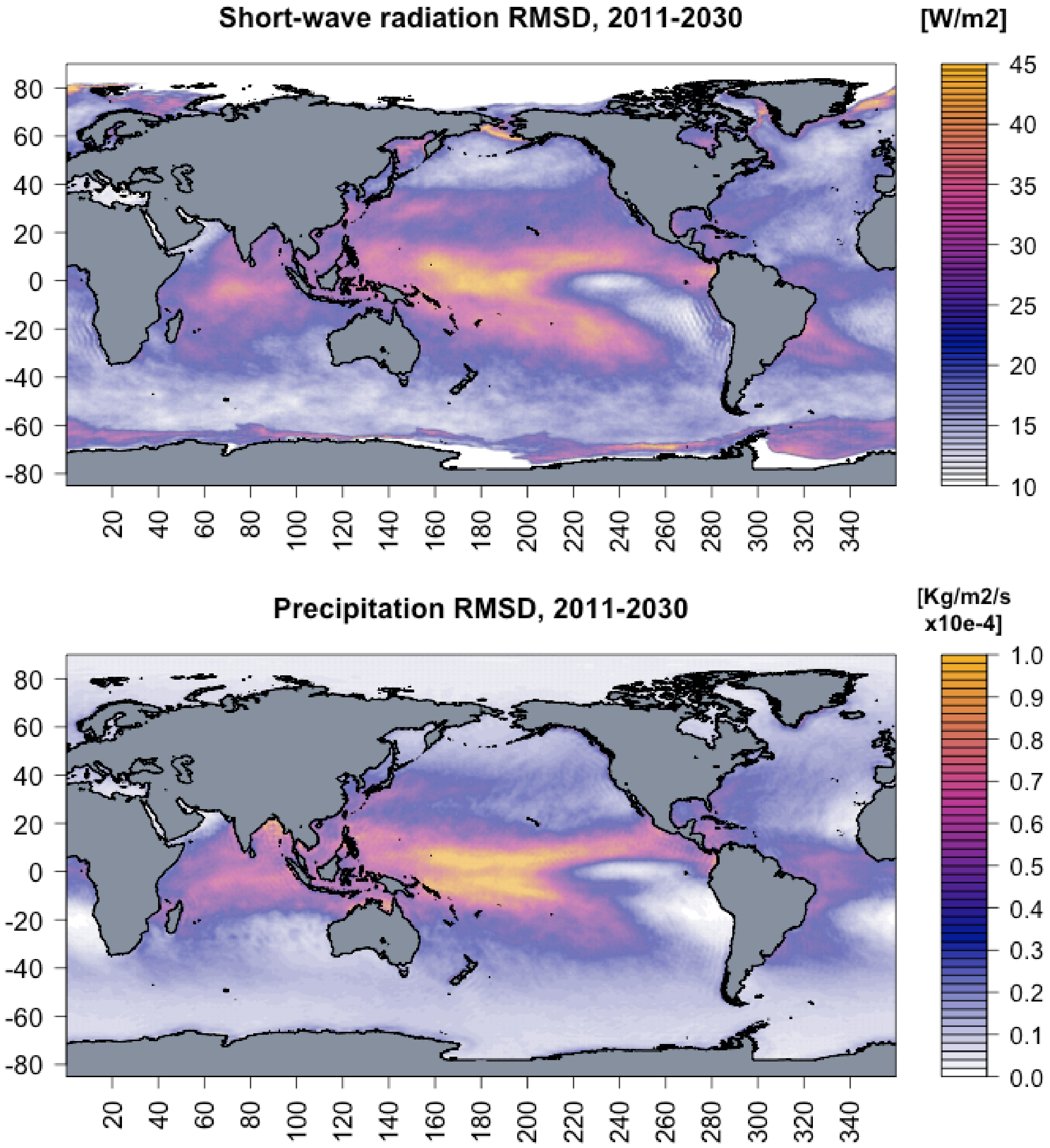

Figure 20- *Short-wave radiation (top) and precipitation (bottom) Root Mean Square Difference between ORCA025-3DVAR1 and ORCA025-OI forcing data, for the period 2011-2030.*

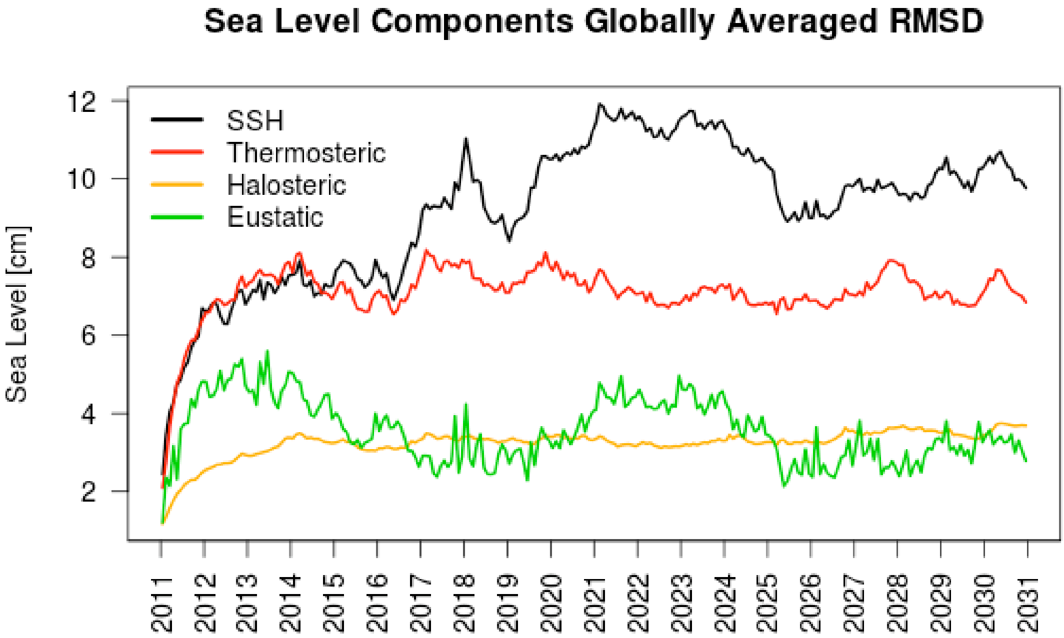

Figure 21- *Globally-averaged RMSD between ORCA025-3DVAR1 and ORCA025-OI simulations of SSH (black line), thermosteric (red line), halosteric (yellow line) and eustatic (green line) sea level components.*

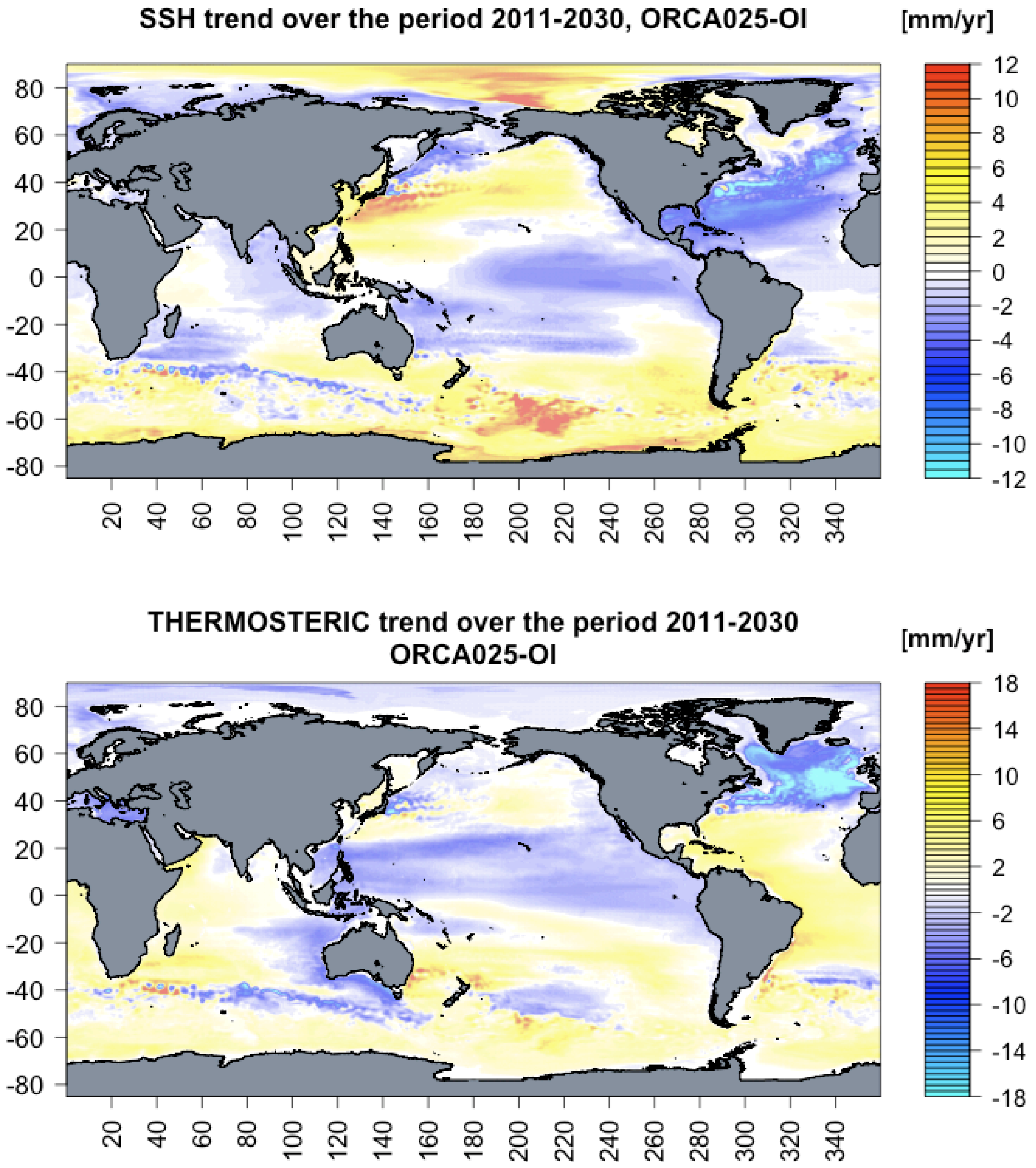

Figure 22- *Maps of projected sea level trend (top) and thermosteric (bottom) trend component for 2011-2030 period, from ORCA025-OI experiment.*

5.4.4- Sea level projections over the next 20 years: Pacific Small Islands region

The western Tropical Pacific is the oceanic area where the two projections mostly diverge in terms of regional sea level trend. Hence, the future projection of sea level change in the Pacific Small Islands region is affected by uncertainties at some islands location. In ORCA025-3DVAR1, the sea level trend is positive north of 18°N, with peaks of 7-8 mm/yr, and it decreases southward reaching values of 1-3 mm/yr in the eastern part and turning to negative in the western part of the domain; south of 10°S the sea level trend is negative with peaks of -4 mm/yr (Figure 23, top panels). On the contrary, in the ORCA025-OI simulation, the sea level is projected to rise almost everywhere north of 4°S, with peaks of 7-8 mm/yr, while it falls in the southern part of the domain. The SSH variations over the next 20 years will almost entirely result from changes in sea water density in terms of both trend and annual cycle (not shown). In particular, the sea level rise which dominates north of 4°S, is attributable to a freshening of sea water induced by a net incoming lateral freshwater transport within the region, resulting in a positive halosteric trend (Figure 23, bottom panels) which prevails on the negative thermosteric trend (Figure 23, middle panels). The regional cooling is induced by a loss of heat from the lateral boundaries of the domain, which in ORCA025-3DVAR1 is more intense with respect to ORCA025-OI. This is not compensated by the halosteric sea level rise, producing a sea level fall in the western part of the domain north of 10°S. The contribution of the heat and freshwater transports to sea level trend have been summarised in Table 2. While the West Tropical Pacific freshening is caused by an increase of precipitation in the ITCZ (Figure 16), the cooling is likely to be due to a slowdown of Trade winds (Figure 17) and the consequent deceleration of the South Equatorial Current (not shown), thus reducing the transport of near-surface warm waters from East to West Tropical Pacific.

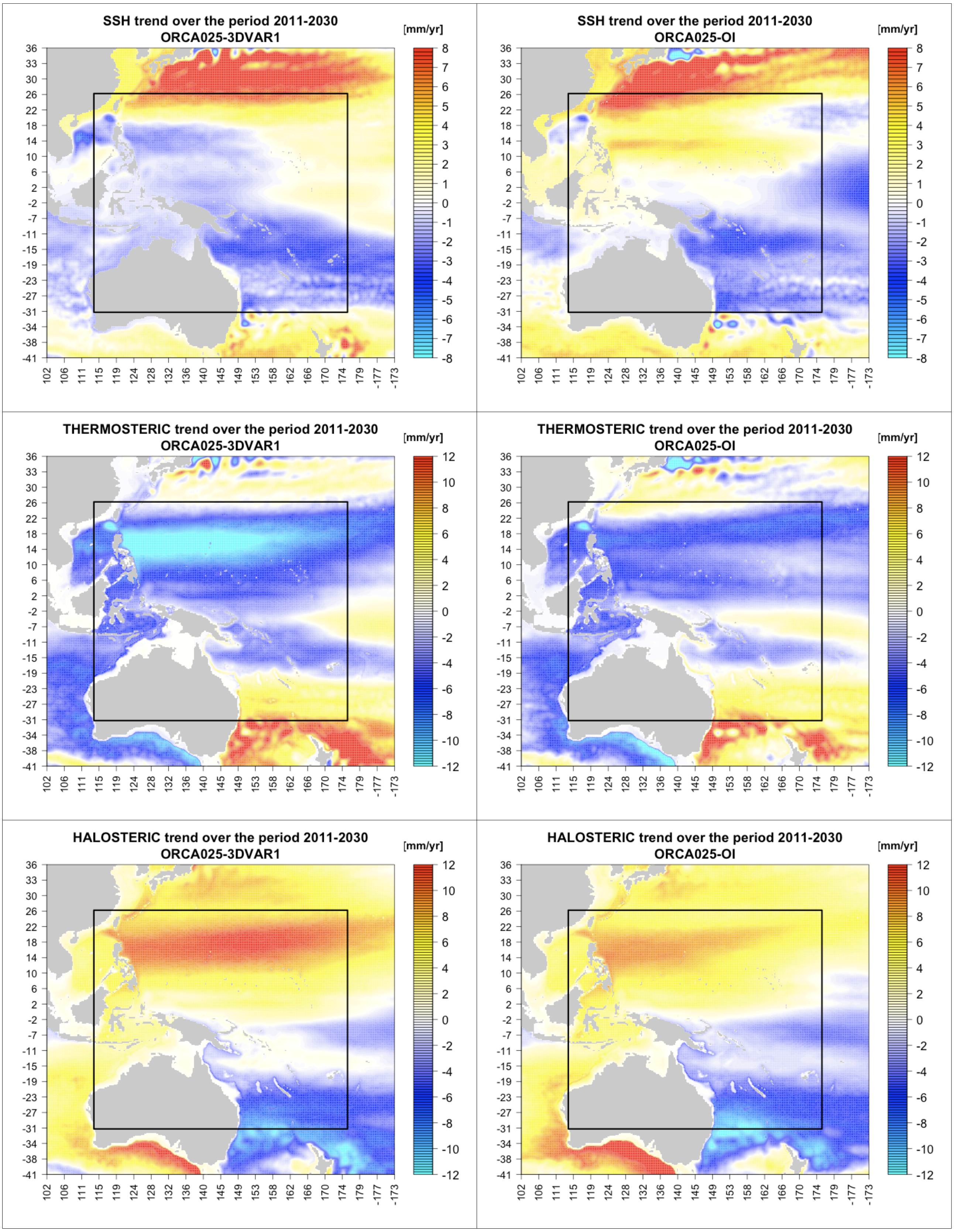

Figure 23- *Projection of sea level trend (top), thermosteric (middle) and halosteric (bottom) components trend for the period 2011-2030, from ORCA025-3DVAR1 (left) and ORCA025-OI (right) experiments. The black rectangle represent the boundaries of the Pacific Small Islands area.*

To quantify the potential impact of future sea level change on coastal areas, we have analyzed the projected SSH trend in correspondence of nine selected Small Islands Developing States (SIDS) (Figure 24). The island locations have been reported in Figure 21 of Chapter 3. In our projections, Palau, Micronesia and Marshall Island, according to ORCA025-OI, and Kiribati, Nauru and Marshall Island, according to ORCA025-3DVAR1, might suffer the impacts of sea level rise in the next 20 years (up to 1.2 mm/yr), while the other islands show a sea level drop. However, only Marshall Island exhibits a positive sea level trend in both the simulations, while the projections agree on predicting a sea level fall for Tuvalu, Samoa, Tonga and Fiji. Those particular zooms on the selected SIDS indicate that in our simulations, the majority of the sites will experience a sea level fall in the next two decades, with a wide range of uncertainties in correspondence of Palau, Micronesia, Kiribati and Nauru, where the two simulations project opposite sea level trends. This suggest that for the northernmost SIDS it is difficult to reach a robust conclusion about future sea level change, due to uncertainties among the two projections.

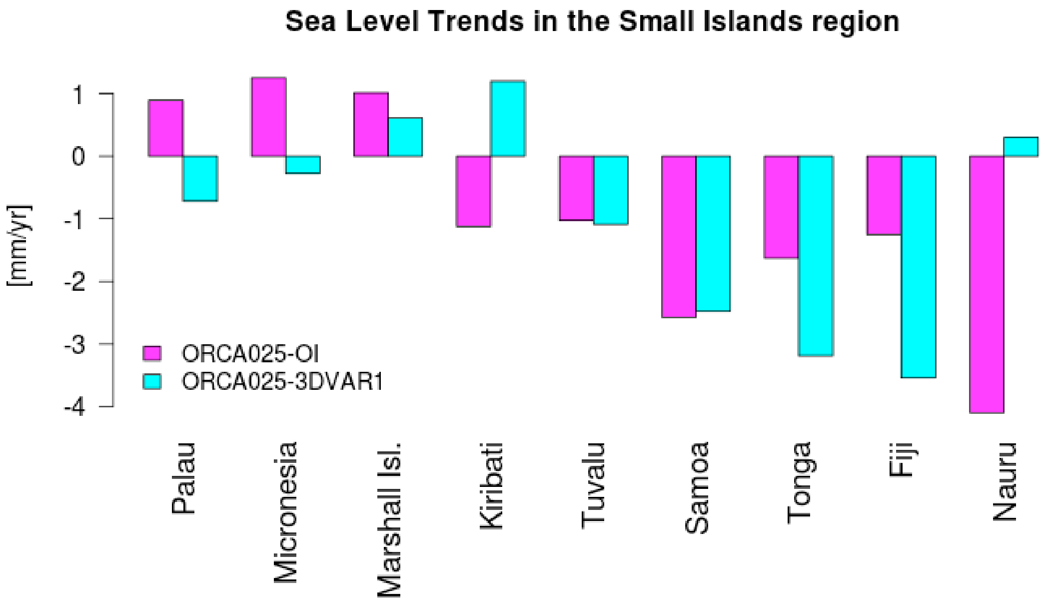

Figure 24- *Sea level trends in correspondence of nine selected Small Islands Developing States in the western Tropical Pacific, as projected by ORCA025-3DVAR1 and ORCA025-OI simulations.*

5.5- Conclusions and discussion

An eddy-permitting OGCM (NEMO-ORCA025), forced with two different sets of atmospheric fluxes from a coarser resolution coupled model (CMCC-CM), has been used to investigate global and regional sea level change in the next 20 years (2011-2030) under a medium-low GHG emission scenario. The two sets of atmospheric fluxes differ for the ocean initial conditions used in the coupled model predictions. With respect to previous studies, the resolution of our ocean model (0.25°) is able to represent a more detailed ocean dynamics with respect to the coarser resolution ocean components of coupled models, usually employed in sea level projections. This represents a major novelty of our method.

In order to assess the reliability of our approach, the model has been firstly validated over the last decade with satellite altimetry data, finding a correct simulation of the major sea level patterns.

In the next 20 years the projected sea level trend exhibits some robust spatial features in our simulations, in agreement with current 21st century AOGCMs sea level projections (Lowe and Gregory, 2006; Landerer et al., 2007; Suzuki and Ishii, 2011; Yin, 2012). These features include a dipole pattern in the North Atlantic and North Pacific with high values of sea level rise, up to 12 mm/yr, in the Kuroshio Current region; sea level rises in the Arctic Ocean and in the ACC region as well, the latter being in contrast with current AOGCMs projections that mostly agree on a sea level fall therein. Differently from the 20st century, when local sea level change have been mostly driven by variations in ocean temperature, in the next 20 years the regional sea level variability will be mostly influenced by its halosteric component. In fact, an increase of the Tropical Pacific precipitation and of sea-ice melting in the Arctic Ocean, as well as a freshening of the North Atlantic (north of 40°N) induced a deceleration of the subtropical gyre, will be the main driving factors of future sea level rise. On the other hand, the main cause of future global-mean sea level still remains the thermal sea water expansion. In particular, in accordance with previous works (e.g. Suzuki et al., 2005; Yin, 2012), in our simulations the global-mean sea level is expected to rise by 1.7 cm at the end of 2030.

By comparing the results of two projections driven by different atmospheric forcing, we can be more confident about the reliability of our results and, at the same, more cautious in the interpretation of future sea level change in areas that exhibit high spread values. Nevertheless, it is worthy to underline that two simulations are probably not sufficient to ensure the complete reliability of our results and a larger ensemble size would be more reliable for projecting future sea level change. The two projections generally agree on the main sea level features. The areas of higher uncertainty remain the one of strong mesoscale activity and, to a lesser extent, the western Tropical Pacific, which presents values of RMSD up to 10 cm. High RMSD in the Tropical Pacific is linked to differences in precipitation and solar radiation between the two sets of forcing, likely attributable to differences in the atmospheric moisture content between the two CMCC-CM simulations. It is interesting to notice how the impact of different atmospheric forcing grows in the first three years of simulation and the RSMD remains steady afterwards.

As a final remark, our sea level projections suggest that under a future mitigation emission scenario (RCP4.5), the SSH shows contained changes and the local sea level rise at most regions is of the same order of magnitude than 2001-2010 regional trends. These results suggest that GHG mitigation strategies can partially reduce the risk of future sea level rise and coastal communities might be able to adapt to its impacts. This result is of particular interest for coastal and highly vulnerable areas, such as the Pacific Small Islands region. Our projections show, in fact, that the majority of SIDS will not suffer from the impact of future sea level rise under a medium-low mitigation scenario. This is particularly true for the islands located south of 10°S (e.g. Tuvalu, Samoa, Tonga and Fiji) where sea level is expected to fall in both the simulations. North of this latitude, high uncertainties affect the results since the two simulations project opposite sea level trend. The territories most vulnerable to future sea level rise will be those located north of 18°N where the two projections agree on a future sea level rise, with peaks of 7-8 mm/yr, driven by a local sea water freshening induced by an increase in the Tropical Pacific precipitation.

In spite of the contained regional sea level change projected for the next two decades under the RCP4.5 mitigation scenario, it is important to underline that the global-mean sea level, even if steady during the first years of simulations, accelerates during the second decade of simulation and it is likely to continue increasing afterwards. For this reason, mitigation strategies considered in RCP4.5 seem not to be enough to fully prevent from impacts of future sea level rise.

In its 2007 report, the IPCC projected a global sea level rise of 18 to 59 cm from 1990 to the 2090s. But the physical climate models used by the IPCC have some limitations, since they do not have an accurate representation of the contribution to sea level rise due to changes in Greenland and Antarctica ice mass (Rahmstorf, 2010). By using past sea level and temperature data to quantify this effect, a number of recent studies have predicted much higher sea level rise for the 21st century, exceeding 1m the IPCC predictions, if GHG emissions continue to increase (Rahmstorf 2007; Grinsted et al., 2009; Jevrejeva et al., 2010). Hence, if the ice sheets will continue to give an important positive contribution to sea level, as discussed in Chapter 4, future sea level could change significantly. Given the observed accelerated mass loss of the Greenland ice sheet in the past decade and the divergent modelling results, it is important to further clarify what potential role, if any, the addition of the ice sheet melting flux into the climate system would play in the future global climate. For this reason, as future work, we plan to perform sea level projections including the ice sheets runoff contribution. In order to extrapolate ice sheets melting in the future, it is necessary to understand the main causes of the current melting and correlate them with the observed Greenland and Antarctica induced sea level change. While in Chapter 4 we have investigated the short-term impact that the ice sheets melting has on the ocean, such analysis will add the long-term impact of future Greenland and Antarctica ice sheets melting.

References

Ablain M., Cazenave A., Valladeau G., Guinehut S., 2009. A new assessment of the error budget of global mean sea level rate estimated by satellite altimetry over 1993–2008. *Ocean Science*, 5, 193-201.

Banks H., Wood R.A., Gregory J.M., 2002. Changes to Indian Ocean subantarctic mode water in a coupled climate model as CO_2 forcing increases. *J. Phys. Oceanogr.*, 32, 2816–2827.

Bellucci A., Gualdi S., Masina S., Storto A., Scoccimarro E., Cagnazzo C., Fogli P., Manzini E., Navarra A., 2012. Decadal climate predictions with a coupled OAGCM initialized with oceanic reanalyses. *Climate Dynamics*, DOI: 10.1007/s00382-012-1468-z. Published on-line.

Bellucci A., Gualdi S., Navarra A., 2010. The double-ITCZ syndrome in coupled general circulation models: the role of large-scale vertical circulation regimes. *J Clim* 23:1127–1145.

Bellucci A., Masina S., Di Pietro P., Navarra A., 2007. Using temperature salinity relations in a global ocean implementation of a multivariate data assimilation scheme. *Mon Wea Rev* 135:3785–3807.

Bryan, K., 1996. The steric component of sea level rise associated with enhanced greenhouse warming: A model study. *Climate Dyn.,* 12, 545–555.

Church J.A., White N.J., Aarup T., Wilson W.S., Woodworth P.L., Domingues C.A. et al., 2008. Understanding global sea levels: past, present and future. *Sustainability Science* 3, 9–22.

Clarke L., Edmonds J., Jacoby H., Pitcher H., Reilly J., Richels R., 2007. Scenarios of Greenhouse Gas Emissions and Atmospheric Concentrations. Sub-report 2.1A of Synthesis and Assessment Product 2.1 by the U.S. Climate Change Science Program and the Subcommittee on Global Change Research. Department of Energy, Office of Biological & Environmental Research, Washington, 7 DC., USA, 154 pp.

Dobricic S., Pinardi N., 2008. An oceanographic three-dimensional assimilation scheme. *Ocean Model* 22:89–105.

Ferrari R. and Paparella F., 2003. Compensation and alignement of thermohaline gradients in the ocean mixed layer. *J. Phys. Oceanogr.*, 33, 2214–2223.

Fichefet T., Morales-Maqueda M.A., 1999. Modeling the inuence of snow accumulation and snow-ice formation on the seasonal cycle of the Antarctic sea-ice cover. *Clim Dyn* 15:251–268.

Gregory J.M., Church J.A, Boer G.J., Dixon K.W., Flato G. M., Jackett D.R., Lowe J.A., O'Farrell S.P., Roeckner E., Russell G.L., 2001. Comparison of results from several AOGCMs for global and regional sea-level change 1900-2100. *Clim. Dyn.*, 18, 241–253.

Gregory J.M. and Huybrechts P., 2006. Ice-sheet contributions to future sea-level change. Philos. Trans. R. Soc. London Ser. A, 364, 1709–1731.

Grinsted A., Moore J.C., Jevrejeva S., 2009. Reconstructing sea level from paleo and projected temperatures 200 to 2100AD, Clim. Dyn., doi:10.1007/s00382-008-0507-2.

Jevrejeva S., Moore J.C., Grinsted A., 2010. How will sea level respond to changes in natural and anthropogenic forcings by 2100? Geophysical Research Letters 37 2010GL042947.

Landerer F.W., Jungclaus J.H., Marotzke J., 2007. Regional dynamic and steric sea level change in response to the IPCC-A1B scenario. *Journal of Physical Oceanography*, vol. 37, issue 2, p. 296-312.

Levitus S., Antonov J., Boyer T., 2005. Warming of the world ocean, 1955 – 2003. Geophys. Res. Lett., 32, L02604, doi:10.1029/2004GL021592.

Lowe J.A. and Gregory J.M., 2005. The effects of climate change on storm surges around the United Kingdom. Philos. Trans. R. Soc. London Ser. A., 363, 1313–1328.

Lowe J. A. and Gregory J. M., 2006. Understanding projections of sea level rise in a Hadley Centre coupled climate model. *J. Geophys. Res.*, 111, C11014, doi:10.1029/2005JC003421.

Madec G., Delecluse P., Imbard M., Lvy C., 1998. OPA 8.1 ocean general circulation model reference manual. *Note du Pole de Modlisation* 11, Institut Pierre-Simon Laplace, 91 p.

Mikolajewicz U. and Voss R., 2000. The role of the individual air–sea flux components in the CO2-induced changes of the ocean's circulation and climate. *Climate Dyn.,* 16, 627–642.

Moss R., Edmonds J., Hibbard K., Manning M., Rose S. et al., 2010. The next generation of scenarios for clmate change research and assessment. *Nature*, 463, 747-756.

Rahmstorf S., 2007. A semi-empirical approach to projecting future sea-level rise. *Science*; 315: 368–70.

Rahmstorf S., 2010. A new view on sea level rise. *Nature Reports Climate Change*, 1004, 44-45.

Roeckner E. et al., 2003. The atmospheric general circulation model ECHAM5. Part I: model description. MPI Rep 349, p 127.

Rudnick D.L. and Ferrari R., 1999. Compensation of horizontal temperature and salinity gradients in the ocean mixed layer. *Science*, 283, 526– 529.

Russell G.L., Gornitz V., Miller J.R., 2000. Regional sea-level changes projected by the NASA/GISS atmosphere-ocean model. *Clim. Dyn.*, 16, 789–797.

Scoccimarro E., Gualdi S., Bellucci A., Sanna A., Fogli P.G., Manzini E., Vichi M., Oddo P., Navarra A., 2011. Effects of tropical cyclones on ocean heat transport in a high resolution coupled general circulation model. *J Clim* 24:4368–4384.

Storto A., Dobricic S., Masina S., Di Pietro P., 2011. Assimilating along-track altimetric observations through local hydrostatic adjustment in a global ocean variational assimilation system. *Mon Wea Rev* 139:738–754.

Strauss B.H., Ziemlinski R., Weiss J.L., Overpeck J.T., 2012. Tidally-adjusted Estimates of Topographic Vulnerability to Sea Level Rise and Flooding for the Contiguous United States. *Environmental Research Letters* 7: 014033 10.1088/1748-9326/7/1/014033.

Suzuki T., Hasumi H., Sakamoto T. T., Nishimura T., Abe-Ouchi A., Segawa T., Okada N., Oka A., Emori S., 2005. Projection of future sea level and its variability in a high-resolution climate model: Ocean processes and Greenland and Antarctic ice-melt contributions. *Geophys. Res. Lett.*, 32, L19706, doi:10.1029/2005GL023677.

Suzuki T. and shii M., 2011. Regional distribution of sea level changes resulting from enhanced greenhouse warming in the Model for Interdisciplinary Research on Climate version 3.2. *Geophys. Res. Lett.*, 38, L02601, doi:10.1029/2010GL045693.

Thorpe A. J., Gregory J.M., Johns T.C., Wood R.A., Mitchell J.F.B., 2001. Mechanisms determining the Atlantic thermohaline circulation response to greenhouse gas forcing in a non-flux-adjusted coupled climate model. *J. Climate,* 14, 3102–3116.

Yin J., 2012. Century to multi-century sea level rise projections from CMIP5 models. *Geophys. Res. Lett.*, 39, L17709, doi:10.1029/2012GL052947.

Yin J., Griffies S.M., Stouffer R.J., 2010. Spatial variability of sea level rise in twenty-first century projections. *J Climate* 23:4585–4607.

Yin J., Overpeck J.T., Griffies S.M., Hu A., Russell J.L., Stouffer R.J., 2011. Different magnitudes of projected subsurface ocean warming around Greenland and Antarctica. *Nature Geosci.* doi:10.1038/ngeo1189.

Conclusions

This PhD thesis focusses on the study of sea level spatial and temporal variability over the global ocean and the investigation of the physical processes responsible for sea level changes. The study has been carried out by means of an eddy-permitting sea-ice/ocean general circulation model (NEMO_LIM2) for both the past and the next 20 years. Due to its high vulnerability to the impacts of sea level rise, particular attention has been dedicated to the western Tropical Pacific, where numerous Small Islands lie a few meters above the mean sea level.

Numerical models are a powerful tool for the investigation of sea level change and in general of the ocean state variability, particularly important in areas affected by lack of observations. They provide a unique chance for estimating past sea level before the satellite altimetry era and for projecting future sea level changes in the forthcoming decades. Nevertheless, numerical models are affected by several biases that could bring to a misleading simulation of the ocean state. We have devoted Chapter 2 to assess the skill of the model in simulating the main present-climate ocean features, in a comparative analysis with observational datasets.

Although the model performance was generally satisfactory, several biases were detected. With the aim to recover from theses biases, corrections to heat, momentum and precipitation air-sea fluxes used to force our model have been implemented. In the comparison with satellite observations we have shown that, with the improvements of the forcing fields that we have achieved, our model is able to correctly reproduce the past mean sea surface height and the regional variability of sea level and its components. Hence, even without data assimilation as many of the previous works take advantage of, our model configuration was proved to be a valid tool for sea level investigation.

In Chapter 3 we have investigated how sea level has changed during the last 20 years (1991-2010), within the different ocean basins, and whether some regions have undergone an acceleration/deceleration in the sea level evolution during the last years. Results show that in the East Pacific and South Atlantic the negative sea level trend has decelerated during the last decade (2001-2010) with respect to the previous one (1991-2000), passing from -5.01 to -3.2 mm/yr in the former and from -2.67 to -1.25 mm/yr in the latter. On the contrary, in the North Atlantic the positive sea level trend has slightly decreased between the two decades, passing from 3.37 to 2.01 mm/yr. The extreme case is the Indian Ocean, where the trend has reversed from negative to positive, falling by -1.49 mm/yr during the period 1991-2000 and rising by 1.45 mm/yr in the last decade. The West Pacific was found to be the region with highest values of sea level rise (3.63 mm/yr during 2001-2010) and hence the most sensitive to this event. We have also demonstrated that the main cause of global sea level changes can be attributed to variations in the ocean density, both in terms of regional trends and seasonal variability. In particular, in the Pacific and Indian Ocean most of sea level trend is induced by temperature variations in the upper 300 m, while in the Arctic and Atlantic Oceans, especially in the south, changes in the salinity field play the major role.

We have performed a regional sea level study on the Small Islands of Pacific, which is one of the most critical and highly sensitive region to sea level rise, in order to understand the causes that there drive sea level to increase. Our results show that the majority of the islands have suffered from sea level rise and in the last 20 years the locally averaged sea level has increased by 2.6 mm/yr. Three factors have been responsible for sea level rise in the Pacific Small Islands region: i) a warming of the near-surface sea waters due to a positive net downward heat flux (0.86 mm/yr); ii) a gain of heat transported by the North and South Equatorial Currents due to the warming of the incoming equatorial waters, which is not compensated by a corresponding heat loss from the region (0.54 mm/yr); iii) an increase in the freshwater transport from the western Pacific into the Small Islands region (0.87 mm/yr). While changes in temperature are concentrated between 100 and 300 m, salinity variations interest the first 100 m of depth only.

The freshwater input into the ocean as a result of land-ice loss and water exchange with terrestrial reservoirs is, together with the thermal expansion of the ocean, one of the two major causes of global sea level change. Furthermore, satellite-derived ice surface elevation combined with ice flux velocity data, have shown a rapid acceleration of ice discharge from Greenland and Antarctica ice sheets during the past two decades. This important source of sea level change is not taken into account in the simulations performed with current ocean models; in fact, due to the lack of time-varying runoff measurements, land and ice sheets runoff contributions are usually assumed not to vary inter-annually. In Chapter 4 we have addressed this important issue by creating a 2003-2010 interannual ice sheet runoff dataset according to the main drainage basin systems. The runoff has been at last used as input in our model simulation in order to detect the short-term response of the ocean, and in particular of sea level and its components, to a realistic ice sheets freshwater income, differently from previous works designed to study the sensitivity of ocean models to an idealized freshwater perturbation.

We have presented a novel method for the estimation of runoff from the ice sheets, showing that the use of satellite gravimetry data (GRACE), combined in the water mass balance equation with atmospheric model fluxes, is a proper strategy to estimate a realistic runoff. In particular our method has combined different gravimetric solutions and water fluxes from both an high resolution atmospheric regional model (RACMO) and global reanalysis (ERA-Interim). This is the first time that such a balance is applied on land-ice. We have also proved that the use of the combined land-atmosphere water mass balance equation led to a large underestimation of the runoff. Furthermore, our method has revealed to be weak for the estimation of Antarctica runoff, which shows an anomalous behavior with no seasonal cycle, due to uncertainties in the precipitation data and above all in gravimetry measurements.

The resulting runoff is significantly higher, by a factor of 20-30, than the climatological runoff previously used. In response of the enhanced and time-varying runoff the sea level rises generally everywhere around Greenland with peaks of 8 cm, off the southern and western coasts, with respect to the experiment using the climatological runoff. The cause of sea level rise is attributable to an increase in its eustatic component, although the halosteric contribution has important local effects particularly in the Baffin Bay. Furthermore, the enhanced income of freshwater produces a decrease of sea surface salinity, up to -0.5 psu, which propagates up to 300 m of depth. The freshening is mainly visible all around Greenland coasts and the freshwater is further advected in the Nordic Seas, in the Labrador Sea and in the North Atlantic subpolar gyre. In addition to a freshening of surface and subsurface waters, the enhanced runoff results in an offshore displacement of the warm core of Greenland rim currents, which in turn modifies the surface and subsurface temperature field. The enhanced input of freshwater has an impact, even if small, in reducing the convection at the site of deep water formation in the Labrador Sea, due to a decrease of salinity and hence of sea water density therein. The slight decline of the convective activity is reflected by a small reduction, up to 1 Sv, of the Atlantic Meridional Overturning Circulation (AMOC). It is worth to note that a time-scale of 8 years does not allow us to investigate the adjustment of the AMOC to enhanced melt water under present-day conditions, rather expected on decadal time-scales.

The use of the newly estimated runoff brings improvements in the attenuation of some model biases. The reduced convection in the Labrador Sea improves the mixed layer depth representation, especially in winter time, which is usually overestimated by the model. Positive impacts are also found in attenuating the model salty biases in the Baffin Bay and Davis Strait within the subsurface and surface waters, respectively.

To accomplish our sea level investigation, in Chapter 5 we have extended the analysis in the future by projecting global and regional sea level changes over the next 20 years and detected the causes of future sea level variations. Future sea level change is a topic of particular interest among the climate community, since global-mean sea level is expected to rise during the 21st century at an even larger rate with respect to the last century, as a result of anthropogenic greenhouse gases (GHG) induced global warming. The projections have been performed by forcing the ocean model with two different sets of atmospheric fluxes, provided by the CMCC-CM (Centro Euro-Mediterraneo per i Cambiamenti Climatici Climate Model), under the RCP4.5 scenario, which is a medium-low stabilization scenario that envisages a range of strategies for reducing GHG emissions before 2100. While most of the currently available projections are based on coarse resolution coupled model simulations (1° to 2°), our projections are performed at an unprecedented resolution of 0.25°, which is a major novelty in our approach allowing the representation of sea level mesoscale variability.

The reliability of our approach has been firstly assessed by validating the model, forced by the CMCC-CM air-sea fluxes, over the last decade. The model was found to capture the salient patterns of past sea level trend and this has motivated us to continue our investigation in the future.

According to our projections, in the next 20 years sea level is expected to rise in the North Atlantic (north of 40°N), in the Arctic Ocean and it will peak, at 12 mm/yr, in the Kuroshio Current region; both the North Atlantic and the North Pacific will be characterized by a dipole-like pattern. We have recognized the main cause of future sea level rise in the ocean freshening, which will be induced by an increase of precipitation in the Tropical Pacific, an enhanced sea-ice melting in the Arctic region and a reduced northward transport of salty water in the North Atlantic. In particular, in the North Atlantic a weakening of the Westerlies will produce a slowdown of the subtropical gyre, which in turn will reduce the transport of salty water to high latitudes, with a consequent increase of the halosteric sea level trend.

Caution should be paid in the interpretation of future sea level change in areas of strong mesoscale activity and, to a lesser extent, in the western Tropical Pacific, where the two projections differ significantly. The high spread in the Tropical Pacific is related to differences in precipitation and solar radiation between the two sets of forcing, likely attributable to differences in the atmospheric moisture content between the two CMCC-CM simulations. It is worth to underline that two simulations are probably not sufficient to ensure the complete reliability of our results and a larger ensemble size would be more reliable for projecting future sea level change.

Our simulations show that, in most regions, the projected 2011-2030 and the 2001-2010 local sea level rise is of the same order of magnitude. These results suggest that GHG mitigation strategies, as those considered in RCP4.5 emissions scenario, can partially reduce the risk of future sea level rise and coastal communities might be able to adapt to its impacts. This result is of particular interest for coastal and highly vulnerable areas, such as the Pacific Small Islands region. Our projections show, in fact, that the majority of Small Islands states will not suffer from the impact of future sea level rise. This is particularly true for the islands located south of 10°S (e.g. Tuvalu, Samoa, Tonga and Fiji) where sea level is expected to fall in both the simulations. North of this latitude, high uncertainties affect the results since the two simulations project opposite sea level behaviour. The Pacific islands most vulnerable to future sea level rise will be those located north of 18°N where the two projections agree on a future sea level increase, with peaks of 7-8 mm/yr, driven by a local sea water freshening induced by an increase in the Tropical Pacific precipitation.

While the halosteric sea level component will be the main driving factor for regional sea level change in the next 20 years, the main cause of future global-mean sea level still remains the thermal ocean expansion. In particular, in our projections the global-mean sea level is expected to rise by 1.7 cm at the end of 2030. It is important to underline that the global-mean sea level, even if rather steady during the first years, accelerates during the second decade of simulation and it is likely to continue increasing afterwards. For this reason, as a final remark, we can conclude that mitigation strategies considered in RCP4.5 scenario does not prevent from future global-ocean thermal expansion and the consequent sea level rise.

Studente: Ida Russo **matricola:** 955560

Dottorato: Scienza e Gestione dei Cambiamenti Climatici

Ciclo: 24°

Titolo della tesi : Sea Level changes over the Global Ocean in the XX and XXI centuries

Abstract.

As a major effect of anthropogenic greenhouse gases induced global warming, sea level rise is a key climate issue of crucial interest in the frame of climate change investigation. The aim of this Ph.D. thesis is to study the relative importance of the different processes that contribute to sea level change during the last decade of the 20th century and the first decade of the 21st century, by using an eddy-permitting Ocean General Circulation Model at a spatial resolution of 1/4°. We have further extended our analysis in the future, by providing projections of sea level change for the next 20 years at an unprecedented resolution of 0.25°, with particular focus on the Pacific Small Island region, which represents a highly vulnerable region to the impacts of sea level rise. The exchange of water between the ocean and Greenland and Antarctica ice-sheets is one of the major causes of sea level change. For this reason, the response of the ocean to a realistic ice-sheets runoff, reconstructed through a combination of gravimetric and atmospheric model data, has been investigated.

Riassunto.

L'innalzamento del livello del mare è una delle principali conseguenze del riscaldamento globale dovuto all'emissione di gas serra in atmosfera ed è quindi di cruciale interesse nello studio dei cambiamenti climatici. L'obiettivo di questa tesi di Dottorato consiste nell'analisi dell'importanza relativa dei vari processi che contribuiscono al cambiamento del livello del mare durante l'ultima decade del 20° secolo e il primo decennio del 21° secolo, mediante l'utilizzo di un modello numerico globale di circolazione oceanica ad alta risoluzione (1/4°). Lo studio è stato in seguito esteso nel futuro, fornendo proiezioni del cambiamento del livello del mare nei prossimo 20 anni e concentrando la nostra analisi sulla regione delle Piccole Isole del Pacifico, che rappresenta una delle aree più vulnerabili agli impatti legati all'innalzamento del livello del mare. Inoltre, la risposta dell'oceano a stime realistiche di scioglimento dei ghiacciai continentali di Antartide e Groenlandia, ricostruite a partire da dati gravimetrici e di modelli atmosferici, è stato investigato, essendo questa una delle principali cause del cambiamento del livello del mare.